ERDC TR-19-9

US Army Corps
of Engineers®
Engineer Research and
Development Center

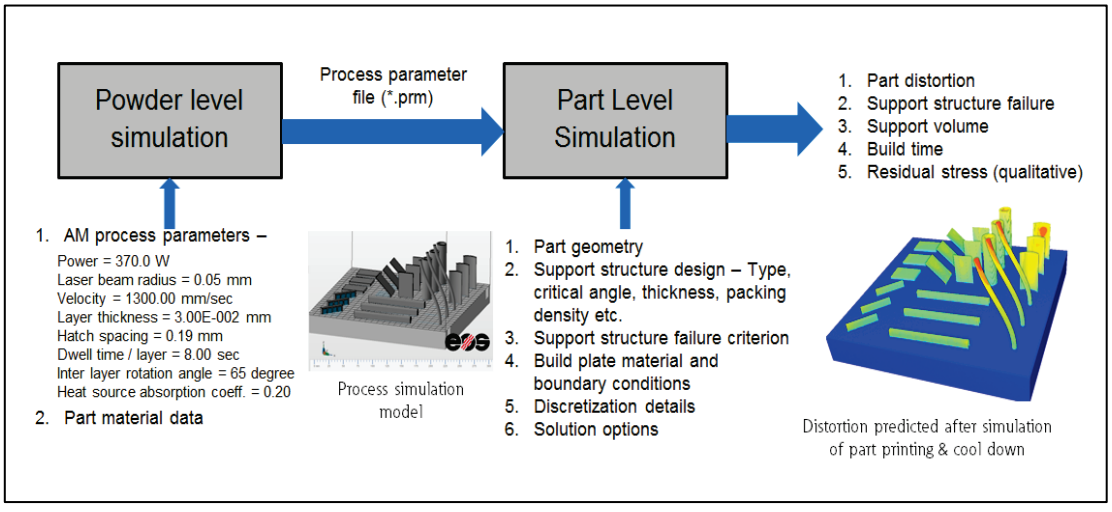
ERDC
ENGINEER RESEARCH & DEVELOPMENT CENTER

Additive Manufacturing of Metallic Materials with Controlled Microstructures

Multiscale Modeling of Direct Metal Laser Sintering and Directed Energy Deposition

Arjun Tekalur, Jacob Kallivayalil, Jason Carroll, Mike Killian,
Benjamin Schultheis, Anil Chaudhary, Zackery B. McClelland,
Jeffrey B. Allen, Jameson D. Shannon, and Robert D. Moser

July 2019



Approved for public release; distribution is unlimited.

Engineer Research and Development Center

The U.S. Army Engineer Research and Development Center (ERDC) solves the nation's toughest engineering and environmental challenges. ERDC develops innovative solutions in civil and military engineering, geospatial sciences, water resources, and environmental sciences for the Army, the Department of Defense, civilian agencies, and our nation's public good. Find out more at www.erdc.usace.army.mil.

To search for other technical reports published by ERDC, visit the ERDC online library at http://acwc.sdp.sirsi.net/client/default.

ERDC TR-19-9
July 2019

Additive Manufacturing of Metallic Materials with Controlled Microstructures

Multiscale Modeling of Direct Metal Laser Sintering and Directed Energy Deposition

Zackery B. McClelland, Jameson D. Shannon, and Robert D. Moser

Geotechnical and Structures Laboratory
U.S. Army Engineer Research and Development Center
3909 Halls Ferry Road
Vicksburg, MS 39180-6199

Jeffrey B. Allen

Information Technology Laboratory
U.S. Army Engineer Research and Development Center
3909 Halls Ferry Road
Vicksburg, MS 39180-6199

Arjun Tekalur, Mike Killian, Jason Carroll, and Jacob Kallivayalil

Eaton Corporation, Plc.
26201 Northwestern Hwy
Southfield, MI 48076

Benjamin Schultheis and Anil Chaudhary

Applied Optimization, Inc.
3040 Presidential Dr.
Suite 100
Fairborn, Ohio 45324

Final report

Approved for public release; distribution is unlimited.

Prepared for U.S. Army Corps of Engineers
Washington, DC 20314-1000

Under Project L31L42, “Additive Manufacturing”

Abstract

The report includes work conducted in a collaborative research and development program between Eaton Corporation and the U.S. Army Engineer Research and Development Center focused on novel multiscale modeling approaches to optimize metal additive manufacturing (AM) processes. The research focused on developing new lower-length scale thermal history predictions with microstructure to property relationships to computationally study a variety of manufacturing parameters and their correlation to defects generation and mechanical properties. Direct metal laser sintering (DMLS – a powder bed AM method) and directed energy deposition (DED – a blown powder AM method) were studied. The results indicated that the developed tools could rapidly predict optimal manufacturing parameters through fast running layer-by-layer thermal models of each respective AM process. Physical test specimens and prototypes were also produced as part of the study to aid in model calibration and validation through mechanical testing and microstructural characterization.

DISCLAIMER: The contents of this report are not to be used for advertising, publication, or promotional purposes. Citation of trade names does not constitute an official endorsement or approval of the use of such commercial products. All product names and trademarks cited are the property of their respective owners. The findings of this report are not to be construed as an official Department of the Army position unless so designated by other authorized documents.

DESTROY THIS REPORT WHEN NO LONGER NEEDED. DO NOT RETURN IT TO THE ORIGINATOR.

Contents

Abstract ... ii

Figures and Tables ... iv

Preface ... x

Unit Conversion Factors ... xi

1 Introduction ... 1
- 1.1 Objective ... 1
- 1.2 Report layout ... 1

2 Direct Metal Laser Sintering (DMLS) ... 2
- 2.1 Distortion ... 2
  - *2.1.1 Numerical prediction approaches* ... *2*
  - *2.1.2 Proposed numerical method* ... *3*
  - *2.1.3 Experimental validation* ... *15*
- 2.2 Residual stress ... 27
  - *2.2.1 Numerical method* ... *27*
  - *2.2.2 Preliminary validation* ... *28*
- 2.3 Porosity mitigation ... 31
  - *2.3.1 Numerical framework for porosity mitigation* ... *31*
  - *2.3.2 Design of Experiments (DOE)* ... *46*
  - *2.3.3 Experimental validation* ... *62*
- 2.4 Heterogeneity in microstructure ... 90
  - *2.4.1 Background* ... *90*
  - *2.4.2 Types of microstructural heterogeneity* ... *92*
  - *2.4.3 Control of microstructural heterogeneity* ... *93*
  - *2.4.4 Numerical method for heterogeneity prediction* ... *94*
  - *2.4.5 Experimental validation for minimization of nonuniformity of microstructure for alloy AlSi10Mg* ... *99*
- 2.5 Conclusions ... 108

3 Directed Energy Deposition ... 109
- 3.1 Manufacturing setup ... 109
- 3.2 Plate configurations ... 111
  - *3.2.1 Layered plates* ... *111*
  - *3.2.2 Functionally graded plates* ... *114*
- 3.3 Selected parameters, results, and key conclusions ... 123

References ... 133

Report Documentation Page

Figures and Tables

Figures

Figure 1. Hatch model (Keller and Ploshikhin 2014). 4
Figure 2. MLE (Keller and Ploshikhin 2014). 4
Figure 3. Cantilever specimens (Keller and Ploshikhin 2014). 5
Figure 4. Comparison of simulation results with experimental results (Keller and Ploshikhin 2014). 5
Figure 5. Alvarez's inherent shrinking method. 6
Figure 6. Depiction of scan strategies (Alvarez et al. 2016). 7
Figure 7. Cantilever deformation (Alvarez et al. 2016). 7
Figure 8. Model Layers (Alvarez et al. 2016). 8
Figure 9. Distortion comparison (Alvarez et al. 2016). 9
Figure 10. Cylinder calibration part. 10
Figure 11. Inherent shrinkage simulation steps. 13
Figure 12. Manual simulation, 3x magnitude. 14
Figure 13. Initial finite element temperature initialization. 14
Figure 14. Improved finite element temperature initialization. 15
Figure 15. Schematic of build plate with recoater direction indicated. 16
Figure 16. IN718 build plate with location of geometries indicated. 16
Figure 17. Laser scanning results. 17
Figure 18. Interpretation of distortion with respect to reference surface. 18
Figure 19. Distortion measurements for IN718 geometries A1-A3. 18
Figure 20. Distortion measurements for IN718 geometries B1-B3. 18
Figure 21. Distortion measurements for IN718 geometries C1-C3. 19
Figure 22. Distortion measurements for IN718 geometries P1-P. 19
Figure 23. Distortion measurements for IN718 geometries I1-I3. 19
Figure 24. Distortion measurements for IN718 geometries V1-V3. 20
Figure 25. Distortion measurements for IN718 geometries T1-T3. 20
Figure 26. Distortion measurements for IN718 geometries S1-S3. 20
Figure 27. Cylinder residual distortion. 22
Figure 28. Cantilever residual distortion. 23
Figure 29. Arch residual distortion. 24
Figure 30. Inclined plate residual distortion. 25
Figure 31. Vertical plate residual distortion. 25
Figure 32. Horizontal plate residual distortion. 26
Figure 33. Spiral residual distortion. 27
Figure 34. Overview of DMLS process simulation work flow. 28

Figure 35. In718 plates–Residual stress measurement using X-ray diffraction technique..... 29
Figure 36.Horizontal In718 Plate – Residual stress prediction per measurement set-up..... 29
Figure 37. 15-5 steel cylinders–Effect of process parameters on residual stress..... 31
Figure 38. Macro-scale simulation process..... 33
Figure 39. Meso-scale simulation process..... 35
Figure 40. ParaGen single-track mode (top) and double-track mode (bottom)..... 38
Figure 41. Poorly melted region..... 38
Figure 42. Criteria for adequate core melting..... 40
Figure 43. Criteria for adequate contour melting..... 40
Figure 44. Iterative approach to find adequate conditions..... 41
Figure 45. Macro-scale simulation..... 42
Figure 46. Layer-scale model of representative part: layer 4,600 of 7,000..... 42
Figure 47. Meso-scale simulation: core..... 43
Figure 48. Meso-scale simulation: contour..... 43
Figure 49. Micro-scale core simulation (default); melt pool (a); temperature (b)..... 44
Figure 50. Micro-scale contour simulation (default); melt pool (a); temperature (b)..... 44
Figure 51. Micro-scale contour simulation (AMP^2); melt pool (a); temperature (b)..... 44
Figure 52. Parameter matrix for each group of 15-5 PH SS cones..... 47
Figure 53. Melt-pool cross sections for A1/A2 default core/contour, B1/B2 middle condition core/contour, and C1/C2 end condition core/contour..... 48
Figure 54. Parameter matrix for each group of AlSi10Mg cones..... 49
Figure 55. Nth track simulations for 190-micron and 130-micron line spacing..... 50
Figure 56. Melt-pool cross section of parameter sets B1, B2, and B3 for the 75-deg cone..... 51
Figure 57. Rows B and C of the 90-deg cone..... 56
Figure 58. Row B of the 75-deg cone..... 57
Figure 59. Row C of the 75-deg cone..... 58
Figure 60. Row B of the 60-deg cone..... 59
Figure 61. Row C of the 60-deg cone..... 60
Figure 62. Row B of the 45-deg cone..... 61
Figure 63. Row C of the 45-deg cone..... 62
Figure 64. Un-etched xy-plane cross sections for 15-5 PH 90^o cones at 25x..... 64
Figure 65. Un-etched xy-plane cross sections for 15-5 PH 90^o cones at 100x..... 64
Figure 66. Un-etched yz-plane cross sections for 15-5 PH 90^o cones at 25x..... 65
Figure 67. Un-etched yz-plane cross sections for 15-5 PH 90^o cones at 100x..... 65
Figure 68. Un-etched xy-plane cross sections for 15-5 PH 75^o cones at 25x..... 66
Figure 69. Un-etched xy-plane cross sections for 15-5 PH 75^o cones at 100x..... 66
Figure 70. Un-etched yz-plane cross sections for 15-5 PH 75^o cones at 25x..... 67

Figure 71. Un-etched yz-plane cross sections for 15-5 PH 75° cones at 100x. 67
Figure 72. Un-etched xy-plane cross sections for 15-5 PH 60° cones at 25x. 68
Figure 73. High-resolution un-etched xy-plane cross-section for 15-5 PH cone A1-60. 69
Figure 74. High-resolution un-etched yz-plane cross-section for 15-5 PH cone A1-60. 69
Figure 75. Un-etched xy-plane cross sections for 15-5 PH 60° cones at 100x. 69
Figure 76. Un-etched yz-plane cross sections for 15-5 PH 60° cones at 25x. 70
Figure 77. Un-etched yz-plane cross sections for 15-5 PH 60° cones at 100x. 70
Figure 78. Un-etched xy-plane cross sections for 15-5 PH 45o cones at 25x. 71
Figure 79. Un-etched xy-plane cross sections for 15-5 PH 45° cones at 100x. 72
Figure 80. Un-etched yz-plane cross sections for 15-5 PH 45° cones at 25x. 72
Figure 81. Un-etched yz-plane cross sections for 15-5 PH 45° cones at 100x. 73
Figure 82. Un-etched xy-plane cross sections for AlSi10Mg 90° cones at 25x. 75
Figure 83. Un-etched xy-plane cross sections for AlSi10Mg 90° cones at 100x. 75
Figure 84. Un-etched yz-plane cross sections for AlSi10Mg 90° cones at 25x. 76
Figure 85. Un-etched yz-plane cross sections for AlSi10Mg 90° cones at 100x. 76
Figure 86. Un-etched xy-plane cross sections for AlSi10Mg 75° cones at 25x. 78
Figure 87. Un-etched xy-plane cross sections for AlSi10Mg 75° cones at 100x. 78
Figure 88. Un-etched yz-plane cross sections for AlSi10Mg 75° cones at 25x. 79
Figure 89. Un-etched yz-plane cross sections for AlSi10Mg 75° cones at 100x. 79
Figure 90. Un-etched xy-plane cross sections for AlSi10Mg 60° cones at 25x. 80
Figure 91. Un-etched xy-plane cross sections for AlSi10Mg 60° cones at 100x. 80
Figure 92. Un-etched yz-plane cross sections for AlSi10Mg 60° cones at 25x. 81
Figure 93. Un-etched yz-plane cross sections for AlSi10Mg 60° cones at 100x. 81
Figure 94. Un-etched xy-plane cross sections for AlSi10Mg 45° cones at 25x. 83
Figure 95. Un-etched xy-plane cross sections for AlSi10Mg 45° cones at 100x. 84
Figure 96. Un-etched yz-plane cross sections for AlSi10Mg 45° cones at 25x. 84
Figure 97. Un-etched yz-plane cross sections for AlSi10Mg 45° cones at 100x. 85
Figure 98. Summary of core-exposure porosity for the four groups of AlSi10Mg cones. 85
Figure 99. Build plate with AlMgSi10 cubes deposited. 86
Figure 100. Contours of constant percentage porosity. 87
Figure 101. Thumbnail representation of porosity micrographs for AlSi10Mg cubes. 88
Figure 102. Validation of process space identified by cube deposition experiments. 88
Figure 103. Single track welds on AlSi10Mg. 89
Figure 104. Example of conduction weld at (220 W, 600 mm/sec). 89
Figure 105. Example of keyhole weld at (340 W, 600 mm/sec). 89
Figure 106. Lack of fusion criterion based on melt pool dimensions. 90

Figure 107. Schematic of the type of solidification microstructure as a function of thermal gradient (G) and the liquid-to-solid interface velocity (R). 91
Figure 108. Herringbone pattern of as-built solidification microstructure. 92
Figure 109. Macro-scale simulation at a) Layer 300; b) Layer 4600..... 95
Figure 110. Meso-scale model of Representative part at a) First stripe; b) Second stripe; c) Third stripe; d) Sixth stripe. 96
Figure 111. Micro-scale prediction of the melt-pool for a) Core region; b) Contour region. 96
Figure 112. G and R for core region. 97
Figure 113. G and R for contour region..... 97
Figure 114. Notional prediction of grain growth and orientation for a zigzag scan of the core region. 98
Figure 115. Microstructure heterogeneity in between core and contour. 99
Figure 116. Etched xy-plane cross sections for AlSi10Mg 90° cones at 25x. 102
Figure 117. Higher magnification xy-plane cross sections for AlSi10Mg 90° cone C3-90..... 102
Figure 118. Higher magnification yz-plane cross sections for AlSi10Mg 90° cone C3-90..... 103
Figure 119. Etched xy-plane cross sections for AlSi10Mg 75° cones at 25x. 105
Figure 120. Etched xy-plane cross sections for AlSi10Mg 60° cones at 25x. 106
Figure 121. Etched xy-plane cross sections for AlSi10Mg 45° cones at 25x. 107
Figure 122. Early concept drawing Eaton-Fraunhofer elliptical coil. 110
Figure 123. Setup for simultaneous induction preheating and laser cladding of thick plates..... 110
Figure 124. Heat pattern from elliptical induction builds up near the end of the cladding pass. 111
Figure 125. Cross section of dual layer Inconel bond coat followed by dual layer Inconel 625 with injected Tungsten Carbide. 113
Figure 126. Plan view (top view) of Inconel 625 with injected tungsten carbide (black spheres). 113
Figure 127. Eight-layer functional graded material (FGM) coating. 114
Figure 128. Material properties for steady-state thermal-fluid simulation of 25 percent tungsten carbide-IN625 mixture on steel. 116
Figure 129. Comparison between observed simulation (top) and experimental (bottom) results for deposition of Tungsten Carbide + IN625 track on steel plate. 117
Figure 130. Results of two-track simulation (top) compared with experimental measurements (bottom). 118
Figure 131. Temperature distribution results from “part level” finite element simulation. 119
Figure 132. Process description for micro-scale simulation of “middle of the layer” tracks. 120
Figure 133. Dimensions required to achieve converged “middle of the layer” geometry..... 120

Figure 134. Simulation quality metrics, 1,400W, 1.5mm pitch x/y. 122
Figure 135. Remelt depth simulation results for building 35%WC+IN625 on IN625. 122
Figure 136. Dip magnitude simulation results for building 35%WC+IN625 on IN625. 123
Figure 137. Layer height simulation results for building 35%WC+IN625 on IN625. 123
Figure 138. Remelt depth simulation results for building IN625 on steel. 124
Figure 139. Dip magnitude simulation results for building IN625 on steel. 124
Figure 140. Layer height simulation results for building IN625 on steel. 125
Figure 141. Illustration of working distance. 125
Figure 142. Four-layer functional graded material (FGM) pads deposited with laser parameters predicted by the numerical model. 127
Figure 143. Computer selected parameter sets #2 and #4 were deposited at 1,400 W power. 128
Figure 144. Computer selected parameter sets #2 and #4 produced deposits that exhibits porosity (indicated by red arrows) in the cladding surface. 128
Figure 145. Eight-layer FGM pad prepared by laser directed energy deposition (DED). 129
Figure 146. Second trial of Computer-selected parameter sets #1 (Pad A) and #2 (Pad B). 129
Figure 147. Second trial of eight-layer FGM pad prepared by laser directed energy deposition (DED). 130
Figure 148. Micrograph of computer-selected parameter set #X. 131
Figure 149. Micrograph of eight-layer build bond-line. 131
Figure 150. Micrograph of eight-layer build surface. 132

Tables

Table 1. Material properties (Alvarez et al. 2016). 8
Table 2. Thermal expansion coefficients (Alvarez et al. 2016). 8
Table 3. Elastic properties for IN-718 (*Inconel Alloy 718* 2017). 11
Table 4. Plastic properties for IN-718 (JMatPro 2003). 12
Table 5. List of geometries. 16
Table 6. Summary of distortion values and error percentages. 21
Table 7. Horizontal In718 plate - Comparison of predicted residual stress with measurements. 30
Table 8. Required material properties. 36
Table 9. Required laser system parameters. 36
Table 10. Required environmental parameters. 37
Table 11. Required powder bed parameters. 37
Table 12. Contour processing conditions. 45
Table 13. Thermal conductivity. 46

Table 14. Parameter matrix for the 90-deg cone. 52
Table 15. Parameter matrix for the 75-deg cone. 52
Table 16. Parameter matrix for the 65-deg cone. 54
Table 17. Parameter matrix for the 45-deg cone. 55
Table 18. Percentage porosity measured by optical porosity. 87
Table 19. Variable parameters for parameter optimization work. 121
Table 20. Parameters for two layers of Inconel 625. 125
Table 21. Parameters for two layers of 35 percent Tungsten Carbide + Inconel 625. 126

Preface

This study was conducted for the Military Engineering Business Area under Project L32L43, "Additive Manufacturing." The technical monitor was Dr. Robert D. Moser.

The work was performed in collaboration with Eaton Corporation, Plc. and Applied Optimization, Inc. by the Concrete and Materials Branch (CMB) and the Research Group (RG) of the Engineering Systems and Materials Division (ESMD), U.S. Army Engineer Research and Development Center (ERDC) Geotechnical and Structures Laboratory (GSL). At the time of publication, Mr. Christopher M. Moore was Chief, CMB; Mr. Jeff Averett was Acting Chief, ESMD; and Mr. R. Nicholas Boone was the Technical Director for Force Projection and Maneuver Support. The Deputy Director of the ERDC-GSL was Mr. Charles W. Ertle, and the Director was Mr. Bartley P. Durst.

COL Ivan P. Beckman was the Commander of ERDC, and Dr. David W. Pittman was the Director.

Unit Conversion Factors

Multiply	By	To Obtain
angstroms	0.1	nanometers
British thermal units (International Table)	1,055.056	joules
degrees (angle)	0.01745329	radians
degrees Fahrenheit	(F-32)/1.8	degrees Celsius
feet	0.3048	meters
inches	0.0254	meters
microinches	0.0254	micrometers
microns	1.0 E-06	meters
mils	0.0254	millimeters
ounces (mass)	0.02834952	kilograms
pounds (force)	4.448222	newtons
pounds (force) per square inch	6.894757	kilopascals
pounds (mass)	0.45359237	kilograms

1 Introduction

This document is the final report of activities, findings, and technical accomplishments of the research project "Additive Manufacturing of Metallic Materials with Controlled Microstructures." Eaton Corporation carried out this project in collaboration with the U.S. Army Engineer Research and Development Center.

1.1 Objective

The primary objective of the project was to define a framework based on a strong analytical foundation that would help tailor material properties through additive manufacturing (AM) process optimization. The microstructures which were obtained through process optimization served as characterization/validation tools and provided metrics that helped to quantify desired mechanical properties such as strength, fatigue, blast resistance, ballistic impact resistance, etc. The project achieved several technical accomplishments that will greatly help in deciding the best course of action for AM practitioners. Some highlights are:

- Detailed analytical understanding of process related issues that will affect First Pass Yield in AM process [see Section 2.1 Distortion and Section 1.2 Residual Stress]
- State of the art method to address part quality in AM, including prediction of process parameters at critical regions [see Section 2.3 Porosity Mitigation]
- Integrated analytical framework that can concurrently address all the above issues
- Framework to provide insight into microstructures generated from the large thermal gradients in the AM process

1.2 Report layout

The report is broadly organized into two sections based on the AM process of focus: Section 1. Direct Metal Laser Sintering (DMLS) and Section 2. Directed Energy Deposition (DED). Each section describes processes and accomplishments in detail, starting from process basics to relevant factors which will help attain the ultimate goal of producing defect-free structures with tailored microstructures. After a brief introduction to the process, a section or second-level subsection describes the procedure followed, details experimental validation, and provides a reference list, as relevant.

2 Direct Metal Laser Sintering (DMLS)

DMLS is a powder-bed fusion process in which metallic parts are additively manufactured layer by layer. However, thermal stress accumulated in layer-by-layer build cycles of DMLS may induce part distortion or delamination and possibly cause the failure of the whole build process. DMLS process modeling plays an important role in proactively minimizing these manufacturing risks and provides the potential to develop tailor-made material properties within the part. DMLS process simulation is a multiscale thermo-mechanical problem wherein melt pool level and part-level, weakly-coupled, thermo-mechanical simulations are performed.

2.1 Distortion

2.1.1 Numerical prediction approaches

Several methods exist for predicting the distortion of additive manufacturing (AM) parts. The traditional method conducts a full fluid-thermal-stress simulation of each AM track. This type of simulation can take weeks, or months, to simulate a few millimeters of track. Simulating a whole part, which contains millions of tracks and is on the order of centimeters in size, would take years. This approach is impractical.

Most approaches in practice today use more approximate methods, which generally reduce the scale of the problem by considering an entire layer, or a group of layers, as bulk material. That is, the entire layer is added to the part all at once, rather than as individual segments of a single track. One method involves using a coupled thermal-stress method on a layer. The subcontractor, Applied Optimization (AO) implemented this method, but the run times were on the order of days and accurate distortion prediction relied on the availability of high-temperature material data. Two similar methods are the inherent strain method (Keller and Ploshikhin 2014) and the +inherent shrinkage method (Alvarez et al. 2016). The inherent strain method deposits layers which have been initialized at a layer-average-strain (calculated via another model). The inherent shrinkage method deposits layers at a pre-assigned temperature. The inherent shrinkage approach was the method of choice in this project; however, both the inherent strain method and the inherent shrinkage method are described

in some detail in the following paragraphs, as the former is used to justify the accuracy of the latter.

2.1.2 Proposed numerical method

This section describes the inherent shrinkage method, the approach used to predict distortion in AM parts.

2.1.2.1 *Validity and basic algorithm of inherent shrinkage method*

The validity of the inherent shrinkage method was justified using works by Megahed et al. 2016, Keller and Ploshikhin 2014, and Alvarez et al. 2016, and by describing the inherent strain method.

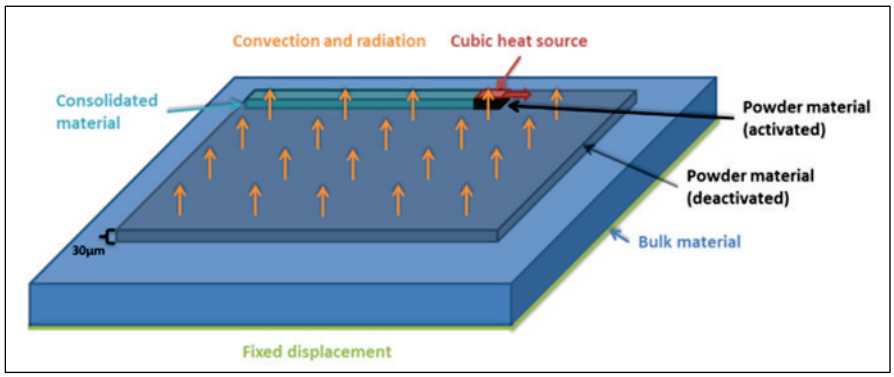
The paper by Megahed discusses prediction of distortion of AM parts through the inherent strain method. It references an earlier paper by Ueda, as one of the first to implement this method. The first step of this method is to perform a high-resolution prediction of the strain by simulating one or more layers of a small part in a transient thermo-mechanical analysis. Then, the average plastic strain components for the entire domain are computed and mapped to the actual part. Note that only plastic strains from the initial model should only be used after they have cooled to the ambient temperature. According to Megahed, this approach requires a complete static analysis to predict the final distortion of the part. It then cites the work by Keller and provides the following information:

> "Since this [inherent strain] technique has been largely validated for welding modeling, it has been adopted for AM and powder bed processes. Keller et al. applied this method for the modeling of a cantilever build process and could analyze the effects of the laser scan strategy on the final distortions of the workpiece (Megahed et al. 2016)."

Accordingly, Applied Optimization (AO) referenced the work of Keller, which describes an implementation of the inherent strain method for 316L Steel. Keller's work first predicts the approximate inherent strain. The paper calls this simulation the hatch model (see Figure 1). The hatch simulation is a 5-mm by 5-mm square with constant build direction. The simulation runs until the layer cools. Keller determines the inherent strain values by averaging the components of the total strain. Although the paper does not

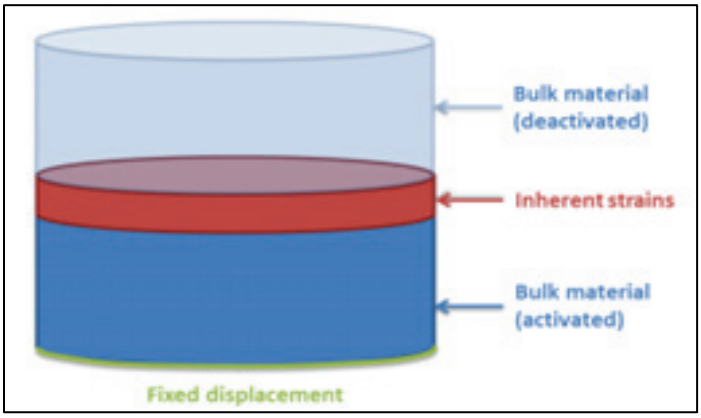
provide details, it states that the total strain distribution is a complex mixture of plastic and thermal strain. The principal components of strain values reported are: (-0.01, -0.001, -0.03) (Keller and Ploshikhin 2014).

Figure 1. Hatch model (Keller and Ploshikhin 2014).



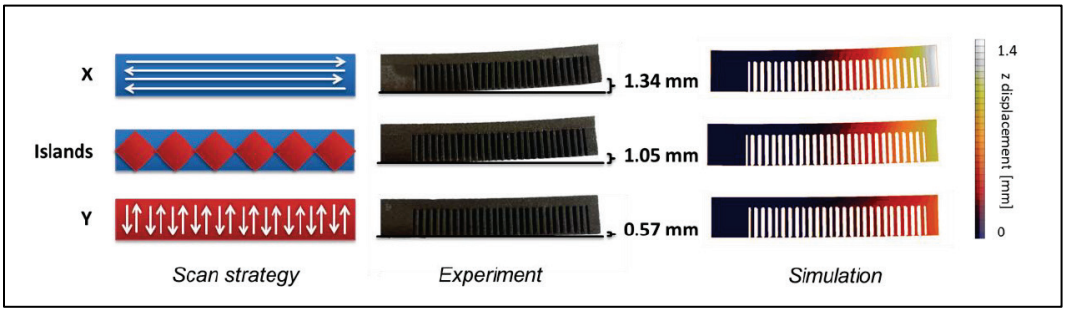
Keller refers to the entire part simulation as the layer simulation. It splits the part into horizontal slices consisting of several powder layers at a time. For the context of this report, AO referred to each of these slices, or groups of powder layers, as model layers. Initially, Keller deactivates all model layers and deposits each model layer one at time. When doing so, its algorithm initializes the model layer uniformly with the inherent strain components, runs a static simulation, deposits a new model layer initialized with the inherent strain, and continues the static analysis. This pattern proceeds until the deposition of all layers completes. Note that for each scan strategy, Keller rotates the inherent strain to match the build direction. Keller defines the initialization of inherent strain in the build direction as the Model Layer Equivalent (MLE) for the build orientation of that specific layer (see Figure 2).

Figure 2. MLE (Keller and Ploshikhin 2014).



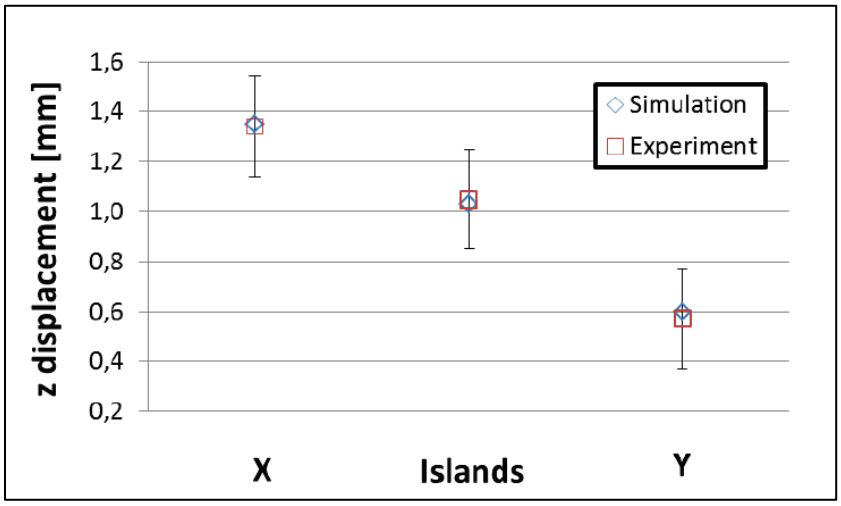
Keller validates the model predictions by manufacturing and simulating several cantilever specimens, shown in Figure 3. Each case has a different scan strategy. In the first case, the deposition is parallel to the length of the cantilever (the x direction). In the second case, the deposition is perpendicular to the length of the cantilever (the y direction). The third case combines parts of the previous two cases, depositing the part using an island scanning strategy.

Figure 3. Cantilever specimens (Keller and Ploshikhin 2014).



Keller compares the simulation results with the experimental results (Figure 4).

Figure 4. Comparison of simulation results with experimental results (Keller and Ploshikhin 2014).

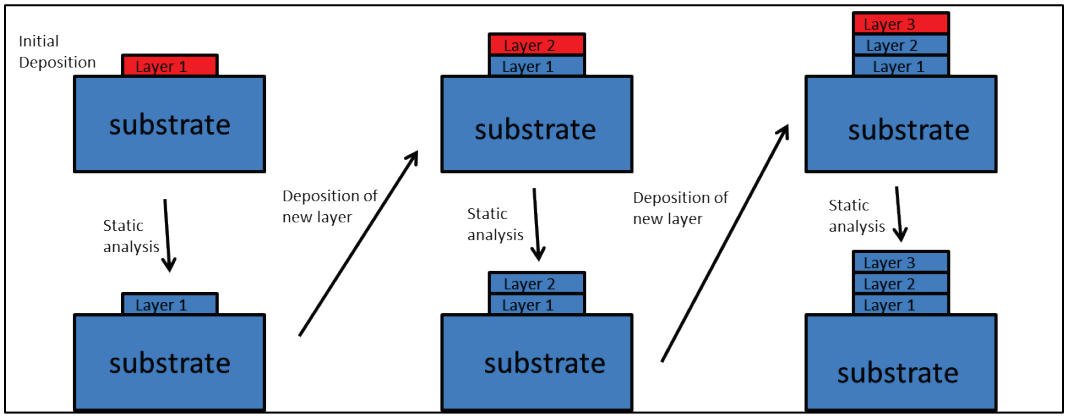


Note that the largest distortion comes from the first case (the x direction), the smallest distortion from the second case (the y direction), and the intermediate distortion comes from the island strategy. The simulation is in good agreement with the experiment.

Note that this method requires the solution of the hatch model. To implement this method, one must run the hatch model for every new material and every new set of build parameters. A better solution would be a method that does not require the hatch simulation, yet still predicts distortion. Note that the values of inherent strain reported by Keller are -0.01,-0.001, and -0.03; this is too small to include plastic strains. Plastic strains are typically larger than 3 percent. In any case, plastic deformation is incompressible. So, the trace of the principle strain components due to plastic strains must add to zero. The strains reported by Keller do not add to zero; therefore, it appears that the reported values are simply the thermal strains.

Alvarez et al. (2016) notes the use of the inherent strain approach as a common method for fast distortion prediction. Alvarez's method, which this report refers to as the inherent shrinkage method, is an attempt to create a simple, fast distortion prediction that does not rely on the use of a hatch model. The paper mentions that the inherent shrinkage method was developed for welding and, and like the inherent strain method, can be extrapolated to AM. The inherent shrinkage method assumes that the distortion is mainly due to the thermal contraction of the part during cooldown. Like the inherent strain method, the inherent shrinkage deposits model layers one at a time. It applies inherent shrinkage by initializing each layer uniformly with a high temperature value, such as the anneal temperature of the material, and by running a static analysis by cooling of the model layer to the ambient. This pattern proceeds until the deposition of all layers completes (see Figure 5).

Figure 5. Alvarez's inherent shrinking method.



Alvarez, like Keller, validates the model predictions by simulating and manufacturing several cantilever specimens, such as in Figure 6. Like Keller, each cantilever has a different scan strategy. In the first case, the deposition is parallel to the cantilever (the x direction). In the second case, the deposition is perpendicular to the cantilever (the y direction). The third case combines parts of the former two, by depositing the part in different scanning islands. Keller refers to this third strategy as island scanning, and Alvarez refers to this as the chess-board strategy (Figure 6). Note the model material is IN-718.

Figure 6. Depiction of scan strategies (Alvarez et al. 2016).

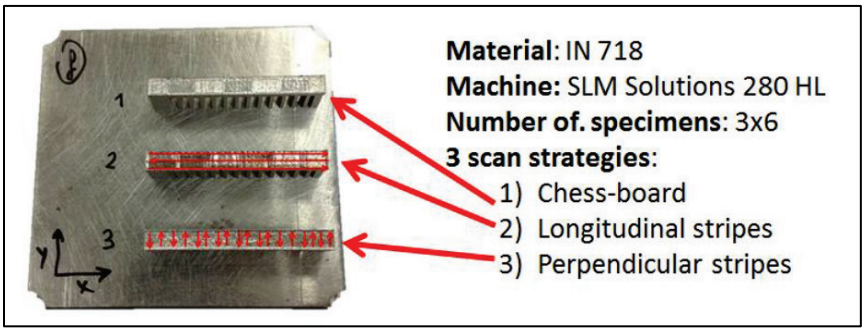
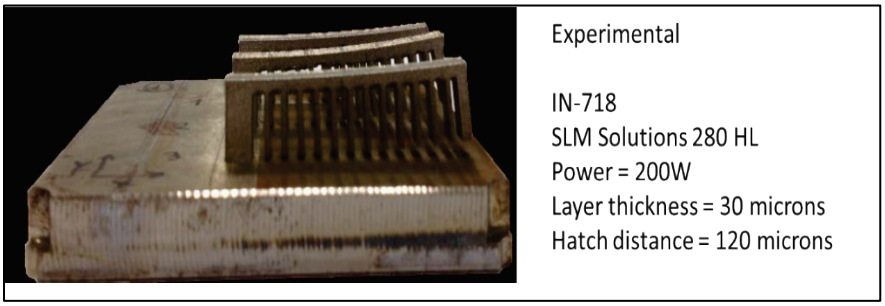


Figure 7 shows some of the manufactured cantilevers that demonstrate the deformations that occur after release of the part from the substrate. Note that this figure also contains the manufacturing parameters.

Figure 7. Cantilever deformation (Alvarez et al. 2016).



Alvarez reports the material properties shown in Table 1 in the simulation. Alvarez uses Abaqus™ software, v 6.14-2, to perform the simulation.

Table 1. Material properties (Alvarez et al. 2016).

INCO 718 MATERIAL PROPERTIES	
Mechanical properties	**Value**
Density (kg/m3)	8146
Young modulus (MPa)	210000
Poisson coefficient	0.38
Yield strength (MPa)	700
Ultimate strength (MPa)	900

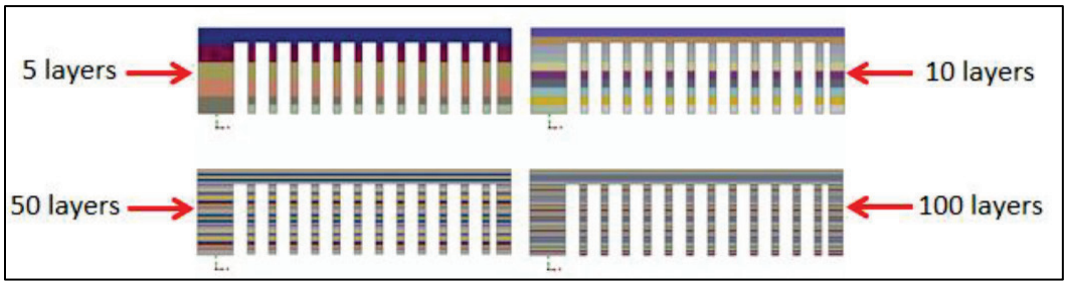
Like with Keller, Alvarez's simulation also accounts for scan strategy in the model. The simulation does so by assuming that each track will shrink more in the longitudinal direction than in any transverse direction. To implement this, Alvarez initializes orthotropic thermal expansion properties. That is, for printing in the x direction, this method assigns a higher thermal expansion coefficient along the x direction than in the y or z directions. Alvarez accommodates different scan strategies by rotating the thermal expansion coefficient values to match the given direction, analogous to Keller's work rotating the inherent strain. For the chess-board model, Alvarez assumes isotropic expansion coefficients. Table 2 shows the values of thermal coefficients used in the simulations.

Table 2. Thermal expansion coefficients (Alvarez et al. 2016).

COMPONENTS OF THERMAL EXPANSION COEFFICIENTS USED IN DIFFERENT MODELS			
	Vertical (Z)	**Longitudinal (X)**	**Transversal (Y)**
Model I – Isotropic $\alpha_{xx} = \alpha_{yy} = \alpha_{zz} = \alpha$	$1.28 \cdot 10^{-5}$	$1.28 \cdot 10^{-5}$	$1.28 \cdot 10^{-5}$
Model II – Orthotropic (longitudinal) $\alpha_{xx} = 2\alpha\,;\ \alpha_{yy} = \alpha_{zz} = \alpha$	$1.28 \cdot 10^{-5}$	$2.56 \cdot 10^{-5}$	$1.28 \cdot 10^{-5}$
Model III – Orthotropic (transversal) $\alpha_{yy} = 2\alpha\,;\ \alpha_{xx} = \alpha_{zz} = \alpha$	$1.28 \cdot 10^{-5}$	$1.28 \cdot 10^{-5}$	$2.56 \cdot 10^{-5}$

Alvarez presents simulation results for 5, 10, 50, and 100 model layers, as shown in Figure 8.

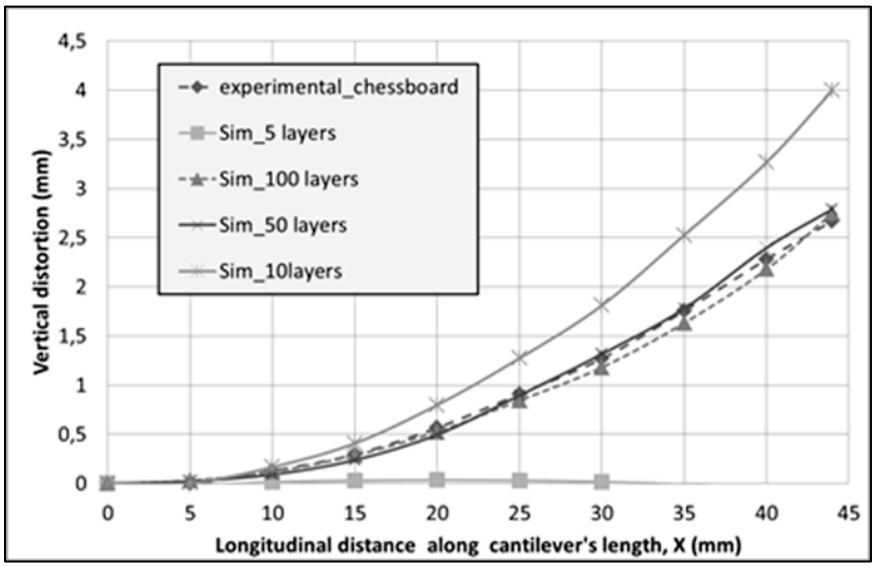
Figure 8. Model Layers (Alvarez et al. 2016).



The simulations initialize the model layers at 1,000, 1,500, and 2,000 C. Alvarez simulates for each combination of scan strategy, temperature, and number of model layers. For the 100-layer model, Alvarez uses 182,098 C3D8R hexagonal elements. This corresponds to a model layer thickness of 120 microns or four powder layers.

Alvarez reports the distortions in the manufactured parts at 10 points along the length of the cantilever. Alvarez compares the measured distortions to the simulated distortions. This comparison is shown for the chess-board strategy in Figure 9.

Figure 9. Distortion comparison (Alvarez et al. 2016).



Note that the simulation matches the experiment well when using 50 or more model layers. The 50-layer model corresponds to eight powder layers per model layer. The 100-layer model corresponds to four powder layers per model layer. Though it is not shown in the Figure 9, the lowest distortion came from the y direction strategy, the median distortion comes from the chess-board strategy, and the highest distortion comes from the x direction strategy. This relative relationship between scan strategies is similar to the conclusion reported by Keller. Alvarez notes that the difference in results between the 50- and 100-layer models was not significant, but that the 100-layer model took 3.5 times longer. This implies that eight powder layers per model layer could be considered a baseline, since the 50-layer model has sufficient accuracy. The 50-layer model took 2.3 hr on an Intel Core i7-3770 3.40 GHz microprocessor with four CPUs. The inherent shrinkage method has an advantage over the

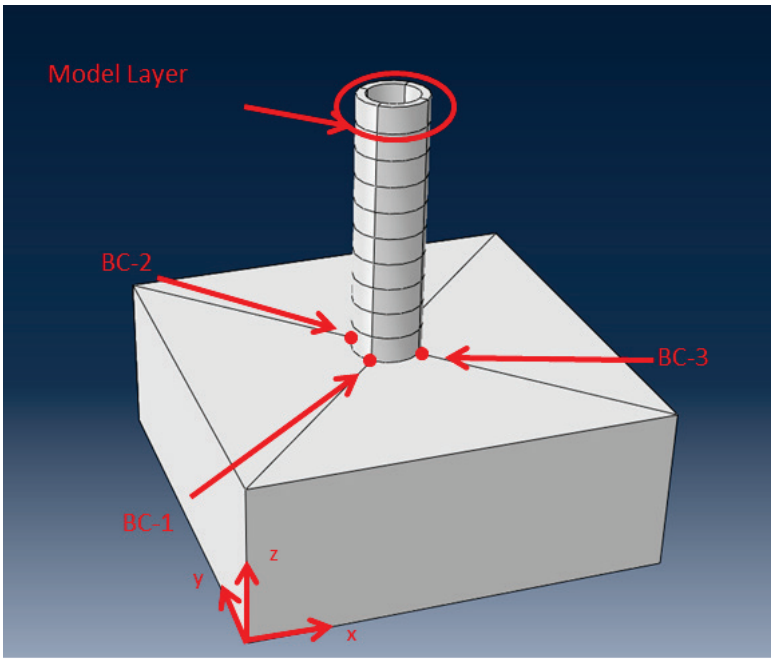
inherent strain method in that it produces reasonable results but is easier to set up. This is because it does not require a hatch model.

Based on these results, AO used the inherent shrinkage model by Alvarez to compute the residual distortions.

2.1.2.2 *Material data and original implementation*

This section describes additional details for the inherent shrinkage method. A simple simulation was manually created in Abaqus CAE to generate an Abaqus input file template. This template was used to create a program for automatic implementation. It also serves to illustrate the procedure. For both these reasons, this simulation used only 10 model layers. The part simulated was a cylinder, one of the calibration parts discussed here. Given the height of the cylinder, 63.5 mm, note that the use of 10 model layers is insufficient to obtain an accurate result. The Abaqus™ part used for this initial simulation is shown in Figure 10.

Figure 10. Cylinder calibration part.



AO created this part manually using Abaqus™ CAE. AO created the model layers using an AO utility software that automatically slices the geometry defined within the Abaqus™ CAE as per a user-defined input. AO created mechanical boundary conditions using the points labeled BC-1, BC-2, and

BC-3. AO constrained BC-1 in all three coordinate directions, BC-2 in the x and z directions, and BC-3 constrained only in the z direction.

BC-1 prevented rigid body translation. BC-1 combined with BC-2 restricted rotation along the line connecting them. BC-3 combined with the latter two prevented all rigid body rotation. The combination of boundary conditions allowed the part to warp and deform, while preventing all rigid body motion. Next, AO placed the points from Figure 10 on the face between the cylinder and the substrate, thus the boundary conditions would hold during all deposition steps and during substrate removal.

Since the inherent shrinkage method used only static analyses, the model required only mechanical properties: elastic modulus, Poisson's ratio, yield stress, and linear thermal expansion coefficient. The yield stress may be a function of plastic strain and strain rate. Properties may be temperature dependent or temperature independent. Note that Alvarez uses temperature-independent properties. AO's simulations used temperature-dependent properties and gave yield stress as a tabular function of plastic strain. See Table 3 and Table 4 for the material properties.

Table 3. Elastic properties for IN-718 (*Inconel Alloy 718* 2017).

Linear Expansion Coefficient 1/K	Temperature K
0.0000128	294
0.0000128	366
0.0000135	477
0.0000139	589
0.0000142	700
0.0000144	811
0.0000151	922
0.0000161	1033
0.0000162	1227

Elastic Modulus (Pa)	Poisson's Ratio	Temperature (K)
2.05E+11	0.311	298
1.99E+11	0.314	400
1.92E+11	0.317	500
1.86E+11	0.321	600
1.79E+11	0.324	700
1.72E+11	0.328	800
1.65E+11	0.331	900
1.58E+11	0.335	1000
1.5E+11	0.338	1100
1.41E+11	0.342	1200
1.33E+11	0.346	1300
1.21E+11	0.35	1373
89400000000	0.358	1400
63900000000	0.372	1423
35500000000	0.39	1500
22200000000	0.403	1528
922000000	0.456	1610

Table 4. Plastic properties for IN-718 (JMatPro 2003).

Yeild Stress (Pa)	Plastic Strain	Temperature (K)
634000000	0	293
638000000	0.0004	293
643000000	0.0008	293
647000000	0.0012	293
651000000	0.0016	293
655000000	0.002	293
659000000	0.003	293
664000000	0.004	293
668000000	0.005	293
672000000	0.006	293
677000000	0.007	293
681000000	0.008	293
685000000	0.009	293
689000000	0.01	293
743000000	0.02	293
796000000	0.03	293
883000000	0.05	293
1050000000	0.1	293

Yeild Stress (Pa)	Plastic Strain	Temperature (K)
589000000	0	588.56
592000000	0.0004	588.56
594000000	0.0008	588.56
597000000	0.0012	588.56
599000000	0.0016	588.56
602000000	0.002	588.56
605000000	0.003	588.56
608000000	0.004	588.56
611000000	0.005	588.56
614000000	0.006	588.56
617000000	0.007	588.56
621000000	0.008	588.56
624000000	0.009	588.56
627000000	0.01	588.56
681000000	0.02	588.56
735000000	0.03	588.56
814000000	0.05	588.56
951000000	0.1	588.56

Yeild Stress (Pa)	Plastic Strain	Temperature (K)
469000000	0	921.89
480000000	0.0004	921.89
491000000	0.0008	921.89
502000000	0.0012	921.89
513000000	0.0016	921.89
524000000	0.002	921.89
532000000	0.003	921.89
540000000	0.004	921.89
548000000	0.005	921.89
556000000	0.006	921.89
564000000	0.007	921.89
572000000	0.008	921.89
580000000	0.009	921.89
587000000	0.01	921.89
643000000	0.02	921.89
691000000	0.03	921.89
749000000	0.05	921.89
838000000	0.1	921.89

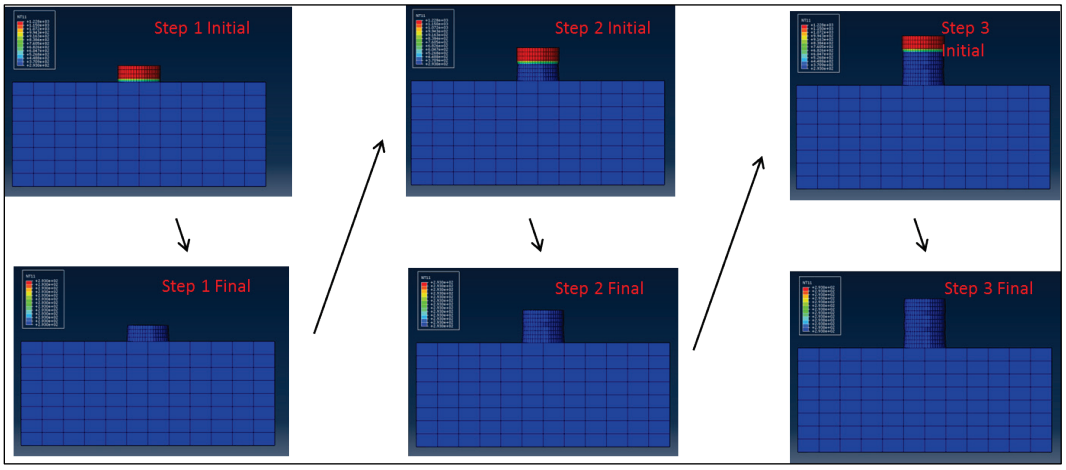
Yeild Stress (Pa)	Plastic Strain	Temperature (K)
221000000	0	1033
223000000	0.0004	1033
226000000	0.0008	1033
229000000	0.0012	1033
232000000	0.0016	1033
234000000	0.002	1033
241000000	0.003	1033
247000000	0.004	1033
254000000	0.005	1033
260000000	0.006	1033
267000000	0.007	1033
273000000	0.008	1033
280000000	0.009	1033
286000000	0.01	1033
319000000	0.02	1033
344000000	0.03	1033
379000000	0.05	1033
425000000	0.1	1033

Yeild Stress (Pa)	Plastic Strain	Temperature (K)
73900000	0	1144.11
74300000	0.0004	1144.11
74700000	0.0008	1144.11
75100000	0.0012	1144.11
75600000	0.0016	1144.11
76000000	0.002	1144.11
76400000	0.003	1144.11
76800000	0.004	1144.11
77300000	0.005	1144.11
77700000	0.006	1144.11
78100000	0.007	1144.11
78600000	0.008	1144.11
79000000	0.009	1144.11
79400000	0.01	1144.11
82400000	0.02	1144.11
84500000	0.03	1144.11
87100000	0.05	1144.11
89600000	0.1	1144.11

Yeild Stress (Pa)	Plastic Strain	Temperature (K)
25500000	0	1255.22
25600000	0.0004	1255.22
25800000	0.0008	1255.22
25900000	0.0012	1255.22
26100000	0.0016	1255.22
26300000	0.002	1255.22
26500000	0.003	1255.22
26800000	0.004	1255.22
27100000	0.005	1255.22
27400000	0.006	1255.22
27600000	0.007	1255.22
27900000	0.008	1255.22
28200000	0.009	1255.22
28400000	0.01	1255.22
30300000	0.02	1255.22
32200000	0.03	1255.22
34100000	0.05	1255.22
37900000	0.1	1255.22

Next, the input data initialized the cylinder at 1,228 K, which equals the annealing temperature for IN-718. The initial temperature of the substrate was 293 K. During the first step, the simulation removed all model layers, except the first one, from the mesh. The simulation assigned the temperature of the first layer to equal the temperature of the substrate, to compute the thermal strain, and then performed a static analysis. To start the second step, the simulation added the second model layer, previously initialized at 1,228 K, and then assigned its temperature to equal the substrate temperature and performed static analysis. The process repeated until every model layer deposited and cooled (see Figure 11).

Figure 11. Inherent shrinkage simulation steps.



In the final step, the simulation removed the substrate and performed a static analysis. Figure 12 shows the results. Please note that the deformation shown was scaled by a factor of three.

2.1.2.3 *Improved implementation*

When the method previously described was used to predict the distortion of the calibration parts, the predicted distortions were much smaller than those measured by CEED. Applied Optimization discovered that the smaller distortions were the result of the temperature initialization of the layers in the model. In each layer, all of which were one element thick, only the top nodes were given the annealing temperature (1,228 K) as the initial temperature (see Figure 13). For the linear elements, this meant the temperature linearly decreased from the top of the element to the bottom of the element, where the temperature was set to the ambient, 293 K, thus the nodes did not change temperature at all at the bottom of the element. This condition restricted the amount of shrinkage possible for each layer.

Figure 12. Manual simulation, 3x magnitude.

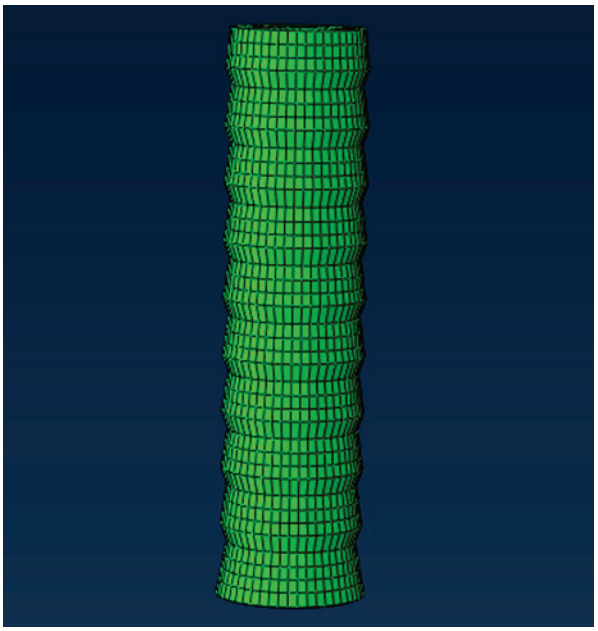
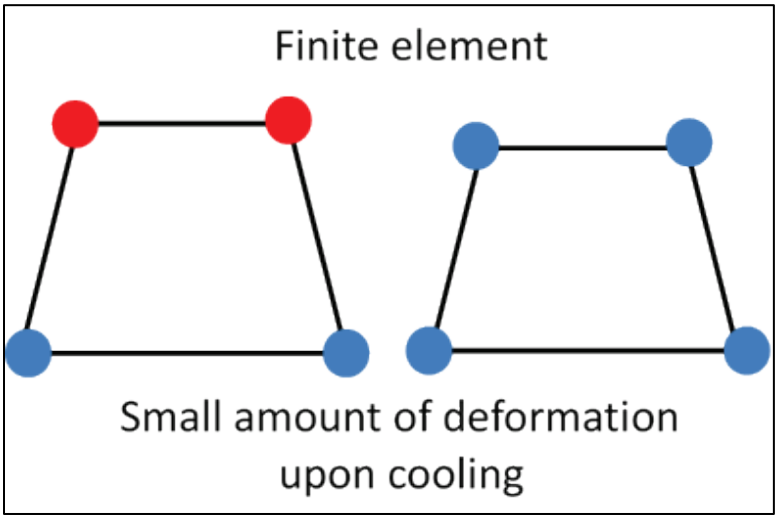
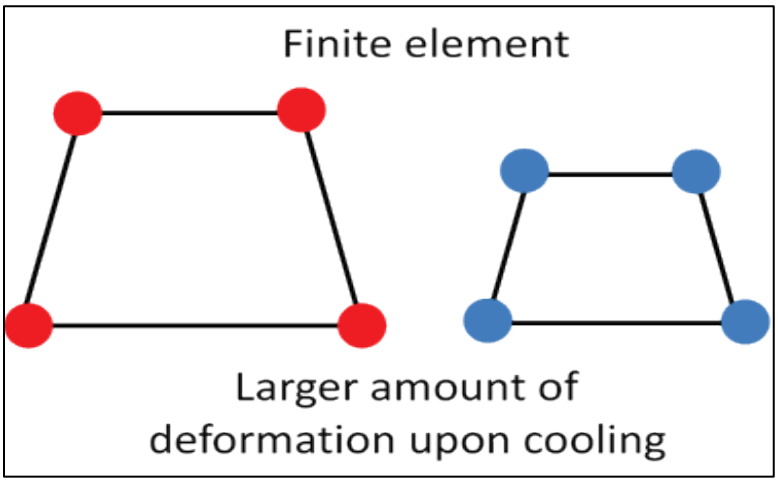


Figure 13. Initial finite element temperature initialization.



When the entire element is initialized at the annealing temperature, as in Figure 14, the amount of shrinkage increases. Applied Optimization resimulated the calibration parts, with the entirety of each new layer initialized at the annealing temperature.

Figure 14. Improved finite element temperature initialization.



2.1.3 Experimental validation

To facilitate comparison with the numerical predictions using two different tools (Applied Optimization and Netfabb), standard geometries were fabricated and subsequent distortion measurements were taken. The distortion in the build direction is critical as it has the potential for recoater blade interference. It is also important for the overall distortion at the end of the build to satisfy geometric and dimensional tolerances. While the numerical models can predict the distortion during the build and for the final geometry after cool down, the measurements for validating numerical predictions were only done on the final geometry because measurements of distortions cannot be taken during the build.

The geometries selected are varied in shape, cross-sectional area, orientation, and presence or absence of support structures. The geometries are shown schematically in Figure 15 and are listed in Table 5. These geometries reflect the variety one is likely to encounter in practice. Further, the location and orientation on the build plate can influence the distortion. The specimens are oriented such that their cross sections experience the minimum interference in the direction of the recoater blade movement. The orientation with respect to the recoater blade is to ensure that in the event of contact with the recoater blade there is minimum distortion due to the contact, ensuring a successful build. The direction of the recoater blade motion is indicated in Figure 15. The geometries were built using Inconel IN718 as shown in Figure 16. The standard build parameters recommended by the machine manufacturer for the respective materials for the EOS 290 printer were utilized to build the geometries.

Figure 15. Schematic of build plate with recoater direction indicated.

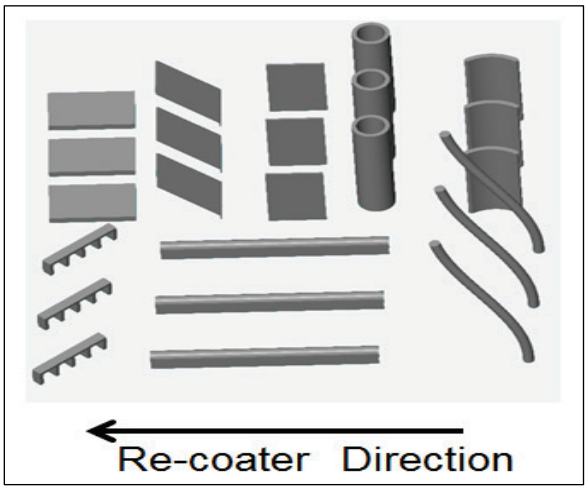
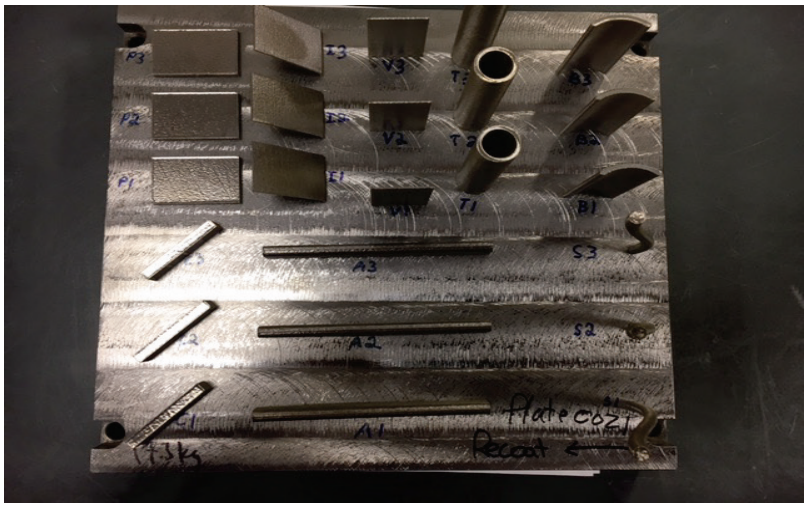


Table 5. List of geometries.

Part type	Part identification
Arch	A1, A2, A3
Blade section	B1, B2, B3
Cantilever beam	C1, C2, C3
Horizontal plate	P1, P2, P3
45° Inclined plate	I1, I2, I3
Vertical plate	V1, V2, V3
Cylindrical tower	T1, T2, T3
Spiral	S1, S2, S3

Figure 16. IN718 build plate with location of geometries indicated.

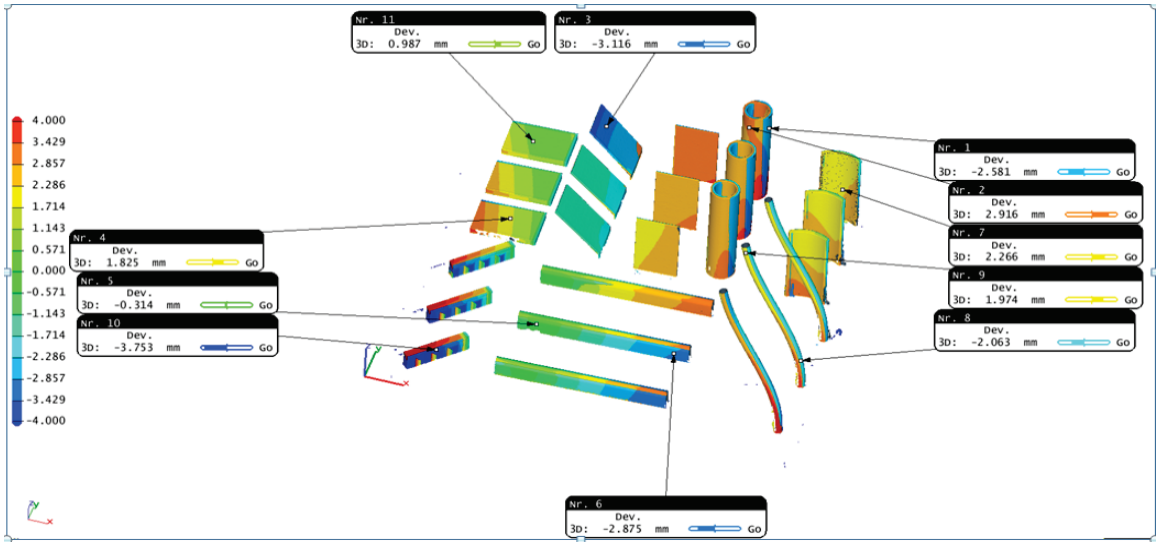


Three methods of distortion measurement in DMLS build plates were considered:

1. Contact probe CMM
2. White light/blue light scanning
3. Laser light scanning

The contact probe is time-consuming and white light scanning involves additional steps for specimen preparation. Given these constraints, laser scanning was the preferred method for distortion measurement. The summary of results from laser scanning the whole build plate is presented in Figure 17.

Figure 17. Laser scanning results.



The measured distortion is in the normal direction with respect to a reference surface defining the CAD geometry. To determine the position of the reference surface, a best-fit curve was generated between the CAD geometry attached to a flat surface and the laser scanned geometry near the base plate. The normal-to-the-reference surface was calculated and the point of intersection between the normal and the laser-scanned surface (comparison surface) was determined. The distortion is positive if the intersection occurs along the outward-normal-to-the-reference surface and negative if the intersection is along the inward-normal-to-the-reference surface as illustrated in Figure 18. Distortion plots for each part thus obtained are shown in Figure 18 through Figure 26.

Figure 18. Interpretation of distortion with respect to reference surface.

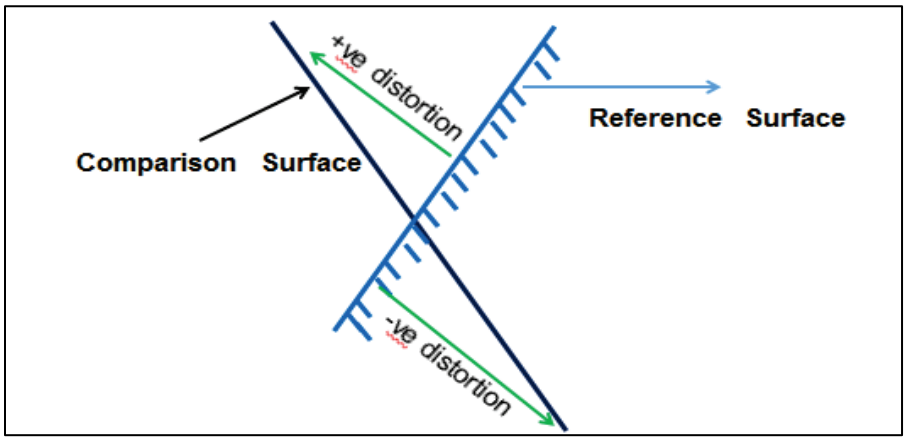


Figure 19. Distortion measurements for IN718 geometries A1-A3.

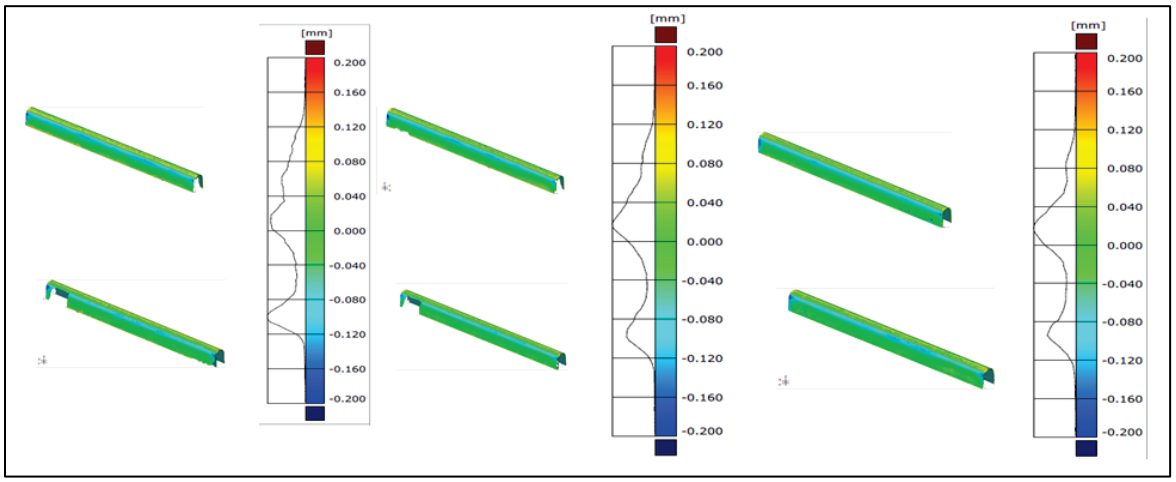


Figure 20. Distortion measurements for IN718 geometries B1-B3.

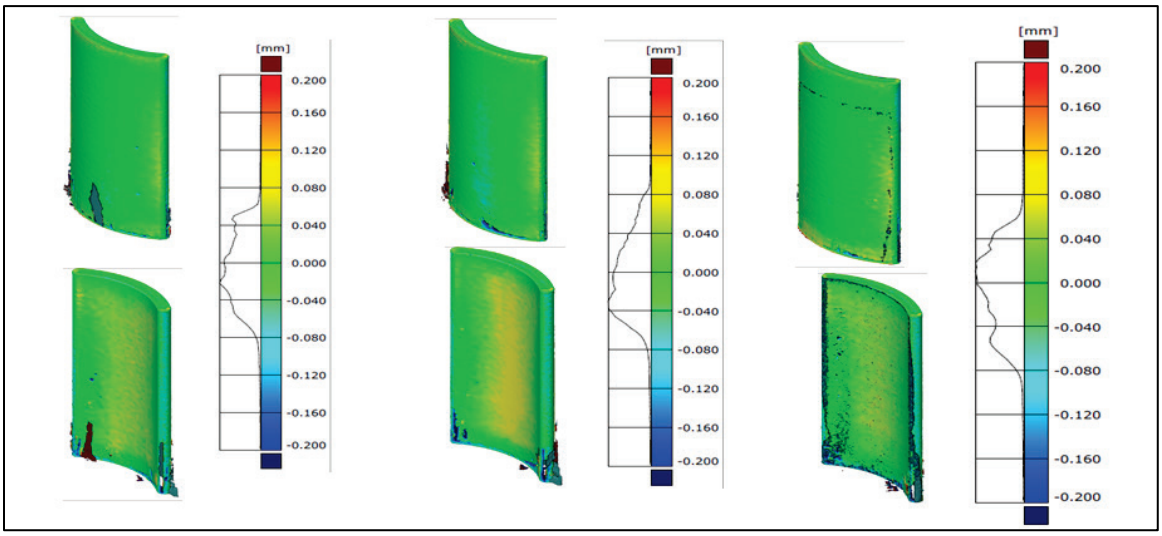


Figure 21. Distortion measurements for IN718 geometries C1-C3.

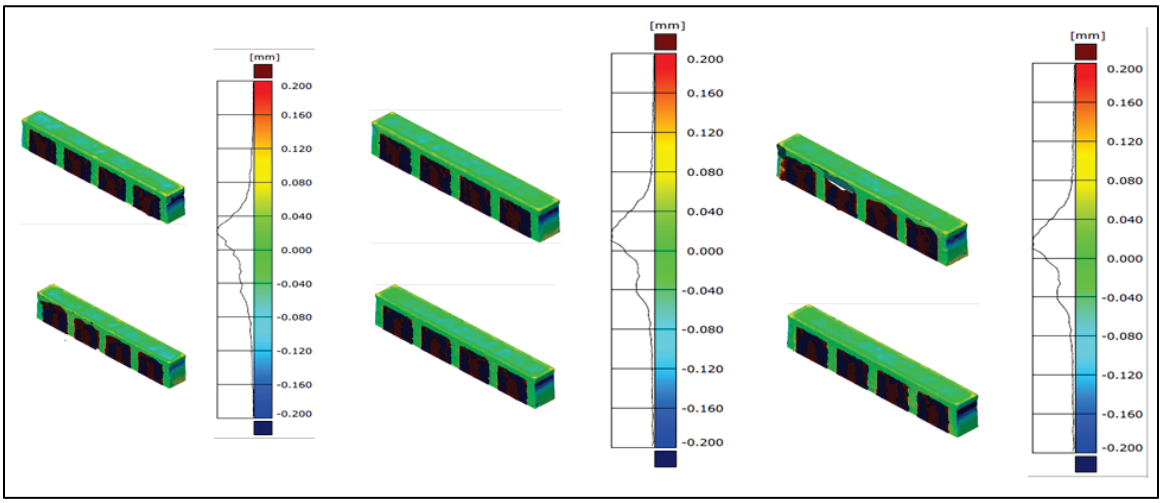


Figure 22. Distortion measurements for IN718 geometries P1-P.

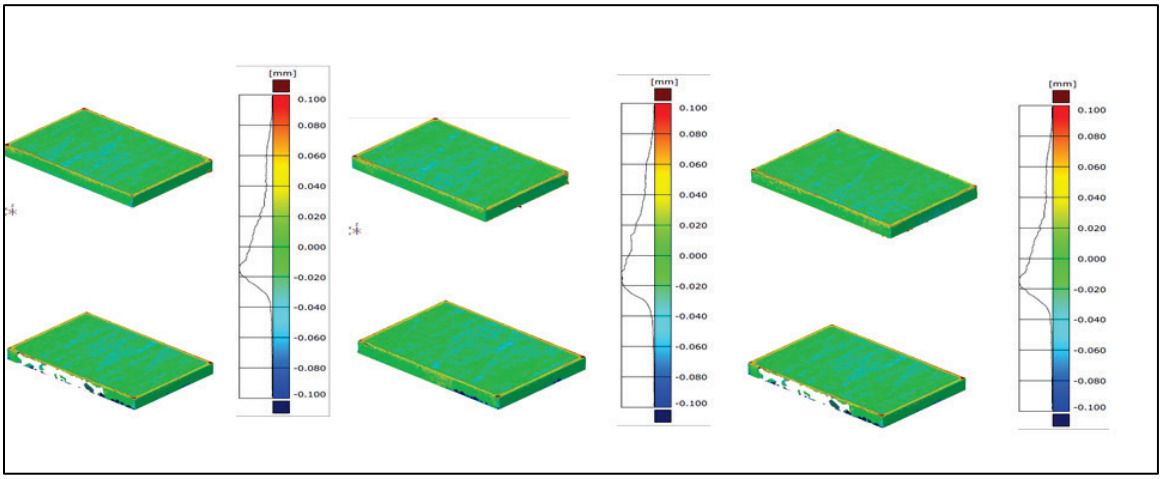


Figure 23. Distortion measurements for IN718 geometries I1-I3.

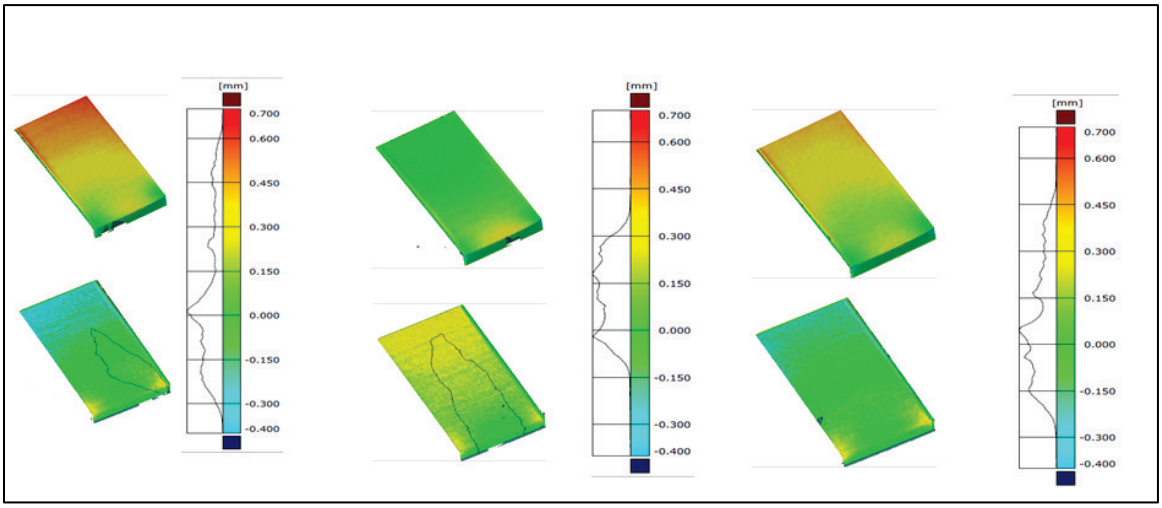


Figure 24. Distortion measurements for IN718 geometries V1-V3.

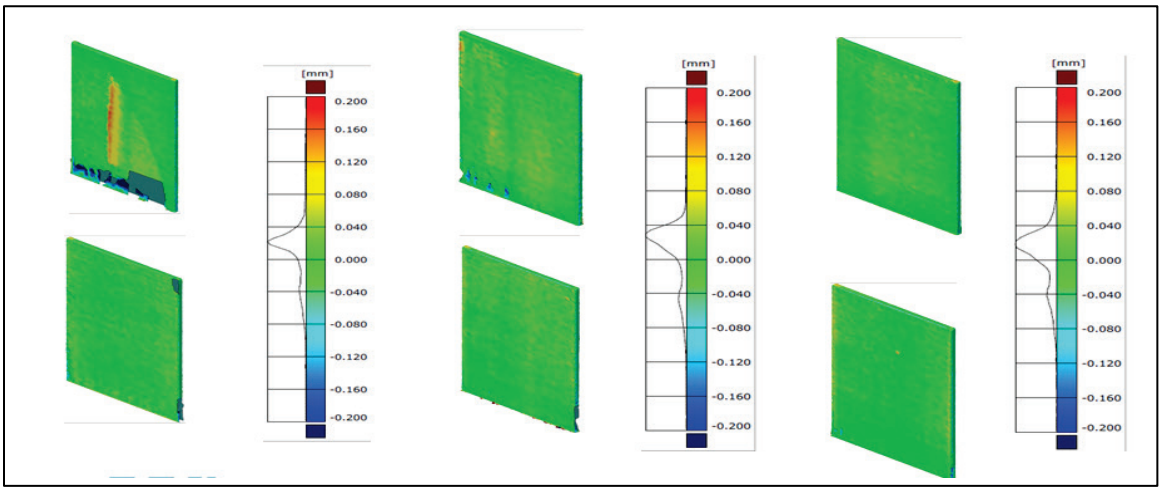


Figure 25. Distortion measurements for IN718 geometries T1-T3.

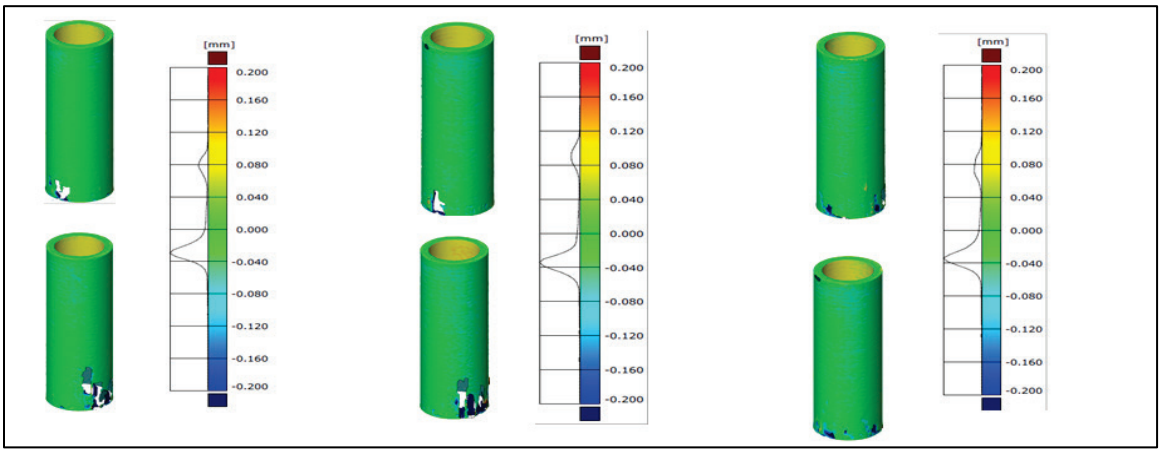
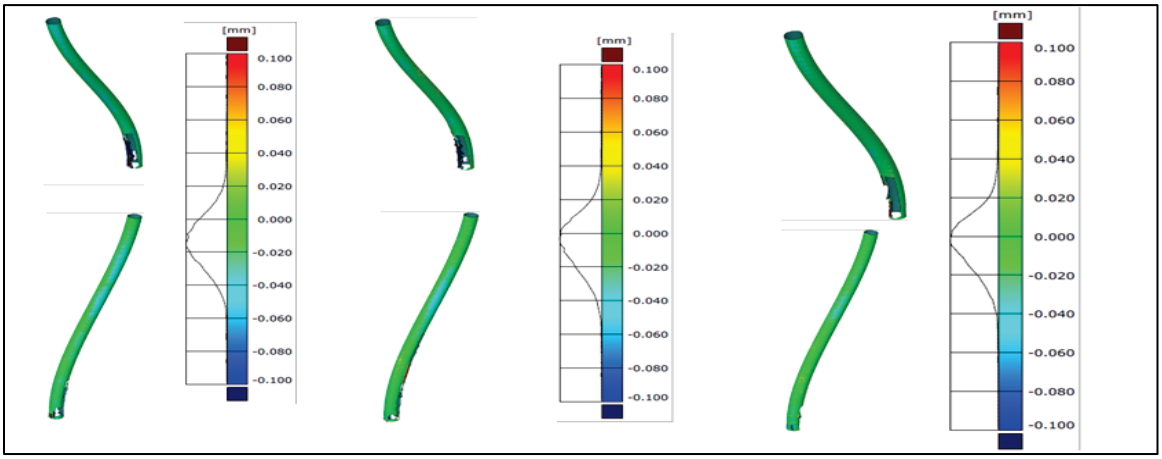


Figure 26. Distortion measurements for IN718 geometries S1-S3.



2.1.3.1 *Summary of results*

Table 6 compares the distortion values between the simulations performed by AO, the simulations performed by Eaton using the Netfabb software by Autodesk, and the CEED measurements data for a particular region for each part.

Table 6. Summary of distortion values and error percentages.

Distortion values (mm)					Percent error	
Part	AO	Netfabb	CEED		AO	Netfabb
Cylinder	0.05	0.1	0.09		44%	11%
Cantilever	0.14	0.12	0.13		8%	8%
Horizontal	0.097	0.15	0.1		3%	50%
Incline	0.33	0.25	0.3		10%	17%
Vertical	0.086	0.11	0.08		7%	38%
Spiral	0.063	0.09	0.06		5%	50%
Arch	0.0635	0.13	0.12		47%	8%

2.1.3.2 *Additional improvements to simulations*

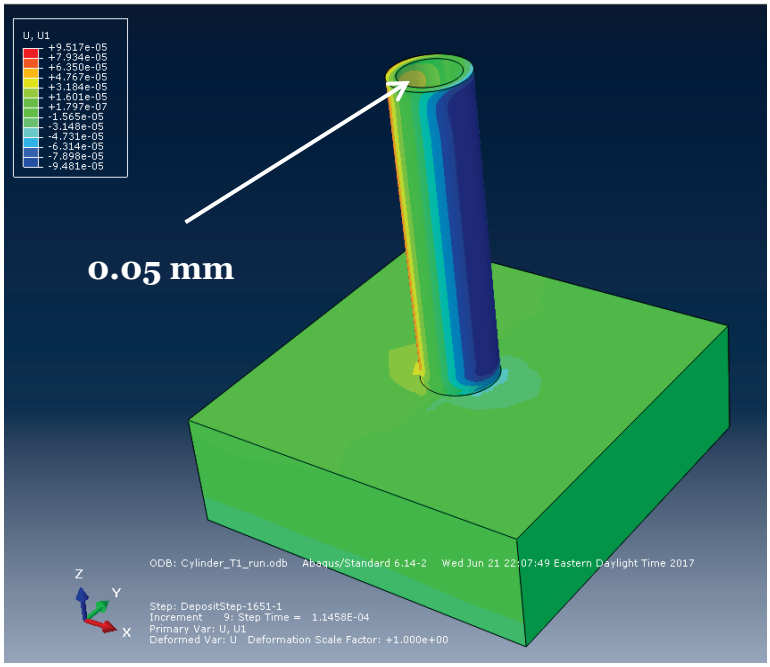
As stated in Section 2.1.2.3, each group of layers deposited was one element thick in the finite element model. More accuracy could be achieved by increasing the number of elements in the thickness direction in each group of layers. Similarly, more accuracy could be achieved by reducing the number of layers deposited at once. The Cantilever and Inclined plate shapes are unique, in that the Cantilever has support material and that the Inclined plate is at a low angle to the horizontal.

2.1.3.3 *Validation of distortion prediction for cylinder calibration part*

Figure 27 shows the x-component of displacement predicted by the AO simulation. The pattern of final configuration predicted by the simulation matched the finished calibration part in that the interior surface contracted radially. However, the distortion in the interior predicted by the simulation was about 44 percent smaller than the measurement of the finished part. The distortion predicted by the simulation was 0.05 mm, while the distortion measured was 0.09 mm. The simulation consisted of 33,417 linear hexahedral elements. Layers were deposited in groups of 15.

Distortion values (mm)					Percent error	
Part	AO	Netfabb	CEED		AO	Netfabb
Cylinder	0.05	0.1	0.09		44%	11%

Figure 27. Cylinder residual distortion.

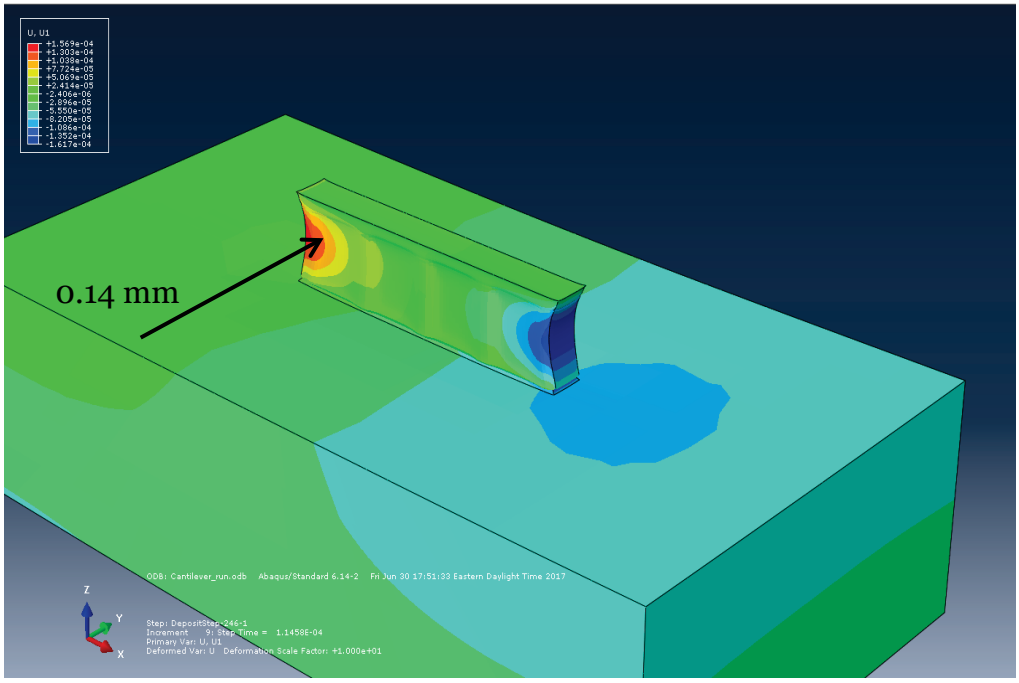


2.1.3.4 *Validation of distortion prediction for cantilever calibration part*

Figure 28 shows the x-component of displacement predicted by the AO simulation. Note that the distortions are scaled by a factor of 10 in the image. The final configuration predicted by the simulation matches the general shape of the calibration part. However, the concave portion of the part was closer to the substrate in this simulation than in a physical instance. This discrepancy is probably due to the way the support material was modeled. AO assumed the support material to have approximately 10 percent of the bulk density of the solid material, and so assigned the elastic modulus to be 10 percent of that of the bulk material. More accuracy could be achieved with a better estimate of bulk density. In the actual region of interest, the simulation predicted 0.14 mm, while the distortion of the finished part measured 0.13 mm — a difference of 8 percent. The simulation consisted of 46,480 linear hexahedral elements. Layers were deposited in groups of five.

Distortion values (mm)					Percent error	
Part	AO	Netfabb	CEED		AO	Netfabb
Cantilever	0.14	0.12	0.13		8%	8%

Figure 28. Cantilever residual distortion.

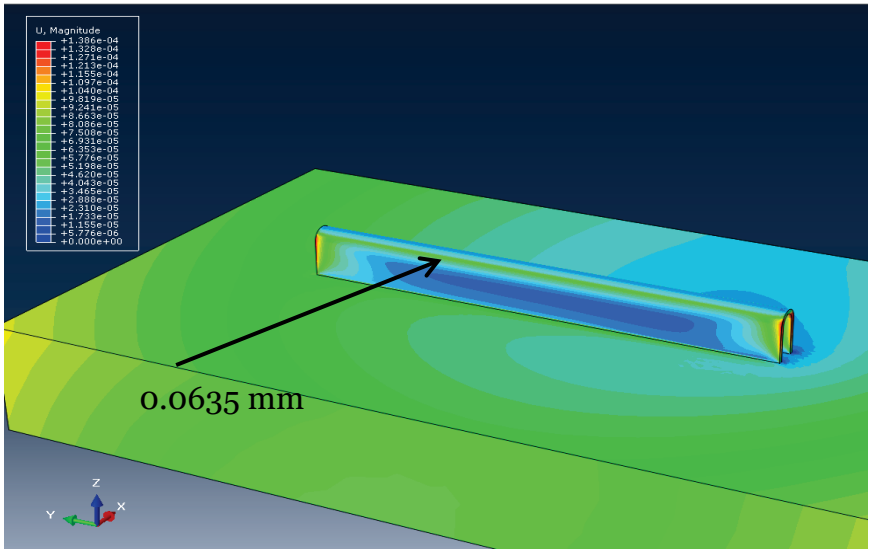


2.1.3.5 *Validation of distortion prediction for arch calibration part*

Figure 29 shows the magnitude of displacement predicted by the AO simulation. The final configuration predicted by the simulation matches the shape of the calibration part. AO was unsure where the part was measured. The measurement taken from the simulation is the light blue region, with a surface normal of approximately 45 deg to the horizontal. The simulation predicted 0.0635 mm displacement while the displacement of the finished part measured 0.12 mm — a 47 percent difference. The simulation consisted of 50,061 linear hexahedral elements. Layers were deposited in groups of five.

Distortion values (mm)					Percent error	
Part	AO	Netfabb	CEED		AO	Netfabb
Arch	0.0635	0.13	0.12		47%	8%

Figure 29. Arch residual distortion.



2.1.3.6 *Validation of distortion prediction for inclined plate calibration part*

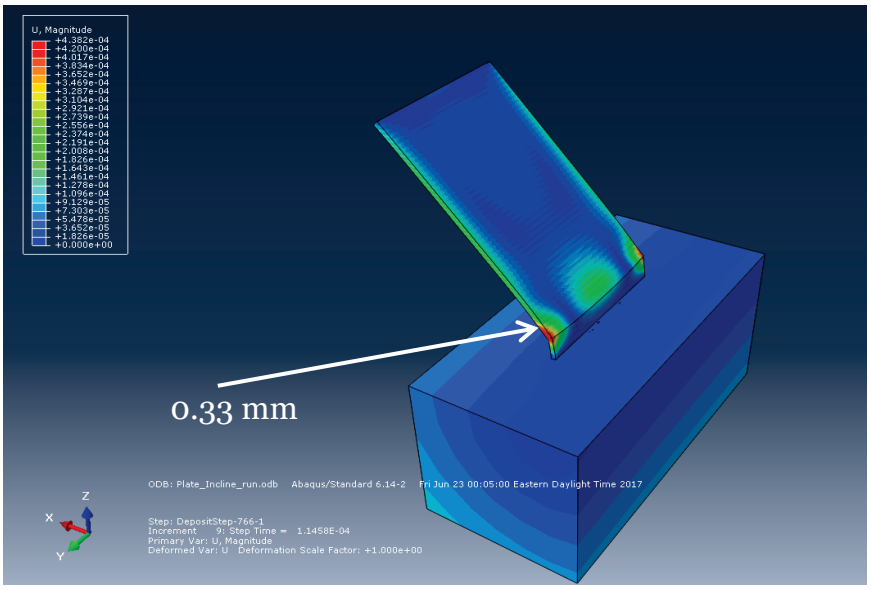
Figure 30 shows the magnitude of displacement predicted by the simulation. The final configuration predicted by the simulation matches well near the bottom of the inclined plate. It was unclear where the measurement was taken on the calibration part. For this simulation, the measurement is taken about 0.8 mm from the edge. The simulation does not match well near the top of the part. Near the bottom, the simulation predicted 0.33 mm, while the distortion of the finished part measured 0.3 mm— a 10 percent difference. The simulation consisted of 57,182 linear hexahedral elements. Layers were deposited in groups of 15.

2.1.3.7 *Validation of distortion prediction for vertical plate calibration part*

Figure 17Figure 31 shows the x-component of distortion predicted by the AO simulation. The final configuration predicted by the simulation matches well with the shape of the finished part. The simulation predicted a displacement of 0.086 mm on the side of the part, while the distortion of the finished part measured 0.08 mm. This is a difference 7.5 percent. The simulation consisted of 43,221 linear hexahedra elements. Layers were deposited in groups of 15.

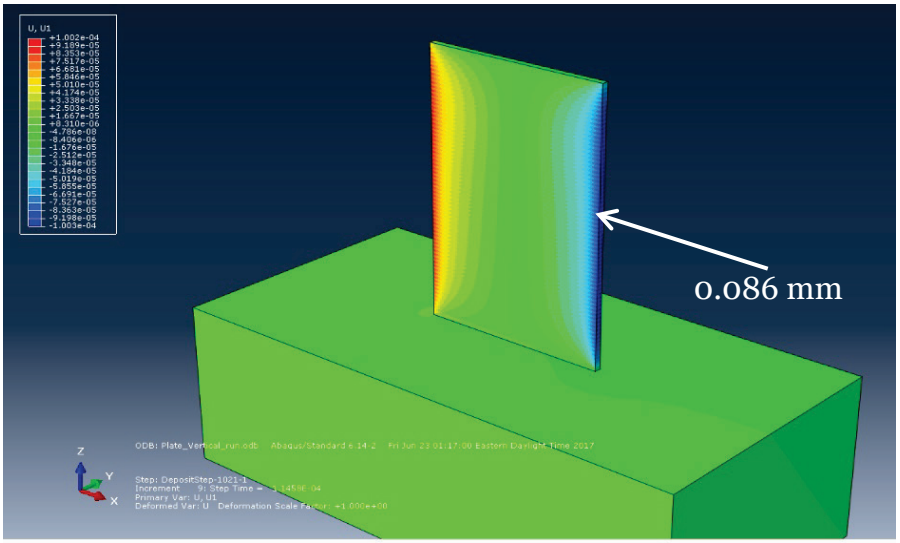
Distortion values (mm)					Percent error	
Part	AO	Netfabb	CEED		AO	Netfabb
Incline	0.33	0.25	0.3		10%	17%

Figure 30. Inclined plate residual distortion.



Distortion values (mm)					Percent error	
Part	AO	Netfabb	CEED		AO	Netfabb
Vertical	0.086	0.11	0.08		7%	38%

Figure 31. Vertical plate residual distortion.

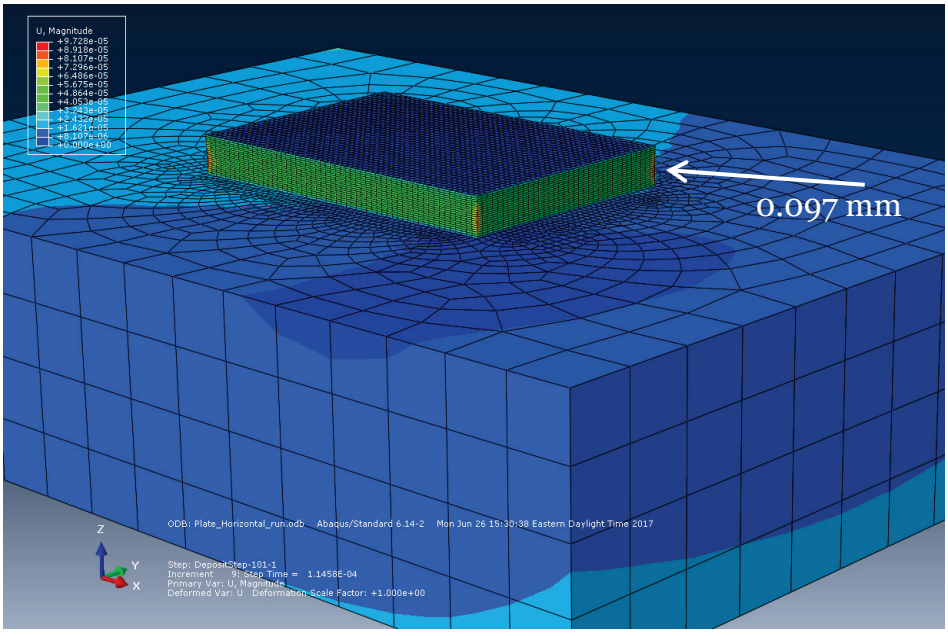


2.1.3.8 *Validation of distortion prediction for flat plate calibration part*

Figure 32 Figure 31 shows the magnitude of displacement predicted by the AO simulation. Given the geometry, it is difficult to tell how well the configuration predicted by the simulation matches with the finished part. It was also not clear exactly where the distortion was measured on the actual part. The measurements taken from this simulation are in the middle of the vertical edges of the part. The distortion predicted by the simulation measured 0.097 mm while the distortion of the finished part measured 0.1mm. This is a difference of 3 percent. The simulation consisted of 36,136 linear hexahedral elements. Layers were deposited in groups of 10. Note that since there is rounding on the edges of finished parts, there is probably a limit to how well this model can predict displacement in regions near the edges.

Distortion values (mm)					Percent error	
Part	AO	Netfabb	CEED		AO	Netfabb
Horizontal	0.097	0.15	0.1		3%	50%

Figure 32. Horizontal plate residual distortion.

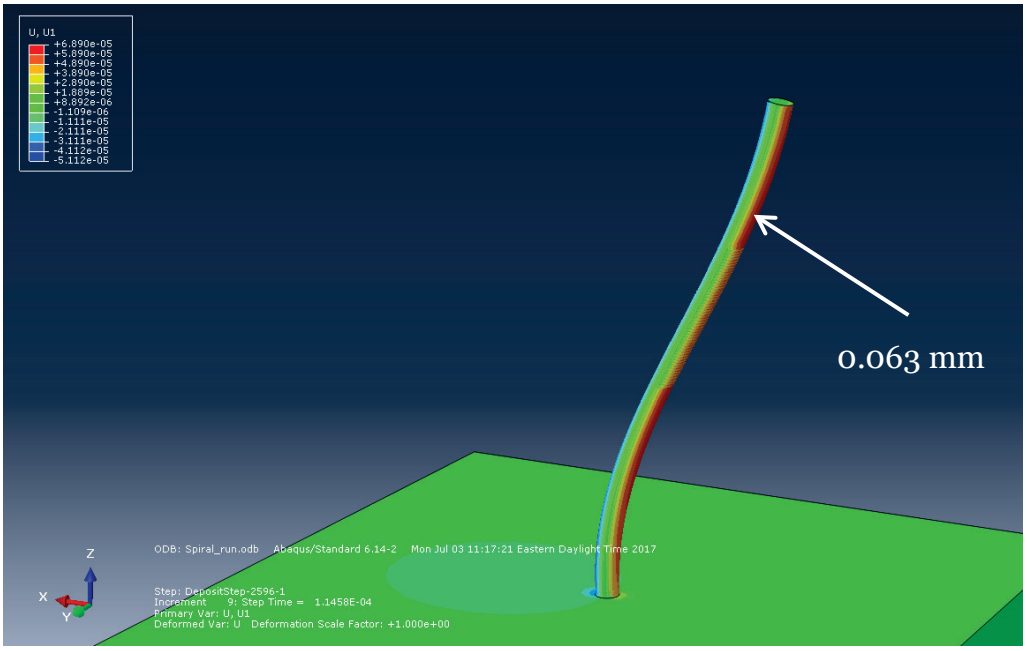


2.1.3.9 *Validation of distortion prediction for spiral calibration part*

Figure 33 shows the x component of displacement predicted by the AO simulation. The final configuration predicted by the simulation matches the general shape of the finished calibration part. The distortion predicted by the simulation measured 0.063 mm while the distortion of the finished part measured 0.06 mm. This is a difference of 5 percent. The simulation consisted of 28,868 linear hexahedral elements. Layers were deposited in groups of 15.

Distortion values (mm)					Percent error	
Part	AO	Netfabb	CEED		AO	Netfabb
Spiral	0.063	0.09	0.06		5%	50%

Figure 33. Spiral residual distortion.



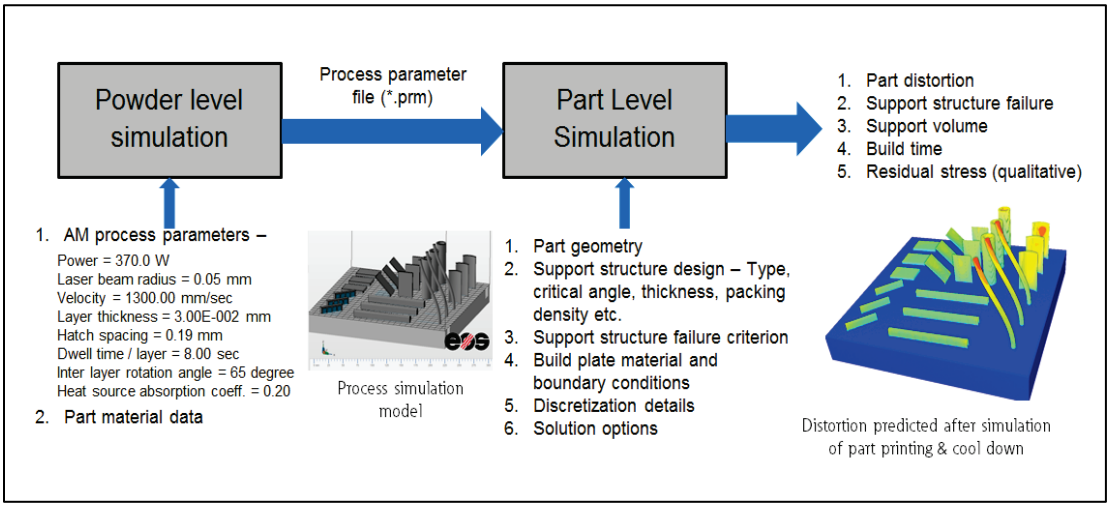
2.2 Residual stress

2.2.1 Numerical method

The residual stress during part buildup was not part of the scope of the project but is shown here for providing insights into this important factor that contributes to first pass yield. The results shown here were computed using a commercial code (Autodesk Netfabb). In the Netfabb tool, process modeling was solved using a multiscale, weakly-coupled, thermo-

mechanical approach with the inherent strain method. Figure 34 shows an overview of this process.

Figure 34. Overview of DMLS process simulation work flow.



The initial melt pool level simulation considers the effect of a heat source at the melt pool level. This analysis models the effect of process parameters on the given melt pool geometry and predicts melt pool level temperature and strain calculations. A part scale simulation then maps results from the melt-pool-level thermal and mechanical loads at each layer to form the actual build geometry. This process facilitates prediction of distortion, residual stress, printing risks such as support structure failure, recoater blade locking, etc.

Part plasticity modeling was performed based on temperature-dependent flow curves defined in the material model. During part level simulation, after completing layer-wise part printing and cool-down load case, the model solves for plasticity correction where-in linear stress state data are solved for the flow curves to determine the true stress state in the part-level model.

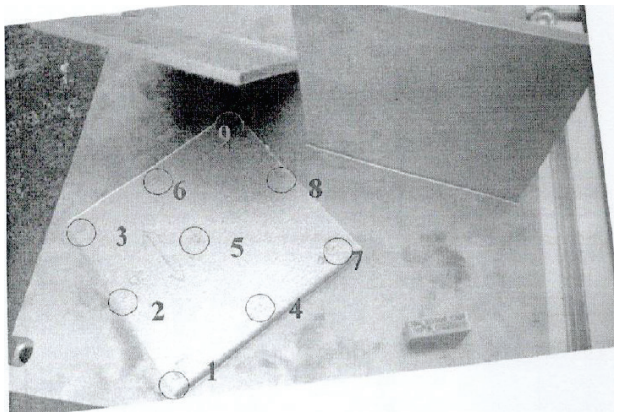
2.2.2 Preliminary validation

Evaluation of the stress prediction approach and development of qualitative capability for residual stress prediction is shown here. For maturing residual stress prediction capability, apart from improving on process modeling code, parallel efforts were addressed on assessing accuracy level through residual stress validation for different

materials/specimen shapes. Here, the residual stress correlation performed for In718 plates and 15-5 steel cylinders are presented.

Three In718 plates were built and their residual stresses measured using an X-ray diffraction technique. Note that residual stress measurement was performed before removal of parts from the build plate. Figure 35 show an overview of the In718 plates printed and measured for residual stress.

Figure 35. In718 plates–Residual stress measurement using X-ray diffraction technique.



Process modeling of the build plate with three In718 plates was performed per the process parameters used in the specimen build. Figure 36 shows residual stress measurements in the printed horizontal plate. Table 7 summarizes the comparison for predicted residual stress.

Figure 36.Horizontal In718 Plate – Residual stress prediction per measurement set-up.

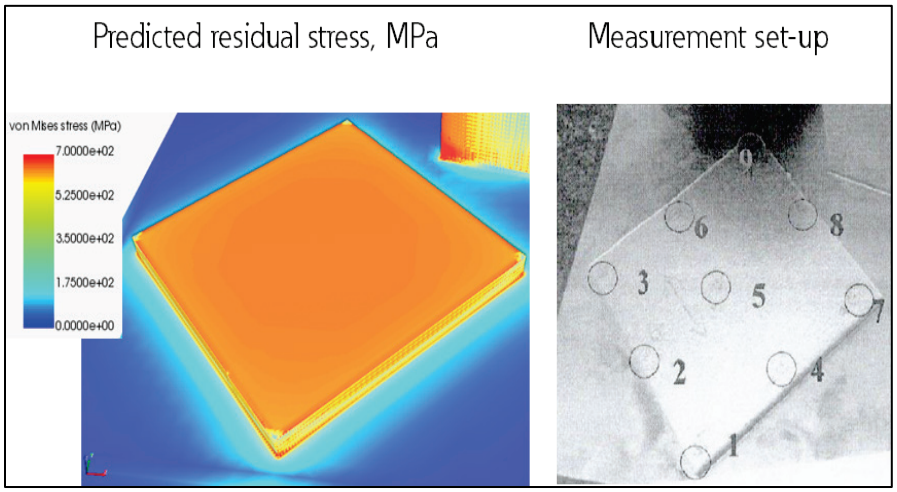


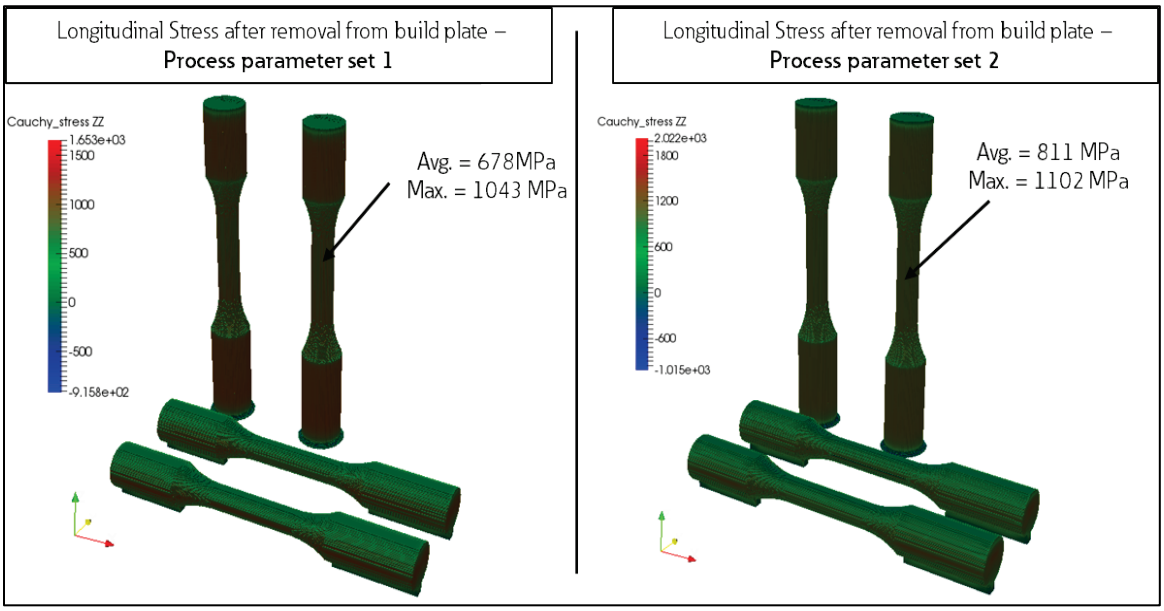
Table 7. Horizontal In718 plate - Comparison of predicted residual stress with measurements.

Location	Stress, MPa			% Error w.r.t. mean
	Measurement	Measurement Tolerance	Prediction	
1	676.4	25.5	646.8	4%
2	598.8	21.6	654.7	-9%
3	533.3	21.9	649.3	-22%
4	604.4	20.5	653.3	-8%
5	560.5	14	664.2	-19%
6	577	26.6	658	-14%
7	553.4	18.2	647.5	-17%
8	450.4	15.4	655.8	-46%
9	774.8	17.2	650.1	16%

A similar comparison was made for tilted and vertical plates. Residual stress prediction accuracy was highest for horizontal plates, except in two cases where predicted residual stress was 200 percent off for certain locations. Further efforts are required to address such concerns.

Another, similar study was performed for 15-5 steel cylinders in which cylinders were printed using two different sets of process parameters and then residual stress was measured in the cylinder. The objective of the effort was to evaluate the effect of changing process parameters on the residual stress induced in the specimens. Process modeling results and residual stress measurements indicated that process modeling results were qualitatively accurate in predicting the effect of process parameters on residual stress. Figure 37 illustrates the effect of process parameters on residual stress for the 15-5 steel cylinders.

Figure 37. 15-5 steel cylinders–Effect of process parameters on residual stress.



2.3 Porosity mitigation

2.3.1 Numerical framework for porosity mitigation

2.3.1.1 *Background*

For the work presented here, it is assumed that inadequate fusion between tracks and between layers is a primary cause of porosity in AM parts. To predict the inter-track and inter-layer fusion at a certain location of a particular geometry, the physics of the process needs to be simulated at the scale of the melt pool. However, the time required to simulate an entire part at the melt-pool scale would be large, because the size of the melt pool (tens of microns for powder bed processes) is much smaller than the size of most AM parts (centimeters). Hence, simulating the entire part at the melt-pool scale is not feasible.

Since the melt pool still needs to be modeled at the location of interest, the next best course of action is to implement multiscale modeling. That is, to utilize a coarse model far away from the region of interest and a much finer model near the region of interest. AO has developed a multiscale modeling approach, Additive Manufacturing Parameter Predictor (AMP2), which consists of three steps: a macro-scale model, a meso-scale model, and a micro-scale model.

The first step of AMP2, the macro-scale model, simulates gradual heating of the part as layers are added. This simulation adds entire layers or groups of layers to the part and applies the heat flux to these layers. The coarseness of this model means the part does not actually reach the high temperatures associated with the melting of an individual track. However, this is not the purpose of this simulation, as this step of the process is intended to capture the build heat-up for the AM part as new layers are added.

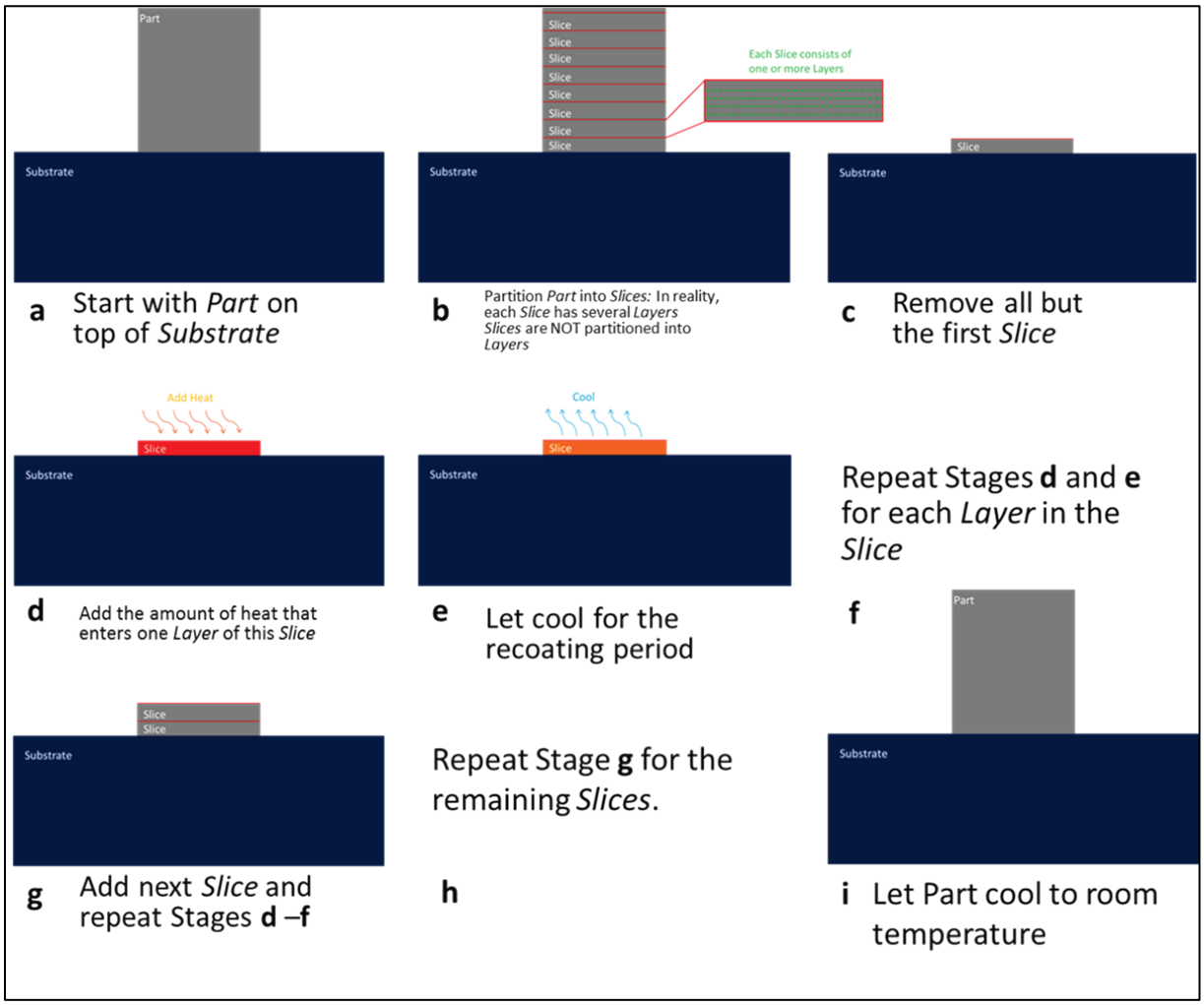
The next step of the process, the meso-scale model, simulates the heat up within a layer. The temperature of this layer is initialized at the temperature predicted by the layer-scale model. Heat is then applied to individual tracks, or groups of individual tracks, in real time. The temperature distribution predicted is not as localized as in reality. This localization, however, is not necessary as the purpose of this model is to capture the average temperature of a region of the layer before the heat source reaches it. As in the layer-scale model, this capture is a good approximation since the heat dissipates before the heat source reaches the region again. Unlike the previous model, this model can reach the higher temperatures associated with melting.

The final step in the process, the micro-scale model, simulates the melt-pool physics of an individual track. The temperatures predicted by the meso-scale model are used as boundary conditions for the material surrounding the melt-pool. Heat is applied to the region, and the thermo-fluid characteristics of the melt pool are simulated. The simulation predicts the temperature distribution, the flow field, and the geometry of the melt pool. These results can be used to predict the inter-track and inter-layer fusion resulting from the given geometry and processing conditions.

2.3.1.2 *Macro-scale model*

The macro-simulation is executed using Abaqus 6.14-2. The process is shown in Figure 38. Preprocessing occurs in stages a and b.

Figure 38. Macro-scale simulation process.



The part is placed on a substrate (a in Figure 38) and split into slices (b). Each slice consists of one or more layers of powder. During simulation, all slices but the first are removed (c). The energy that goes into one layer is put into the whole slice as a body flux (d). This occurs in the time it takes to deposit one layer of this slice. The slice is allowed to cool for the recoating period of the machine (e). This process is repeated for the remaining layers in the slice (f). The next slice is added, and stages d-f are repeated for that slice (g). Stage g is repeated for the remaining slices (h), and the part is then allowed to cool (i). The material properties required are specific heat, density, and thermal conductivity.

The bottom surface of the substrate is held at room temperature, or at the temperature of a heated substrate, to model the thermal mass of the substrate, since the whole substrate is not modeled. The outside surfaces

of the part and the top surface of the substrate are given a convective boundary condition to model heat loss to the surrounding powder bed.

Because the heat flux is applied to multiple layers, rather than one, and the heat is applied over a longer period than any local region will see the heat source, the heat flux is diluted. The first dilutes over space, allowing the heat to be absorbed by more mass than is present, and the second dilutes in time, allowing more time for heat transfer. Both circumstances cause the maximum temperature of the build to be lower than in actuality. This is not a problem, however, as the goal of this simulation is not to get the peak temperature of the build. The purpose of this simulation is to obtain the approximate temperature of a layer after the recoat time has been applied. Since the maximum temperatures of the build are highly localized and dissipate quickly, they do not contribute much to the average temperature of the build; thus, the simulation can predict reasonable temperatures at the end of the recoat steps. The simulation is most accurate after the final recoat step of the final layer of a slice, as the amount of energy and mass that have been added to the slice is the same as in actuality.

The temperature distribution from the macro-model is imported as an initial condition into the meso-model. For the most accuracy, it is best to choose a layer that is the final layer of a slice in the macro-simulation.

2.3.1.3 *Meso-scale model*

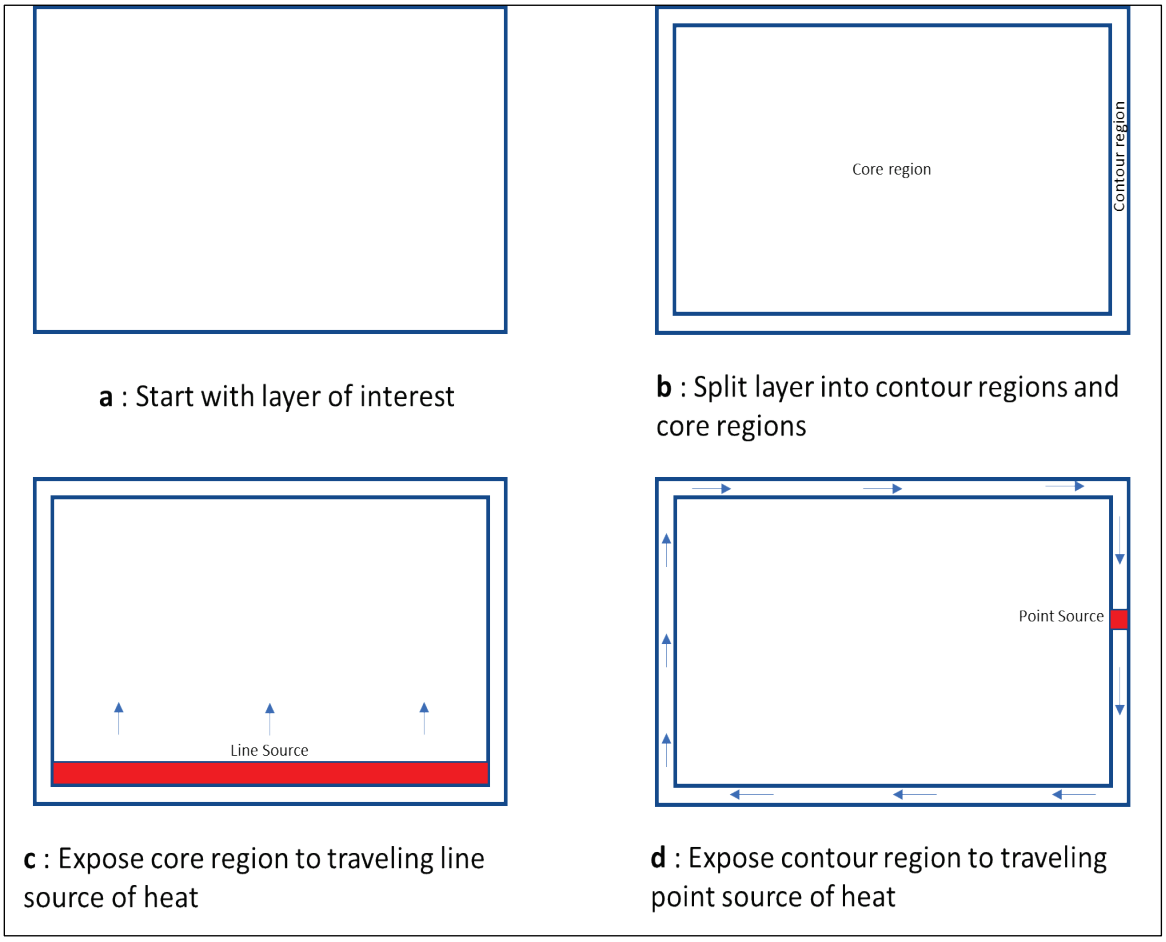
The meso-simulation is executed with Abaqus 6.14-2. The process is shown in Figure 39.

Preprocessing occurs in stages a and b. As in the macro-scale model, the part is placed on a substrate. In this case, however, the region of the part above the layer of interest is removed (a). The top surface is then split into contour regions and hatch regions (b). The core regions are split into rows for application of a line source of heat, and the contour region is split into increments for application of a point source of heat. To avoid clutter, this is not shown in Figure 39. During simulation, heat is added as a moving line source (c) in the core region and a moving point source (d) in the contour region. In both cases, the heat is applied over the time it takes the beam to scan over the applicable region. Stages c and d can be given in any order and as many times as necessary. The boundary conditions and required material properties are the same as for the macro-scale model.

However, since the heat source is less diluted than in the macro-scale model, the temperatures can reach melting and sometimes boiling temperature. Both the former and the latter usually only occur in the contour region where the heat is the least diluted.

As in the macro-scale model, the heat flux, particularly in the core region, is diluted in time and space, which can cause the local temperature to be less than melting temperature. This is not a problem because, like the macro simulation, the meso-scale simulation is intended to model the average temperature rise of different regions of the layer. The temperatures predicted by this simulation are used to initialize the temperature of the micro-scale simulation.

Figure 39. Meso-scale simulation process.



2.3.1.4 *Micro-scale model*

The micro-scale simulation was executed using AO's software package, ParaGen, which uses OpenFOAM as the solver. ParaGen created a steady

state simulation because the scale of the melt pool is much smaller than the scale of the part, and at the scale of the melt pool, the local geometry surrounding the melt pool does not change quickly. The ParaGen model uses a thermal boundary condition predicted by the meso-scale model.

Table 8 lists the material properties ParaGen requires for powder bed fusion. Note that ParaGen models surface tension as a linear function of temperature, which requires a point, a surface tension value (σ) and its corresponding temperature (T), and the slope (dσ/dT). These are the last three entries in Table 9. (The values shown here were used to implement simulations for the representative part from 15-5 SS. Values with an * or ** are approximate values, from 316 SS or 17-4 SS respectively, used in place of missing 15-5 SS values.)

Table 8. Required material properties.

Material Data	Value	Units	Ref.
Conductivity**	Table 6	W/m.K	1
Density	Table 6	kg/m^3	3
Specific Heat	Table 6	J/kg.K	3
Latent heat of fusion	2.66E+05	J/kg	2
Latent heat of vaporization	6.00E+06	J/kg	2
Solidus Temperature	1738	K	3
Liquidus Temperature	1756	K	3
Boiling temperature	3090	K	2
Emissivity of solid*	0.57	1	2
Emissivity of liquid*	0.4	1	2
Laser absorptance of solid*	0.38	1	2
Laser absorptance of liquid*	0.38	1	2
Viscosity*	5.82E-07	m^2/s	2
σ_0*	1.76	N/m	2
T_0*	1973	K	2
dσ/dT*	-3.80E-04	N/mK	2

Table 9. Required laser system parameters.

Laser Sytem	Description	Value (Core/Contour)	Units
Power	Power of laser	195/111	J/s
Spot diameter	diameter of laser at substrate	1.00E-04	m
Velocity	Speed of laser travel	1.085/0.823	m/s
Z angle	Angle of between axis of laser and laser path	0	degrees
Sub angle	Angle between laser axis of laser and substrate	90	degrees
Distribution	Distribution of laser at substrate (gaussian or uniform)	gaussian	N/A

Table 10 shows the parameters ParaGen requires to model heat transfer to the environment.

Table 10. Required environmental parameters.

Environmental Parameter	Description	Value	Units
Intitial Temperature	Temperature of surrounding material	373	K
Ambient Temperature	Temperature of ambient	293	K
Free convection	Free convection coefficient	25	$W/m^2.K$
Ambient Pressure	Pressure of ambient	101325	Pa

Table 11 shows the parameters ParaGen requires to model the powder bed.

Table 11. Required powder bed parameters.

Powder Bed Parameter	Description	Value	Units
Relative density	Density of particle gas mixture as compared to solid	0.5	1
Bed drop	Distance substrate moves between layers	2.00E-05	m
Power Diameter	Average diameter of powder	2.00E-05	m

ParaGen currently has two modes: a single-track mode and a double-track mode. In the single-track mode, ParaGen simulates the melt-pool physics of a virgin track on a flat substrate. In the double-track mode, ParaGen simulates the deposition of a track onto a previously existing track. Figure 40 shows track dimensions predicted for both the single-track mode (top) and the double-track mode (bottom).

The double-track mode requires the height (above the substrate) of the preexisting track, the width of the preexisting track, and the hatch distance to be used for the second track. For cases where a track is near the edge, the distance from the center of the track to the edge of the substrate is also required. The work in this report focuses on double-track simulations, which are used to predict processing parameters for the core region and are least likely to yield porosity. The double-track mode was also used to predict processing conditions for the contour region. Figure 41 describes the reasoning and includes a diagram of a scan pattern near the edge of the build.

Figure 40. ParaGen single-track mode (top) and double-track mode (bottom).

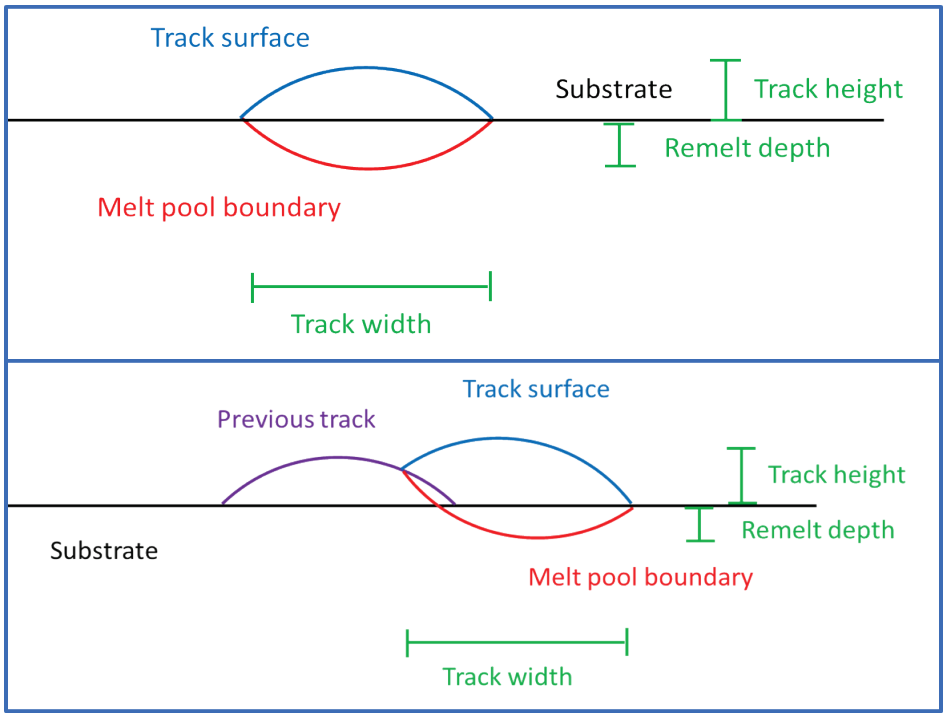
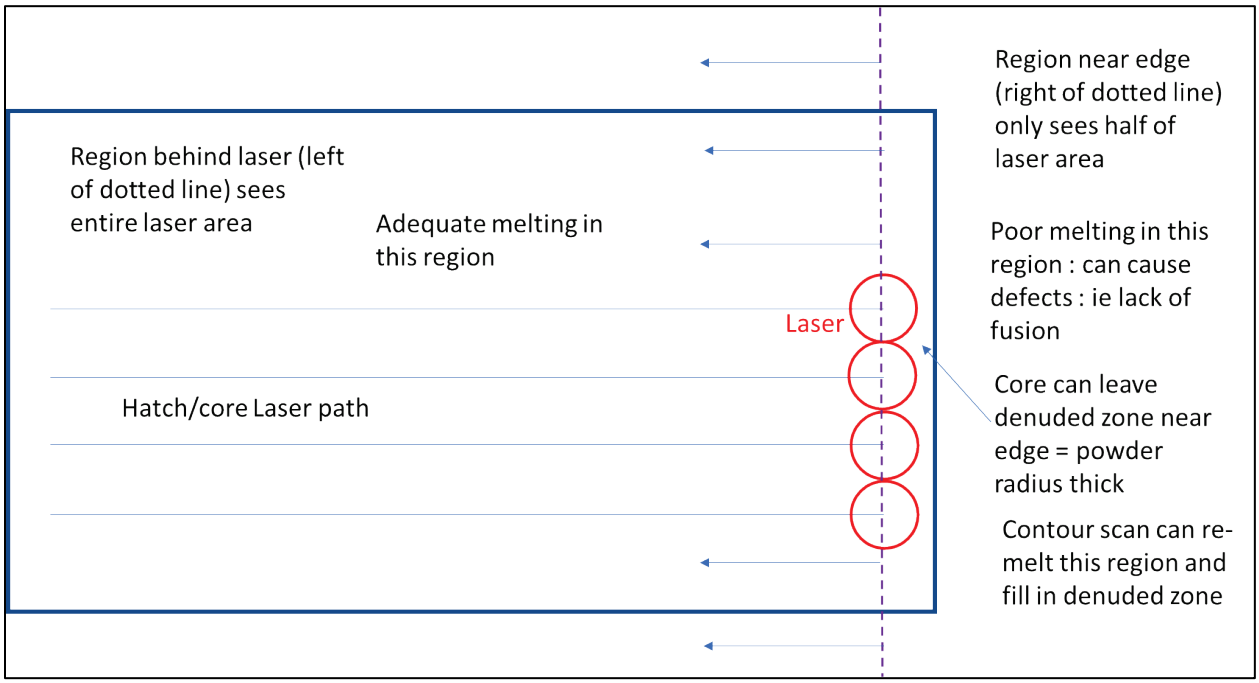


Figure 41. Poorly melted region.



Note that the core laser path does not go to the edge of the build (the solid blue line, because powder from outside the melt pool/laser path can be dragged into the melt pool by escaping interparticle gas. If the laser path went all the way to the edge of the part, powder from outside would be dragged in, making the part larger than desired. Note also that the region near the outside of the part will not be properly melted from the core exposure because this is the region where the laser either turns on and off or where it turns around. Also, the particles in this region see only half the laser area, while the core region sees the whole laser area, making it necessary to use a contour track, which remelts and smooths out the poorly melted region and also fills in the denudation zone created by the core exposure.

Since finding the size of the poorly melted region near the edge of core exposure is difficult and geometry dependent, it was assumed for this model that the size of the poorly melted region is approximately the size of one half of a track that runs parallel to the boundary. If the previous track is melted sufficiently in contour track simulation, then the poorly melted region is assumed to be melted.

2.3.1.5 *Criteria for adequate melt-pools*

Figure 42 shows the criteria for adequate melting in the core region. The minimum layer thickness needs to be greater than the bed-drop, and the minimum melting (remelt) into the previous layer should be larger than the powder radius. The layer thickness and remelt allow adequate fusion between layers. The overlap between tracks should be larger than the powder radius, which allows adequate fusion between tracks. The dip between the tracks should be minimized to create as flat a surface as possible. This minimization will help keep a homogenous powder distribution for the next layer, which will help prevent lack of fusion.

Figure 43 shows the criteria for adequate melting in the contour region. Note first that the core offset is set, so the denudation zone created by the core exposure ends at the boundary of the part. The edge melt needs to be greater than the bed-drop, so adequate fusion with the previous layer on the edge of the part can occur. The overlap between the core and the contour needs to be greater than the powder radius, allowing adequate fusion between the core and contour regions.

Figure 42. Criteria for adequate core melting.

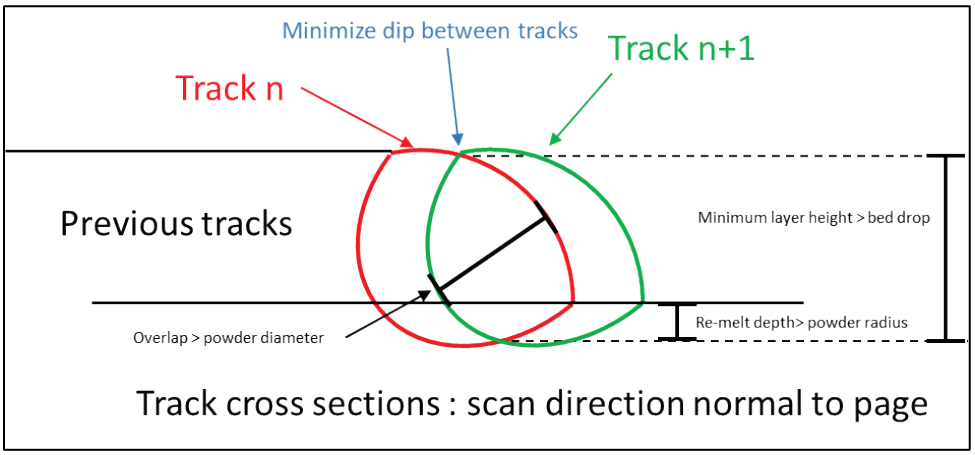
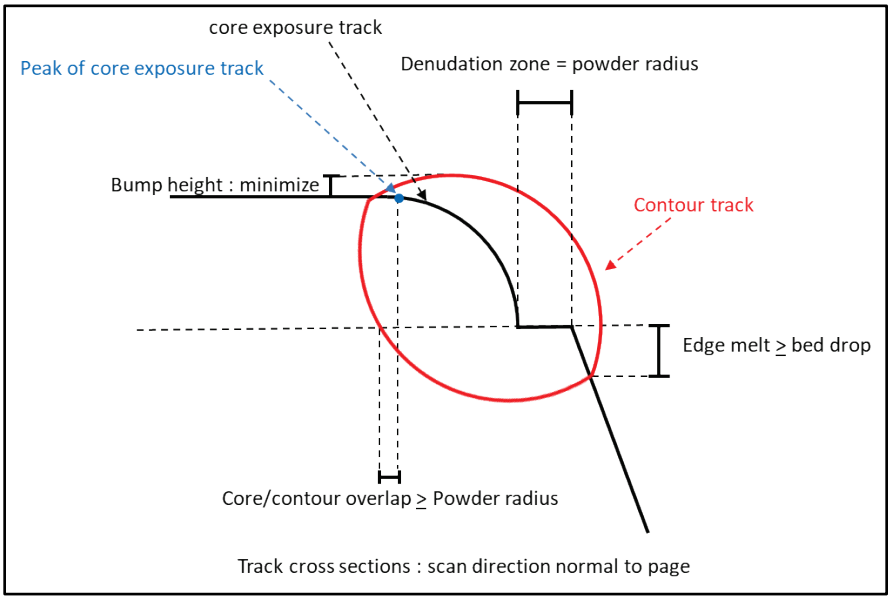


Figure 43. Criteria for adequate contour melting.



2.3.1.6 *Methods for finding conditions that satisfy criteria*

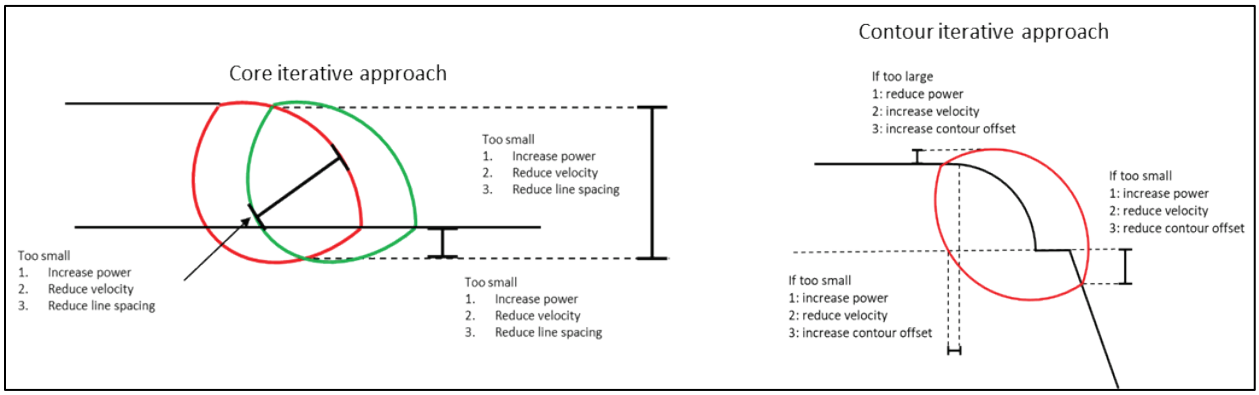
Two methods can be used to find conditions that satisfy criteria: a brute force method or an iterative method.

The brute force method requires the simulation of an entire matrix of conditions, after which the conditions that satisfy criteria are chosen. The advantage of this method is that it can explore the whole solution space. Its disadvantage is that it requires many simulations and is time intensive.

The iterative method starts with a simulation of an estimated set of conditions. If the resulting melt-pool does not meet the criteria, the

conditions can be perturbed and resimulated until the melt-pool matches the criteria (see Figure 44). In the interest of time, the iterative approach was used for this experiment.

Figure 44. Iterative approach to find adequate conditions.



2.3.1.7 *Post application to representative part*

2.3.1.7.1 *Macro-scale simulation*

Figure 45 shows the macro-scale model of the representative part at layers: (a) 300 and (b) 4600. Layer 4600 is shown, because it is the approximate location of a crack during the actual build.

2.3.1.7.2 *Meso-scale simulation*

Figure 47 shows several images of the meso-scale simulation at (a) partway through the first stripe, (b) partway through the second stripe, (c) partway through the third stripe, and (d) the beginning of the 6th stripe near what is assumed to be the crack initialization point. The red arrow marks the current stripe direction.

Similarly, Figure 48 shows several images of the contour portion of the meso-scale simulation. Figure 48(a), (b), (c), and (d) are in chronological order respectively.

Figure 46 is a closer view of Figure 6b.

Figure 45. Macro-scale simulation.

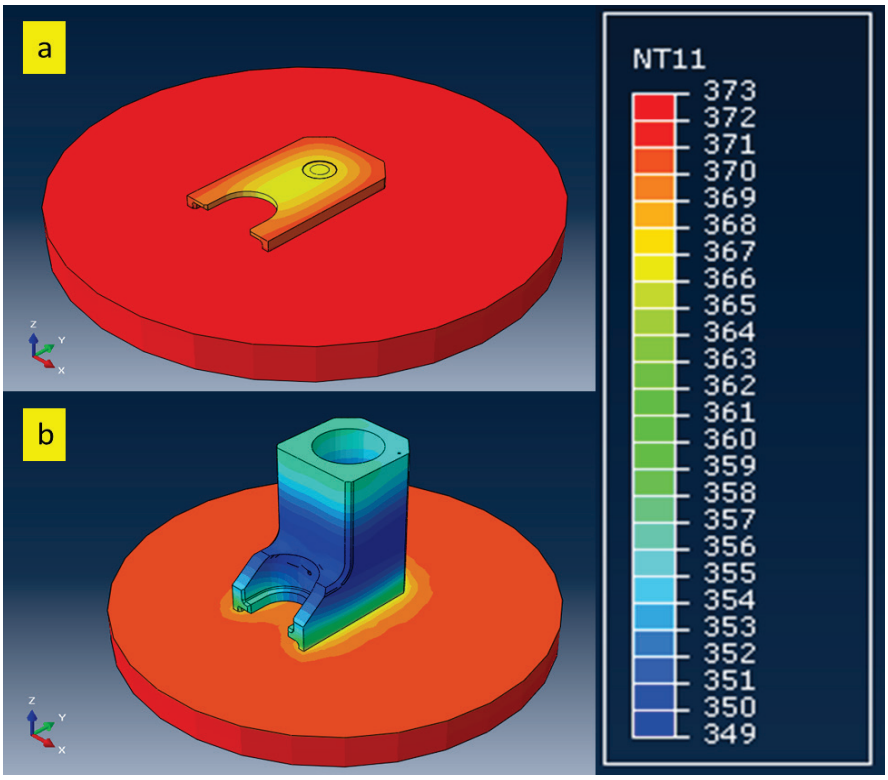


Figure 46. Layer-scale model of representative part: layer 4,600 of 7,000.

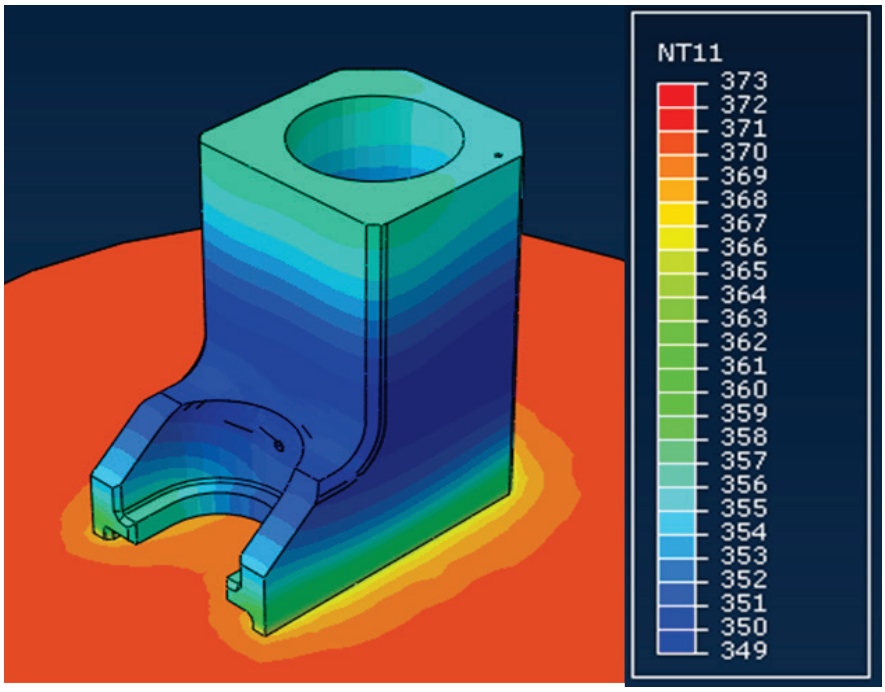


Figure 47. Meso-scale simulation: core.

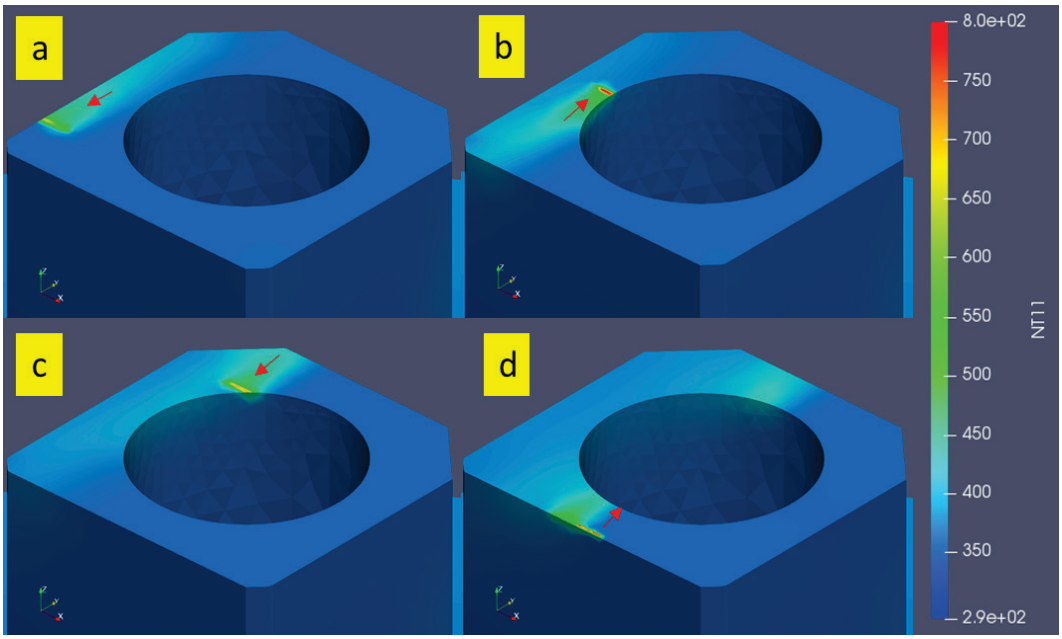
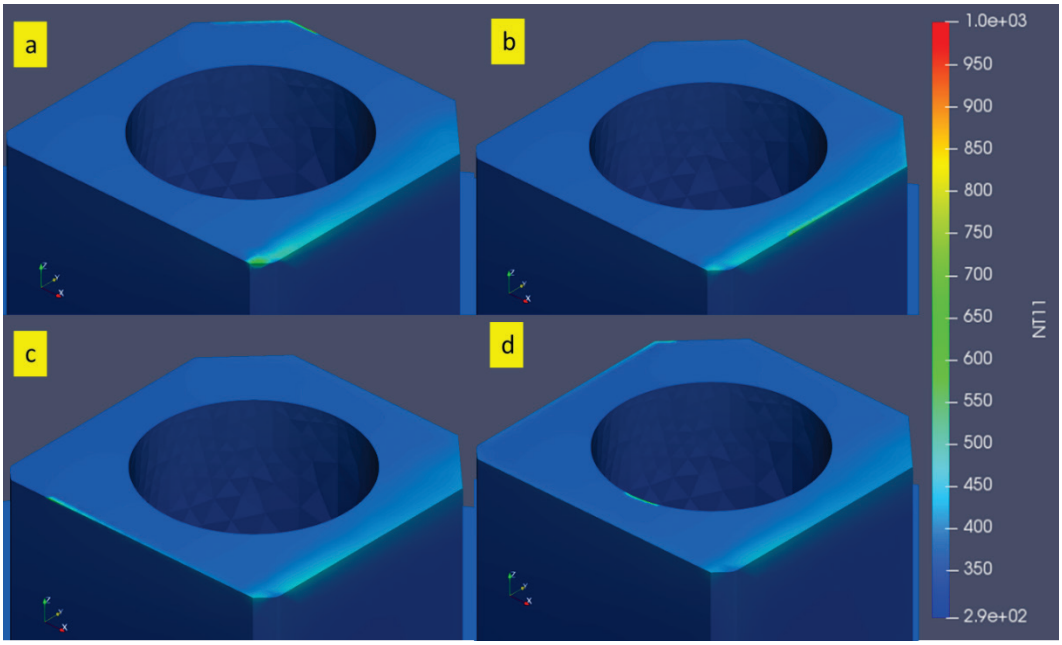


Figure 48. Meso-scale simulation: contour.



2.3.1.7.3 *Micro-scale simulation*

Figure 49 and Figure 50 show the melt-pool cross sections that the simulation predicts for the core region and the contour region for the default parameters. Figure 51 shows the melt-pool cross sections for the contour region using sub-optimal parameters predicted by the AMP^2 process. Part (a) of Figure 49 through Figure 51 show the fraction of liquid

in each cell (alpha), ranging from 0 (solid) to 1 (liquid). The alpha field allows measurement of melt-pool dimensions where alpha =0.5 is the assumed boundary of the melt pool. Part (b) of Figure 49 through Figure 51 show the temperature distribution associated with each region. The translucent portion shown in each image is the projected geometry of the previous track. Note that in the interest of time, the minimum layer thickness was not calculated for this particular simulation or considered in the melting criteria (it is considered in later sections).

Figure 49. Micro-scale core simulation (default); melt pool (a); temperature (b).

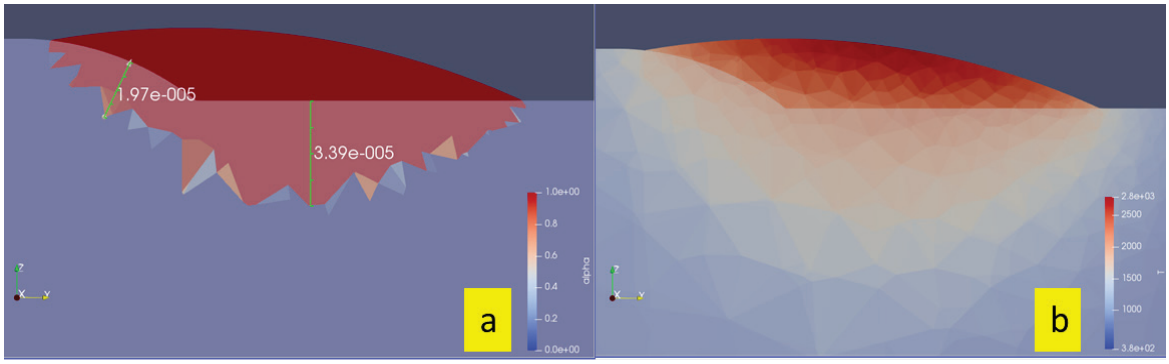


Figure 50. Micro-scale contour simulation (default); melt pool (a); temperature (b).

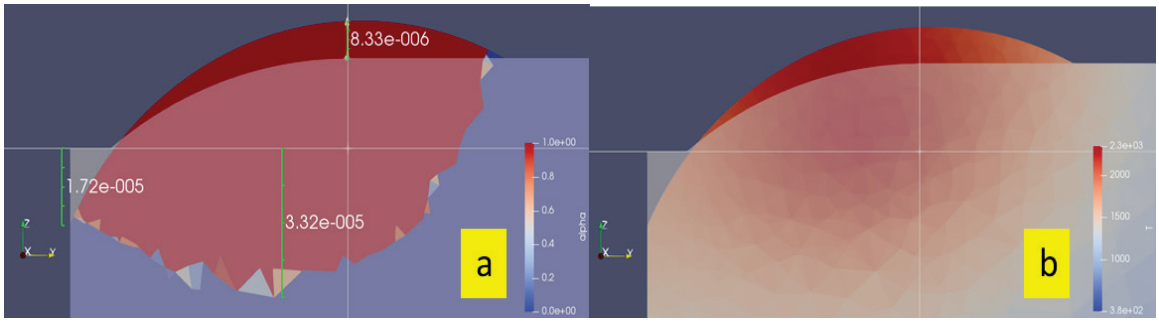


Figure 51. Micro-scale contour simulation (AMP²); melt pool (a); temperature (b).

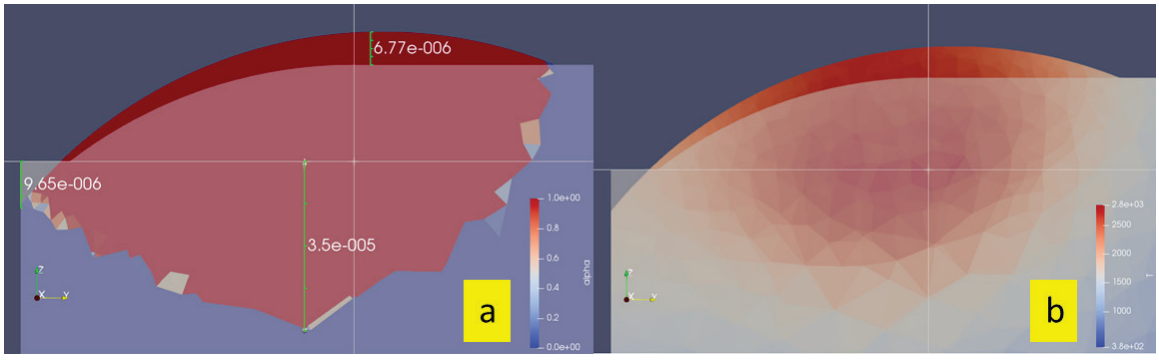


Table 12 shows the processing conditions used for the default contour simulation and for the AMP2 simulation. Note that the previous track is placed such that the denudation zone is at the STL boundary. The AMP2 value for global offset is calculated as the sum of laser spot radius and the mean powder radius. All other parameters are the same.

Table 12. Contour processing conditions.

	Global Offset (µm)	Contour Offset (µm)	Core Offset
Default	56	0	Track placed so denudation zone is at STL boundary
AMP^2	60	0	Track placed so denudation zone is at STL boundary

2.3.1.7.4 *Discussion*

As stated at the end of Section 2.3.1.4, the micro-model of the core region was simulated to obtain the appropriate previous track size for the contour simulation. A single-track simulation yielded a track width of 118 microns. The track height was assumed to be the step height (20 microns).

The micro-model of the contour region for both the default and AMP^2 conditions used 118 microns as the track width of the previous track. Again, for both the default and AMP^2 conditions, the previous track was placed so that the denudation zone ended at the STL boundary.

The default conditions for the core exposure melt sufficiently into both the previous track and the previous layer. Both the default and AMP^2 contour conditions melt sufficiently into the previous layer (remelt depth > 30 microns) and the last core track (> 10 microns) and have an acceptable bump height (< 10 microns). The default set of conditions provide an edge-melt of 18 microns, which is close enough to the layer height (20 microns) for sufficient edge-melting. The suboptimal set predicted by AMP^2 provides an edge-melt of 10 microns, which is only half the layer height and d. Note the sub-optimal contour conditions predicted by AMP^2 are very close to the default conditions, highlighting the importance of picking correct conditions, as the results may be very sensitive to these choices.

2.3.1.7.5 *Steel thermal properties*

Table 13 shows the thermal properties for steel that were used in the AMP^2 simulations in Section 2.3.1.7. The conductivity values in Table 13 were obtained from Sabau and Porter (2008). All other values were obtained from *Thermo-Calc Software*. Note that the conductivity values listed in Table 13 are for 17-4 PH, as it is very similar to 15-5 PH SS.

Table 13. Thermal conductivity.

Temperature (K)	Conduction (W/m.K)	Density (kg/m³)	Specific heat (J/kg.K)
300	11.0	7.78E+03	511
400	12.5	7.77E+03	534
500	13.0	7.73E+03	656
600	15.0	7.67E+03	788
700	17.0	7.64E+03	857
800	19.0	7.61E+03	709
900	21.0	7.59E+03	968
1,000	23.0	7.64E+03	888
1,100	24.0	7.62E+03	600
1,200	25.0	7.58E+03	618
1,300	26.0	7.53E+03	636
1,400	26.5	7.48E+03	655
1,500	28.0	7.43E+03	742
1,600	29.0	7.35E+03	859
1,700	31.0	7.27E+03	743
1,750	32.0	7.19E+03	3,651
2,000	32.0	6.95E+03	809
2,250	32.0	6.95E+03	809
2,500	32.0	6.95E+03	809
2,750	32.0	6.95E+03	809
3,000	32.0	6.95E+03	809

2.3.2 Design of Experiments (DOE)

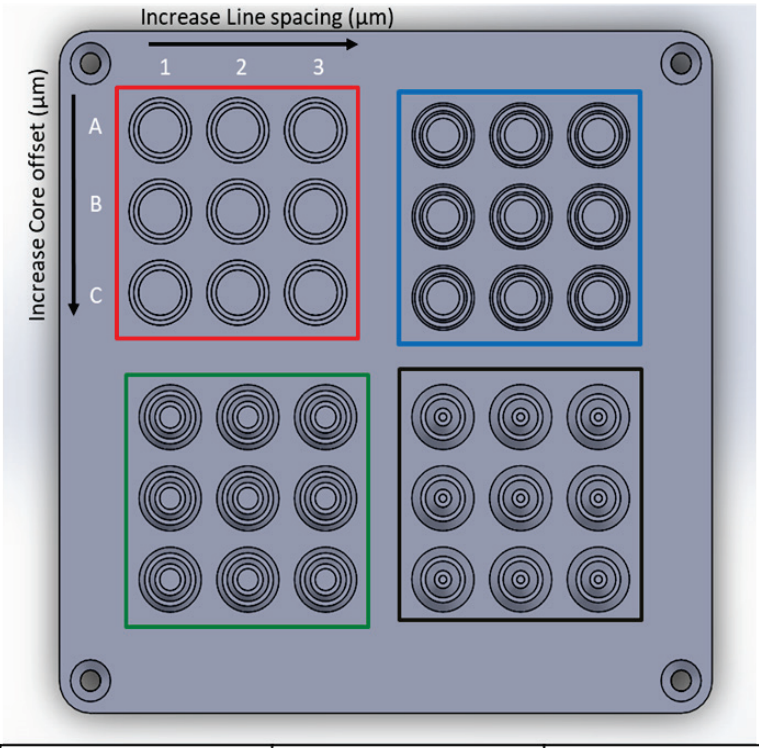
2.3.2.1 *15-5 PH SS DOE*

The purpose of the 15-5 PH SS DOE is to investigate how line spacing, contour offset, and up/down-skin angle affect the lack-of-fusion porosity in the part interior and in the contour region.

The DOE contains four cone geometries and nine parameter sets. Figure 52 shows the parameter matrix used for each group of cones in the 15-5 PH SS build. Note that the line spacing increases in each row from the default 90 microns to 140 microns. In the columns, the core offset increases from the default 3 microns to 43 microns. The expected result is the porosity in the core region will increase with increasing line spacing and that the porosity in the contour will increase with increasing core offset. Specifically, little to no porosity is expected for the default conditions. Limited porosity is

expected for the middle conditions (120-micron line spacing and 23-micron core offset). A significant amount of porosity is expected for the end conditions (140-micron line spacing and 43-micron core offset). Our reasoning is explained in the following paragraphs.

Figure 52. Parameter matrix for each group of 15-5 PH SS cones.

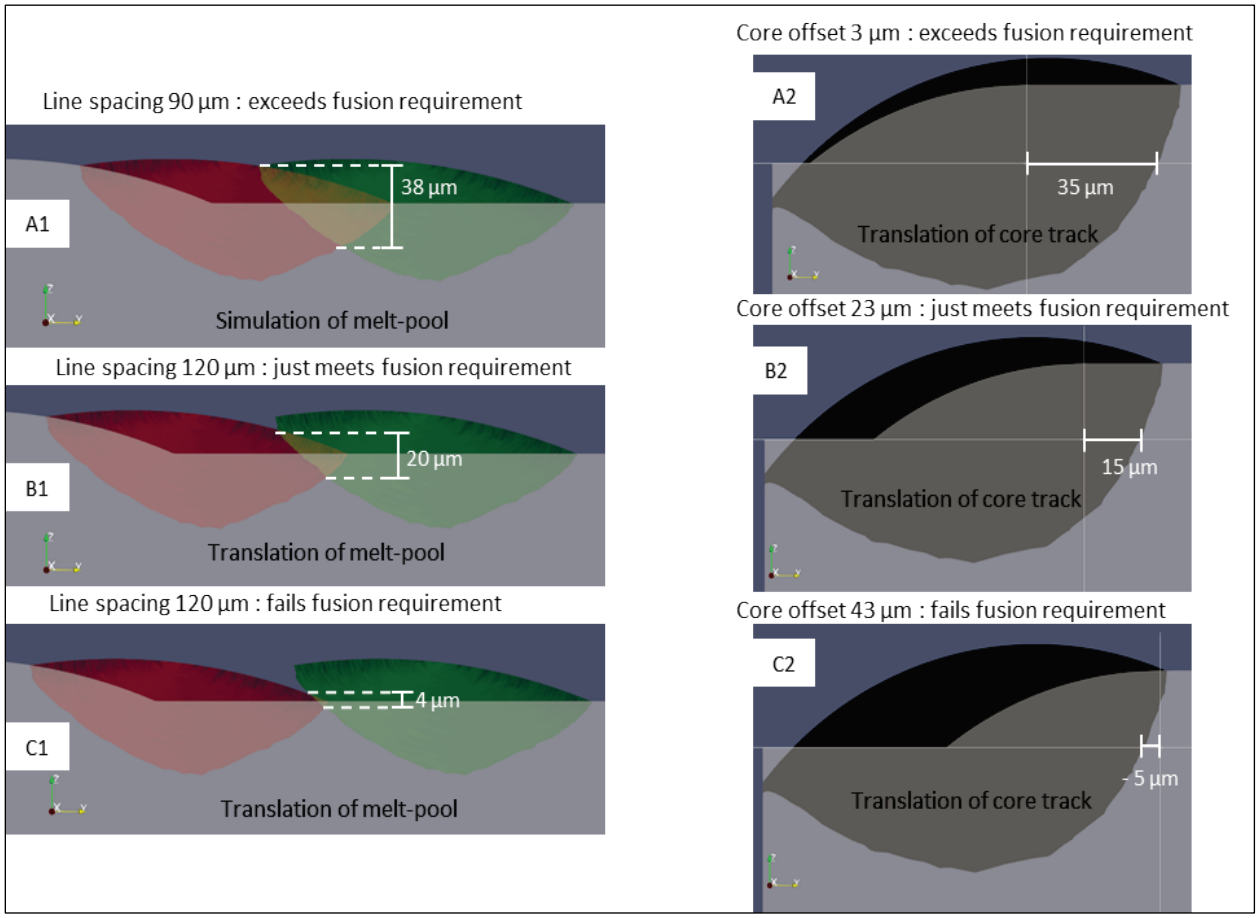


Column	1		2		3	
Row	Line Spacing	Core offset	Line Spacing	Core offset	Line Spacing	Core offset
A	90	3	120	3	140	3
B	90	23	120	23	140	23
C	90	43	120	43	140	43

Figure 53 A1 shows the melt-pool cross section from the nth core track simulation for the default condition. (The green represents the melt-pool created by the nth track, the red the n-1th track, and the yellow is the intersection between the two.) This condition meets and exceeds the core track melting criteria, though only the minimum layer thickness is shown. Figure 53 A2 shows the melt-pool cross section from the contour simulation for the default condition. (The black represents the melt-pool created by the contour track. The curved clear region represents the end of the core exposure.) This meets and exceeds the core/contour overlap contour condition. Little porosity is expected with these conditions. To find a first-order approximation for line spacings and core offsets which

would produce limited and extreme porosity, the melt pools and core exposure tracks were translated until the melt pools met and then failed the criteria. These are Figure 53 B1/B2 and C1/C2, respectively. These translations act as an approximation for the simulations for nth tracks and contour tracks at these line spacings and contour offsets. This was done in the interest of time. Note the bed drop is 20 microns, and the powder diameter is 30 microns.

Figure 53. Melt-pool cross sections for A1/A2 default core/contour, B1/B2 middle condition core/contour, and C1/C2 end condition core/contour.

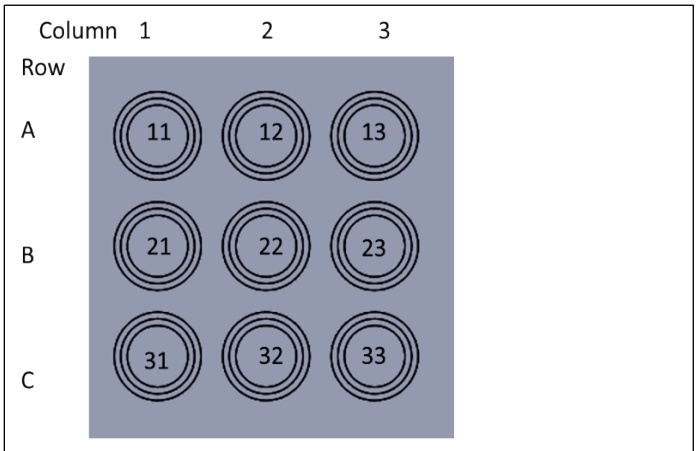


2.3.2.2 *AlSi10Mg DOE*

The AlSi10Mg build was made 1) to validate the model for prediction of lack-of-fusion porosity as it depends on line spacing, up/down skin angle, and the distance between core and contour exposures; and 2) to validate the model for microstructural heterogeneity, as it depends on the solidification rate and the thermal gradient of the melt-pool boundary. The design of experiment (DOE) contains four cone geometries and thirty-six parameter sets. (Purpose 2 is discussed in Section 2.4)

Figure 54 shows the parameter matrix pattern used for each group of cones for the AlSi10Mg build. Parameter set A1 corresponds to the default conditions. Parameter sets B1 and C1 correspond to conditions designed by optimization to reduce porosity in the core and in between the core and the contour. The second entry of each row contains the same parameters as the first entry of that row but with an increase in the contour offset. The third entry of each row contains the same parameters as the first entry of that row but with a decrease in the contour offset. These latter two conditions are designed to increase the distance between the core and the contour exposures, which should decrease the fusion between the regions and increase lack-of-fusion porosity.

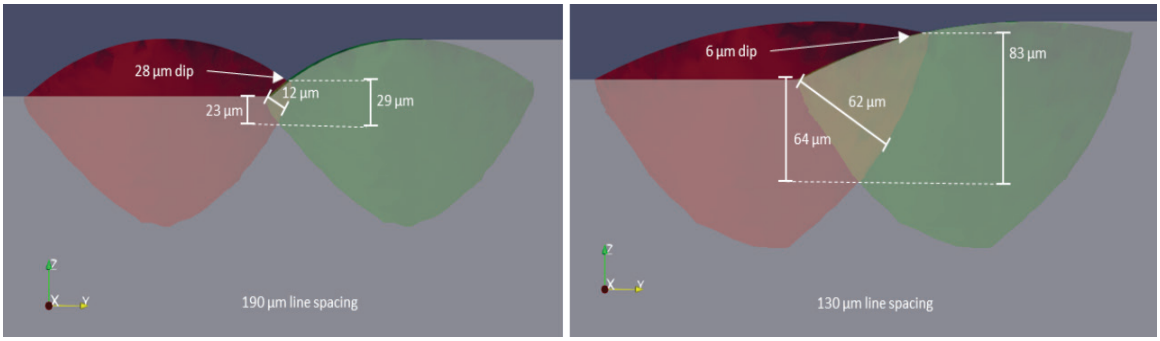
Figure 54. Parameter matrix for each group of AlSi10Mg cones.



	1	2	3
A	Default	Default + core offset	Default + contour offset
B	AO1	AO1 + core offset	AO1 + contour offset
C	AO2	AO2 + core offset	AO2 + contour offset

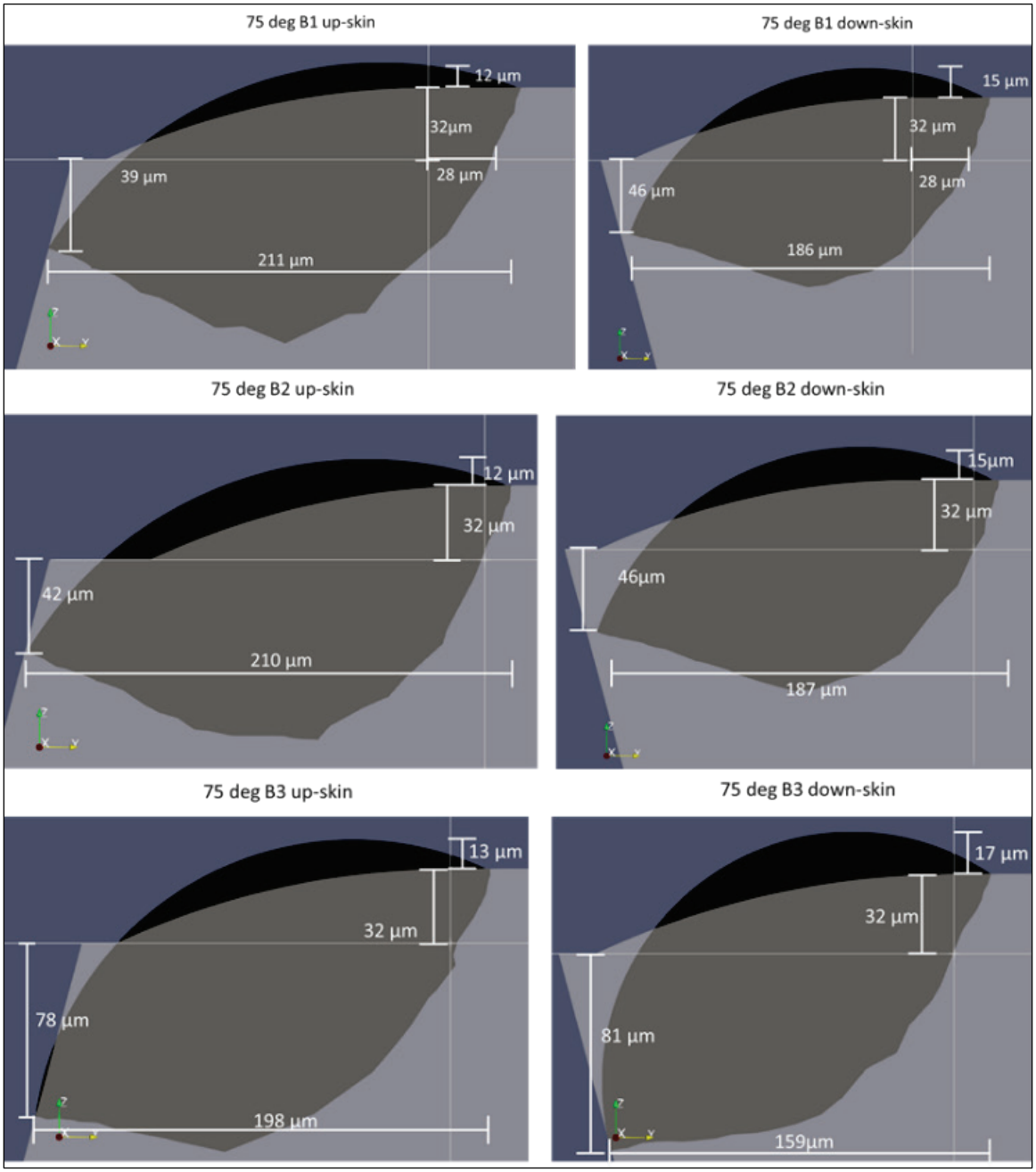
Note the only change to the core parameters was the line spacing. This was changed from the default of 190 microns because the simulation of the nth track using the default condition yielded a melt pool which did not meet criteria. The first perturbation in parameters was chosen to be the line spacing. The single-track melt-pool simulation conducted earlier provided a first-order prediction of 130 microns for the line spacing. On simulation of the nth track using this line spacing, the melt-pool was found to meet criteria. In the interest of time, 130 microns was set as the line spacing for all non-default parameter sets. The melt-pool cross sections of the nth track simulations for both line spacings are shown below in Figure 55. The bed drop and average powder diameter are both 30 microns.

Figure 55. Nth track simulations for 190-micron and 130-micron line spacing.



The contour conditions for no lack of fusion were found by iterating on power and contour offset. The core/contour overlap value was increased or decreased (via power/contour offset iteration) to find contour conditions intended to produce lack of fusion. Figure 56 shows the simulated melt-pool cross sections for parameter sets B1, B2, and B3 for the 75-deg cone. Rows B and C for all other groups have similar simulation results. The parameter matrices are shown in Section 2.3.2.2.1.

Figure 56. Melt-pool cross section of parameter sets B1, B2, and B3 for the 75-deg cone.



2.3.2.2.1 *Parameter matrices for AlSi10Mg build*

Table 14 through Table 17 show the parameter matrices used for the 90-deg cone, the 75-deg cone, the 60-deg cone, and the 45-deg cone. Note the common conditions among all parameter sets are the global offset (65 microns), the core power (370 W), and the core velocity (1300 mm/s).

Legend for Table 14 through 17:

- US = up-skin
- DS = down-skin
- Note 1: Use 10 microns more than the default
- Note 2: Use 10 microns less than the default

Table 14. Parameter matrix for the 90-deg cone.

	1		2		3	
A	Number of Contours	Default	Number of Contours	Default	Number of Contours	Default
	Core Offset (µm)	Default	Core Offset (µm)	Note 1	Core Offset (µm)	Default
	Contour Offset (µm)	Default	Contour Offset (µm)	Default	Contour Offset (µm)	Note 2
	Contour Power (W)	Default	Contour Power (W)	Default	Contour Power (W)	Default
	Contour Velocity (mm/s)	Default	Contour Velocity (mm/s)	Default	Contour Velocity (mm/s)	Default
	Line Spacing (µm)	Default	Line Spacing (µm)	Default	Line Spacing (µm)	Default
B	Number of Contours	1	Number of Contours	1	Number of Contours	1
	Core Offset (µm)	58	Core Offset (µm)	80	Core Offset (µm)	58
	Contour Offset (µm)	40	Contour Offset (µm)	40	Contour Offset (µm)	18
	Contour Power (W)	160	Contour Power (W)	160	Contour Power (W)	160
	Contour Velocity (mm/s)	400	Contour Velocity (mm/s)	400	Contour Velocity (mm/s)	400
	Line Spacing (µm)	130	Line Spacing (µm)	130	Line Spacing (µm)	130
C	Number of Contours	1	Number of Contours	1	Number of Contours	1
	Core Offset (µm)	58	Core Offset (µm)	83	Core Offset (µm)	58
	Contour Offset (µm)	40	Contour Offset (µm)	40	Contour Offset (µm)	15
	Contour Power (W)	150	Contour Power (W)	150	Contour Power (W)	150
	Contour Velocity (mm/s)	200	Contour Velocity (mm/s)	200	Contour Velocity (mm/s)	200
	Line Spacing (µm)	130	Line Spacing (µm)	130	Line Spacing (µm)	130

Table 15. Parameter matrix for the 75-deg cone.

1	2	3

A	Number of Contours	Default		Number of Contours	Default		Number of Contours	Default
	Core Offset (µm)	Default		Core Offset (µm)	Note 1		Core Offset (µm)	Default
	US Contour Offset (µm)	Default		US Contour Offset (µm)	Default		US Contour Offset (µm)	Note 2
	US Contour Power (W)	Default		US Contour Power (W)	Default		US Contour Power (W)	Default
	US Contour Velocity (mm/s)	Default		US Contour Velocity (mm/s)	Default		US Contour Velocity (mm/s)	Default
	DS Contour Offset (µm)	Default		DS Contour Offset (µm)	Default		DS Contour Offset (µm)	Note 2
	DS Contour Power (W)	Default		DS Contour Power (W)	Default		DS Contour Power (W)	Default
	DS Contour Velocity (mm/s)	Default		DS Contour Velocity (mm/s)	Default		DS Contour Velocity (mm/s)	Default
	Line Spacing (µm)	Default		Line Spacing (µm)	Default		Line Spacing (µm)	Default
B	Number of Contours	1		Number of Contours	1		Number of Contours	1
	Core Offset (µm)	58		Core Offset (µm)	86		Core Offset (µm)	58
	US Contour Offset (µm)	40		US Contour Offset (µm)	40		US Contour Offset (µm)	12
	US Contour Power (W)	180		US Contour Power (W)	180		US Contour Power (W)	180
	US Contour Velocity (mm/s)	400		US Contour Velocity (mm/s)	400		US Contour Velocity (mm/s)	400
	DS Contour Offset (µm)	55		DS Contour Offset (µm)	55		DS Contour Offset (µm)	27
	DS Contour Power (W)	140		DS Contour Power (W)	140		DS Contour Power (W)	140
	DS Contour Velocity (mm/s)	400		DS Contour Velocity (mm/s)	400		DS Contour Velocity (mm/s)	400
	Line Spacing (µm)	130		Line Spacing (µm)	130		Line Spacing (µm)	130
C	Number of Contours	1		Number of Contours	1		Number of Contours	1
	Core Offset (µm)	58		Core Offset (µm)	91		Core Offset (µm)	58
	US Contour Offset (µm)	40		US Contour Offset (µm)	40		US Contour Offset (µm)	7
	US Contour Power (W)	170		US Contour Power (W)	170		US Contour Power (W)	170
	US Contour Velocity (mm/s)	200		US Contour Velocity (mm/s)	200		US Contour Velocity (mm/s)	200
	DS Contour Offset (µm)	55		DS Contour Offset (µm)	55		DS Contour Offset (µm)	22
	DS Contour Power (W)	130		DS Contour Power (W)	130		DS Contour Power (W)	130
	DS Contour Velocity (mm/s)	200		DS Contour Velocity (mm/s)	200		DS Contour Velocity (mm/s)	200
	Line Spacing (µm)	130		Line Spacing (µm)	130		Line Spacing (µm)	130

Table 16. Parameter matrix for the 65-deg cone.

	1		2		3	
A	Number of Contours	Default	Number of Contours	Default	Number of Contours	Default
	Core Offset (µm)	Default	Core Offset (µm)	Note 1	Core Offset (µm)	Default
	US Contour Offset (µm)	Default	US Contour Offset (µm)	Default	US Contour Offset (µm)	Note 2
	US Contour Power (W)	Default	US Contour Power (W)	Default	US Contour Power (W)	Default
	US Contour Velocity (mm/s)	Default	US Contour Velocity (mm/s)	Default	US Contour Velocity (mm/s)	Default
	DS Contour Offset (µm)	Default	DS Contour Offset (µm)	Default	DS Contour Offset (µm)	Note 2
	DS Contour Power (W)	Default	DS Contour Power (W)	Default	DS Contour Power (W)	Default
	DS Contour Velocity (mm/s)	Default	DS Contour Velocity (mm/s)	Default	DS Contour Velocity (mm/s)	Default
	Line Spacing (µm)	Default	Line Spacing (µm)	Default	Line Spacing (µm)	Default
B	Number of Contours	1	Number of Contours	1	Number of Contours	1
	Core Offset (µm)	58	Core Offset (µm)	78	Core Offset (µm)	58
	US Contour Offset (µm)	20	US Contour Offset (µm)	20	US Contour Offset (µm)	0
	US Contour Power (W)	200	US Contour Power (W)	200	US Contour Power (W)	200
	US Contour Velocity (mm/s)	400	US Contour Velocity (mm/s)	400	US Contour Velocity (mm/s)	400
	DS Contour Offset (µm)	58	DS Contour Offset (µm)	58	DS Contour Offset (µm)	38
	DS Contour Power (W)	120	DS Contour Power (W)	120	DS Contour Power (W)	120
	DS Contour Velocity (mm/s)	400	DS Contour Velocity (mm/s)	400	DS Contour Velocity (mm/s)	400
	Line Spacing (µm)	130	Line Spacing (µm)	130	Line Spacing (µm)	130
C	Number of Contours	1	Number of Contours	1	Number of Contours	1
	Core Offset (µm)	58	Core Offset (µm)	78	Core Offset (µm)	58
	US Contour Offset (µm)	20	US Contour Offset (µm)	20	US Contour Offset (µm)	0
	US Contour Power (W)	190	US Contour Power (W)	190	US Contour Power (W)	190
	US Contour Velocity (mm/s)	200	US Contour Velocity (mm/s)	200	US Contour Velocity (mm/s)	200
	DS Contour Offset (µm)	58	DS Contour Offset (µm)	58	DS Contour Offset (µm)	38
	DS Contour Power (W)	110	DS Contour Power (W)	110	DS Contour Power (W)	110
	DS Contour Velocity (mm/s)	200	DS Contour Velocity (mm/s)	200	DS Contour Velocity (mm/s)	200
	Line Spacing (µm)	130	Line Spacing (µm)	130	Line Spacing (µm)	130

Table 17. Parameter matrix for the 45-deg cone.

	1		2		3	
A	Number of Contours	Default	Number of Contours	Default	Number of Contours	Default
	Core Offset (µm)	Default	Core Offset (µm)	Note 1	Core Offset (µm)	Default
	US Contour Offset (µm)	Default	US Contour Offset (µm)	Default	US Contour Offset (µm)	Note 2
	US Contour Power (W)	Default	US Contour Power (W)	Default	US Contour Power (W)	Default
	US Contour Velocity (mm/s)	Default	US Contour Velocity (mm/s)	Default	US Contour Velocity (mm/s)	Default
	DS Contour Offset (µm)	Default	DS Contour Offset (µm)	Default	DS Contour Offset (µm)	Note 2
	DS Contour Power (W)	Default	DS Contour Power (W)	Default	DS Contour Power (W)	Default
	DS Contour Velocity (mm/s)	Default	DS Contour Velocity (mm/s)	Default	DS Contour Velocity (mm/s)	Default
	Line Spacing (µm)	Default	Line Spacing (µm)	Default	Line Spacing (µm)	Default
B	Number of Contours	1	Number of Contours	1	Number of Contours	1
	Core Offset (µm)	58	Core Offset (µm)	78	Core Offset (µm)	58
	US Contour Offset (µm)	20	US Contour Offset (µm)	20	US Contour Offset (µm)	0
	US Contour Power (W)	210	US Contour Power (W)	210	US Contour Power (W)	210
	US Contour Velocity (mm/s)	400	US Contour Velocity (mm/s)	400	US Contour Velocity (mm/s)	400
	DS Contour Offset (µm)	58	DS Contour Offset (µm)	58	DS Contour Offset (µm)	38
	DS Contour Power (W)	120	DS Contour Power (W)	120	DS Contour Power (W)	120
	DS Contour Velocity (mm/s)	400	DS Contour Velocity (mm/s)	400	DS Contour Velocity (mm/s)	400
	Line Spacing (µm)	130	Line Spacing (µm)	130	Line Spacing (µm)	130
C	Number of Contours	1	Number of Contours	1	Number of Contours	1
	Core Offset (µm)	58	Core Offset (µm)	78	Core Offset (µm)	58
	US Contour Offset (µm)	20	US Contour Offset (µm)	20	US Contour Offset (µm)	0
	US Contour Power (W)	200	US Contour Power (W)	200	US Contour Power (W)	200
	US Contour Velocity (mm/s)	200	US Contour Velocity (mm/s)	200	US Contour Velocity (mm/s)	200
	DS Contour Offset (µm)	58	DS Contour Offset (µm)	58	DS Contour Offset (µm)	38
	DS Contour Power (W)	110	DS Contour Power (W)	110	DS Contour Power (W)	110
	DS Contour Velocity (mm/s)	200	DS Contour Velocity (mm/s)	200	DS Contour Velocity (mm/s)	200
	Line Spacing (µm)	130	Line Spacing (µm)	130	Line Spacing (µm)	130

2.3.2.2.2 *Melt-pool cross sections for rows 2 and 3 of Tables B6.1-4*

Figures 57 through 63 show the simulated melt-pool cross sections for rows B and C of Table 14 through Table 17. Note that only the 90-deg cone shows both rows in a single figure (Figure 57). Since the other cones have both an up-skin and a down-skin, the rows are shown in separate figures (Figure 58 through Figure 63).

Figure 57. Rows B and C of the 90-deg cone.

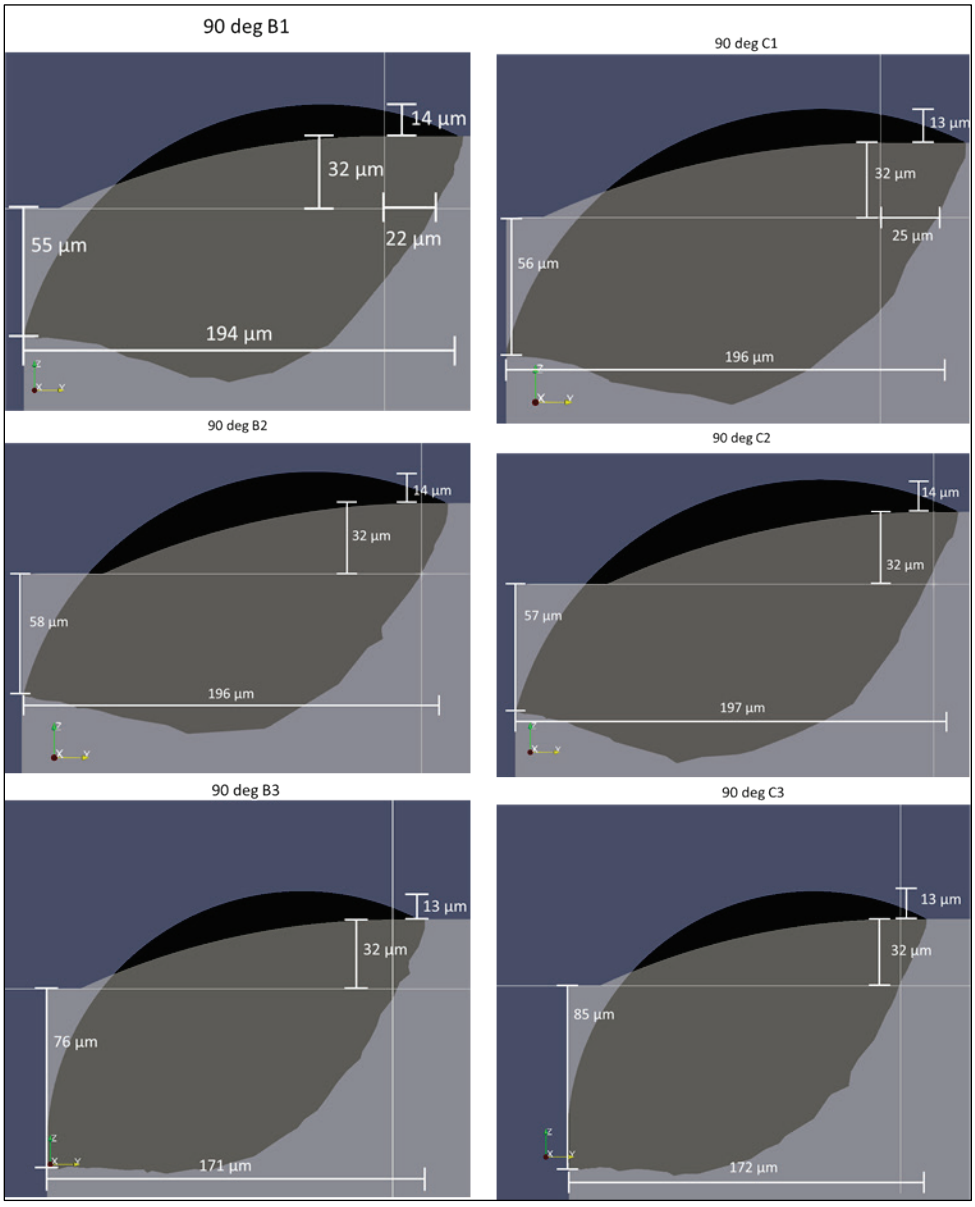


Figure 58. Row B of the 75-deg cone.

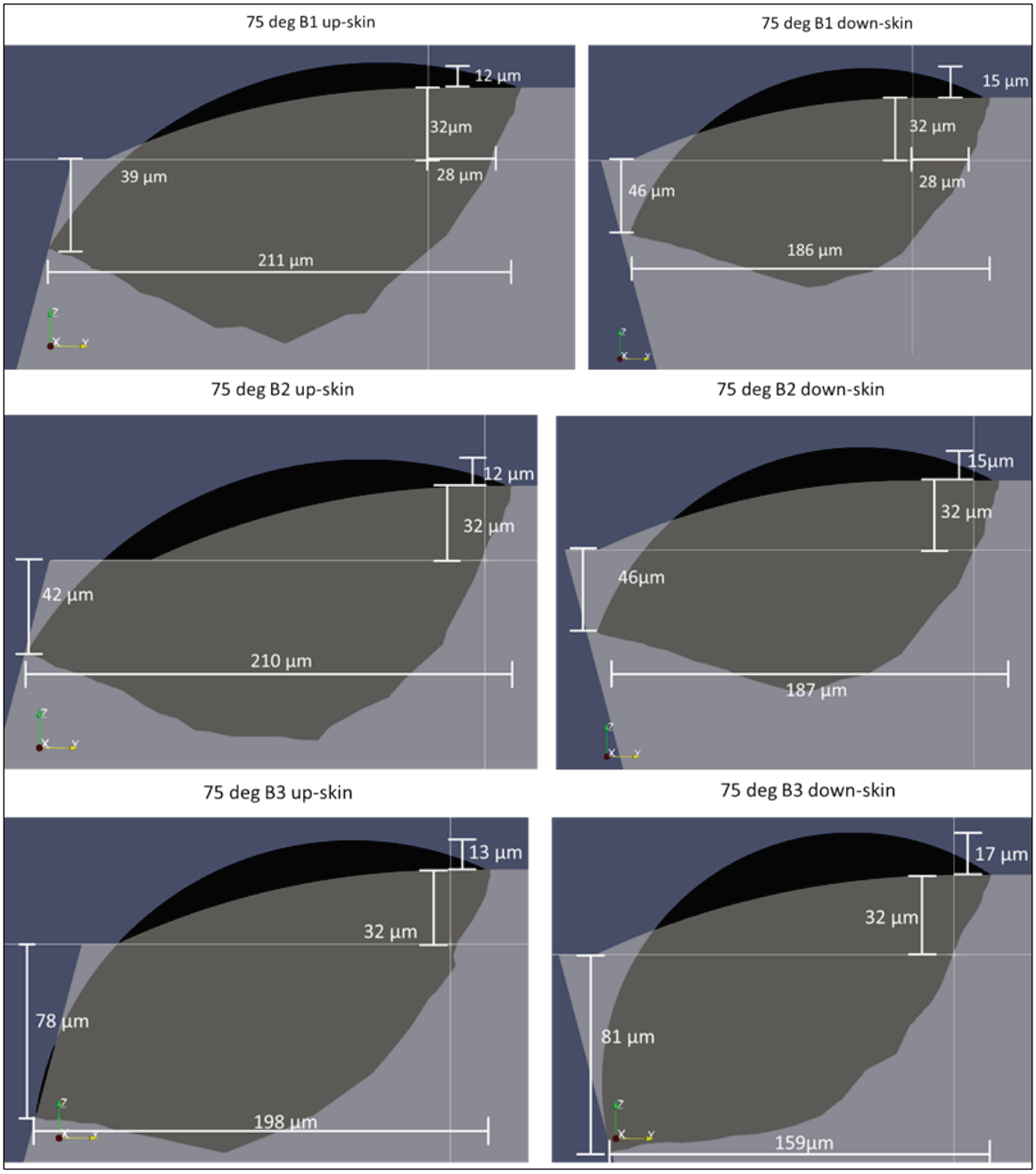


Figure 59. Row C of the 75-deg cone.

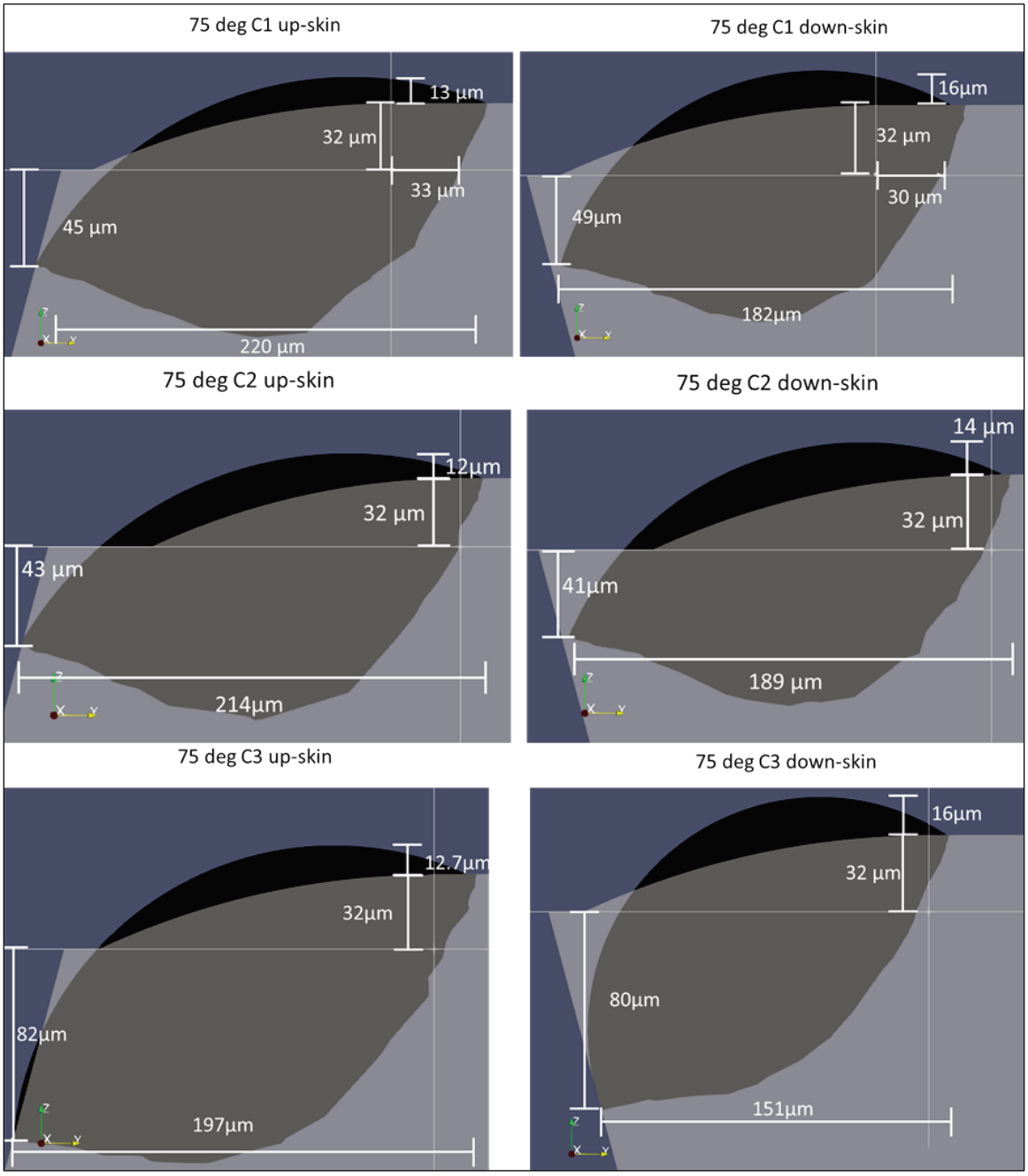


Figure 60. Row B of the 60-deg cone.

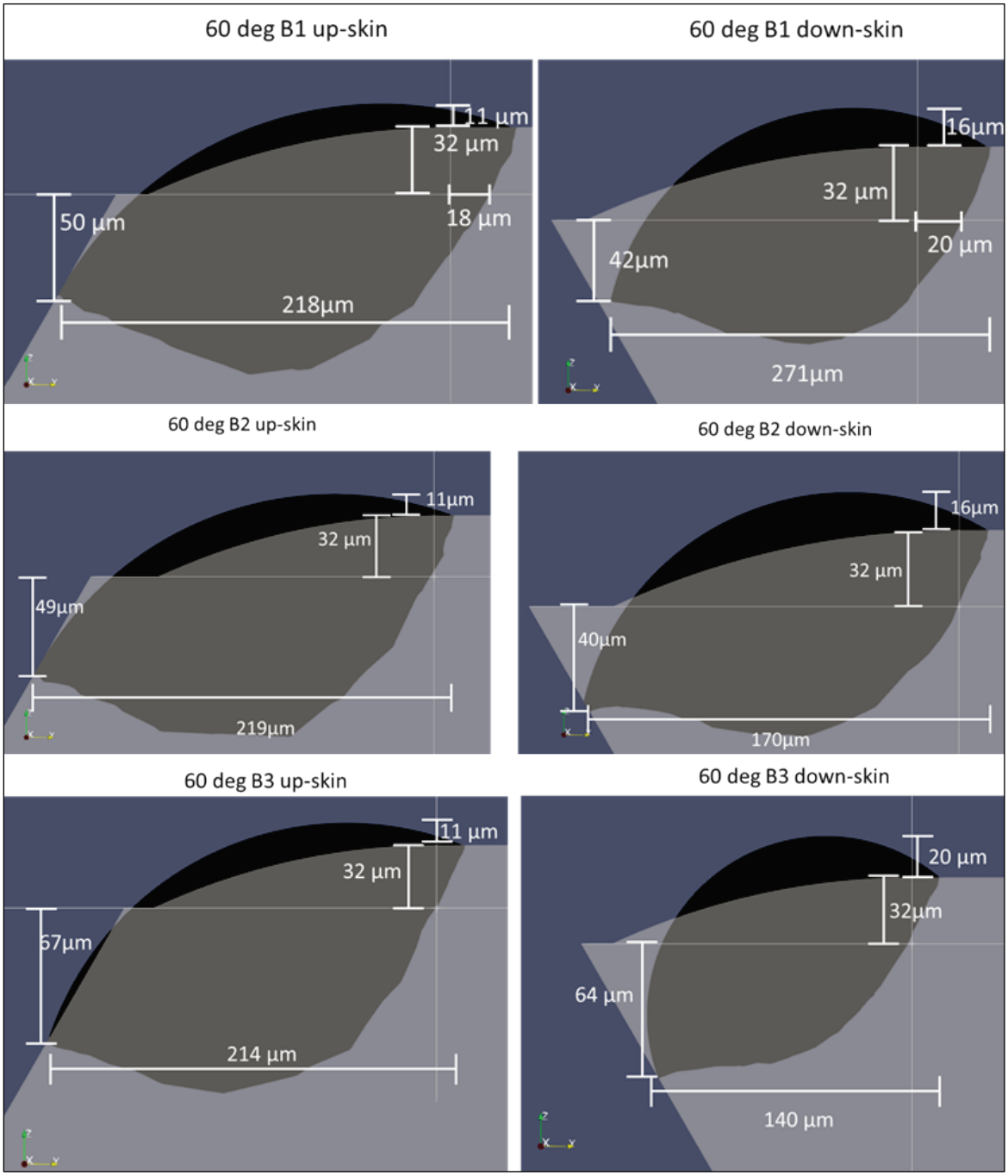


Figure 61. Row C of the 60-deg cone.

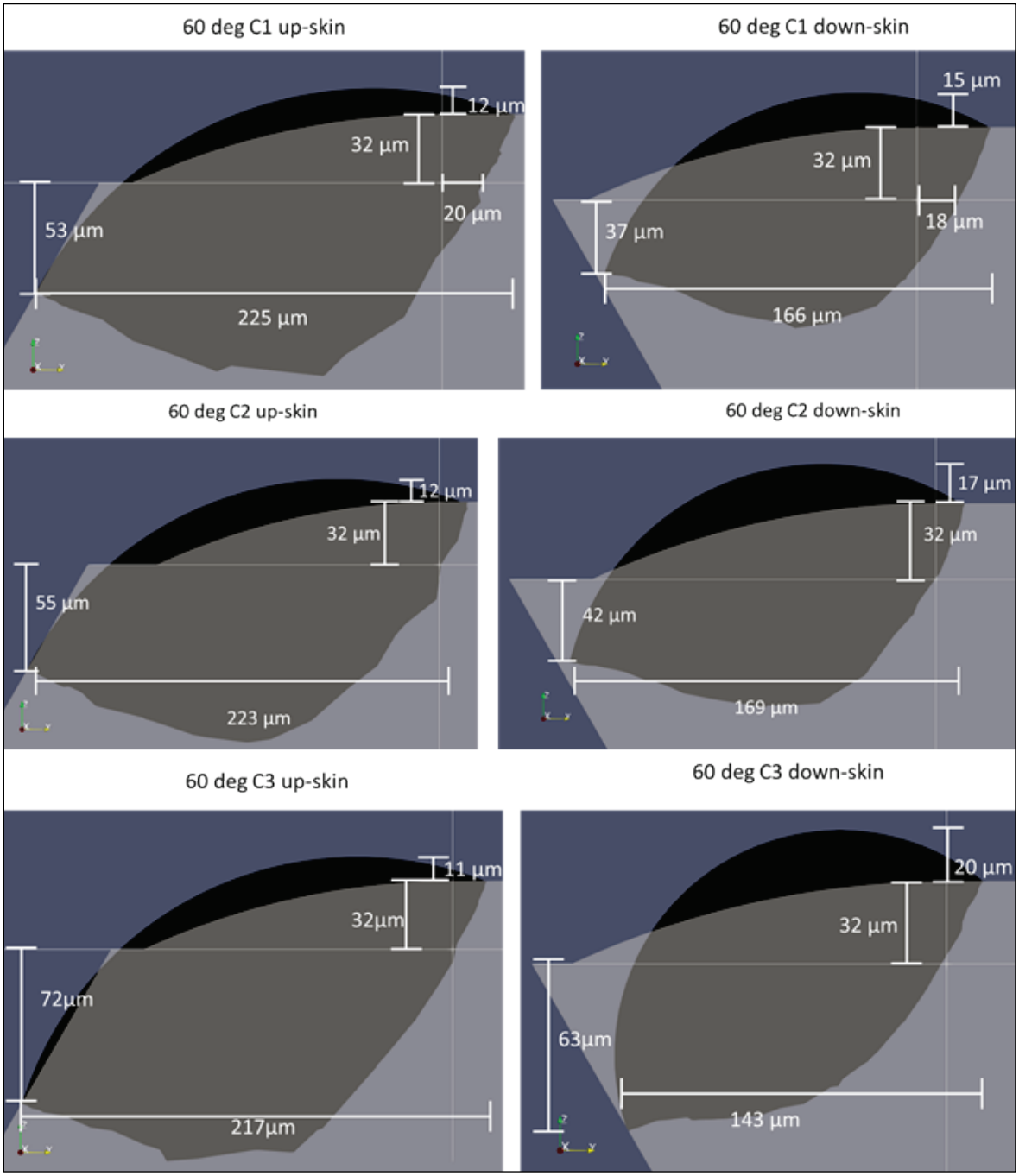


Figure 62. Row B of the 45-deg cone.

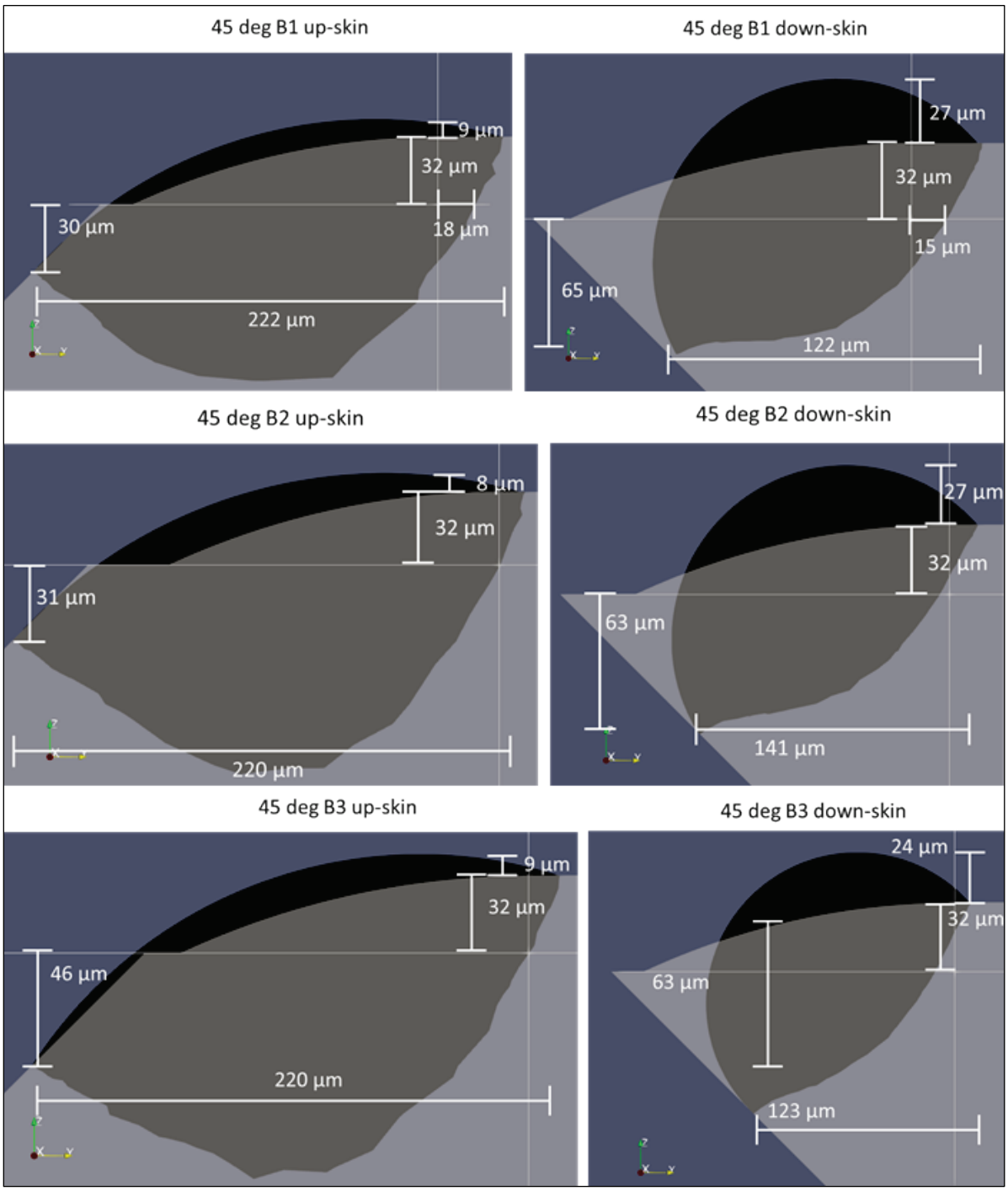
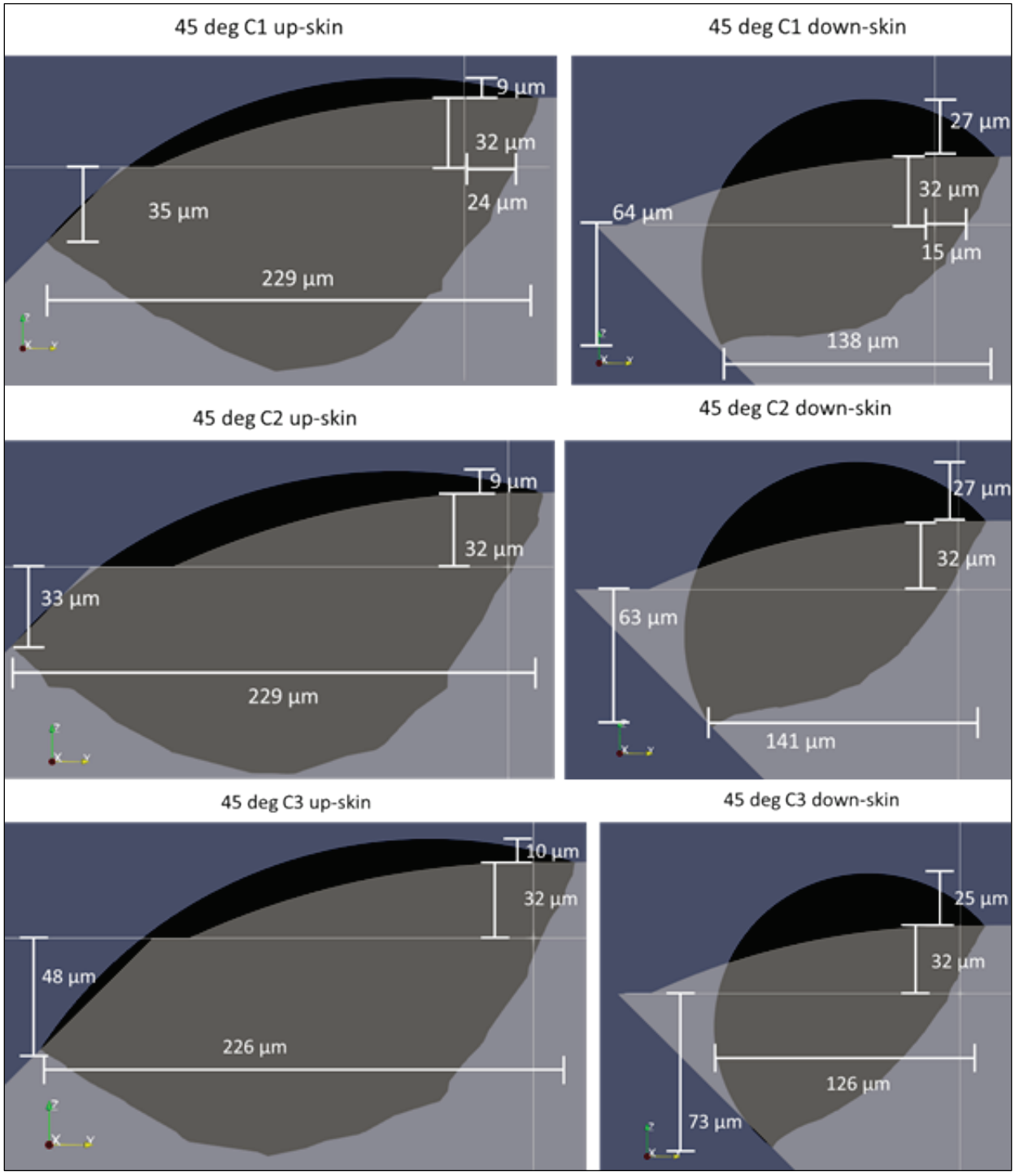


Figure 63. Row C of the 45-deg cone.



2.3.3 Experimental validation

This section shows the results of the experiment which was conducted to test the validity of the porosity mitigation model.

2.3.3.1 *15-5 PH SS*

This section shows the results from the 15-5 PH SS DOE. Each set of cones is shown in its own section.

2.3.3.1.1 *15-5 PH SS 90° cones*

Figure 64 and Figure 66 show the un-etched 25x images of xy-plane and yz-plane cross sections for 15-5PH 90◦ cones, respectively. Figure 65 and Figure 67 show the un-etched 100x images of core-exposure region xy-plane and yz-plane cross sections. The red circles and ovals in and Figure 66 highlight the porosity near to or connected to the surface/edge of the part. The white numbers in each corner of each cross section represent the bulk measured porosity. Figure 65 and Figure 67 show results of the image analysis, with defects marked in red. In some of the cross sections, there are large dark regions in the interior or on the edge of the parts. These are gouges created when the specimens were labeled and do not represent porosity.

Figure 64 and Figure 66 show how the core exposure porosity increases with increased line spacing (from left to right/columns 1-3). The increase in porosity is evident from these images and as well as the porosity measurements data shown in Figure 65 and Figure 67. With increasing core offset (from top to bottom/ rows A-C), there is an increase in near-surface or edge porosity. There is little to no surface-connected porosity.

2.3.3.1.2 *15-5 PH SS 75° cones*

Figure 68 and Figure 70 show the un-etched 25x images of xy-plane and yz-plane cross sections for 15-5PH 75° cones. Figure 69 and Figure 71 show the un-etched 100x images of core exposure region xy-plane and yz-plane cross sections. The red circles and ovals in Figure 68 and Figure 70 highlight the porosity near to or connected to the surface/edge of the part. The white numbers in each corner of each cross section represent the bulk measured porosity. Figure 69 and Figure 71 show results of the image analysis, with defects marked in red. In some of the cross sections, there are large dark regions in the interior or on the edge of the parts. These are gouges created when the specimens were labeled and do not represent porosity.

Figure 64. Un-etched xy-plane cross sections for 15-5 PH 90° cones at 25x.



Figure 65. Un-etched xy-plane cross sections for 15-5 PH 90° cones at 100x.

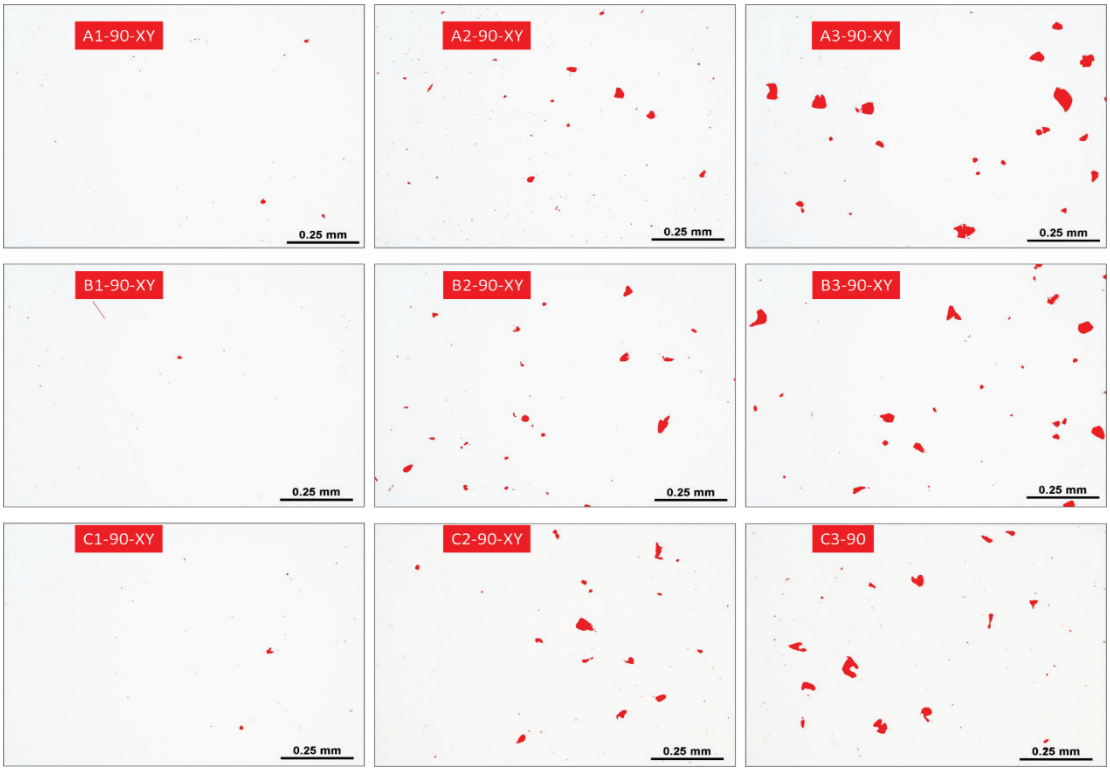


Figure 66. Un-etched yz-plane cross sections for 15-5 PH 90° cones at 25x.

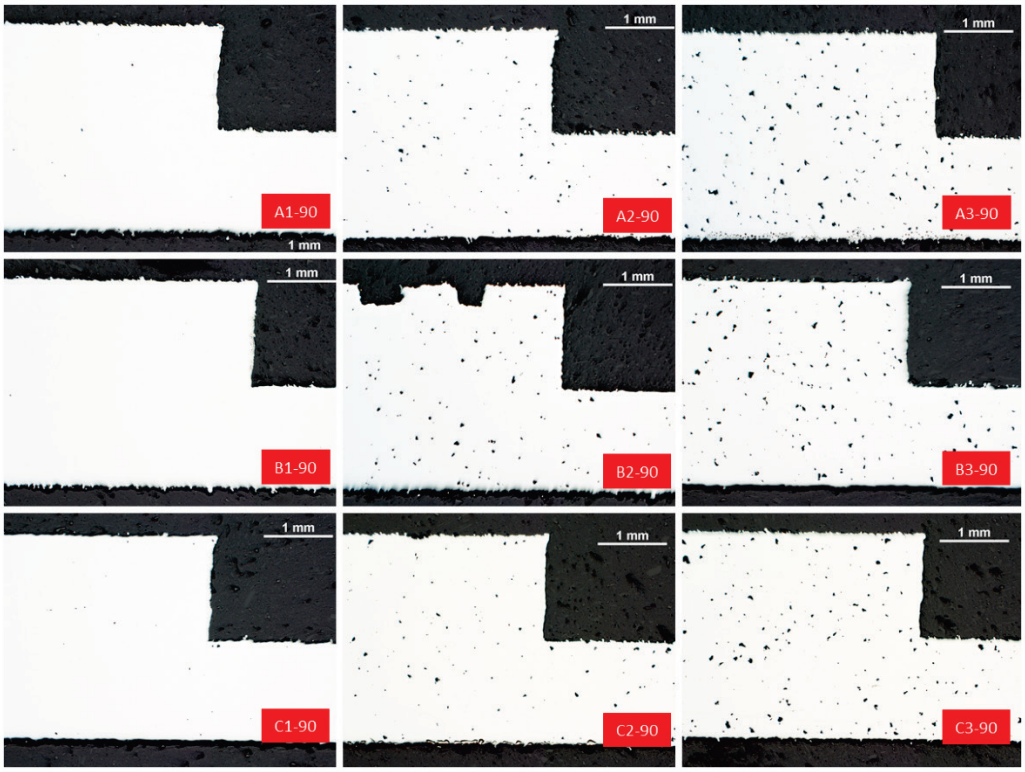


Figure 67. Un-etched yz-plane cross sections for 15-5 PH 90° cones at 100x.



Figure 68. Un-etched xy-plane cross sections for 15-5 PH 75° cones at 25x.

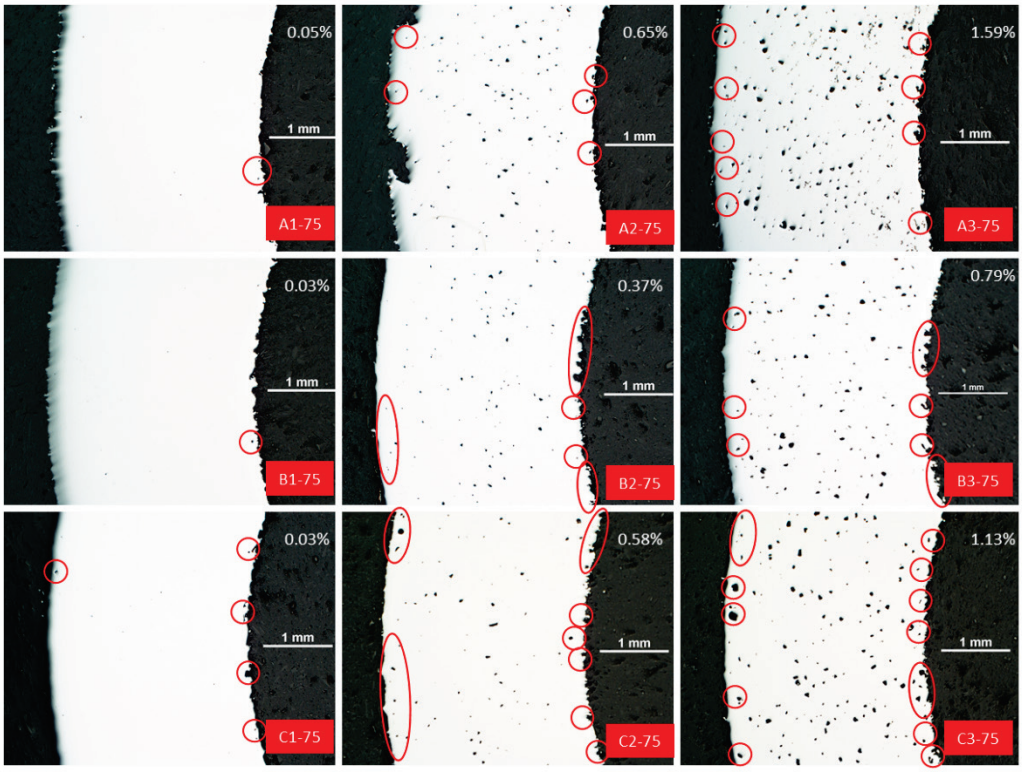


Figure 69. Un-etched xy-plane cross sections for 15-5 PH 75° cones at 100x.

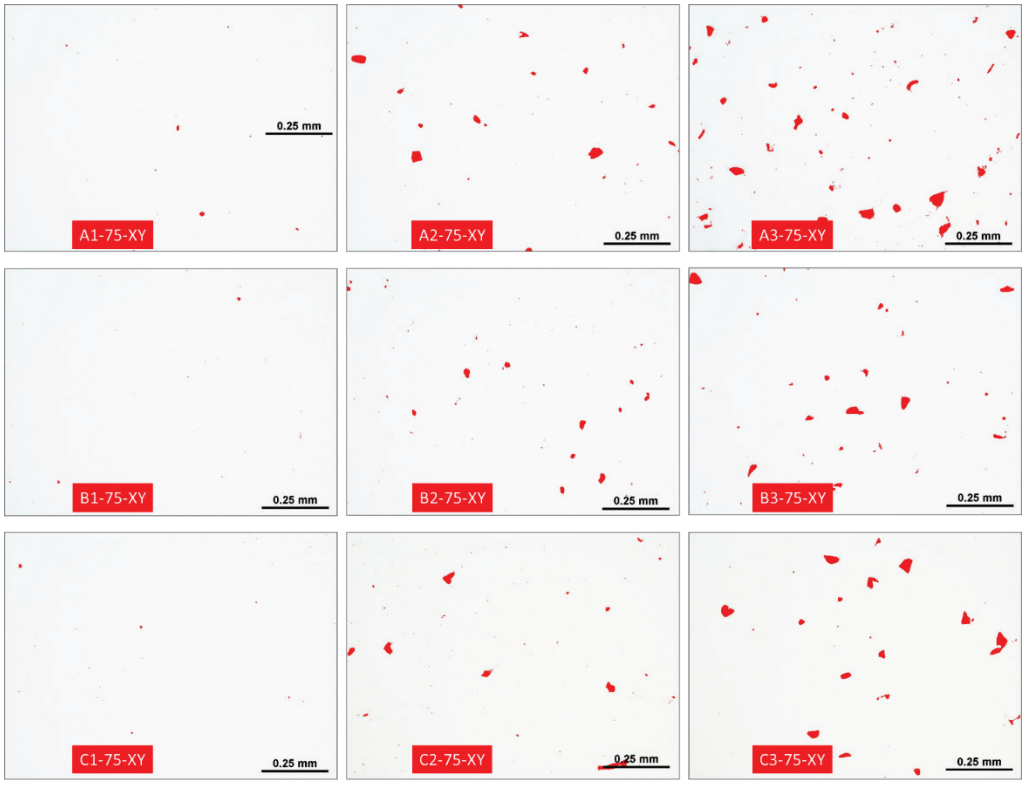


Figure 70. Un-etched yz-plane cross sections for 15-5 PH 75° cones at 25x.

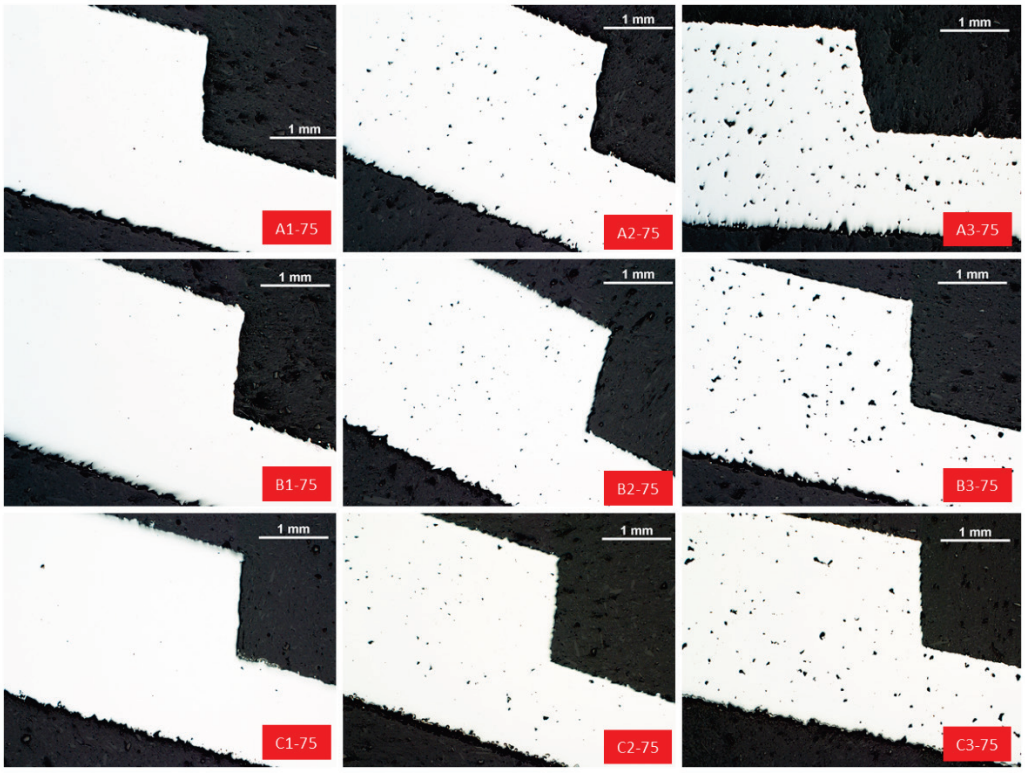
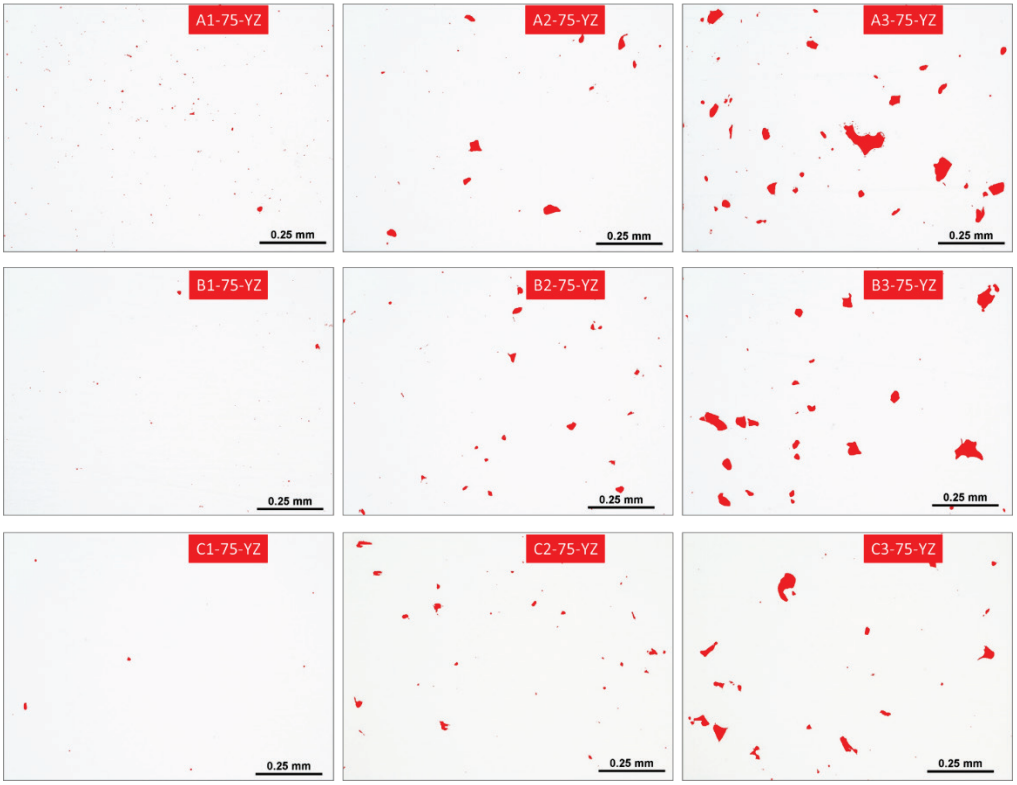


Figure 71. Un-etched yz-plane cross sections for 15-5 PH 75° cones at 100x.



As with the 90o cones, the bulk porosity increases with increased line spacing, and the porosity near the surface increases with increased core offset. Isolated surface-connected porosity is visible. Figure 69 and Figure 71 show porosity measurements data for xy-plane and yz-plane cross sections.

2.3.3.1.3 *15-5 PH SS 60o cones*

Figure 72 and Figure 76 show the un-etched 25x images of xy-plane and yz-plane cross sections for 15-5PH 600 cones. Figure 75 and Figure 77 show the un-etched 100x images of core-exposure region xy-plane and yz-plane cross sections. The red circles and ovals in Figure 72 and Figure 76 highlight the porosity near to or connected to the surface/edge of the part. The white numbers in each corner of each cross section represent the bulk measured porosity. Figure 75 and Figure 77 show results of the image analysis, with defects marked in red. Figure 73 and Figure 74 show high resolution images of the xy and yz-plane cross sections respectively. In some of the cross sections, there are large dark regions in the interior or on the edge of the parts. These are gouges created when the specimens were labeled and do not represent porosity.

Figure 72. Un-etched xy-plane cross sections for 15-5 PH 60o cones at 25x.

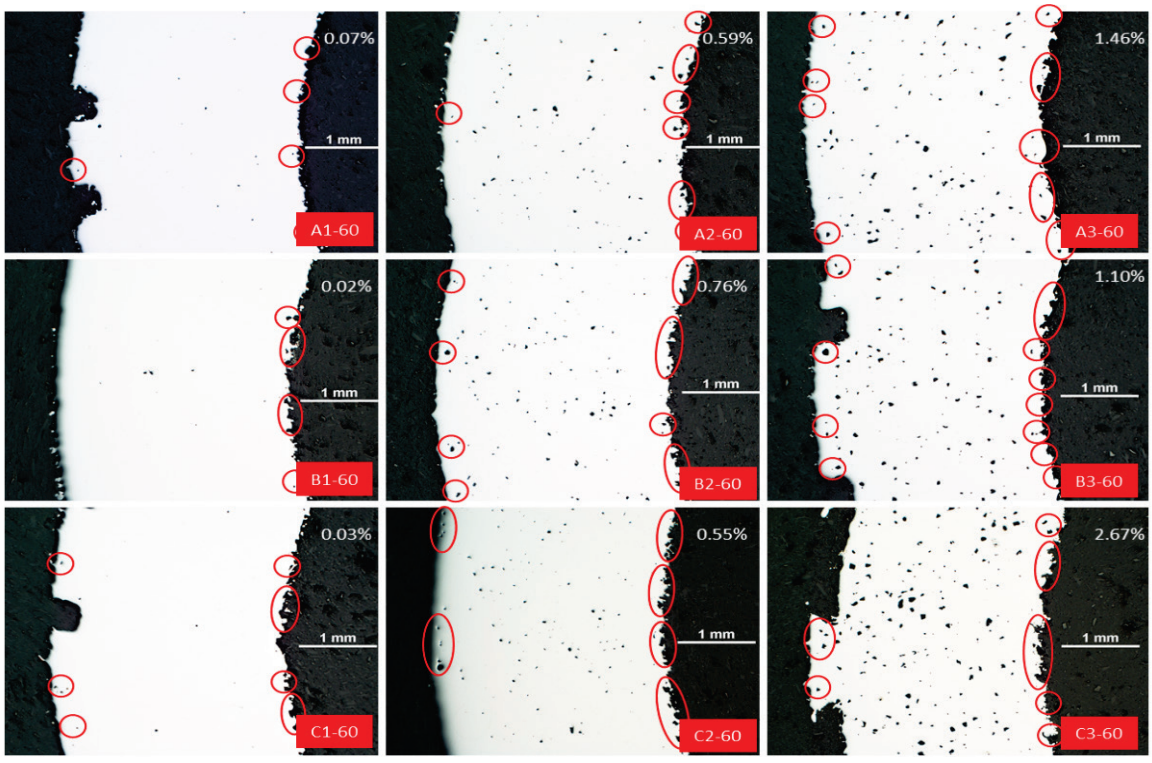


Figure 73. High-resolution un-etched xy-plane cross-section for 15-5 PH cone A1-60.

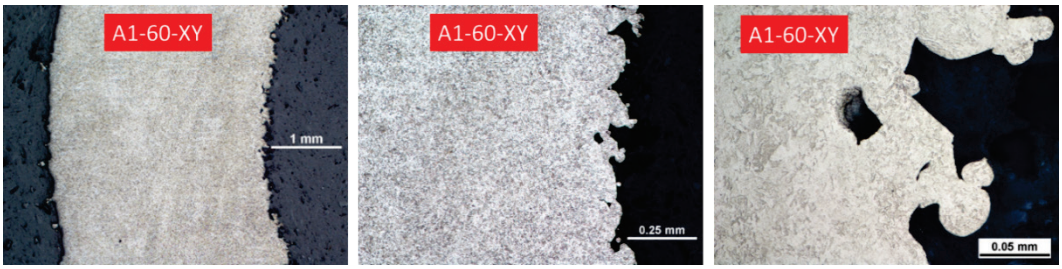


Figure 74. High-resolution un-etched yz-plane cross-section for 15-5 PH cone A1-60.

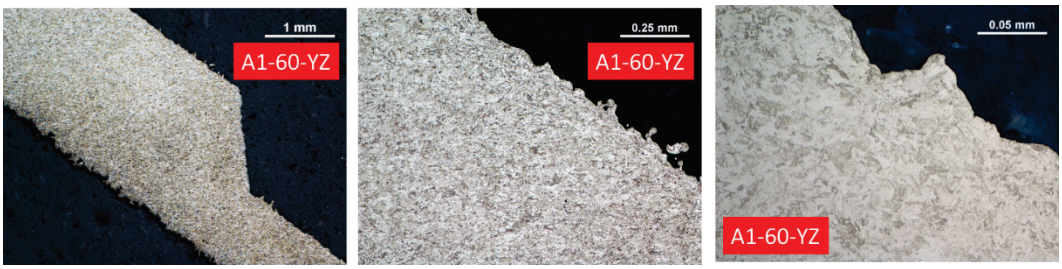


Figure 75. Un-etched xy-plane cross sections for 15-5 PH 60° cones at 100x.

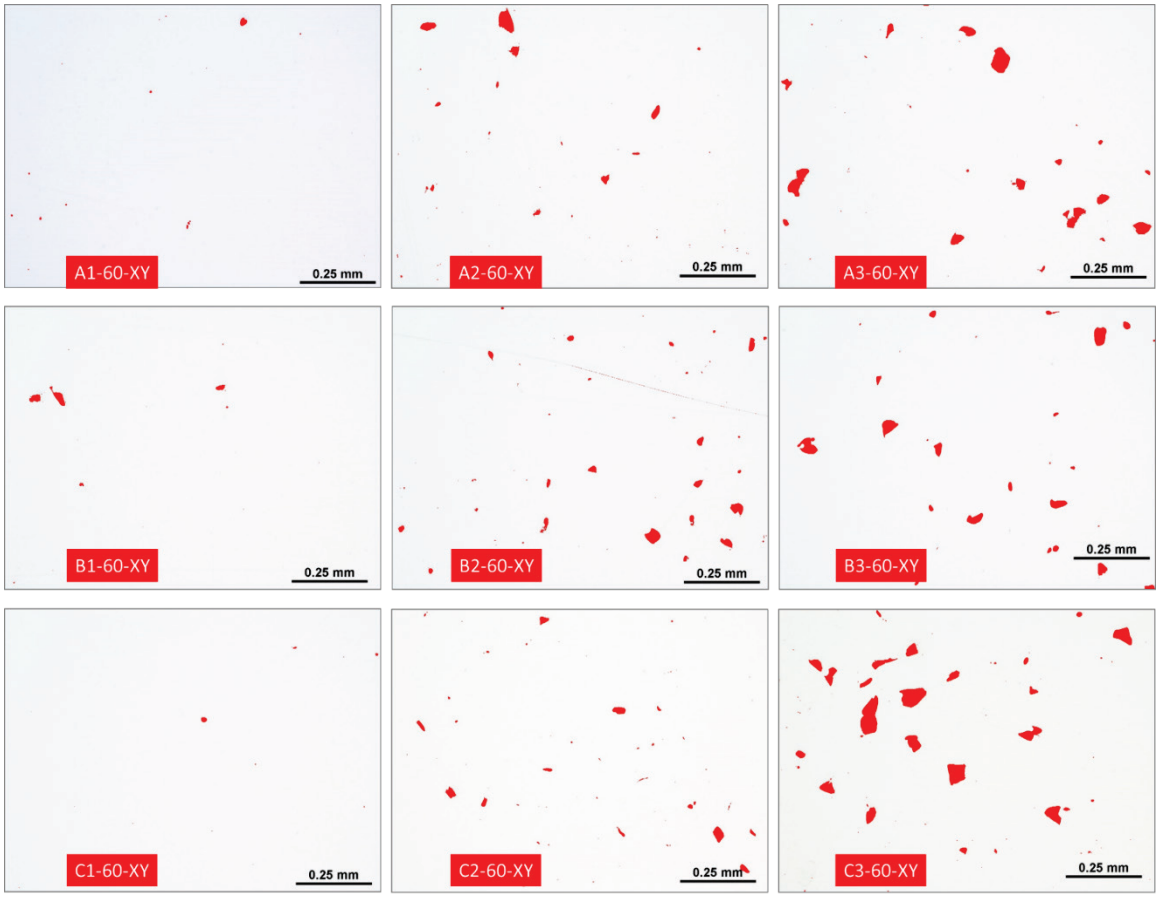


Figure 76. Un-etched yz-plane cross sections for 15-5 PH 60° cones at 25x.

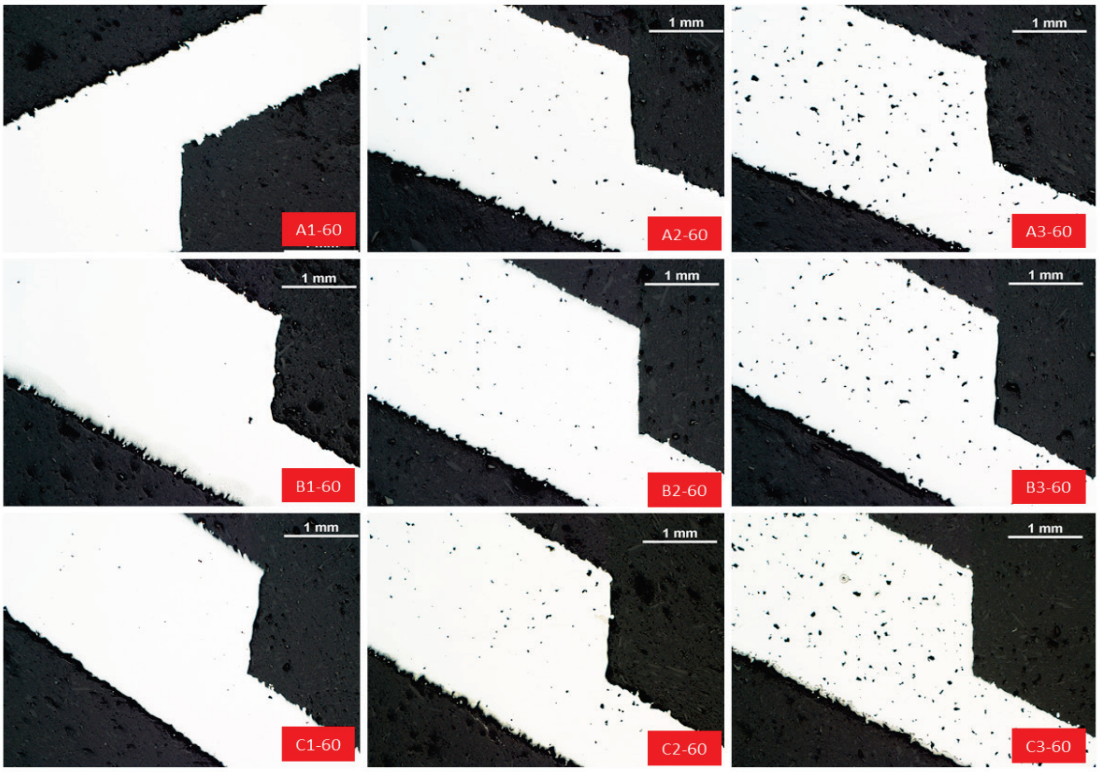
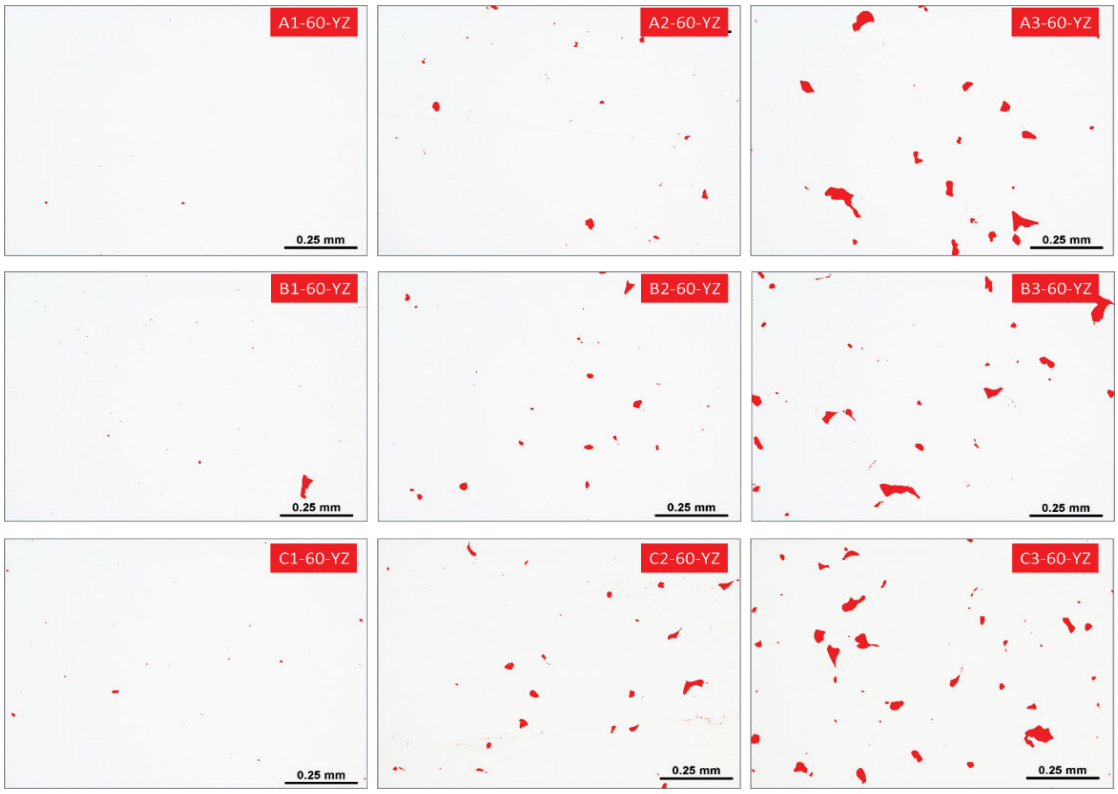


Figure 77. Un-etched yz-plane cross sections for 15-5 PH 60° cones at 100x.



As with the 90° and 75° cones, the bulk porosity increases with increasing line spacing. There is more surface-connected porosity than in either of the former set of cones, particularly on the down-skin (concave) side. There is a trend for increase in surface porosity with core offset on the up-skin (convex surface). Figure 73 shows a near surface pore. This particular pore is not surface connected, but situations where the pores are surface connected are seen in the 25x images. Figure 74 provides an illustration of the surface finish. Figure 75 and Figure 77 show porosity measurements data for xy-plane and yz-plane cross sections.

2.3.3.1.4 *15-5 PH SS 45° cones*

Figure 78 and Figure 80 show the un-etched 25x images of xy-plane and yz-plane cross sections for 15-5PH 45° cones, respectively. Figure 79 and Figure 81 show the un-etched 100x images of core-exposure region xy-plane and yz-plane cross sections. The red circles and ovals in Figure 78 and Figure 80 highlight the porosity near to or connected to the surface/edge of the part. The white numbers in each corner of each cross section represent the bulk measured porosity. Figure 79 and Figure 81 show results of the image analysis, with defects marked in red. In some of the cross sections, there are large dark regions in the interior or on the edge of the parts. These are gouges created when the specimens were labeled and do not represent porosity.

Figure 78. Un-etched xy-plane cross sections for 15-5 PH 45o cones at 25x.

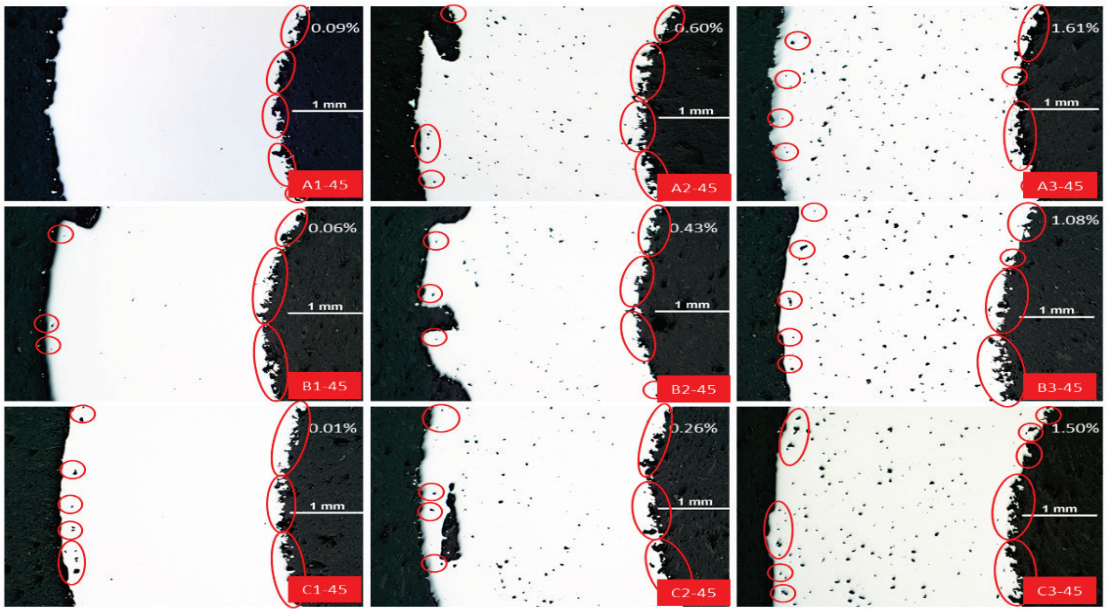


Figure 79. Un-etched xy-plane cross sections for 15-5 PH 45° cones at 100x.



Figure 80. Un-etched yz-plane cross sections for 15-5 PH 45° cones at 25x.

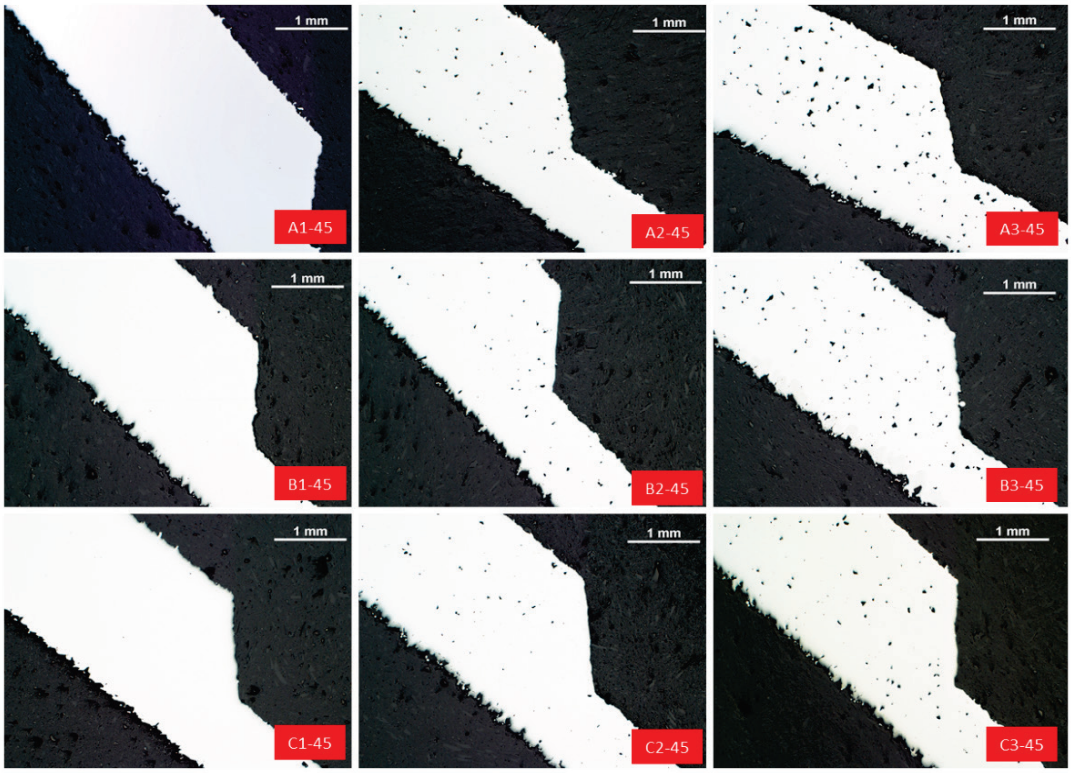


Figure 81. Un-etched yz-plane cross sections for 15-5 PH 45° cones at 100x.



Figure 78 and Figure 80 show the cross sections for the nine 450 cones. As with the previous three sets of cones, the bulk porosity increases with increasing line spacing. There is also increasing surface porosity with increasing core offset on the up-skin. There is a larger amount of surface-connected porosity on the down-skin surfaces.

2.3.3.1.5 *15-5 PH SS cone conclusions*

The following conclusions are derived from the 15-5 PH DOE in regards to the control of build defect mitigation. Please note the following conclusions are derived based on the hypothesis that defect mitigation is dependent on the understanding of the solidification profile for an individual track, its interaction with the adjacent track, and its interaction with the top surface of the preceding layer. Of particular importance is the depth and volume of rewetting. Specifically:

- Increase of line spacing resulted in increase in build porosity. This is consistent with the hypothesis, namely that an increase in line spacing decreases the overlap between the AM solidification profiles for the adjacent tracks. This would effectively decrease the depth of rewetting between adjacent tracks and reduce the minimum thickness of the

layer, which would cause porosity when the minimum layer thickness is smaller than the bed-drop.
- Increase of the core offset resulted in increase in build porosity. This is consistent with the hypothesis, namely that an increase in core offset reduces the depth of remelt between the core and contour exposure tracks, which would increase the near surface defects.
- The surface porosity increases with decreasing skin angle. This is consistent with the hypothesis, namely that the thermal conditions of up-skin and down-skin edges change as a function of the skin angle. The effect of lower thermal conductivity of powder below the down-skin surface causes higher temperatures in the build and nonuniform melt behavior adjacent to the edge. This is potentially correlated with the increased surface-connected porosity with decreasing skin angle.
- Location dependent parameters need to be designed in order to mitigate the build defects in the core and contour exposure and to mitigate the surface-connected porosity. The surface-connected porosity cannot be healed by post deposition hot isostatic pressing and is thus detrimental to the fatigue strength of AM materials.

In summary, there is increased porosity with higher line offset and higher core offset. The porosity increased with reduction in the skin angle. Location dependent design of process parameters is needed in order to mitigate build defects for a complex part for which fatigue strength is important.

2.3.3.2 *AlSi10Mg*

This section shows the results from the AlSi10Mg DOE. Each set of cones is shown in its own section.

2.3.3.2.1 *AiSi10Mg 90° cones*

Figure 82 and Figure 84 show the un-etched 25x images of xy-plane and yz-plane cross sections for AlSi10Mg 90° cones, respectively.Figure 83 and Figure 85 show the un-etched 100x images of core exposure region xy-plane and yz-plane cross sections.

Figure 82. Un-etched xy-plane cross sections for AlSi10Mg 90° cones at 25x.

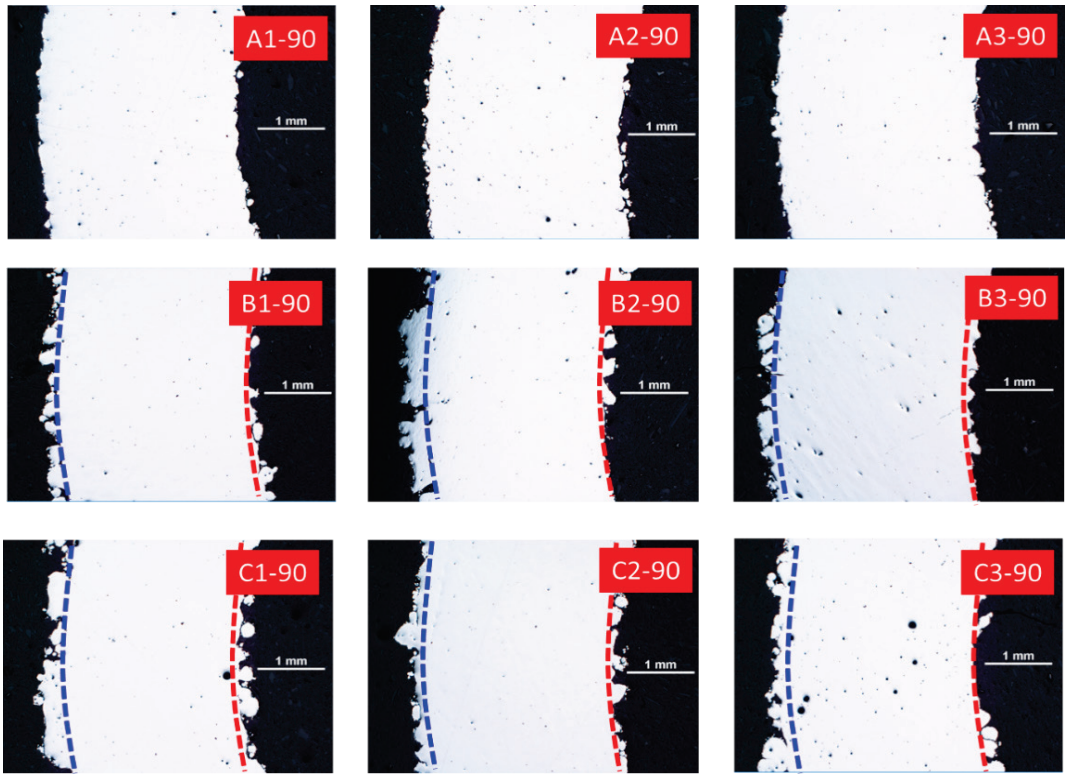


Figure 83. Un-etched xy-plane cross sections for AlSi10Mg 90° cones at 100x.

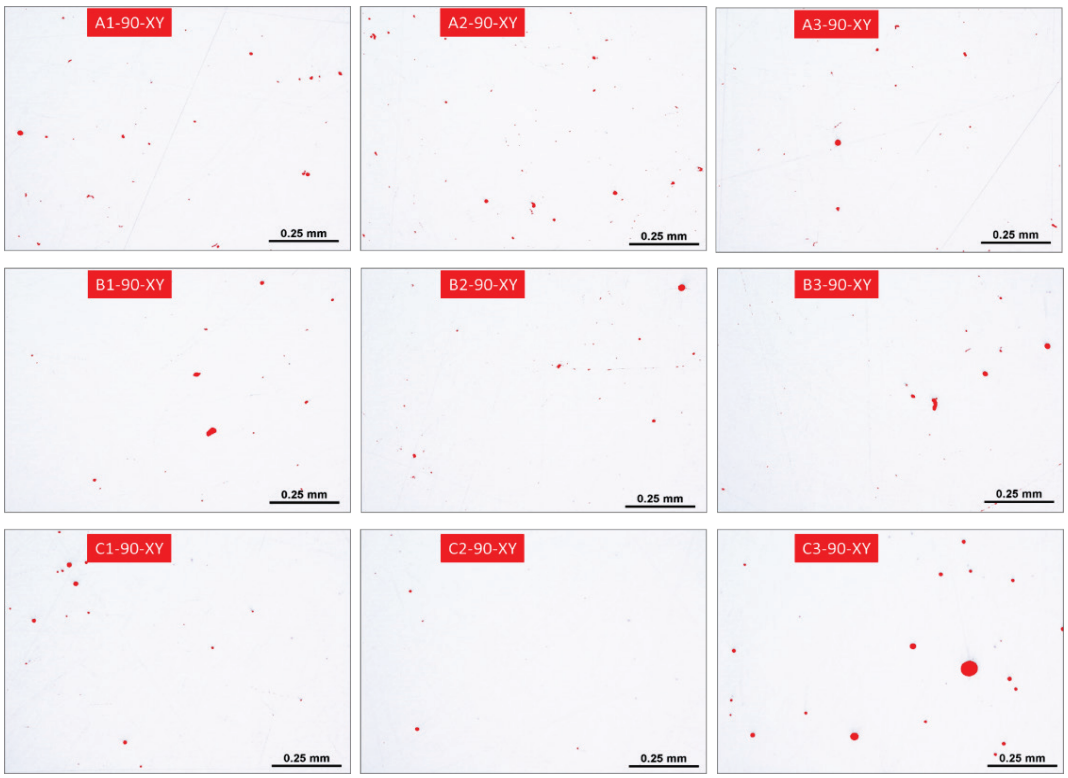


Figure 84. Un-etched yz-plane cross sections for AlSi10Mg 90° cones at 25x.

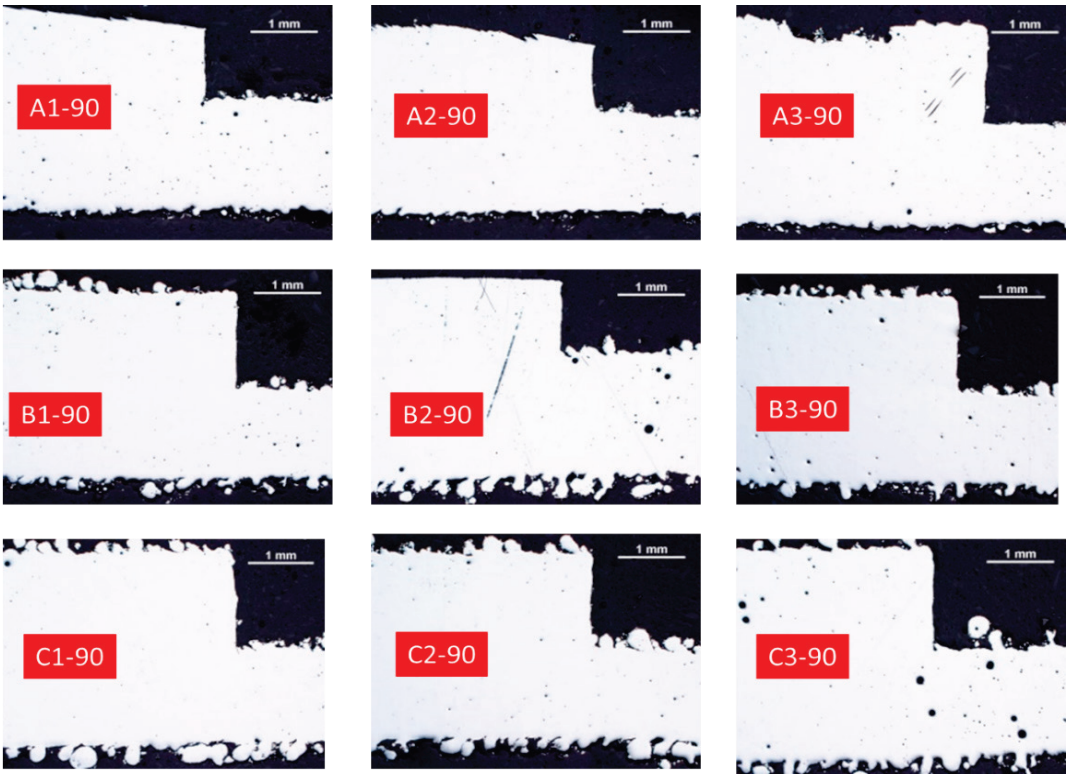


Figure 85. Un-etched yz-plane cross sections for AlSi10Mg 90° cones at 100x.



The blue and red dotted lines indicate the ideal surface for OD and ID. The core exposure porosity is lower for cones B1-90 and C1-90 as compared to the default condition, A1-90. Larger, spherical pores are observed in the third column. Larger pores are observed in the region where the wall thickness of the cones is reduced by 50 percent, which corresponds to higher build temperature because the time taken by the laser to melt the entire layer is half as much as compared to the lower region. This allows increased transience during the melting process. There is no surface-connected porosity, but there is significant amount of satellite formation.

2.3.3.2.2 *AiSi10Mg 75° cones*

Figure 86 and Figure 88 show the un-etched 25x images of xy-plane and yz-plane cross sections for AlSi10Mg 75° cones, respectively. Figure 87 and Figure 89 show the un-etched 100x images of core exposure region xy-plane and yz-plane cross sections.

The core exposure porosity for cones B2-75 and C2-75 is much lower than for cone A1-75. The porosity for cones B1-75 and C1-75 is higher. This is anomalous. It may be necessary to repeat the experiment to validate this observation, particularly since this is only set of cones where it is observed. Larger, spherical pores are observed in the third column. The density of pores is highest for cone C3-75 in the down-skin region. This is where the contour exposure power is high and the heat input will remain in the build longer.

2.3.3.2.3 *AiSi10Mg 60° cones*

Figure 90 and Figure 92 show the un-etched 25x images of xy-plane and yz-plane cross sections for AlSi10Mg 600 cones. Figure 91 and Figure 93 show the un-etched 100x images of core exposure region xy-plane and yz-plane cross sections.

The core exposure porosity is lower for cones B2-60 and C2-60 as compared to cone A1-60. The porosity is much higher in the down-skin region. Larger spherical pores are observed in the third column. The density of pores is highest for cone C3-75 in the down-skin region. Isolated surface-connected porosity is also observed.

Figure 86. Un-etched xy-plane cross sections for AlSi10Mg 75° cones at 25x.

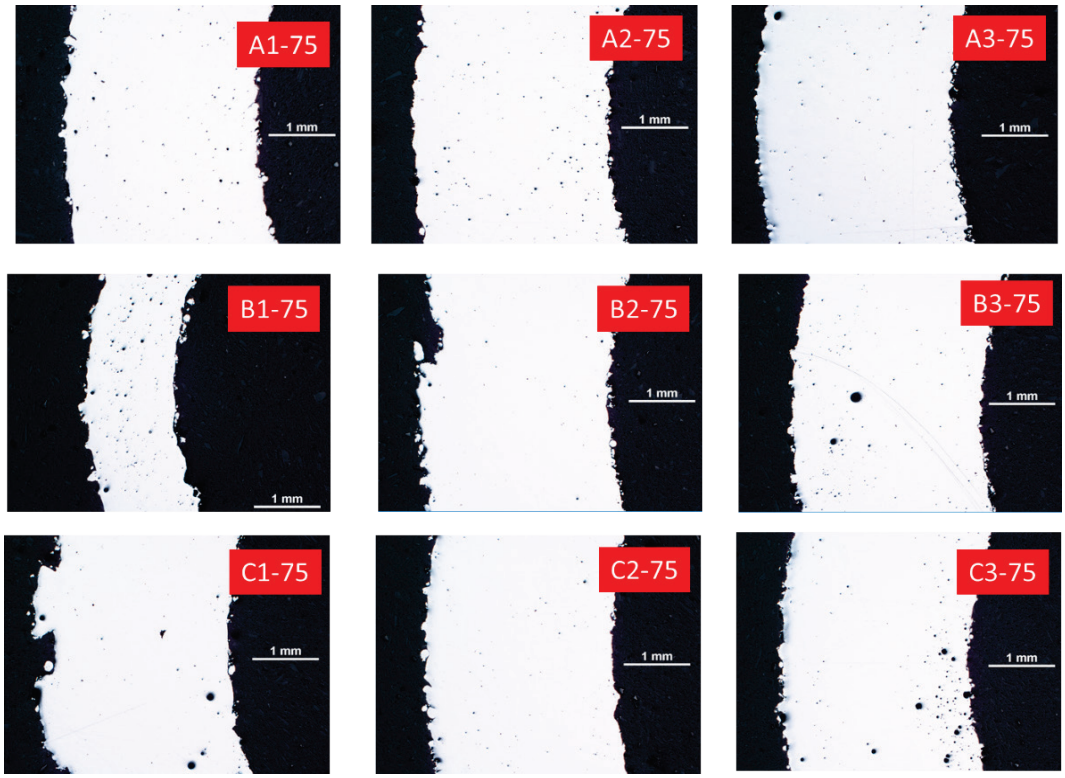


Figure 87. Un-etched xy-plane cross sections for AlSi10Mg 75° cones at 100x.

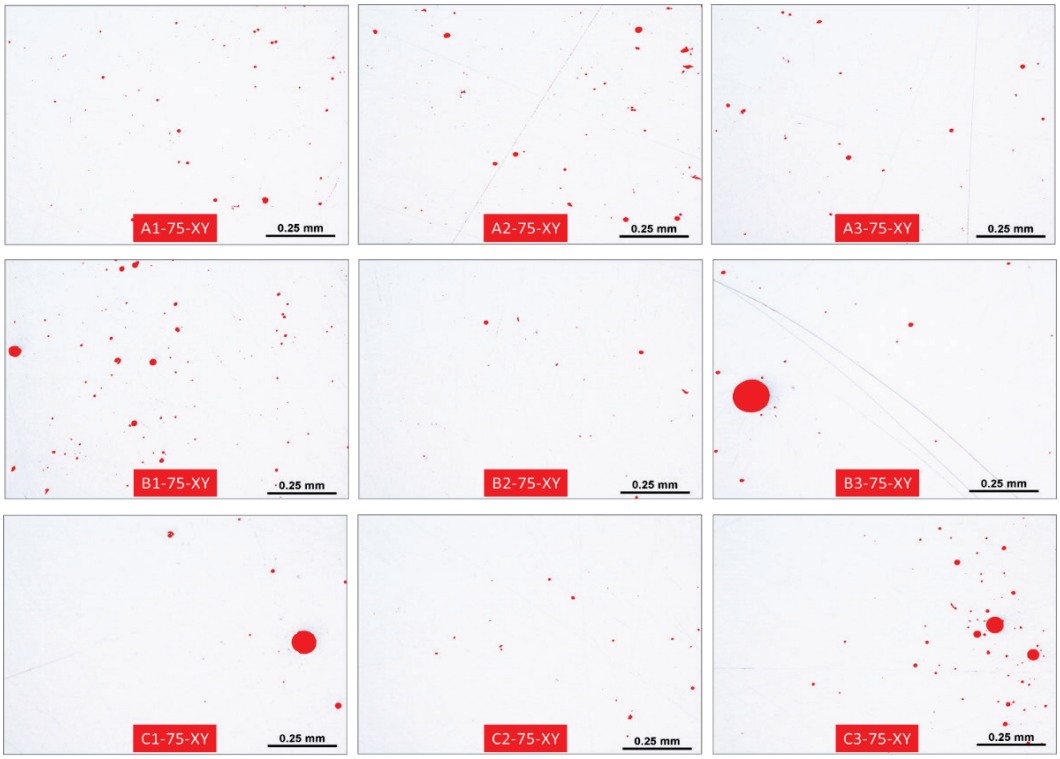


Figure 88. Un-etched yz-plane cross sections for AlSi10Mg 75° cones at 25x.

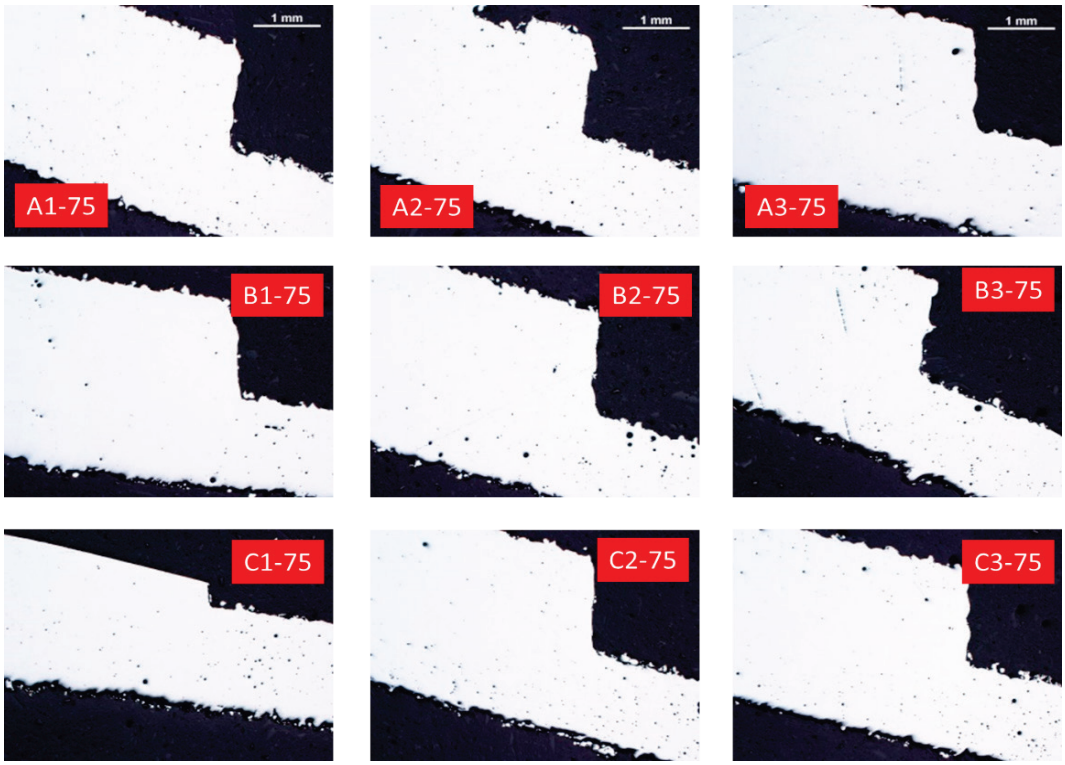


Figure 89. Un-etched yz-plane cross sections for AlSi10Mg 75° cones at 100x.



Figure 90. Un-etched xy-plane cross sections for AlSi10Mg 60° cones at 25x.

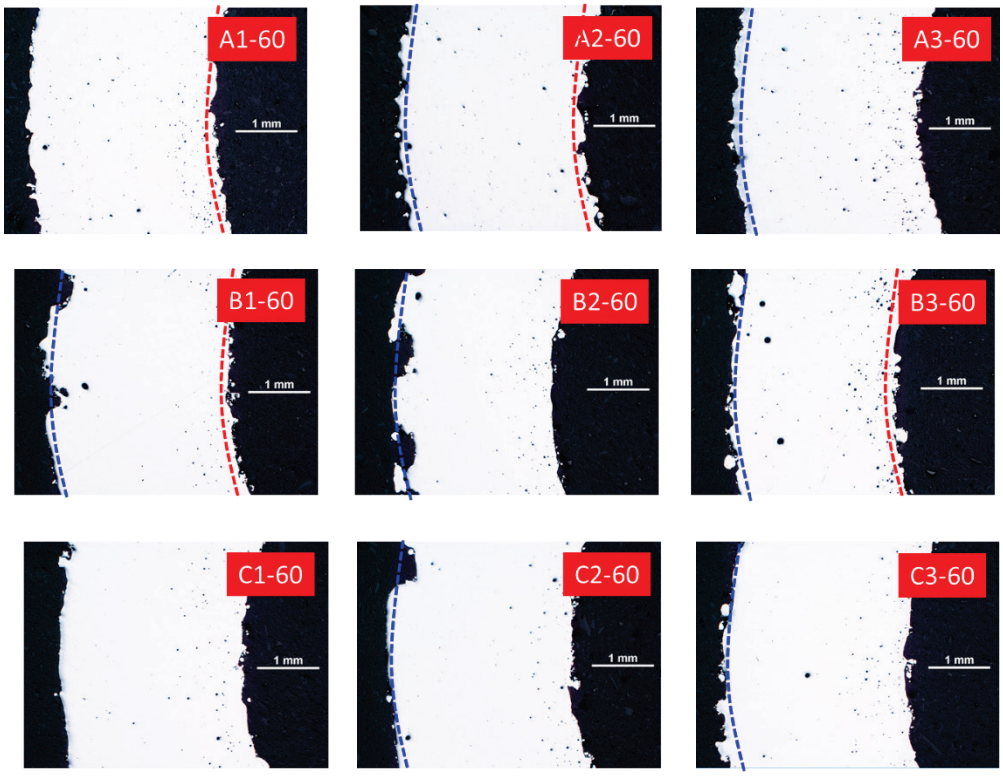


Figure 91. Un-etched xy-plane cross sections for AlSi10Mg 60° cones at 100x.

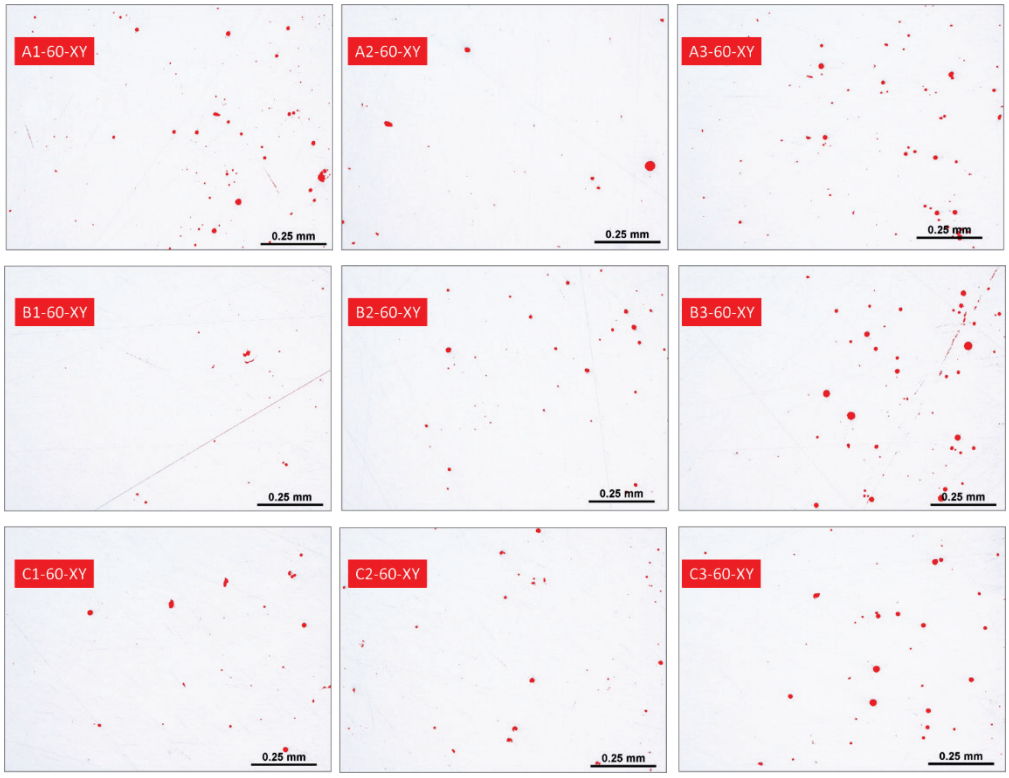
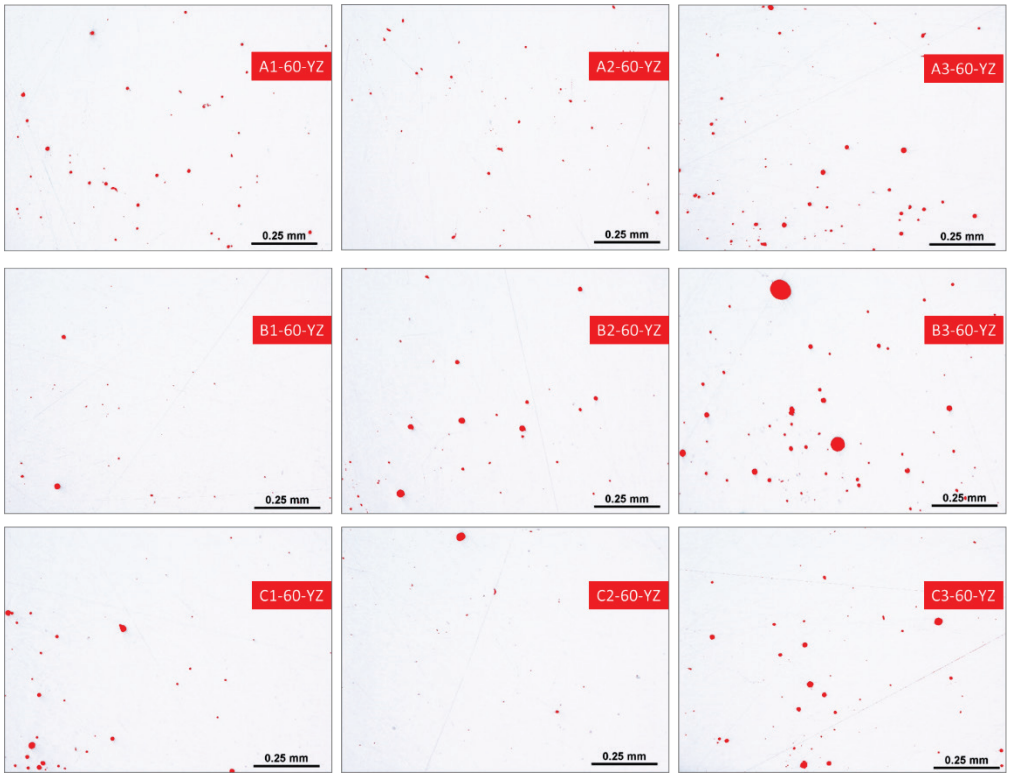


Figure 92. Un-etched yz-plane cross sections for AlSi10Mg 60° cones at 25x.



Figure 93. Un-etched yz-plane cross sections for AlSi10Mg 60° cones at 100x.



2.3.3.2.4 *AiSi10Mg 45⁰ cones*

An experimental approach is necessary to relate the process variables such as laser power and velocity to porosity. This approach augments the numerical simulations as the numerical simulations do not explicitly predict the amount and size distribution of the porosity present. To rationalize results from the numerical solutions and to develop transfer functions relating the process variables to the porosity, a separate set of aluminum cubes (AlSi10Mg) was deposited by varying the laser power and velocity. Six power levels (220, 250, 280, 310, 340, 370 W) and eight speed settings (600, 800, 1,000, 1,200, 1,400, 1,600, 1,800, 2,000 mm/second) were utilized to deposit the cubes. A fixed hatch spacing of 190 microns and a layer thickness of 30 microns were employed for depositing all the cubes. The build plate with the deposited cubes are shown in Figure 99.

Figure 94 and Figure 96 show the un-etched 25x images of xy-plane and yz-plane cross sections for AlSi10Mg 45◦ cones. Figure 95 and Figure 97 show the un-etched 100x images of core exposure region xy-plane and yz-plane cross sections.

The core exposure porosity is lower for cones B2-45 and C2-45 as compared to A1-45. The porosity is much higher in the near surface regions. Some surface-connected porosity is observed.

2.3.3.2.5 *AlSi10Mg cone conclusions*

Figure 98 shows a summary of the core exposure build defects for the four groups of cones. The A1 cone corresponds to the default EOS build conditions. The B1 and C1 conditions were designed using ICME simulations. These conditions show lower build defects than the default parameters, except for the 75⁰ cones (this behavior is assessed to be an anomaly).

Larger, spherical pores are observed in the third column where the fusion between the core and contour exposure tracks is lower. It is hypothesized that such non-optimal fusion between the core and contour exposure tracks introduces perturbation in the build, which culminates in build defects. Larger pores are observed in the region where the wall thickness of the cones is reduced by 50 percent, which corresponds to higher build temperature because the time taken by the laser to melt the entire layer is

half as much as compared to the lower region. This allows increased transience during the melting process. The build porosity is markedly higher near the down-skin surface. The amount of surface-connected porosity becomes higher with reduced down-skin angle.

2.3.3.2.6 *Experimental correlational approach for porosity*

An experimental approach is necessary to relate the process variables such as laser power and velocity to porosity. This approach augments the numerical simulations as the numerical simulations do not explicitly predict the amount and size distribution of the porosity present. To rationalize results from the numerical solutions and to develop transfer functions relating the process variables to the porosity, a separate set of aluminum cubes (AlSi10Mg) was deposited by varying the laser power and velocity. Six power levels (220, 250, 280, 310, 340, 370 W) and eight speed settings (600, 800, 1,000, 1,200, 1,400, 1,600, 1,800, 2,000 mm/second) were utilized to deposit the cubes. A fixed hatch spacing of 190 microns and a layer thickness of 30 microns were employed for depositing all the cubes. The build plate with the deposited cubes are shown in Figure 99.

Figure 94. Un-etched xy-plane cross sections for AlSi10Mg 45° cones at 25x.

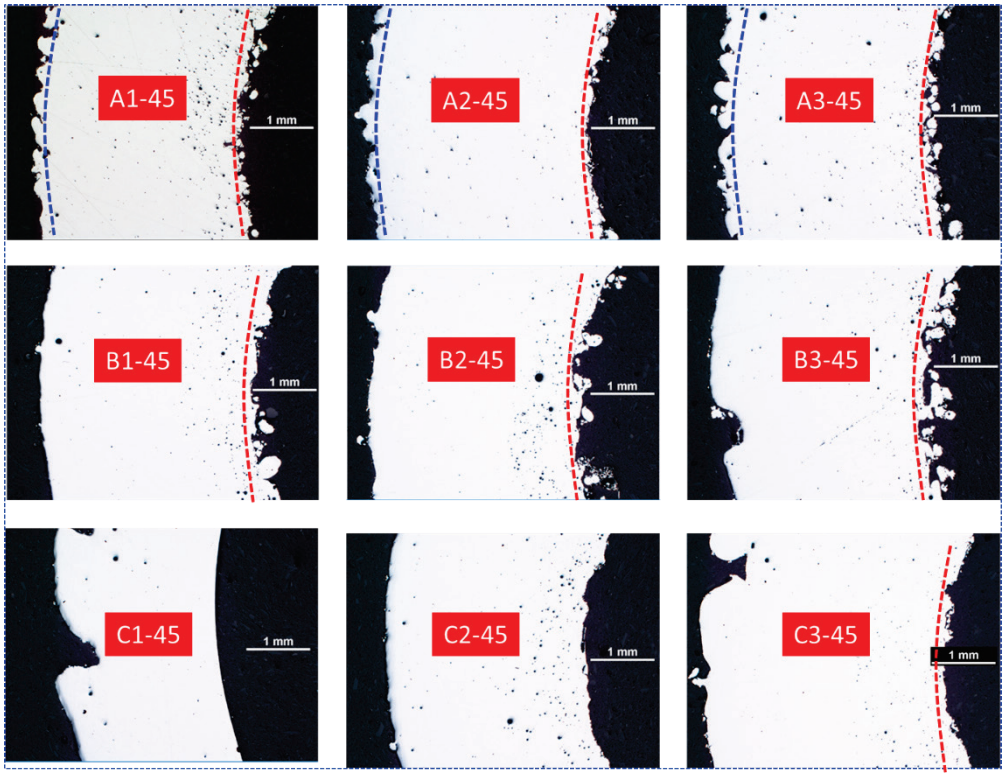


Figure 95. Un-etched xy-plane cross sections for AlSi10Mg 45° cones at 100x.

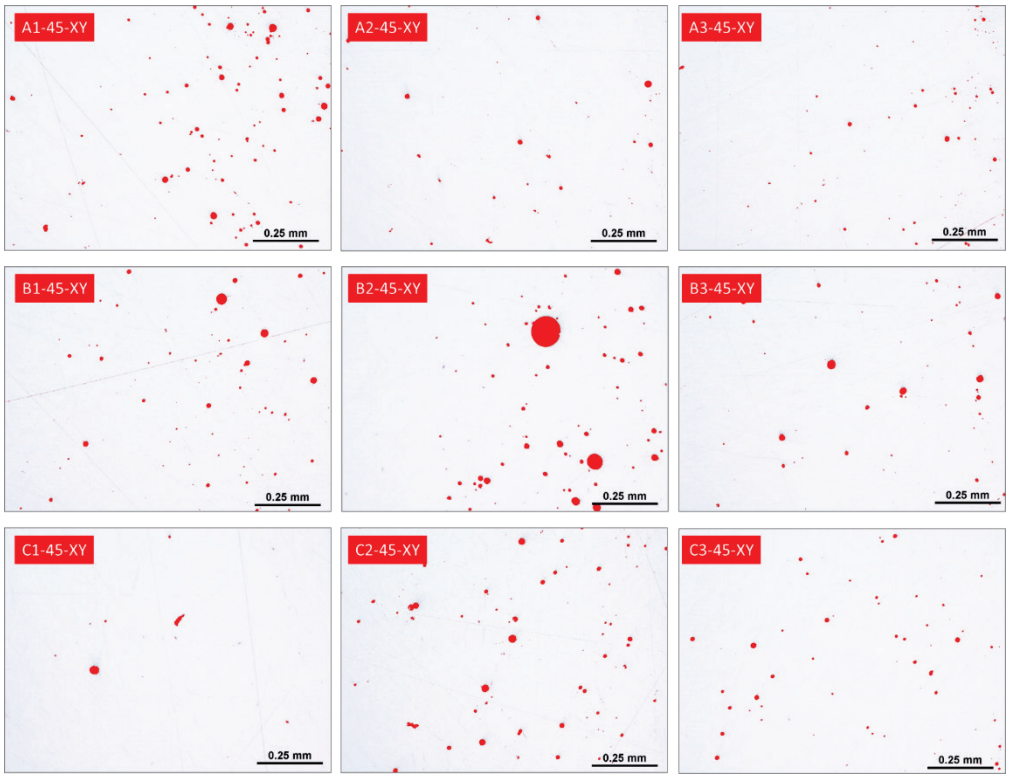


Figure 96. Un-etched yz-plane cross sections for AlSi10Mg 45° cones at 25x.



Figure 97. Un-etched yz-plane cross sections for AlSi10Mg 45° cones at 100x.

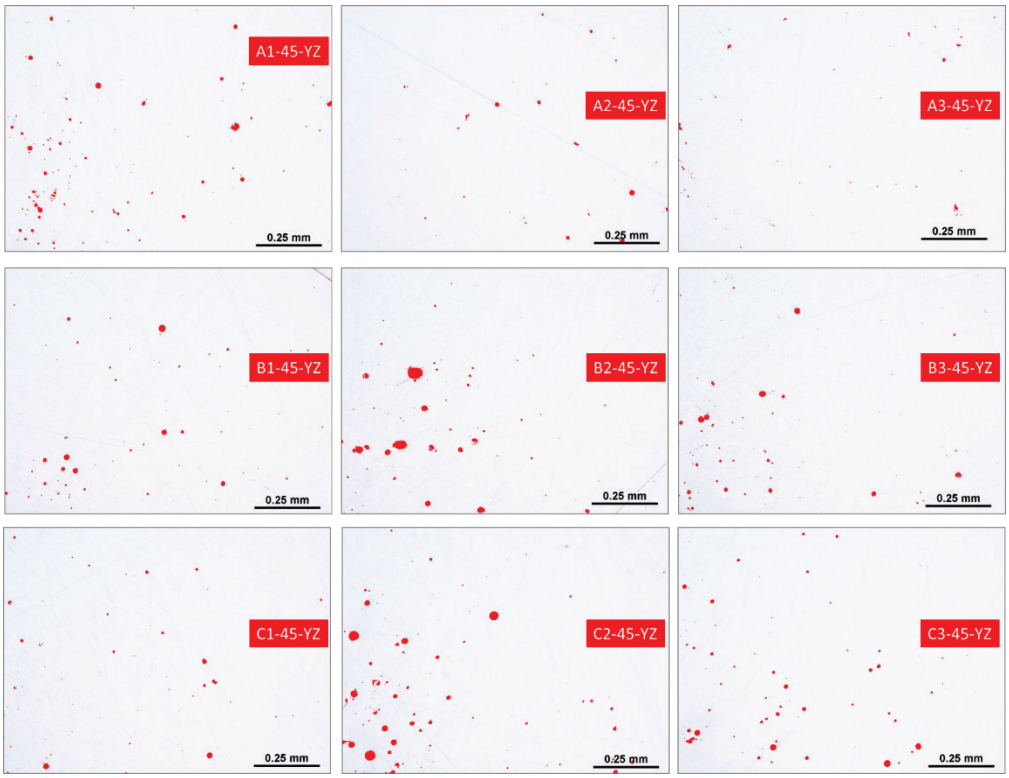
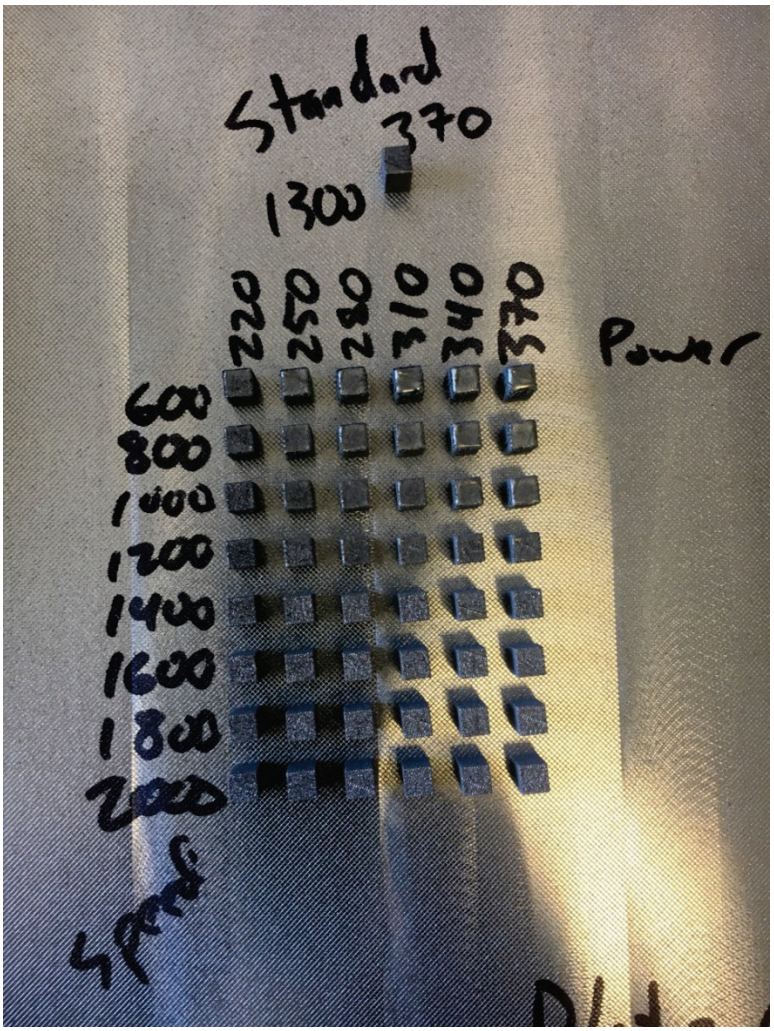


Figure 98. Summary of core-exposure porosity for the four groups of AlSi10Mg cones.

A1-90 0.15%	A2-90 0.17%	A3-90 0.11%	A1-75 0.22%	A2-75 0.41%	A3-75 0.16%
B1-90 0.14%	B2-90 0.11%	B3-90 0.16%	B1-75 0.56%	B2-75 0.08%	B3-75 1.24%
C1-90 0.11%	C2-90 0.02%	C3-90 0.47%	C1-75 0.62%	C2-75 0.08%	C3-75 0.73%
A1-60 0.47%	A2-60 0.23%	A3-60 0.46%	A1-45 0.85%	A2-45 0.26%	A3-45 0.27%
B1-60 0.12%	B2-60 0.23%	B3-60 0.69%	B1-45 0.57%	B2-45 1.88%	B3-45 0.47%
C1-6o 0.23%	C2-60 0.23%	C3-05 0.41%	C1-45 0.15%	C2-45 0.75%	C3-45 0.37%

Figure 99. Build plate with AlMgSi10 cubes deposited.

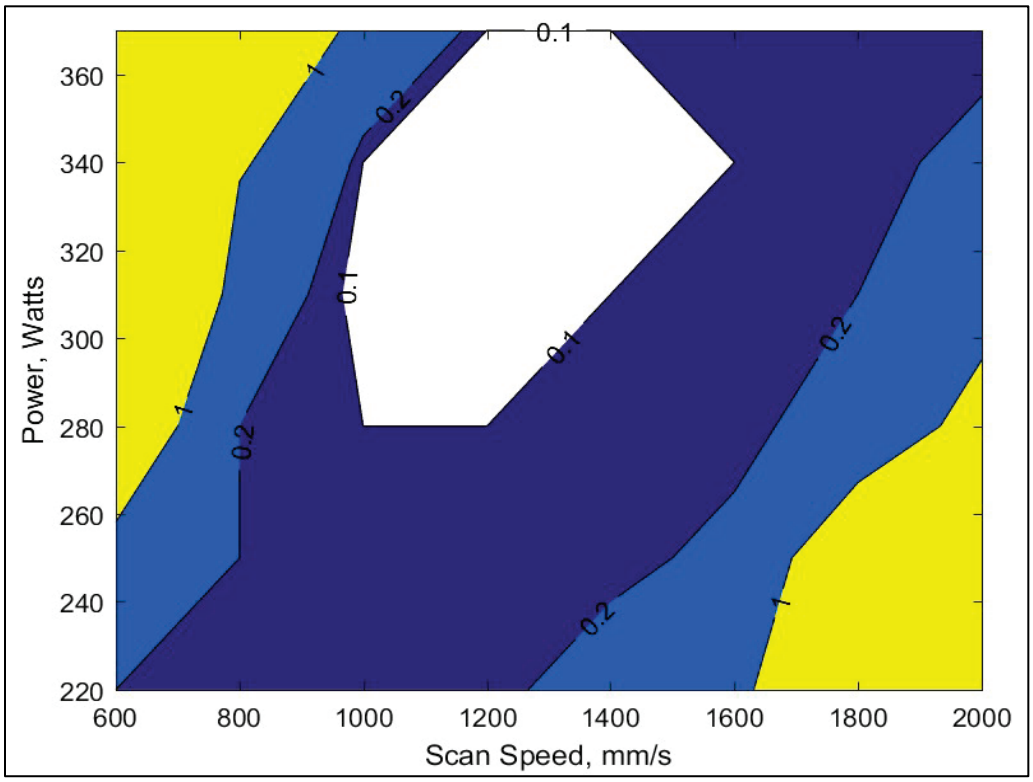


The porosity from these cube deposits was then determined by optical metallography to determine the porosity. The percentage porosity measured is presented in Table 18, and contour plots of constant percentage porosity are shown in Figure 100. A thumbnail sketch of the micrographs obtained is presented in Figure 101. The expected behavior of key holing porosity at low speeds and high powers is observable at the conditions identified with a red background. Similarly, at low powers and high speeds, porosity due to lack of fusion between laser tracks is identified by conditions with a blue background. The acceptable operating range identified by conditions with a green background separates these two regions of key holing porosity and lack-of-fusion porosity. The manufacturer's recommended operating condition for AlSi10Mg is also identified in Figure 100.

Table 18. Percentage porosity measured by optical porosity.

Watts\m/sec	600	800	1,000	1,200	1,400	1,600	1,800	2,000
220	0.25	0.15	0.07	0.25	0.4	0.85	2.1	5.95
250	0.6	0.2	0.1	0.1	0.15	0.25	1.4	2.8
280	1.8	0.2	0.1	0.1	0.15	0.15	0.4	1.6
310	5.15	0.45	0.07	0.045	0.07	0.1	0.2	0.85
340	6.35	1.15	0.1	0.045	0.065	0.1	0.1	0.35
370	5.8	2.45	0.65	0.1	0.1	0.1	0.15	0.15

Figure 100. Contours of constant percentage porosity.



The thumbnail sketch shown in Figure 101 can be used to define the process parameters to maximize productivity or minimize distortion. To verify the validity of the process window for laser power and distortion, parts were printed at the conditions identified in grey on the thumbnail chart. The parts were inspected by X-ray-CT scanning to verify they were free of porosity. The printed parts and the X-ray-CT scan images are presented in Figure 102.

Figure 101. Thumbnail representation of porosity micrographs for AlSi10Mg cubes.

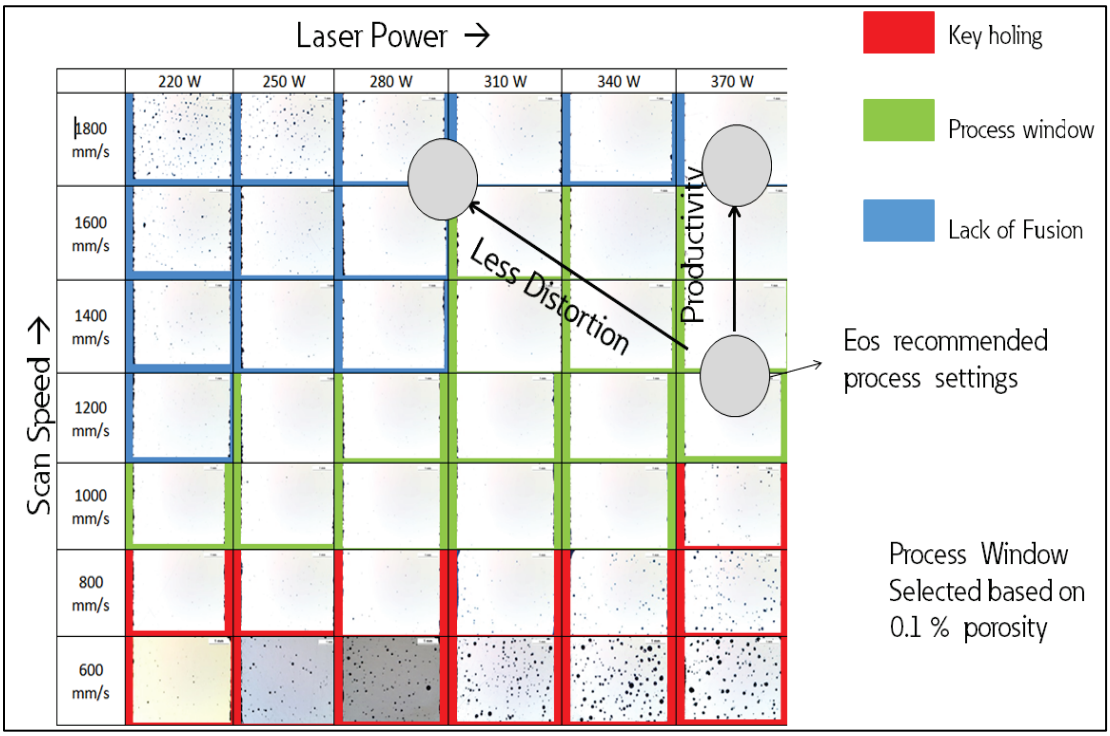
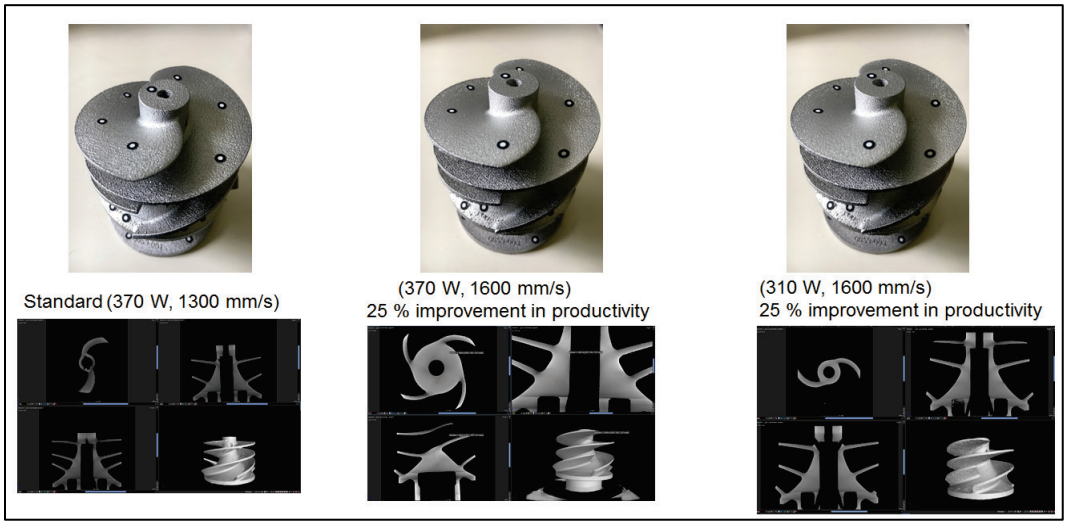


Figure 102. Validation of process space identified by cube deposition experiments.



To develop a correlational approach to porosity, the lack of fusion porosity is assumed to be based on the overlap between melt pool shapes, and the keyholing porosity is assumed to be due to exceeding a critical energy density. To determine the overlap between melt pools and keyholing single track weld beads were deposited as shown in Figure 103. Examples of weld pools when the laser operates in conduction mode and keyholing mode are shown in Figures 104 and 105.

Figure 103. Single track welds on AlSi10Mg.

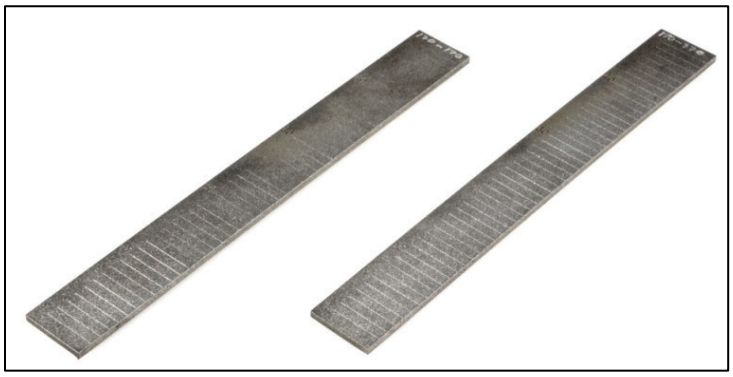


Figure 104. Example of conduction weld at (220 W, 600 mm/sec).

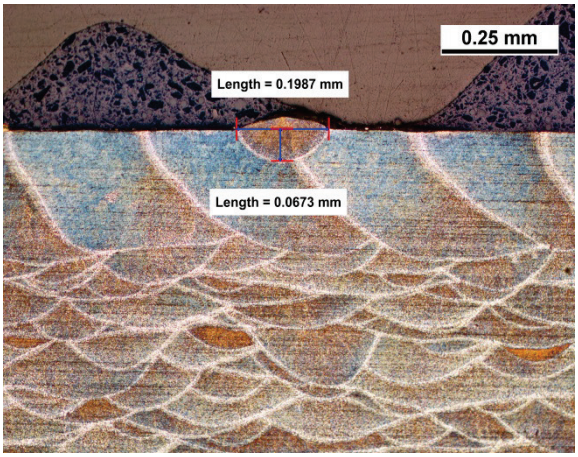
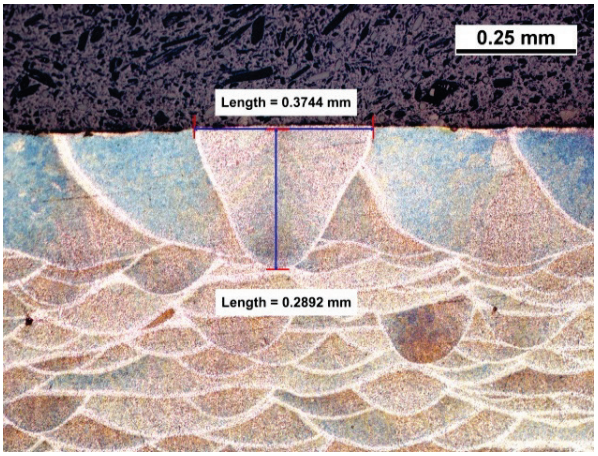


Figure 105. Example of keyhole weld at (340 W, 600 mm/sec).



From the melt pool dimensions determined a criterion proposed by Tang (2017) and is used to determine the lack of fusion boundary. The criterion is:

$$\left(\frac{H}{W}\right)^2+\left(\frac{L}{D}\right)^2<\approx 1$$

Where:

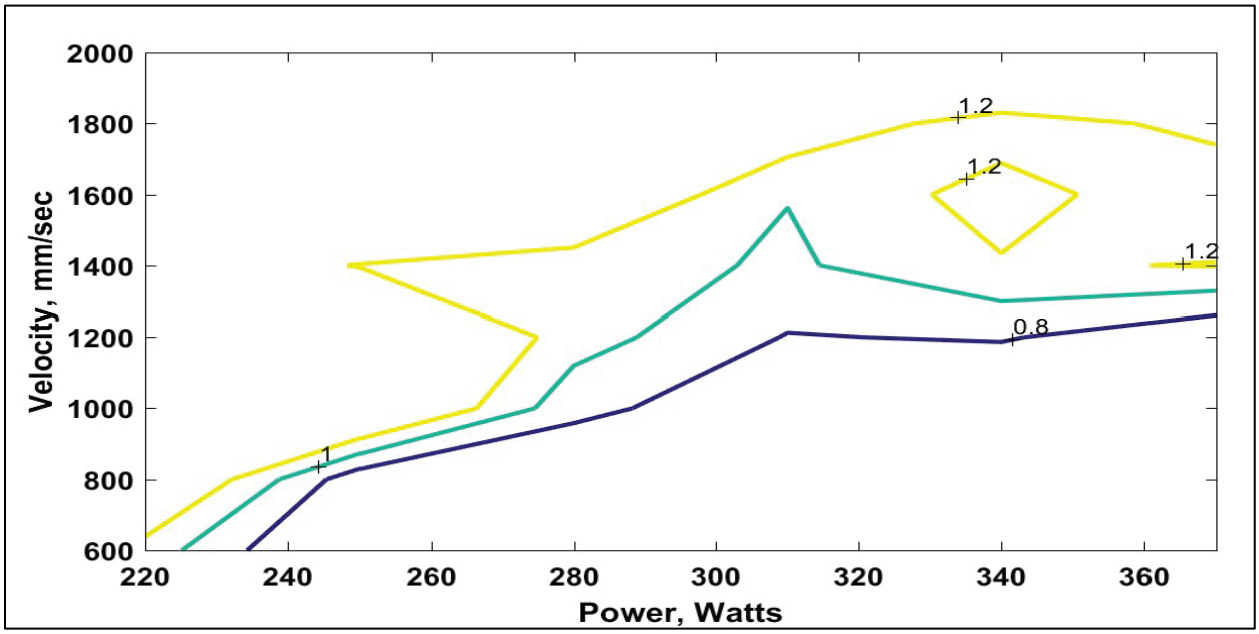
H = the hatch spacing
W = the melt pool with, L is the layer thickness
D = the melt-pool depth.

For a constant hatch spacing of 190 microns and a layer thickness of 30 microns, the criterion is plotted for the power, and velocities used in the cube deposition experiments. The lack of fusion boundary does correspond to the process boundary identified in Figure 106.

2.4 Heterogeneity in microstructure

This section describes the numerical method for predicting heterogeneity in a solidification microstructure and experimental data for its validation.

Figure 106. Lack of fusion criterion based on melt pool dimensions.



2.4.1 Background

The as-built AM microstructure due to layer-by-layer deposition is a result of the solidification microstructure and its solid-state transformations. The solidification microstructure is a function of the thermal gradient (G)

and the liquid-to-solid interface velocity (R). Figure 107 is a schematic of the type of solidification microstructure formed as a function of G and R parameters. The solid-state transformations are a function of the thermal cycling, resulting from the layer-by-layer deposition. The AM multiscale model may be used to predict the thermal cycling, which can serve as input for the prediction of solid-state transformation of the as-built microstructure.

The solidification microstructure for the as-built material presents with a herringbone pattern, as illustrated in Figure 108. This Thijs et al. (2010) describes the origin of the herringbone pattern to be the zigzagging of the thermal gradient, which accompanies the zigzag scan strategy. To predict the microstructural evolution of a given location, the AM process needs to be simulated at the melt-pool scale. Once the melt-pool physics of the desired region have been simulated, the G and R values are calculated from its results, which are then used as input to predict the solidification microstructure. Prediction is accomplished using multiscale modeling as described in the following subsections.

Figure 107. Schematic of the type of solidification microstructure as a function of thermal gradient (G) and the liquid-to-solid interface velocity (R).

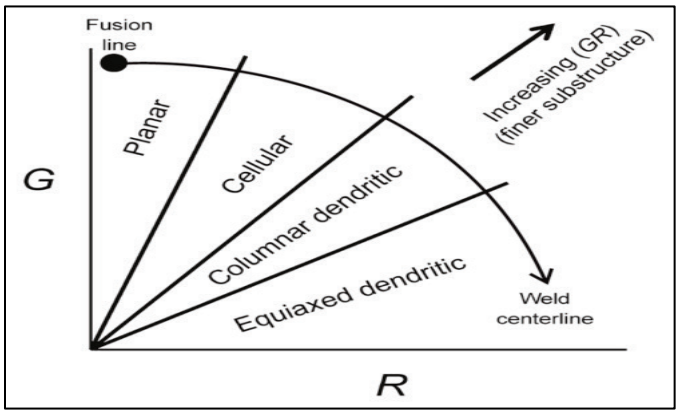
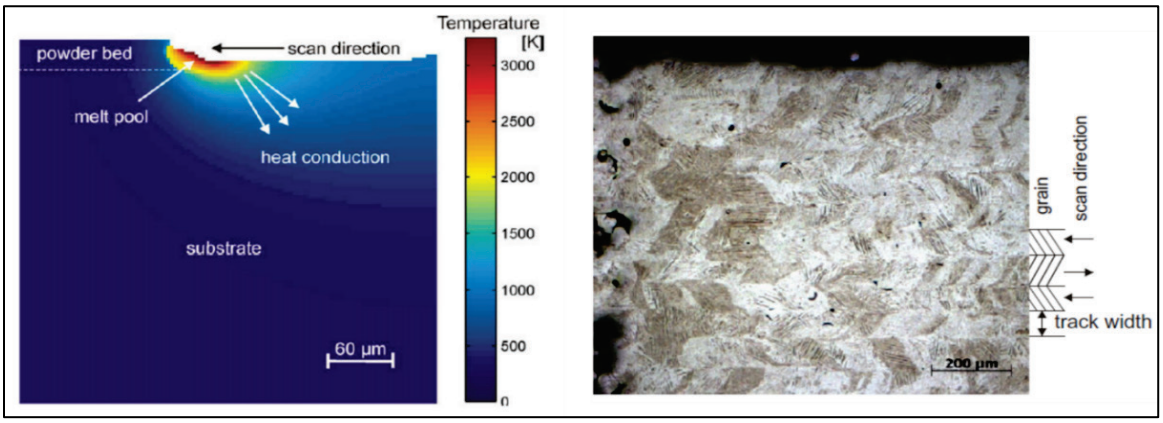


Figure 108. Herringbone pattern of as-built solidification microstructure.



2.4.2 Types of microstructural heterogeneity

The types of heterogeneity of interest are grain morphology, crystallographic texture, phase transformations, microstructure feature size, layer banding, lack-of-fusion and porosity defects, and surface roughness (Kok et al. 2018). Specifically:

- Grain morphology: Grain morphology is a function of the ration G/R, which in turn depends on the process parameters. Although a columnar grain morphology is most common for AM, a columnar-to-equiaxed transition is feasible under certain circumstances (Carter et al. 2014).
- Crystallographic texture: Grain growth near the melt-pool boundary is dominated by the base metal. Further away from the melt boundary, the microstructure is dominated by competitive growth (DebRoy et al. 2018). Dendrites with easy-growth directions aligned closely with the maximum heat flow direction at the liquid-to-solid interface achieve competitive growth during the solidification process. This growth ultimately determines the crystallographic texture for the as-built AM material.
- Phase transformations: Solidification phenomena in AM occur under highly transient conditions whereby both solidification and solid-state transformations may occur with significant undercooling. This can potentially result in nonequilibrium of phase formation and crystallographic texture. The stability of the liquid-solid interface leads to variability in phase selection and morphologies, which manifests as heterogeneity.
- Microstructure feature size: The microstructure scale is inversely proportional to the cooling rate, which is given as the product G*R.

During AM, the cooling rate at the liquid-to-solid interface is nonuniform, which results in a nonuniform microstructure feature sizes.

- Layer banding: Layer banding typically occurs to the thermal cycling in the build caused by the successive deposition of tracks and layers.
- Lack-of-fusion: The lack-of-fusion is a result of inadequate melting of the powder and/or the top surface of the previously deposited material. The lack-of-fusion can occur between successive layers or between successive tracks.
- Porosity: The term porosity is utilized herein to denote gas porosity or keyhole porosity. The gas pores may originate at the melting front during the phase change and consolidation as well as at the solidification front due to the change in solubility that may accompany phase change.
- Surface roughness: The surface tension force seeks to minimize the surface area of the melt pool. An idealization of the melt-pool top surface is a sector of a circular arc. The line spacing between adjacent tracks needs to be such that the fusion between the tracks creates a surface that is as flat as possible. However, the nonuniformity of temperature in the build, fine geometry features, and melting of discrete particles of powder result in a rough surface, which can promote the further occurrence of build defects.

2.4.3 Control of microstructural heterogeneity

The purpose for control of microstructure heterogeneity is to attain optimal mechanical performance for the AM material. In this regard, the first goal for this control is to mitigate the occurrence of lack-of-fusion and porosity defects and to minimize the surface roughness because they are directly detrimental to fatigue performance of the material. Of particular concern are surface-connected defects because they cannot be healed by hot isostatic processing, and the location where they occur may be an internal surface, which cannot always be finish machined. The second goal of this control is to minimize the nonuniformity of the as-built microstructure. The procedures utilized to attain these two goals are as follows:

- Mitigate build defects: The mitigation of build defects is performed by building on the understanding of how the AM solidification profiles must occur with respect to each other for the successive tracks, layers as well as for the fusion between the core, skin, and contour exposure tracks. The details of this procedure are described in Section 2.3 on the

correlation of cause for the occurrence of porosity. The selection of process parameters to mitigate the build defects is performed using the multiscale model for the AM process.

- Minimize nonuniformity of microstructure: The primary factors that govern the solidification microstructure and the solid-state transformations are the G and R parameters and thermal cycling. The end result for the grain morphology, crystallographic texture, phase transformations, microstructure feature size, and layer banding is a convolution of the effects of nonuniformity of G and R and thermal cycling. These occur due to the changing boundary conditions for the build, rate of heat loss to the build environment, and part geometry. Thus, at a foundational level, the minimization of nonuniformity of microstructure is addressed by selecting process parameters to create similar G and R conditions as possible for different types of tracks. The accompanying thermal cycling is then expected to be similar (to a first order estimate) as well. To this end, it is useful to account for the build-scale part heat-up during deposition, the in-layer heat-up during the deposition of a single layer, and the thermal behavior of the melt pool. This information is generated by comparing the results obtained for different locations in the build using the multiscale model for the AM process.

2.4.4 Numerical method for heterogeneity prediction

The numerical method for the calculation of the G & R parameters is illustrated using a generic industrial part geometry—denoted as representative part. Figure 109, Figure 110, and Figure 111 show the macro-scale, meso-scale, and micro-scale model for the representative part. The 3-D distributions of G and R parameters are readily calculated from the results of the micro-scale simulation using ParaView as a post-processor. Figure 112 shows the G and R data for the core region. Figure 113 shows the G and R data for the contour region.

The numerical procedure for the prediction of the herringbone pattern of solidification microstructure as a function of scan strategy is computationally demanding. An example of a basic prediction for four core exposure tracks followed by two contour exposure tracks is shown in Figure 114. This prediction was performed using a cellular automata algorithm. The black portion represents a moving melt pool. There are four back-and-forth passes, which are followed by two passes in an orthogonal direction. The two tracks in the orthogonal direction are meant

to emulate a sample condition that can occur during the contour passes, which create the nonuniformity of G and R parameters. Each colored region represents a grain with orientation unique to that color.

Figure 109. Macro-scale simulation at a) Layer 300; b) Layer 4600.

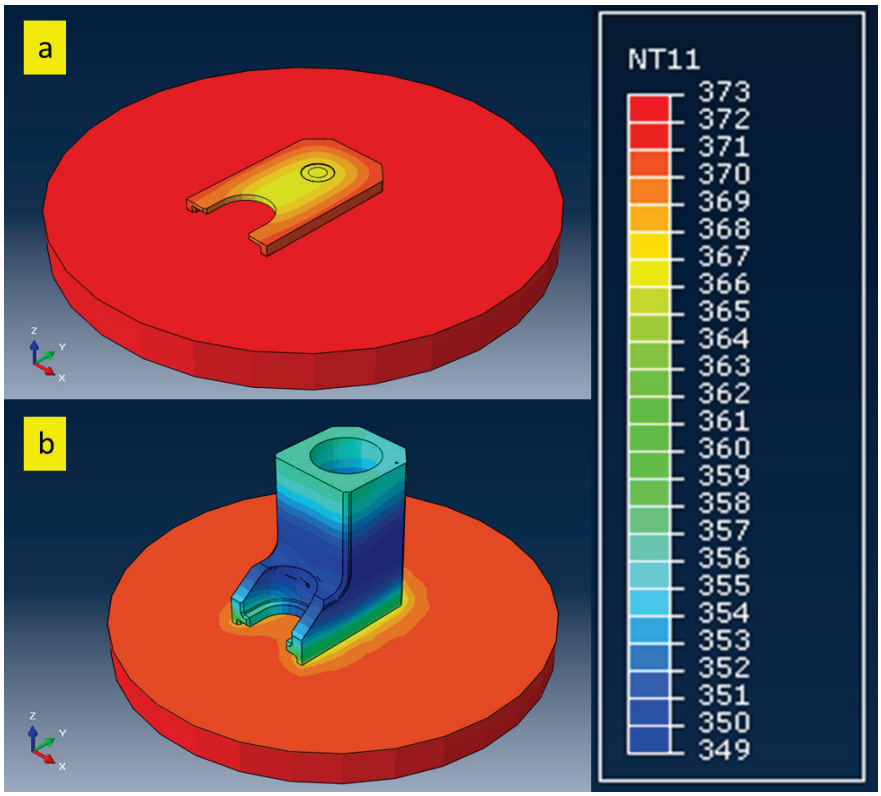


Figure 110. Meso-scale model of Representative part at a) First stripe; b) Second stripe; c) Third stripe; d) Sixth stripe.

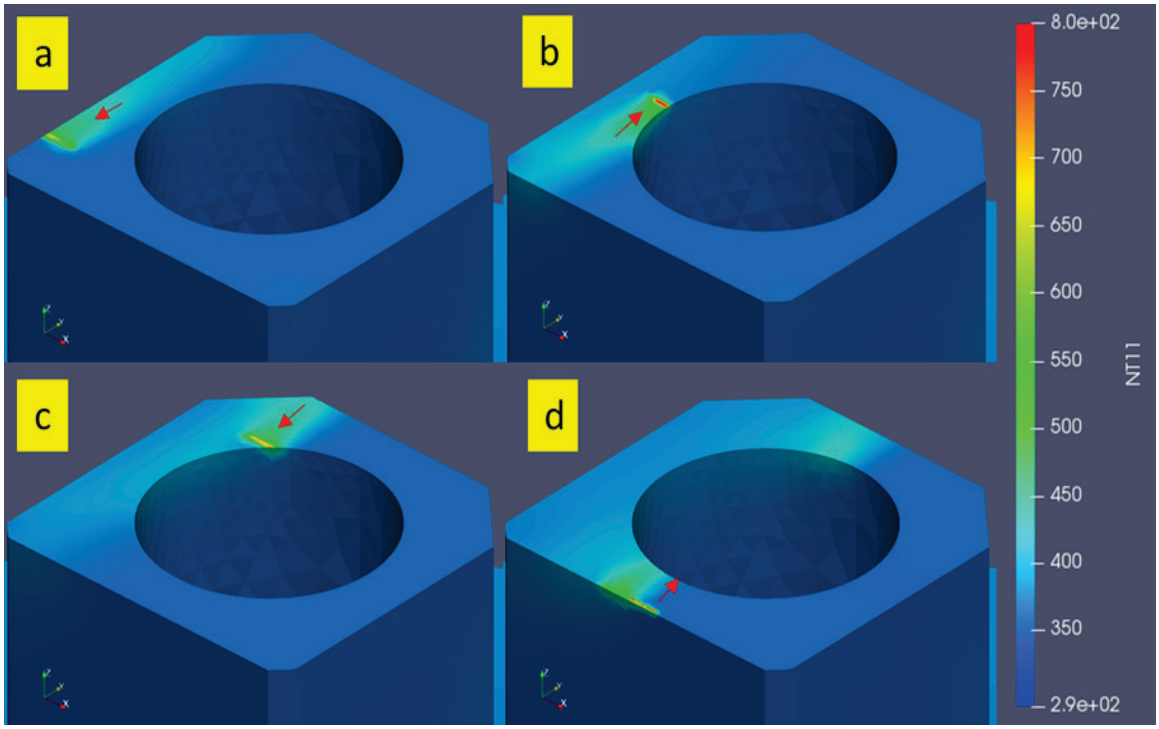


Figure 111. Micro-scale prediction of the melt-pool for a) Core region; b) Contour region.

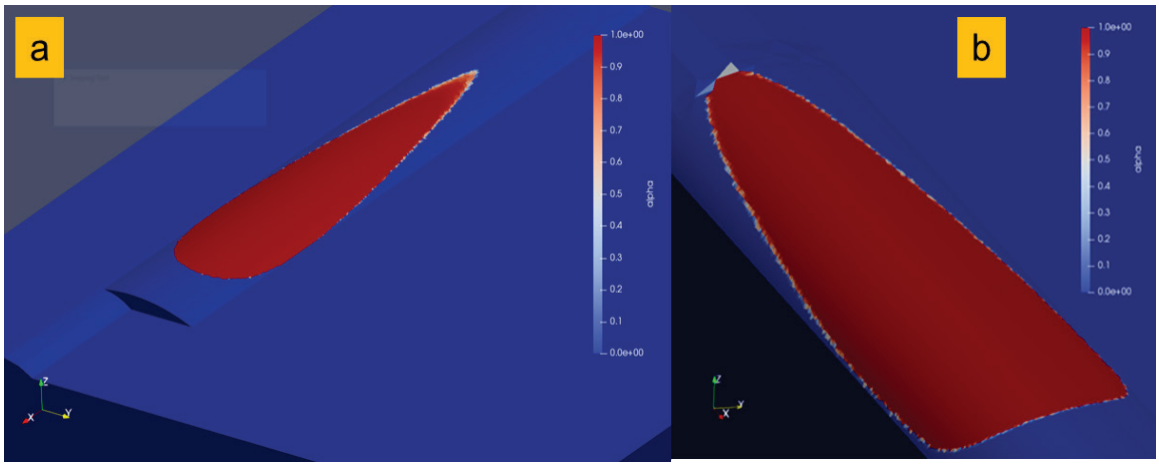


Figure 112. G and R for core region.

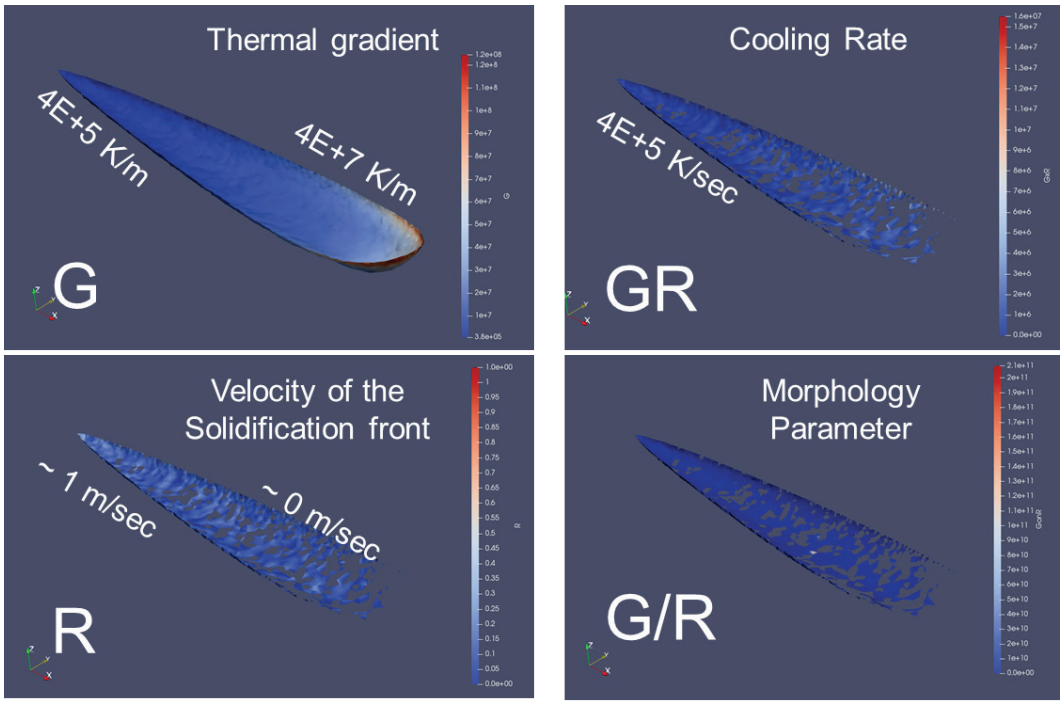


Figure 113. G and R for contour region.

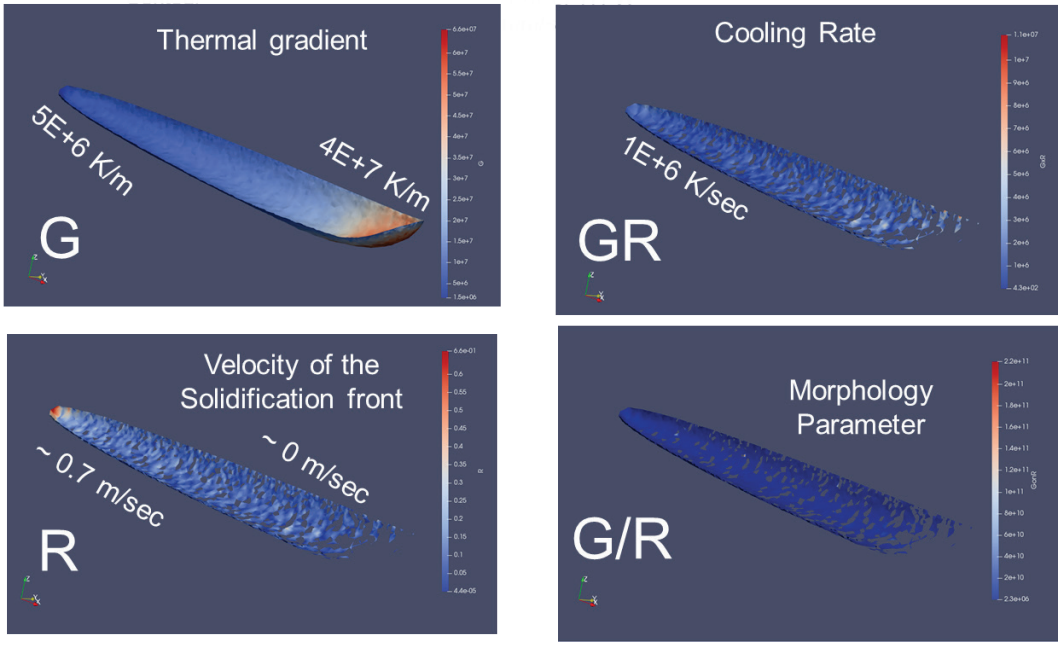
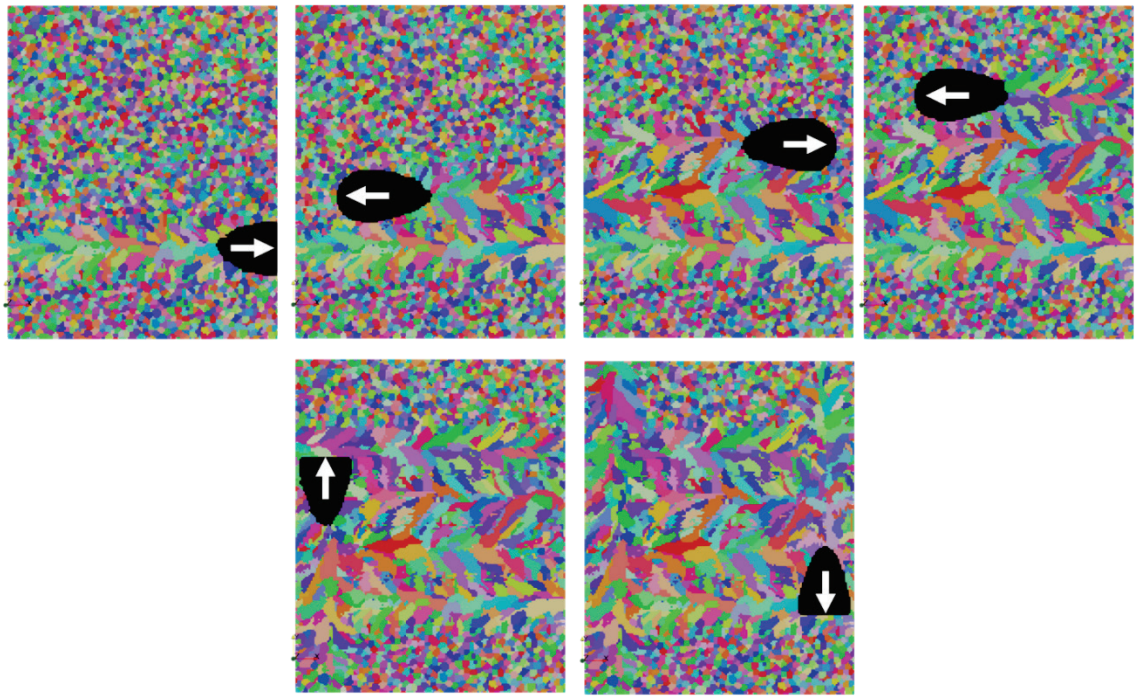
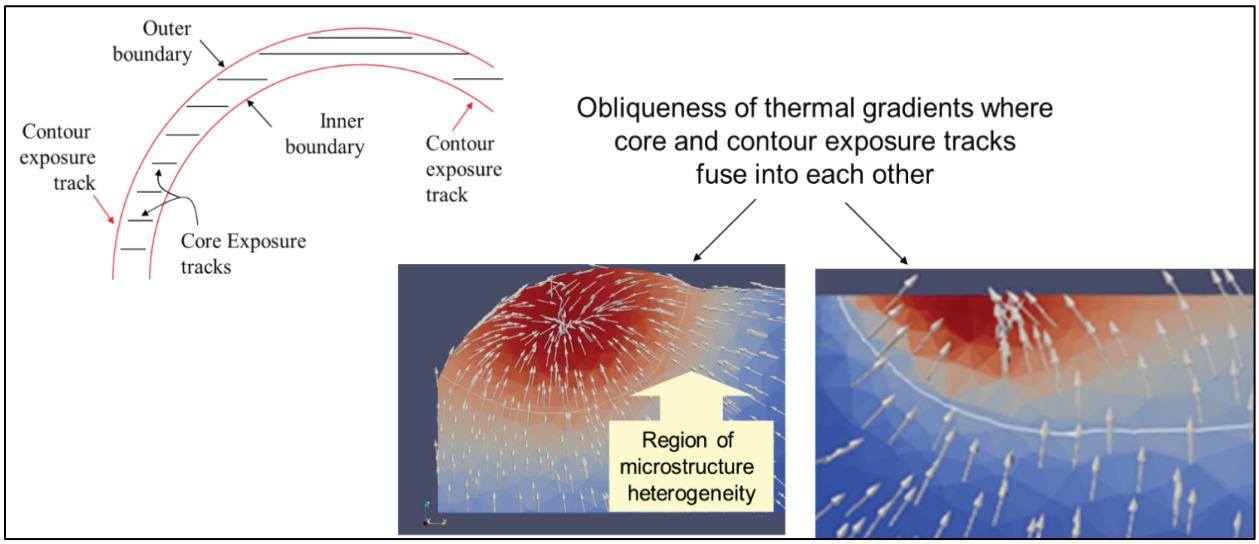


Figure 114. Notional prediction of grain growth and orientation for a zigzag scan of the core region.



A likely location for microstructural heterogeneity is at the fusion region between the contour and core exposure tracks (Figure 115). In this region, the core and contour tracks fuse with each other at oblique angles, causing the thermal gradients created by the core and contour exposures to be obliquely oriented to each other. In addition, the contour parameters are often quite different from the core parameters, which changes the shape and size of the melt pool as well as in the velocity of the solidification front. All these conditions combine to create microstructural heterogeneity. A schematic of grain growth and orientation due to two post-contour passes is also shown in Figure 115. Thus, the numerical method to minimize microstructure heterogeneity comprises the tuning of the type of contour exposure strategy and the core and contour exposure parameters.

Figure 115. Microstructure heterogeneity in between core and contour.



2.4.5 Experimental validation for minimization of nonuniformity of microstructure for alloy AlSi10Mg

Figure 54 shows the DOE setup for alloy AlSi10Mg. The details of the process parameters selected for this DOE were described in Section 2.3.2.2. Its purpose was to make a first attempt to provide parameters that can be utilized to mitigate build defects and minimize nonuniformity of microstructure for AlSi10Mg. The EOS default parameters for AlSi10Mg have a more limited success in producing defect-free deposits. This is due to a complex phenomenology for the melting and solidification behavior for AlSi10Mg. Thus, the process parameters for the DOE were specifically designed for each set of down-skin and up-skin angles. The first deposit in the first column (i.e., for cone A1) was deposited using EOS default parameters. Two new sets of process parameters were designed in order to improve upon the EOS default parameters. These two sets of parameters were utilized for the second and third cones in the first column (i.e., for cones B1 and C1). The core offset was increased in the second column, while keeping the contour offset unchanged (i.e., for cones A2, B2, C2). The contour offset was increased in the third column, while keeping the core offset unchanged (i.e., for cones A3, B3, C3). The specific aspects of the phenomenology that makes the powder bed processing of AlSi10Mg challenging are as follows:

- Increase in surface roughness due to the formation of satellites: This is a combined result of two material properties for AlSi10Mg: low absorptance and low melt viscosity. The low absorptance requires the use of high power, which results in higher temperature in the upper regions of the melt pool. The lower melt viscosity allows the molten metal to spread laterally to a larger extent as compared to other alloys. This spread of the molten metal results in melting of adjacent particles as well as the attachment of partially melted particles to the surface of the build. Note that this behavior occurs track-by-track and layer-by-layer in the internal regions of the build as well, creating increased levels of surface roughness, which in turn increases the propensity for build defects. One way to mitigate the surface roughness is to utilize high scanning velocity. Another way is to utilize two contour exposure passes. Additional options may include the use of a combination of pre- and post-contour passes. The use of AM process simulation predicts the AM solidification profile as a function of processing parameters. Such predictions were analyzed to obtain adequate remelt for the previously deposited tracks and layers to mitigate the propensity for lack-of-fusion defects caused by the surface roughness.
- Oxidation: Aluminum powder absorbs moisture in the atmosphere. During melting, the water reacts with the aluminum powder to form oxides, which have a higher melting point. Depending on the choice of processing parameters, these oxide particles do not melt, creating lack-of-fusion defects and the nucleation sites for fatigue failure (Tang 2017). The use of AM simulation to prediction of the AM melt pool was utilized to mitigate this effect.
- Gas porosity: During the oxidation reaction between the aluminum powder and the absorbed moisture, hydrogen gas is released. Due to the fast scan velocity, the melting to solidification time for the melt pool is correspondingly smaller. Thus, the hydrogen gas bubbles have smaller time available to rise and escape from the melt pool. The result is gas porosity. Weingarten et al. (2015) reports that > 90 percent of volume for the circular pores in the AlSi10Mg builds is hydrogen. The AM process simulation needs to be utilized to predict the velocity of the bubbles and compare it with the melting to solidification time in order to assess the potential for the mitigation of gas porosity. The process design to optimize the gas porosity is planned for the upcoming technical effort during 2018.
- Nonuniformity of the level of oxidation: Although aluminum has high thermal conductivity, the build temperature during melting can be

locally high depending on the down-skin angle because the heat cannot conduct away into the loose powder below the down-skin surface. The result in increased oxidation on the material and correspondingly higher potential for the occurrence of gas porosity. Thus, the process parameters need to account for not only the core and contour exposure but also for the skin exposure. This includes the definition of the skin width in terms of the vertical skin and horizontal skin. Depending on the part geometry, the width of the skin exposure can become variable. The process parameters may need to gradually change from the start of the skin exposure to the contour exposure passes. The process design to minimize the nonuniformity of oxidation and the corresponding occurrence of gas porosity is planned for the upcoming technical effort during 2018.

The experimental evidence and its analysis for each group in the AlSi10Mg DOE for elements of nonuniformity of microstructure is shown in Sections 5.1 to 5.4. Section 5.10 provides an overall conclusion of this analysis for AlSi10Mg.

No preheating of the powder: Please note that all builds were produced with no preheating of the AlSi10Mg powder to mitigate the absorbed moisture.

2.4.5.1 *Nonuniformity of microstructure for AlSi10Mg 90° cones*

Figure 116 shows the etched 25x images of xy-plane cross sections for AlSi10Mg 90° cones. Figure 117 shows high magnification views of the C3-90 cone shown in Figure 116. Figure 118 shows etched yz-plane cross sections for AlSi10Mg 90° cones at varying magnifications.

Figure 116. Etched xy-plane cross sections for AlSi10Mg 90° cones at 25x.

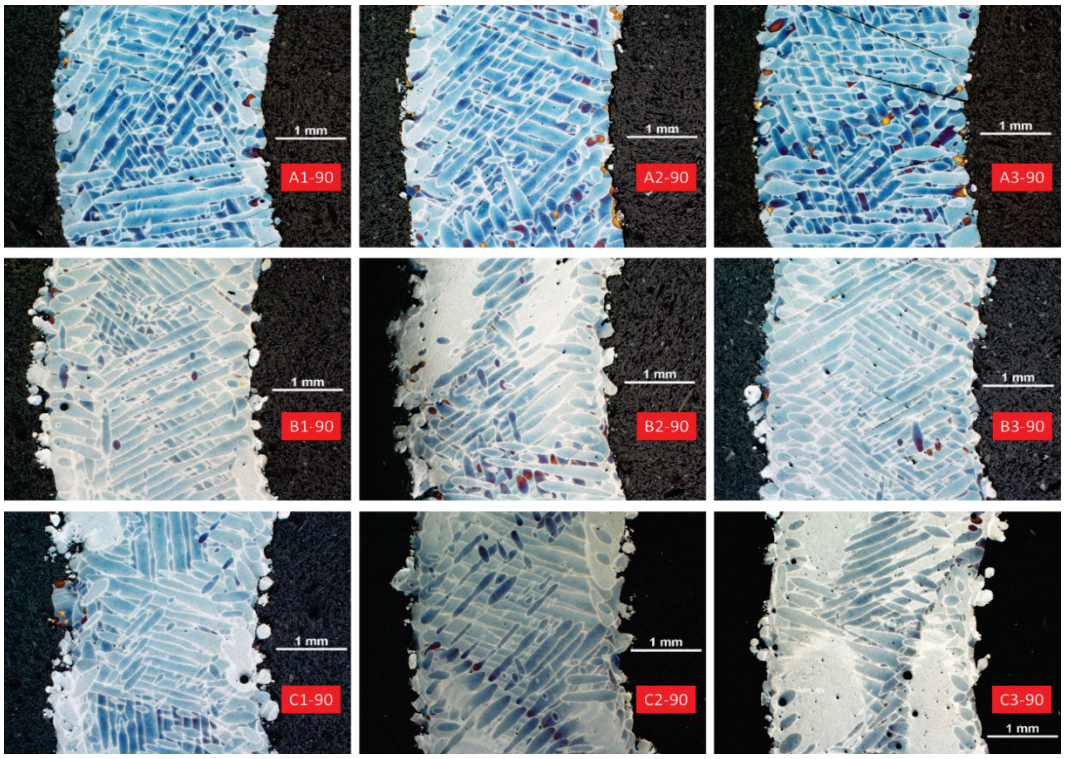


Figure 117. Higher magnification xy-plane cross sections for AlSi10Mg 90° cone C3-90.

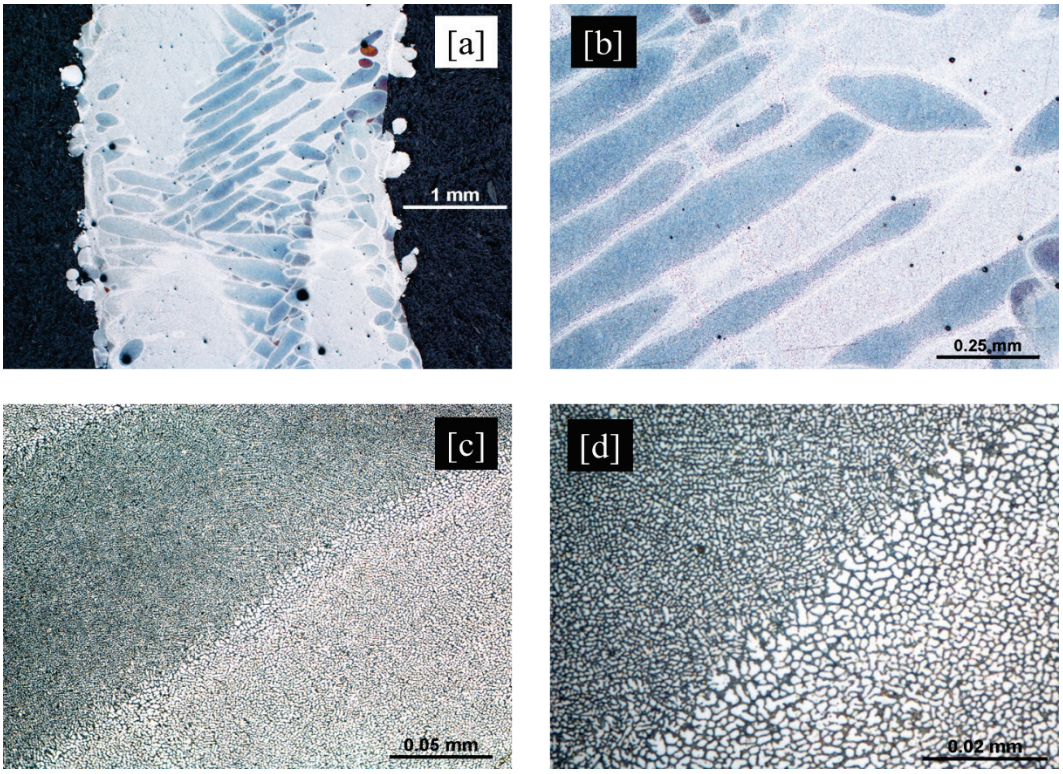
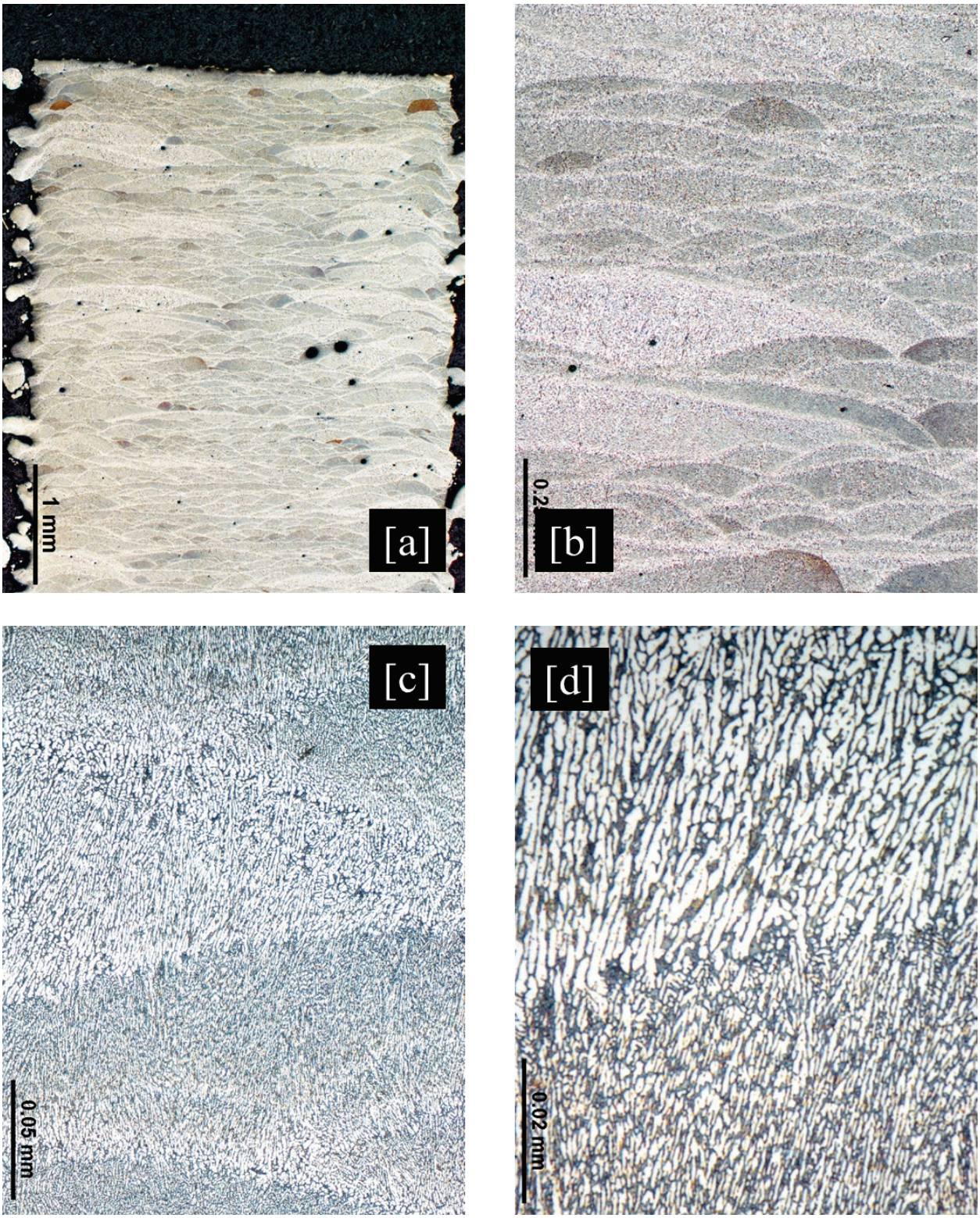


Figure 118. Higher magnification yz-plane cross sections for AlSi10Mg 90° cone C3-90.



The observations gathered from Figures 116 to 118 in regards to the various aspects of nonuniformity of microstructure are as follows:

- Grain morphology: This is seen most clearly for cone C3-90 which corresponds to a larger than optimal core offset and lower than optimal contour offset, which creates weaker fusion between the core exposure and contour exposure tracks.
- Crystallographic texture: This is most evident for cone C3-90, where the deposition conditions separate the G & R conditions between the core and contour exposures more clearly.
- Microstructure feature size: This is seen in Figures 117c-d and 118c-d. The coarsening of the feature size corresponds to the heat affected region (Tang 2017).
- Layer banding: This is observed in Figure 118a-b.
- Formation of satellites: This is more pronounced for the second and third row cones.
- Nonuniformity of the level of oxidation: The light blue regions correspond to higher levels of oxidation. These regions are observed in the contour exposure regions, particularly for the third row of cones where the energy density for the contour pass is highest.

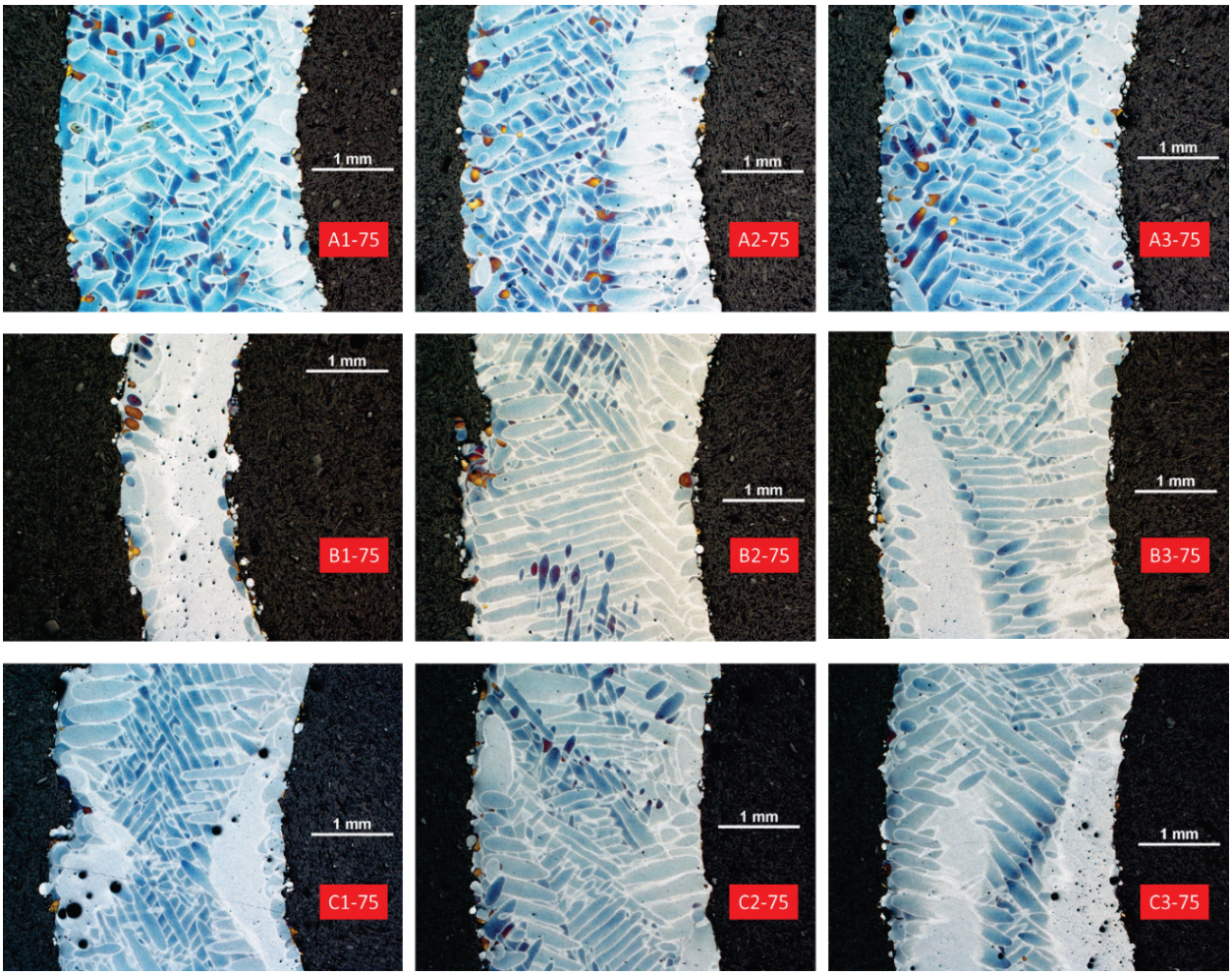
2.4.5.2 *Nonuniformity of microstructure for AiSi10Mg 75° cones*

Figure 119 shows the etched 25x images of xy-plane cross sections for AlSi10Mg 90° cones.

- Grain morphology: The change in grain morphology is more pronounced than the 90° cones and is seen in the second and third row of cones.
- Crystallographic texture: The change in texture is more pronounced than the 90° cones and is seen most clearly in cones C1-75 and B3-75.
- Formation of satellites: The formation of satellites is less on the up-skin (OD) surface than the down-skin (ID) surface. This is due to the consideration that for the up-skin surface, the newly melted powder resides atop solid material from the previous layer. The higher conductivity of the solid material promotes rapid solidification for the melt pool, curtailing the formation of satellites. For the down-skin surface, the newly melted powder resides on top of powder, which has a much lower thermal conductivity. This allows the material to remain in the melted state for a longer duration, allowing the satellites to form.

- Nonuniformity of the level of oxidation: These regions are most prominent near the down-skin surface where the material remains hotter for a longer duration, promoting oxidation.

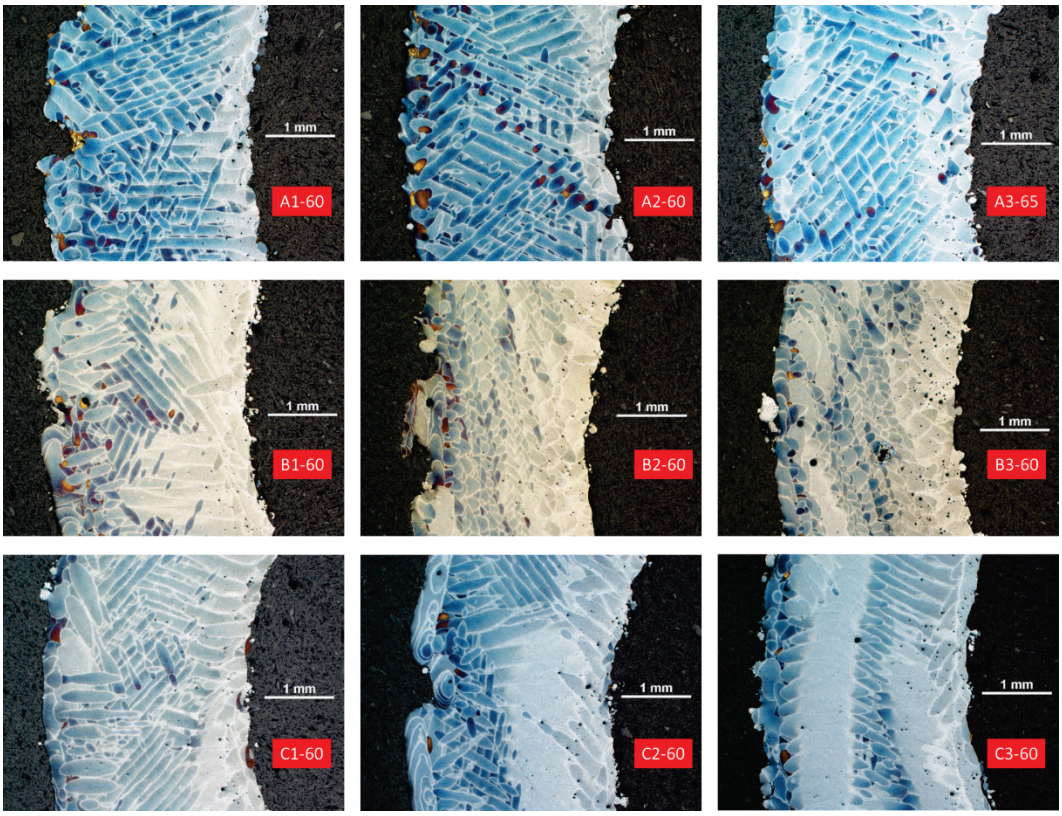
Figure 119. Etched xy-plane cross sections for AlSi10Mg 75° cones at 25x.



2.4.5.3 *Nonuniformity of microstructure for AiSi10Mg 60° cones*

Figure 120 shows the etched 25x images of xy-plane cross sections for AlSi10Mg 90° cones.

Figure 120. Etched xy-plane cross sections for AlSi10Mg 60° cones at 25x.

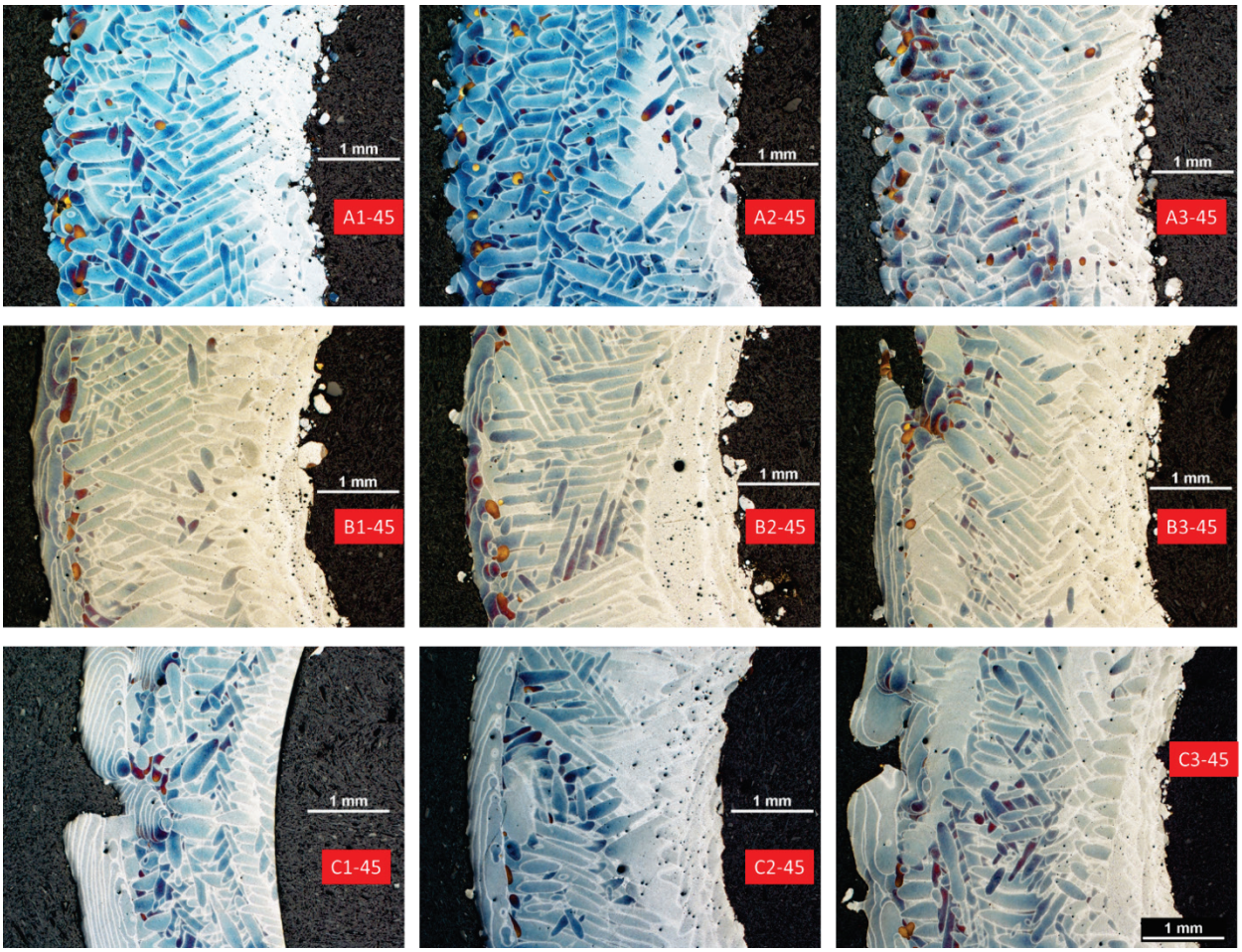


- Grain morphology: The change in grain morphology is more pronounced than the 90° and 75° cones and is seen in the second and third row of cones.
- Crystallographic texture: The change in texture is more pronounced than the 90° and 75° cones and is seen most clearly in cones C3-60 and B3-60.
- Formation of satellites: For the second and third row of cones, the formation of satellites is less on the up-skin (OD) surface than the down-skin (ID) surface.
- Nonuniformity of the level of oxidation: These regions are most prominent near the down-skin surface in the second and third row of cones.

2.4.5.4 *Nonuniformity of microstructure for AiSi10Mg 45° cones*

Figure 121 shows the etched 25x images of xy-plane cross sections for AlSi10Mg 90° cones.

Figure 121. Etched xy-plane cross sections for AlSi10Mg 45° cones at 25x.



- Grain morphology: The change in grain morphology is significantly more pronounced than the 90°, 75°, and 60° cones and is seen in the second and third row of cones.
- Crystallographic texture: The change in texture is more pronounced than the 90°, 75°, and 60° cones and is seen clearly near the OD and ID for the second and third row of cones.
- Formation of satellites: For the second and third row of cones, the formation of satellites is less on the up-skin (OD) surface and more on than the down-skin (ID) surface as compared to the 75° and 60° cones.
- Nonuniformity of the level of oxidation: These regions are most prominent near the down-skin surface in the second and third row of cones.

2.5 Conclusions

The conclusions for the AlSi10Mg microstructural heterogeneity prediction are as follows:

- Grain morphology: There is little change in grain morphology for the default EOS parameters for AlSi10Mg. This is because the input energy density for the contour exposure passes is small, resulting in a smaller amount of melting near the edge. The ICME designed parameters utilize higher energy density for contour exposure, which results in changes in grain morphology that are inversely proportional to the up-skin and down-skin angles.
- Crystallographic texture: The change in crystallographic texture is observed near the OD and ID for the cones. This change is larger for smaller down-skin angles, and they are most evident for the case where the process parameters are defined so as to separate the G and R conditions between the core and contour exposures more clearly.
- Microstructure feature size: An observation of coarsening of the feature size is attributed to the heat-affected region. This assertion is based on historical data reported in Reference 5.
- Layer banding: The layer banding is a consequence of the layer-by-layer deposition and the coarsening of microstructure in the heat-affected zones.
- Formation of satellites: The formation of satellite is less on the up-skin (OD) surface than the down-skin (ID) surface. This is due to the consideration that for the up-skin surface, the newly melted powder resides atop solid material from the previous layer. The higher conductivity of the solid material promotes rapid solidification for the melt pool, curtailing the formation of satellites. For the down-skin surface, the newly melted powder resides on top of powder, which has a much lower thermal conductivity. This allows the material to remain in the melted state for a longer duration, allowing the satellites to form.
- Nonuniformity of the level of oxidation: Regions with higher levels of oxidation are observed in the contour exposure regions, particularly for the third row of cones where the energy density for the contour pass is highest.
- Nonuniformity of the level of oxidation: These regions are most prominent near the down-skin surface where the material remains hotter for a longer duration, promoting oxidation.

3 Directed Energy Deposition

3.1 Manufacturing setup

Two setups were used for the Directed Energy Deposition (DED) work in late 2017 and early 2018. The first setup was used for plates 1.25-in.-thick, while the second setup handled the thinner, 0.5-in.-thick plates. Previous work with thick plates was intended to apply only 0.4 mm- (0.016 in.-) thick layers of the carbide. Inconel 625 cladding with injected tungsten carbide was applied without preheat. Keeping the cladding thin was thought to avoid or to minimize cracking in the deposit. In past work, the thin tungsten carbide layers were primarily sound but still exhibited some minor cracking. These minor cracks should compromise the functionality of the DED layers on the thick plates.

With follow-on thick plate work, the new objective was to increase the deposit thickness to a minimum of 0.9 mm (0.035 in.) in a single pass. It was expected that cracking could be avoided by simultaneously preheating, cladding, and post heating the thick plate. For this work, Eaton and Fraunhofer designed and fabricated a new elliptical induction coil specifically for DED on flat plates, as shown in Figure 122. The cladding head was positioned at the center of the ellipse. The coil is aligned in the cladding travel direction and straddles the bead centerline. In this manner, the leading edge of the coil preheats the plate area ahead of the torch. The center portion of the induction coil adds more uniform heat to the melt pool area, enabling the process to travel faster. The field from the rear portion of the coil engages the recently deposited cladding effectively post heating and tempering the cladding bead. It is designed for laser cladding flat plate with simultaneous induction heating. The coil is intended to eliminate cracking in thick, carbide injected coatings.

Figure 123 displays the setup with the actual induction preheat coil. To avoid back reflection of the laser beam into the cladding head, the plate is positioned at a 10-deg angle. The cladding head itself is angled further within the induction coil and is shrouded in aluminum foil to reflect heat and reflection of the beam. Figure 124 is a better image of the induction heating field produced by the elliptical coil during cladding. The thick plate is clamped in the jaws of a chuck. There is no backing plate to assist in removing heat from the plate. As cladding progresses, heat continues to build up, resulting in excessive distortion.

Figure 122. Early concept drawing Eaton-Fraunhofer elliptical coil.

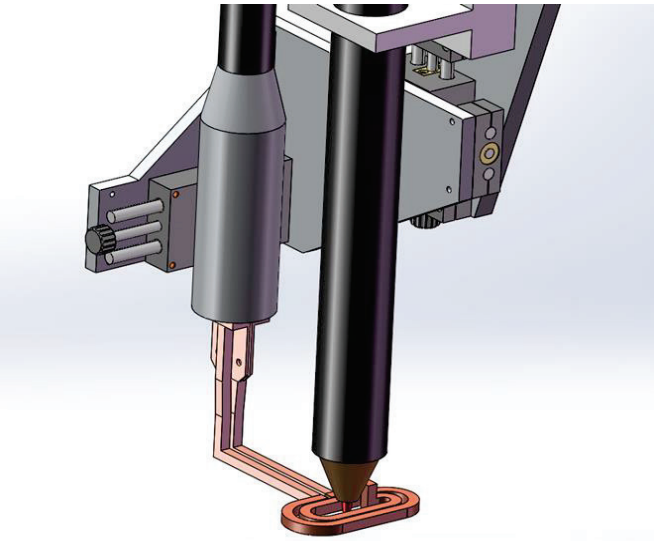


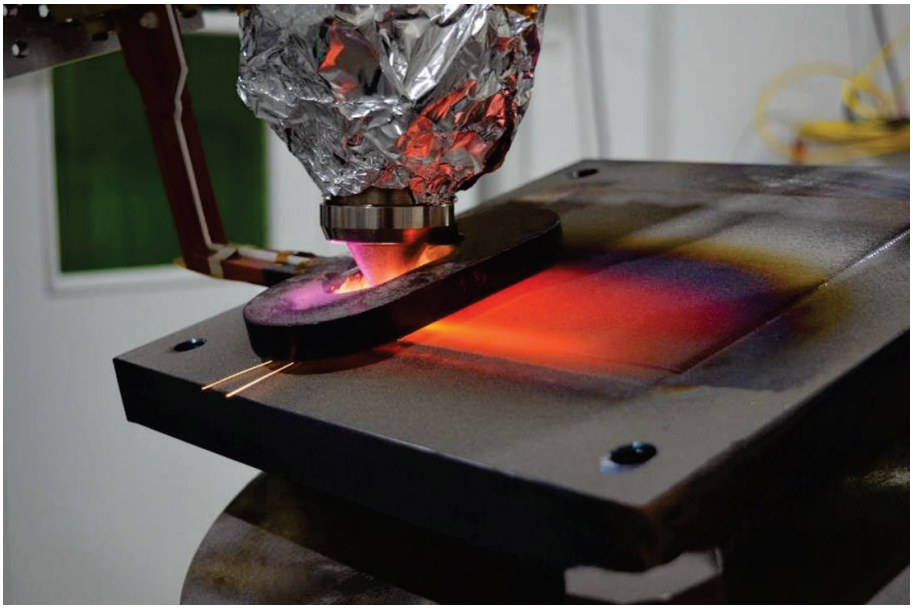
Figure 123. Setup for simultaneous induction preheating and laser cladding of thick plates.



Induction heating enables the deposition of thicker clad layers without cracking.

Heat removal from the bottom of the thick plate is insufficient.

Figure 124. Heat pattern from elliptical induction builds up near the end of the cladding pass.



3.2 Plate configurations

Thick plates of ASTM A36 structural steel used with the simultaneous induction heating method measured 12 in. x 12 in. x 1.25 in. These thick plates were designed to be laser clad within a central area measuring 8 in. x 8 in. Minimum layer thickness was 0.9 mm (0.035 in.). The base plate was rotated 90 deg between successive layers.

Two groups of thin plates, also ASTM A36 structural steel, measured 12 in. x 12 in., with a thickness of only 0.5 in. The first group (A) had parameters predicted by numerical model. Two pads were deposited on each of two thin plates. Each wear pad measured approximately 3.5 in. x 8 in. and corresponded to a specific computer-selected parameter set, #1 through #4.

Group (B) thin plates were prepared to evaluate a more complex, functionally-graded coating. These plates held eight-layer deposits made up of four materials, each deposited in two layers. The 8 in. x 8 in. cladding pad centralized on the 12 in. x 12 in. plate. Two plates were made with the complex functionally graded coating.

3.2.1 Layered plates

Thick plates prepared with simultaneous induction heating had functional graded coatings that included two layers of Inconel 625 followed by two

layers of Inconel 625 with injected tungsten carbide. Each of the four layers had a thickness of 0.4 mm (0.16 in.). Between layers, the base plate was rotated 90 deg.

3.2.1.1 *Deposition results*

Laser cladding with simultaneous induction preheat prevented cracking in this dual layer topcoat. However, the thick plate experienced significant distortion. A backing plate is needed to remove some heat buildup during cladding. A water-cooled backing plate would be an excellent choice.

3.2.1.2 *Metallography/characterization*

The simultaneous induction heating with laser cladding was to enable deposition of thick cladding, 0.9 mm (0.035 in.) minimum, without cracking. Figure 125 is a cross-section micrograph of a resulting preheated topcoat of Inconel 625 with injected tungsten carbide. A major portion of the spherical black tungsten carbide appears to have dissolved into the matrix. However, the micrograph did not produce any cracking.

Figure 126 is a plan view (top view) of the Inconel 625 with injected tungsten carbide. The micrograph is shown after grinding, polishing and etching to reveal the microstructure.

The layered cladding was applied with induction cladding. Note absence of cracking, 25X.

Distribution of spherical Tungsten Carbide is uniform.

Figure 125. Cross section of dual layer Inconel bond coat followed by dual layer Inconel 625 with injected Tungsten Carbide.

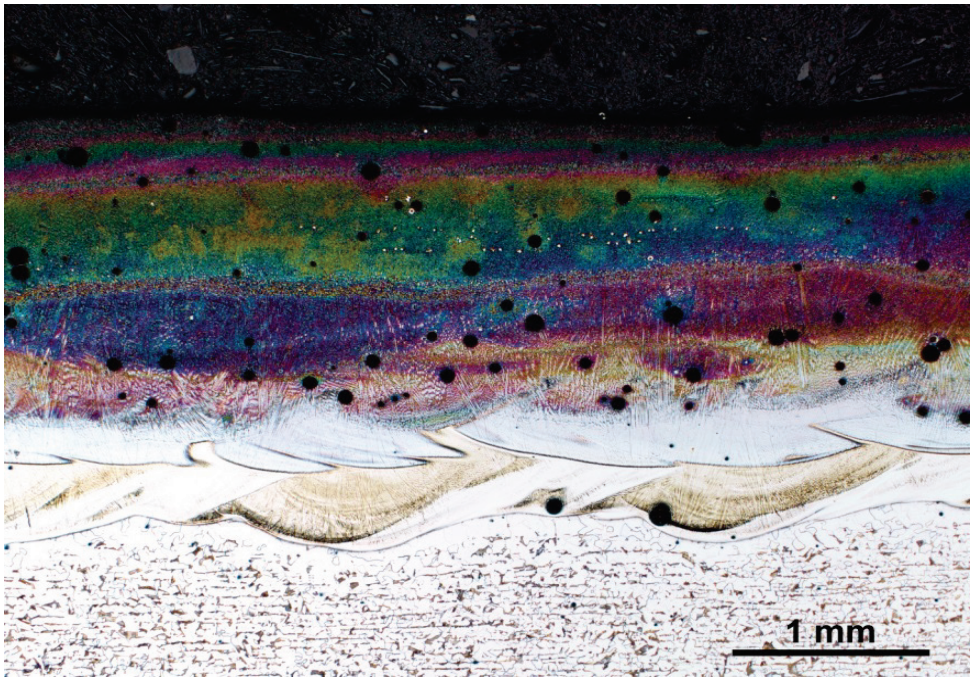
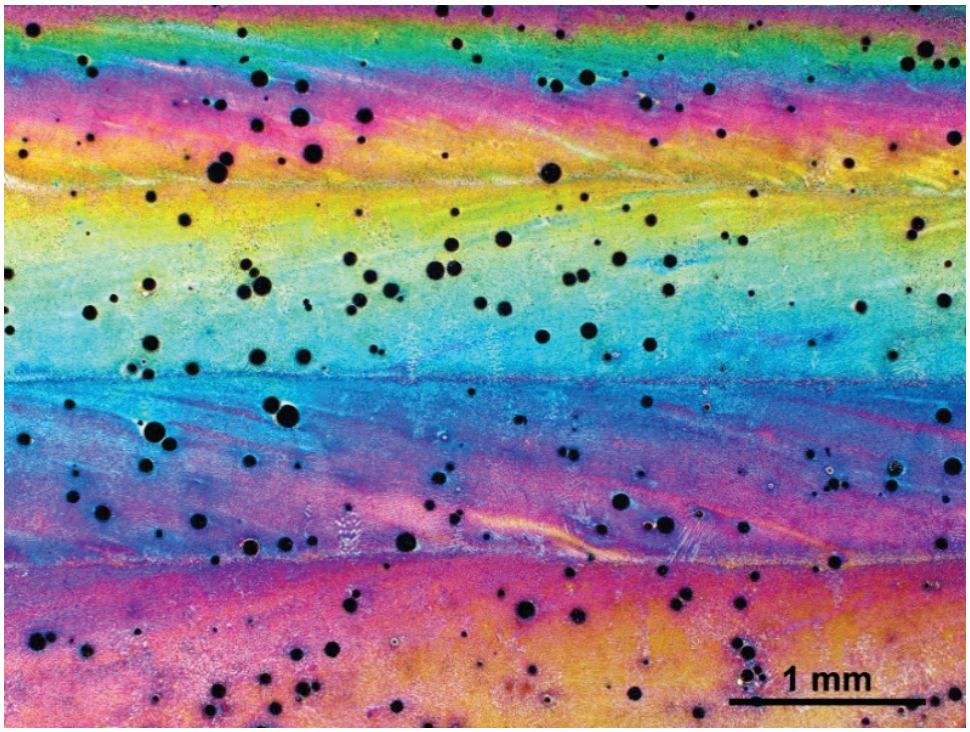


Figure 126. Plan view (top view) of Inconel 625 with injected tungsten carbide (black spheres).



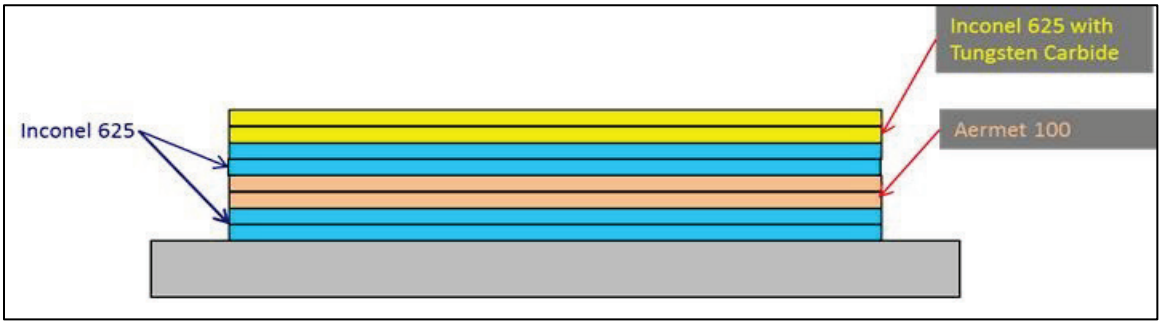
3.2.2 Functionally graded plates

Group A thin plates (0.5 in. thick, with numerical model-selected parameters) had four-layer functional graded coatings. A two-layer bond coat of Inconel 625 was followed by a two-layer topcoat of Inconel 625 with injected tungsten carbide. Each layer had a thickness of 0.4 mm (0.016 in.). Between successive layers, the base plate was rotated 90 deg.

Group B thin plates had a complex, functionally-graded coating that included eight layers. The bond coat consisted of two layers of Inconel 625. The next two layers were made of Carpenter Cartech® Aermet 100 Alloy, aircraft steel. Aermet 100 combines high hardness and strength with ductility and toughness. Many additive manufactured tools are made with Aermet 100 Alloy.

After the Aermet 100 Alloy came two additional layers of Inconel 625, a ductile, high-temperature material. The topcoat of the complex functionally graded material consisted of two layers of Inconel 625 with injected tungsten carbide. A pictorial diagram of the eight-layer Functional Graded Material coating appears in Figure 127.

Figure 127. Eight-layer functional graded material (FGM) coating.



The coating is made up of multiple layers of Inconel 625, Aermet 100 steel and Inconel 625 with injected tungsten carbide.

3.2.2.1 *Numerical approach for parameter selection*

This section describes the approach used by Applied Optimization (AO) to computationally predict optimal processing conditions for a functionally-graded material consisting of Inconel 625 and Tungsten Carbide. In the initial step, “effective,” temperature-dependent material data was defined for the continuum model simulations. These data were then used to complete one- and two-track calibration simulations which mirrored

conditions used in the calibration builds at Fraunhofer. Next, AO completed a time-dependent Finite Element simulation to determine overall heat-up levels for an 8-in. by 8-in. cladding build. Finally, these heat-up data were used to initialize several steady-state thermal-fluid track simulations, which were used to define a range of optimal processing conditions.

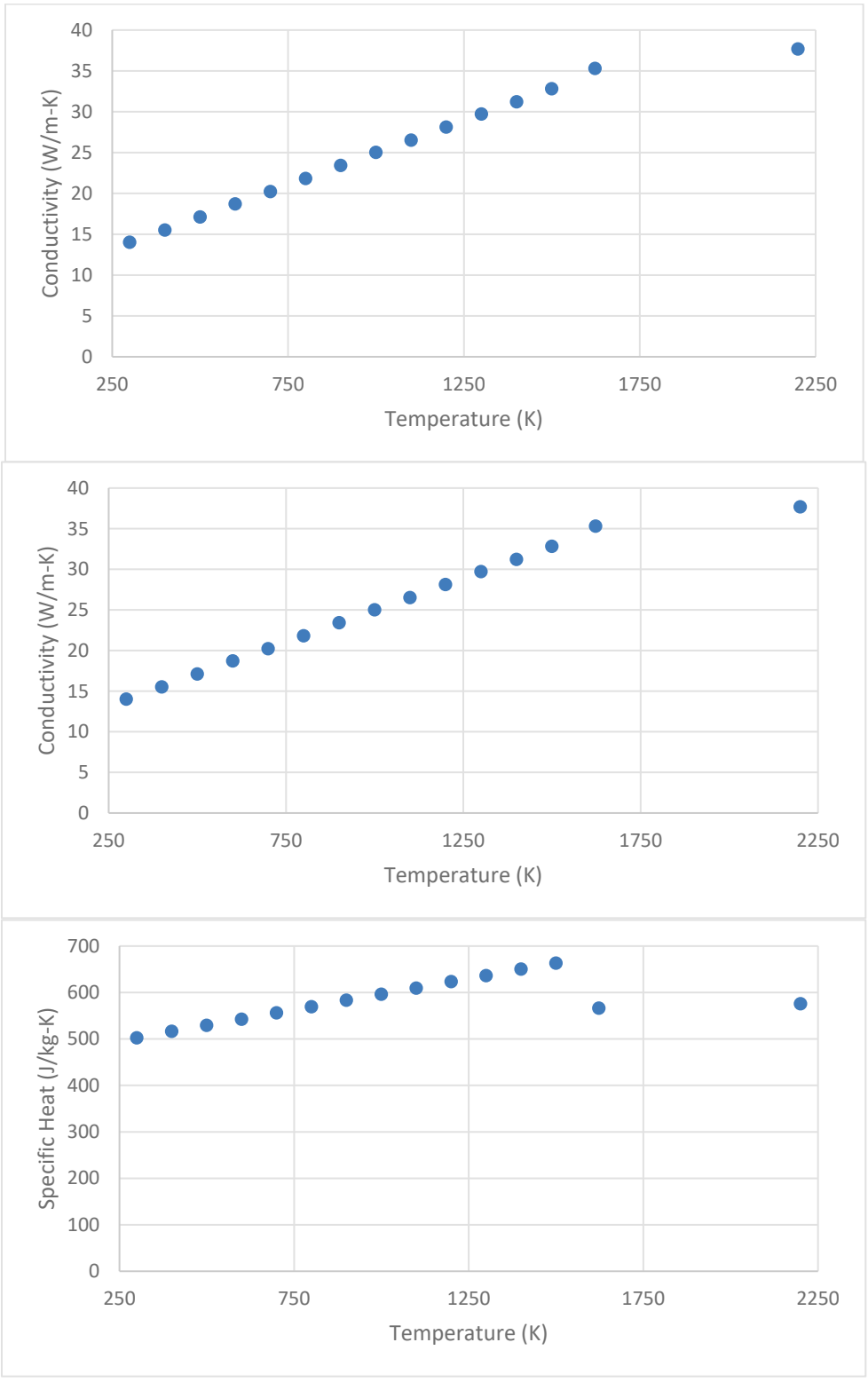
To accurately simulate processing of a material with radically different components, such as IN625 and tungsten carbide, one of two general methods may be used. The first method is to model the entire process in a time-dependent sense with clear distinction between phases. The second method is to model the process as a continuum with properties derived as a combination of the properties of each phase. For this work, latter approach was taken. In addition, a functionally-graded material will exhibit different material properties in different regions of the build. The steady-state thermal-fluid simulation tool at AO does not model spatially-distributed material properties, so this aspect was modeled by observing that the spatial distribution of properties roughly aligned with the thermal distribution. Temperature-dependent properties are built in to the steady-state thermal-fluid simulation tool, so this analogy provided a path to model processing of a functionally-graded material.

3.2.2.2 *Property determination*

For each build, a steel substrate was used. Here, thermal properties of stainless steel 316 (Bobkov et al. 2008) were used. Thermal conductivity and specific heat of tungsten carbide were obtained from Xiong et al. (2009), while density was assumed constant at 15,800 kg/m^3. Laser absorptivity of tungsten carbide was obtained from Paul et al. (2007). For IN625, liquid-state material properties were taken from Ozel et al. (2016), while lower temperature solid state properties were taken from the technical bulletin on IN625 by Special Metals (2013). Laser absorptivity of IN625 was obtained from Lia et al. (2017).

For the steady-state thermal-fluid calibration simulations, steel thermal conductivity, specific heat, and density were used up to 1,500 K, and a weighted average of IN625 and tungsten carbide properties were used at higher temperatures. Figure 128 illustrates the simulation using a 25 percent tungsten carbide-IN625 mixture. A new weighted average was generated for each case that had a different tungsten carbide content. The laser absorptivity was also taken as a weighted average of tungsten carbide and IN625 absorptivity.

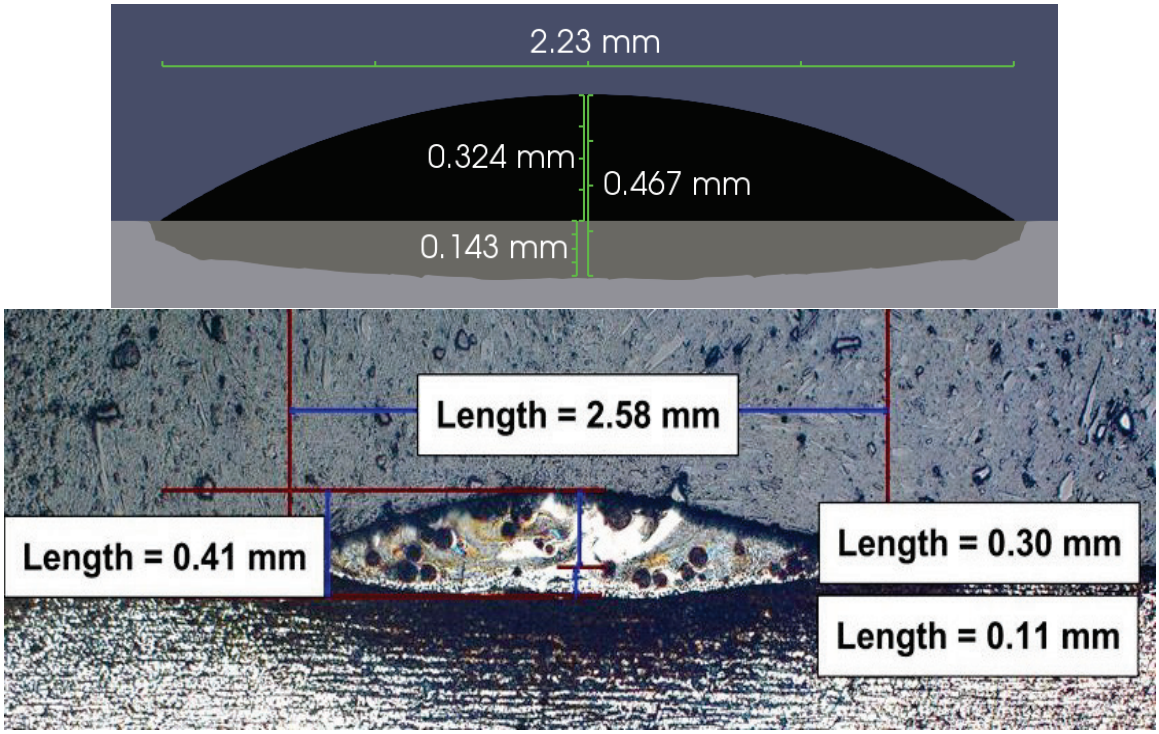
Figure 128. Material properties for steady-state thermal-fluid simulation of 25 percent tungsten carbide-IN625 mixture on steel.



3.2.2.3 *One- and two-track calibration*

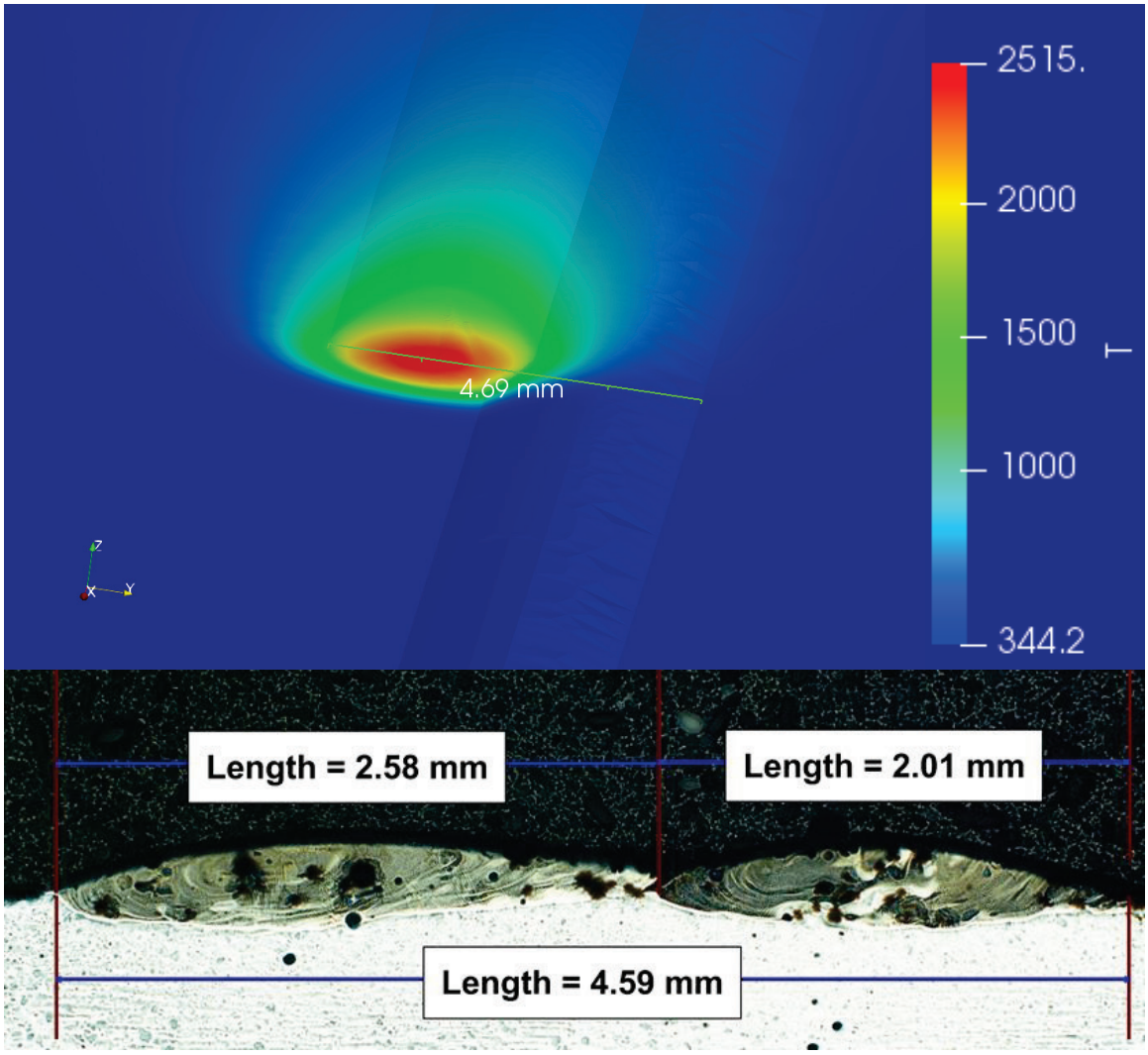
To ensure accuracy of the simulation results, a calibration process was completed based on data from one- and two-track calibration builds completed at Fronhaufer. This process helped for correction of simulation parameters, which were less well defined. Calibration included the diameter of the powder cloud at the level of the build plane and the slope of surface tension as a function of temperature. Once these parameters were properly adjusted, the comparison shown in Figure 129 was obtained. Here, the simulated width is within about 10 percent of the experimental value, the remelt depth is within about 30 percent, and the height above the substrate is within 8 percent. This was deemed sufficient to continue with further simulations.

Figure 129. Comparison between observed simulation (top) and experimental (bottom) results for deposition of Tungsten Carbide + IN625 track on steel plate.



Two overlapping tracks were then simulated, mirroring conditions from the Fraunhofer builds. As seen in Figure 130, the simulated width is only 2 percent different from the experimentally measured value.

Figure 130. Results of two-track simulation (top) compared with experimental measurements (bottom).

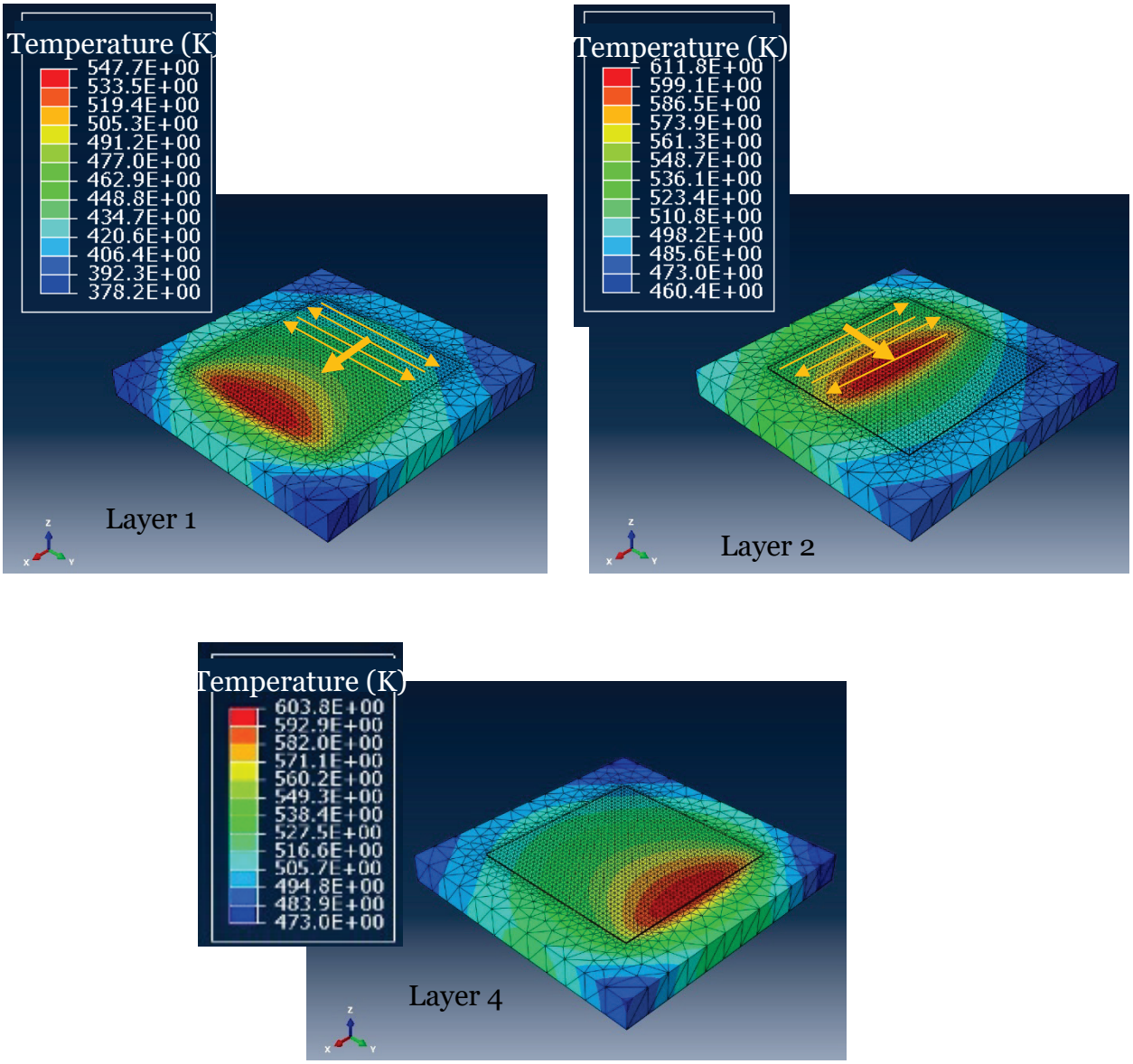


3.2.2.3.1 *Prediction of process parameters for functionally-graded build*

The build consisted of a 12 in. x 12 in. by x 1.25-in. steel base plate with an 8 in. by 8 in. square deposit. The deposit consisted of two layers of IN625 deposited onto the base plate, followed by two layers of a 35 percent Tungsten Carbide-IN625 mixture on top. Prediction of optimized process parameters began by completing a “part level” simulation using the SAMP finite element software. This simulation used nominal parameters and large time-steps which encompassed 10 tracks worth of material at once. The goal was not to obtain a locally precise temperature profile but a broader background temperature profile that could be used to initialize steady-state thermal-fluid simulations. The results of this simulation are

shown in Figure 131. From these results, it can be seen that the max temperature stabilizes around 600 K after the first layer.

Figure 131. Temperature distribution results from "part level" finite element simulation.



These temperature profiles were used as an initial condition for several sequences of ParaGen simulations, one sequence for each set of a machine parameters. The sequences were necessary because ParaGen is currently not optimized for computing "middle of the layer" tracks, though this work is planned for future versions. Currently, the shape and dimensions of the previously deposited material must be defined as input for each simulation. To compute parameters for a track in the middle of a layer,

where each track appears similar in shape and size, a series of ParaGen simulations were ran in which dimensions of the previously deposited material were varied based on results of the previous simulation. This was done until an equilibrium was reached. To facilitate this process, batch scripts read specific simulation outputs and modified inputs of the subsequent simulation accordingly. A summary flow chart for this process is shown in Figure 132.

Figure 132. Process description for micro-scale simulation of "middle of the layer" tracks.

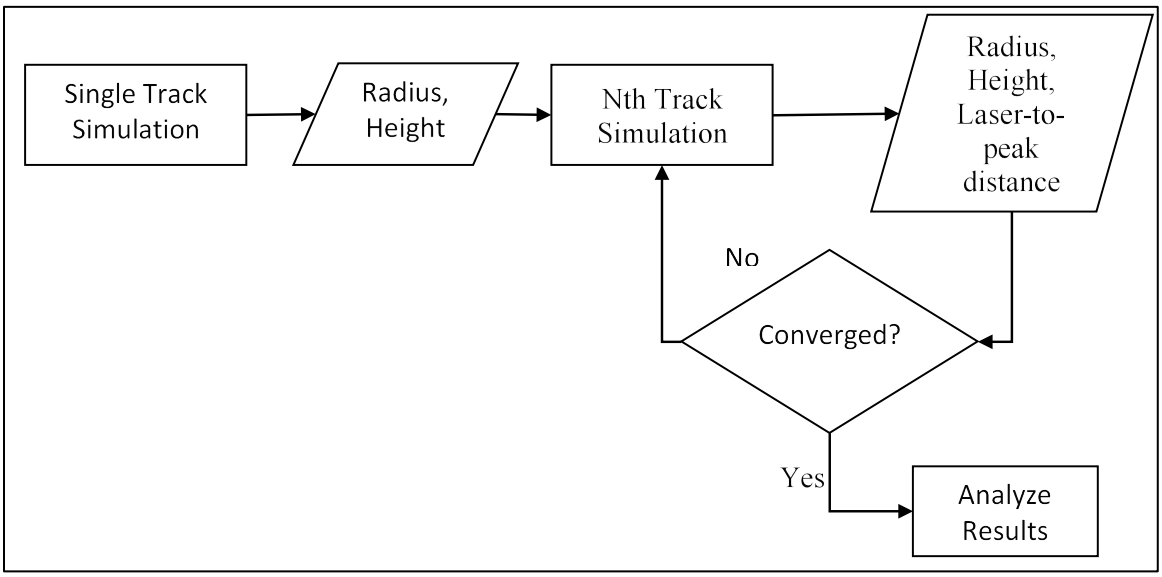
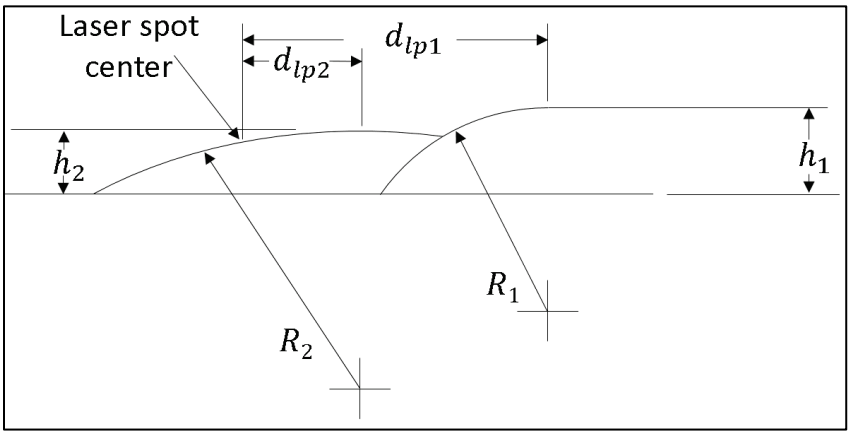


Figure 133 illustrates the convergence dimensions.

Figure 133. Dimensions required to achieve converged "middle of the layer" geometry.



For the geometry to be converged and represent a valid result, the following conditions need to be met:

$$h_1 = h_2$$

$$R_1 = R_2$$

$$d_p = d_{lp1} - d_{lp2}$$

d_p is the x-y pitch, or the hatch distance. The center of the laser spot is often offset from the track peak by some distance. The distance to the currently deposited track is denoted as d_{lp2} and the distance to the previous track as d_{lp1}. This offset is not known a priori, so it must be determined iteratively through the process described in Figure 132.

To select optimal process parameters, a matrix of conditions was defined for simulation of each set of two layers. Table 19 shows the conditions that were varied. All other conditions were held constant. Travel speed was fixed at 1.2 m/min., beam spot diameter at 3 mm, and powder feed rate at 10 g/min.

Table 19. Variable parameters for parameter optimization work.

IN625 on Steel		35%WC+IN625 on IN625	
Power (W)	Power (W)	Power (W)	Pitch x/y (mm)
2,000	1	1,100	1
2,100	1	1,200	1
2,200	1	1,300	1
2,300	1	1,400	1
2,000	1.5	1,100	1.5
2,100	1.5	1,200	1.5
2,200	1.5	1,300	1.5
2,300	1.5	1,400	1.5
2,000	2	1,100	2
2,100	2	1,200	2
2,200	2	1,300	2
2,300	2	1,400	2

Figure 134 shows a cross section of a "middle of the layer" simulation with quality metrics indicated.

Figure 134. Simulation quality metrics, 1,400W, 1.5mm pitch x/y.

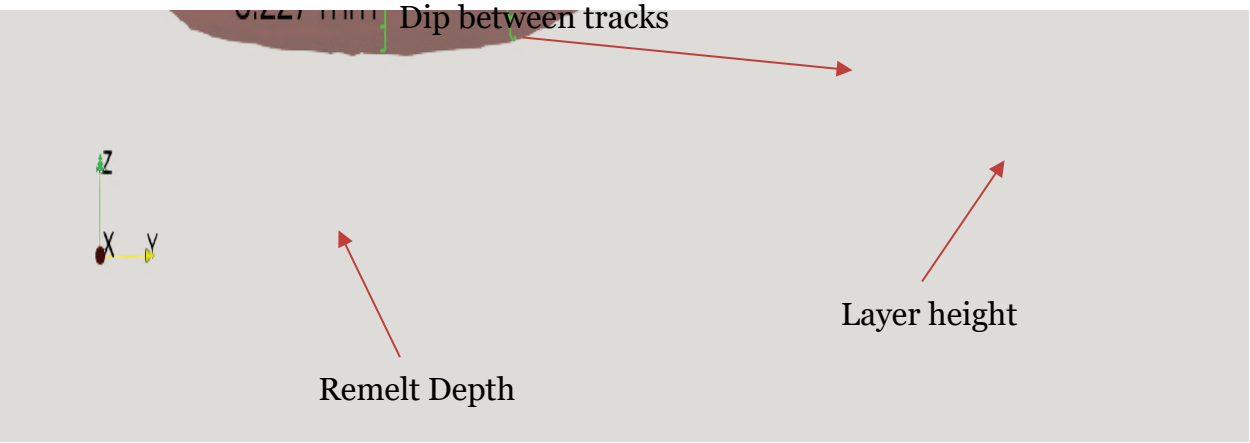


Figure 135, Figure 136, and Figure 137 show plots of the quality metrics from the simulations of 35 percent Tungsten Carbide + IN625 on IN625. To obtain fully dense parts with minimal lack-of-fusion, the remelt depth should be greater than the dip magnitude by some margin of safety, which must be determined experimentally. If it is assumed that 0.1 mm is a good margin of safety, the plots indicate that all cases will have minimal lack-of-fusion except for the highest pitch and lowest power cases–pitch x/y = 2 mm and power = 1,100 and 1,200 W.

Figure 135. Remelt depth simulation results for building 35%WC+IN625 on IN625.

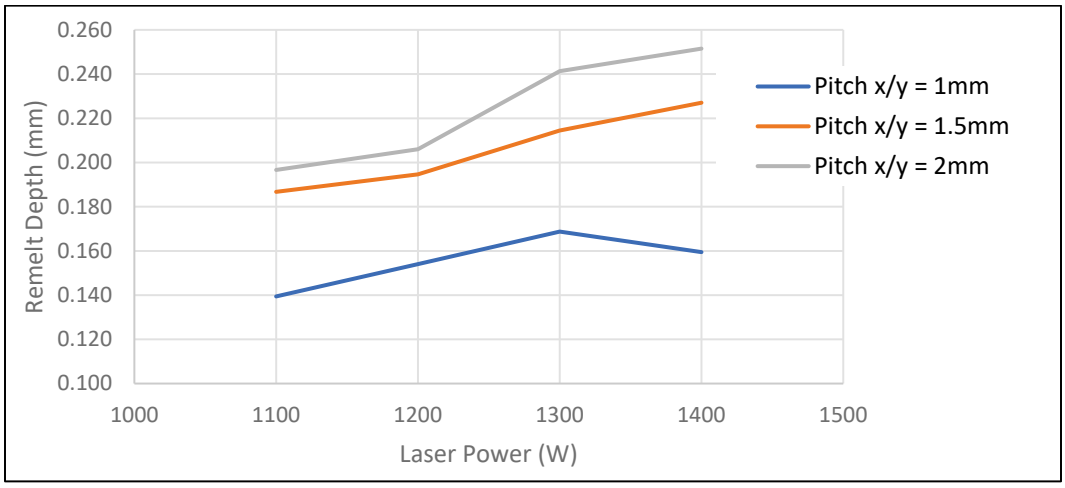


Figure 136. Dip magnitude simulation results for building 35%WC+IN625 on IN625.

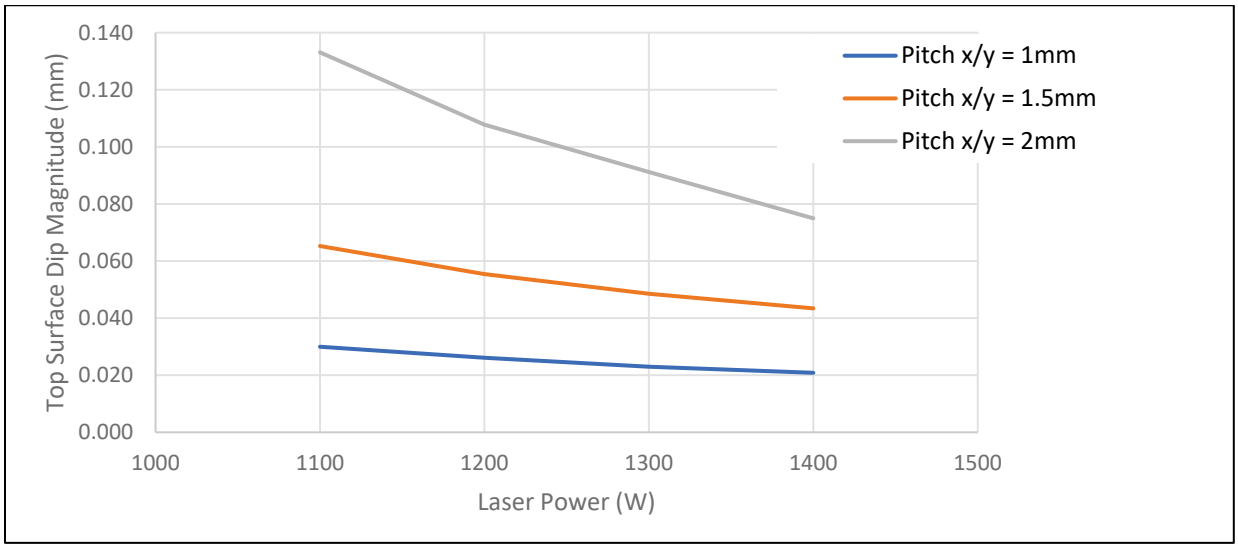


Figure 137. Layer height simulation results for building 35%WC+IN625 on IN625.

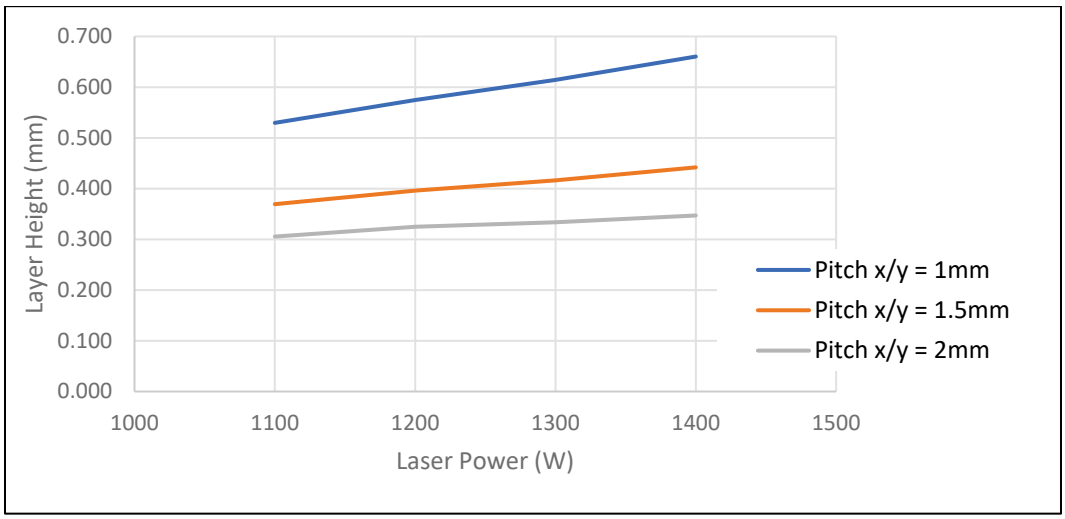


Figure 138, Figure 139, and Figure 140 show plots of the quality metrics from the simulations of IN625 on steel. If it is again assumed that 0.1 mm is a good margin of safety, the plots indicate that all cases will have minimal lack-of-fusion.

3.3 Selected parameters, results, and key conclusions

Due to the wide selection of seemingly good parameter options, four builds were recommended. Each build would use the same working distance as the calibration builds, where this is defined as shown in Figure 141. The base plate of each build would be steel. The bottom two layers would be Inconel 625, and the top two layers would be 35 percent tungsten carbide

+ Inconel 625. The parameters for the two Inconel 625 layers were be defined as indicated in Table 20 and for the two 35 percent tungsten carbide + Inconel 625 layers as indicated in Table 21. These are denoted "computer selected parameters."

Figure 138. Remelt depth simulation results for building IN625 on steel.

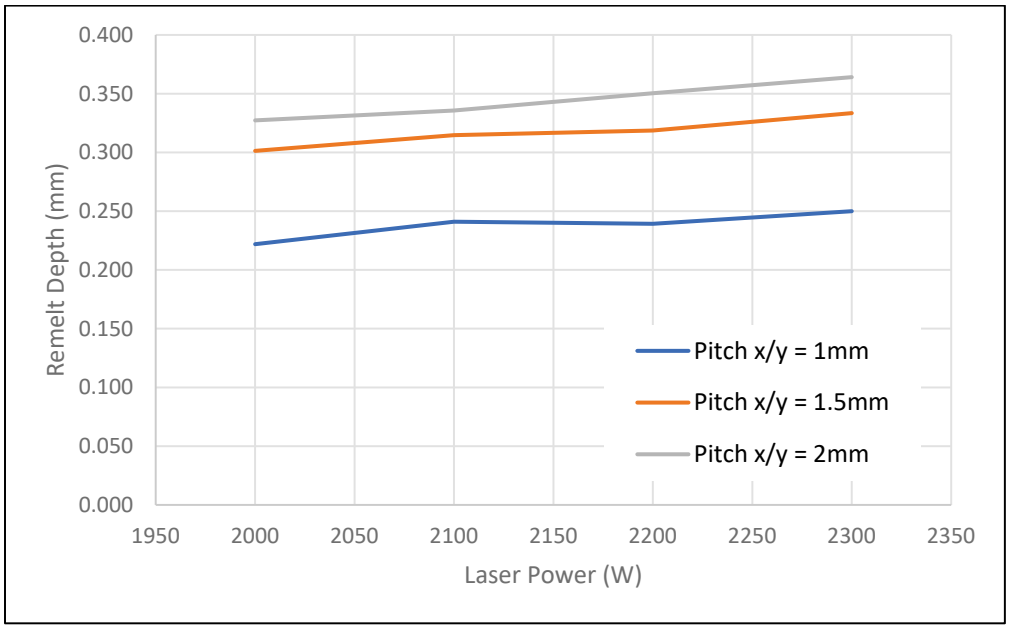


Figure 139. Dip magnitude simulation results for building IN625 on steel.

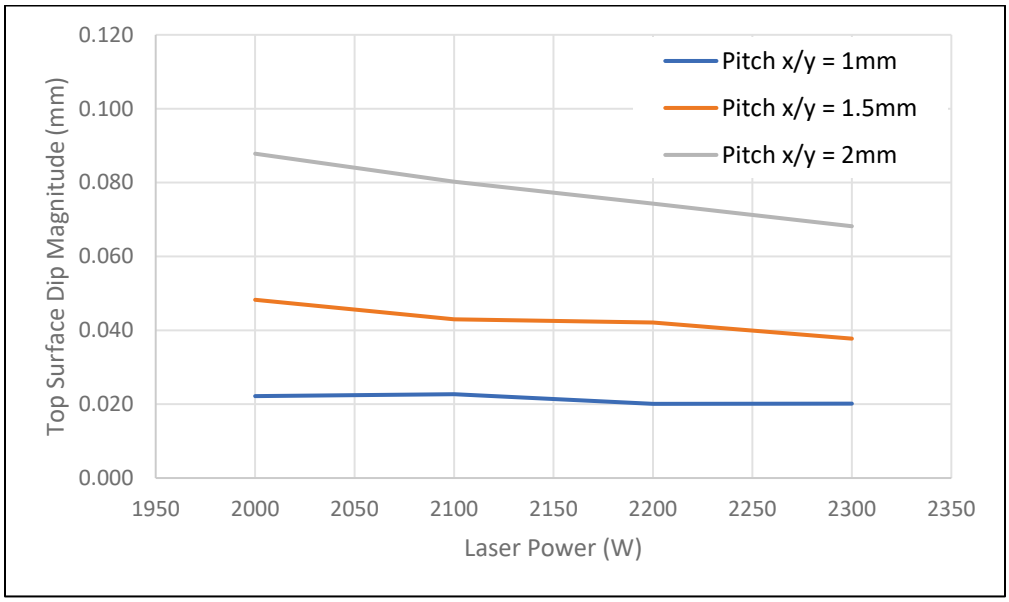


Figure 140. Layer height simulation results for building IN625 on steel.

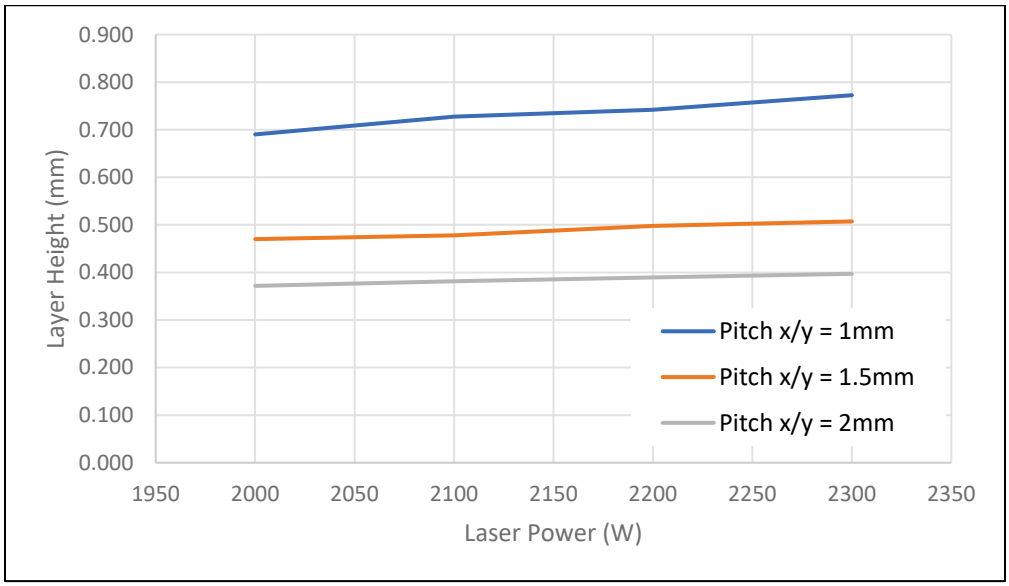


Figure 141. Illustration of working distance.

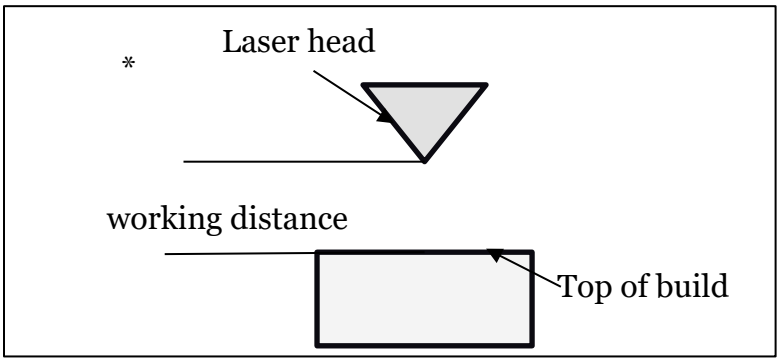


Table 20. Parameters for two layers of Inconel 625.

Powder Type	Laser Power (watts)	Travel Speed (m/min.)	Beam Spot Diameter (mm)	Powder Feed Rate (g/min.)	Pitch x/y (mm)	Pitch Z (mm)
Inconel 625	2,200	1.2	3	10	1.5	0.5

Table 21. Parameters for two layers of 35 percent Tungsten Carbide + Inconel 625.

	Powder Type	Hard Particle Type	Laser Power (watts)	Travel Speed (m/min.)	Beam Spot Diameter (mm)	Powder Feed Rate (g/min.)	Pitch x/y (mm)	Pitch Z (mm)
1	Inconel 625	Tungsten Carbide	1,200	1.2	3	10	1.5	0.4
2	Inconel 625	Tungsten Carbide	1,400	1.2	3	10	1.5	0.4
3	Inconel 625	Tungsten Carbide	1,200	1.2	3	10	1.0	0.6
4	Inconel 625	Tungsten Carbide	1,400	1.2	3	10	1.0	0.6

3.3.1.1 *Deposition results*

Group A plates, 0.5 in. thick and with computer selected parameters, were deposited without incident. These parameters had subtle variations from parameters previously used for depositing Inconel-Tungsten Carbide. There was no visible cracking in the Group A samples, despite the lack of preheat. Cladding thickness was 0.4 mm (0.016 in.) minimum. Distortion was minimal because the plates had been bolted down to a heavy steel frame during cladding.

Group B plates, also 0.5-in.-thick, were time consuming to clad because of the material and parameter changes required every two layers. Despite the large number of layers on relatively thin plate, no cracking was observed, and distortion was minimal due to use of heavy steel frame. The thin plates were clad and allowed to cool while they were attached to the steel frame.

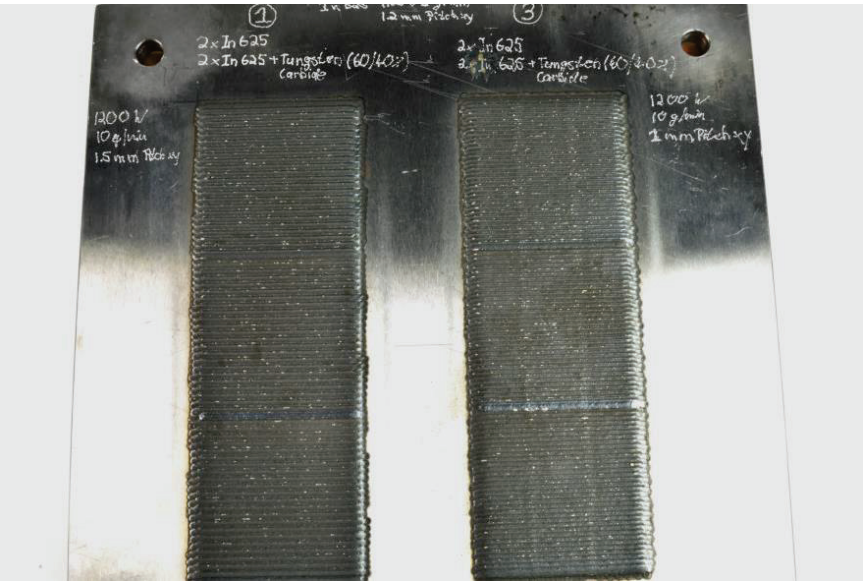
3.3.1.2 *Metallography/characterizations*

Figure 142 is an overview photograph of the cladding pads with topcoats produced with computer-selected parameter sets #1 and #3. Parameter set #1 appears to produce a smooth and uniform cladding. Parameter set #3 is also good but slightly rougher and more irregular than parameter set #1.

Cladding pads with topcoats selected from parameter sets #2 and #4 are displayed in Figure 143. These computer-selected parameters operating at 1,400 W power produced rougher deposits. Both deposits also show small pores that were not present with deposits from parameter sets #1 and #3 corresponding to 1,200 W.

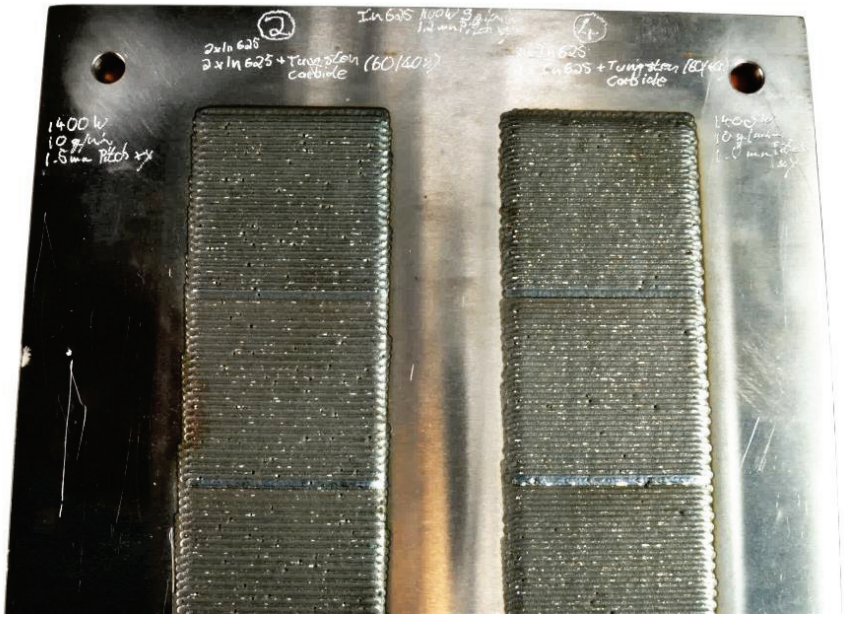
Figure 144 is a close-up view of the surface porosity resulting from computer parameter sets #2 and #4. Arrows indicate examples of surface porosity.

Figure 142. Four-layer functional graded material (FGM) pads deposited with laser parameters predicted by the numerical model.



Dual layers were applied with Inconel 625 and Inconel 625 with injected tungsten carbide, using topcoat parameter sets #1 and #3.

Figure 143. Computer selected parameter sets #2 and #4 were deposited at 1,400 W power.



Both cladding pads exhibit porosity at the surface. A higher magnification view appears in Figure 144 .

Figure 144. Computer selected parameter sets #2 and #4 produced deposits that exhibits porosity (indicated by red arrows) in the cladding surface.

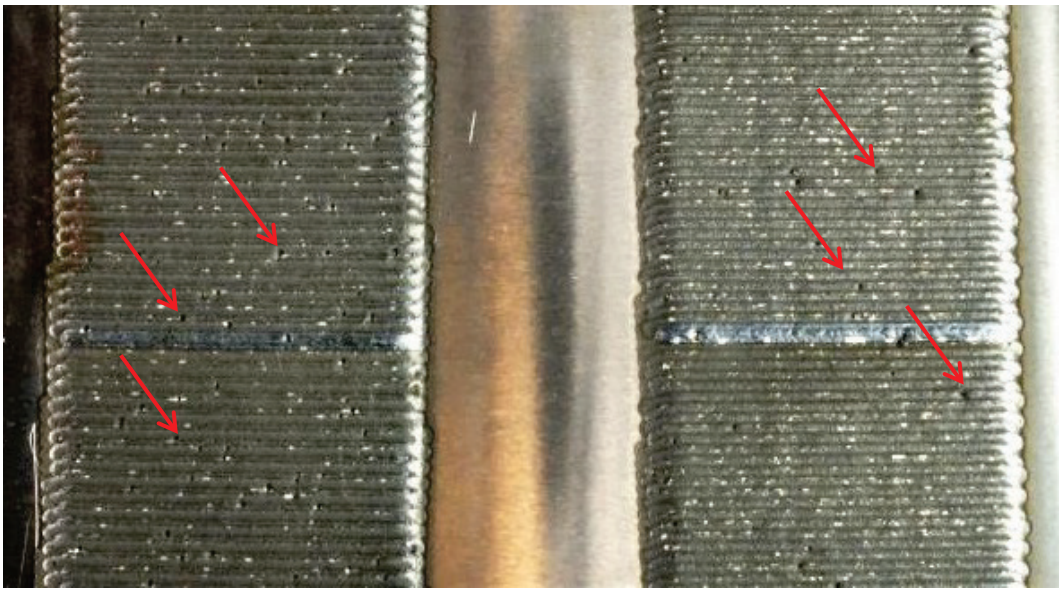
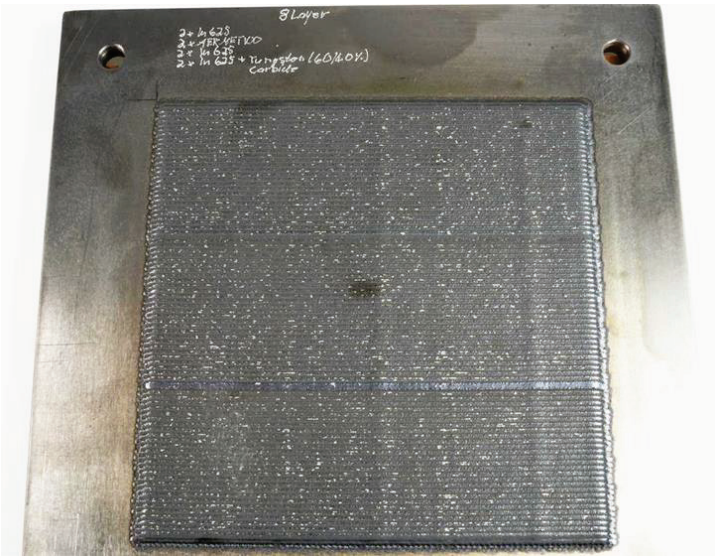


Figure 145. Eight-layer FGM pad prepared by laser directed energy deposition (DED).



Dual layers of the following powders were applied in order from the substrate outward: Inconel 625, Aermet 100, Inconel 625 and Inconel 625 with injected Tungsten Carbide (topcoat).

The build articles shown in Figures 138 through 141 were provided as deliverables. Parameters sets #1 and #2 and the eight-layer build were then repeated, and metallography was performed. One plate was used to deposit parameters sets #1 and #2, shown in Figure 146, while another plate was used to deposit the eight-layer build, shown in Figure 147.

Figure 146. Second trial of Computer-selected parameter sets #1 (Pad A) and #2 (Pad B).

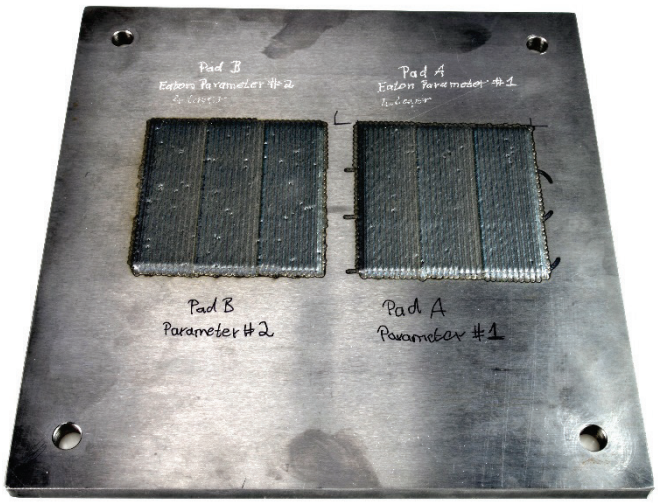


Figure 147. Second trial of eight-layer FGM pad prepared by laser directed energy deposition (DED).



The internal micrographs for Pad A and Pad B exhibit similar characteristics. This includes some small internal porosity in the full IN625 and mixed IN625/Tungsten Carbide regions (no larger than ~50 um), some vertical cracking in the mixed region, and a few small defects in the mixed region which may be caused by lack-of-fusion. Figure 148 shows a sample etched micrograph from Pad A. With the cracking in a vertical orientation across two build layers, it is likely a result of residual stress. The small round porosity is not a big concern because its shape provides only small stress concentration. The apparent lack-of-fusion porosity will need to be investigated further to determine whether it is in fact porosity and whether the chosen parameters can be adjusted to avoid it.

Micrographs were similarly obtained for the eight-layer build. This build appears to exhibit similar characteristics to the four-layer builds, with vertical cracks extending through the top two IN625+WC layers and micro-porosity visible in the pure IN625 and Aermet layers (see Figure 149 and Figure 150). More work will need to be completed to determine the root cause and further mitigation strategies for the vertical cracking.

Figure 148. Micrograph of computer-selected parameter set #X.

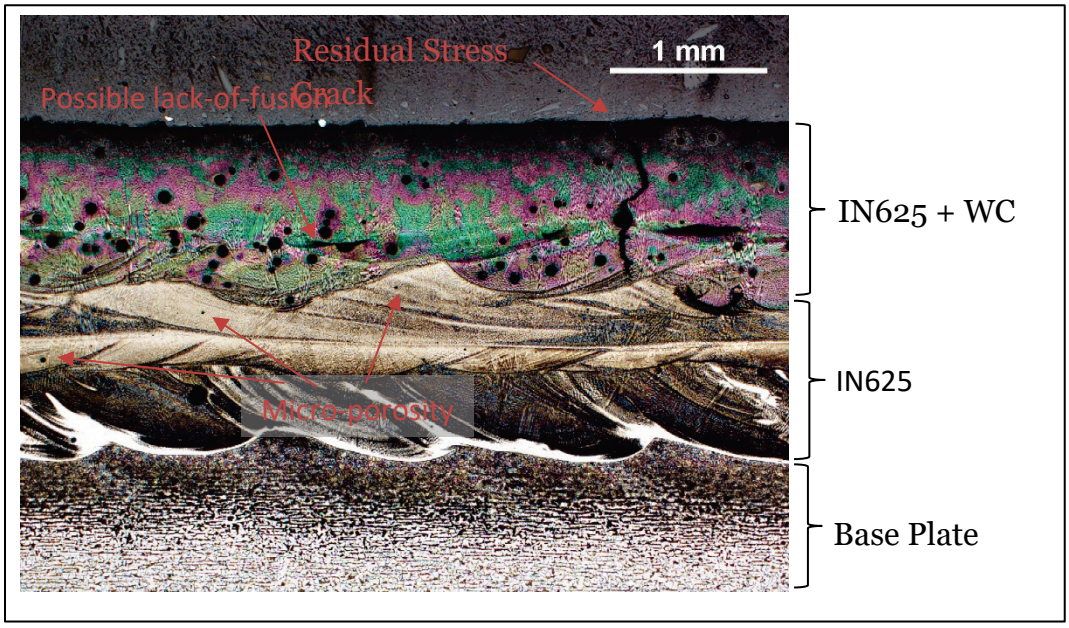


Figure 149. Micrograph of eight-layer build bond-line.

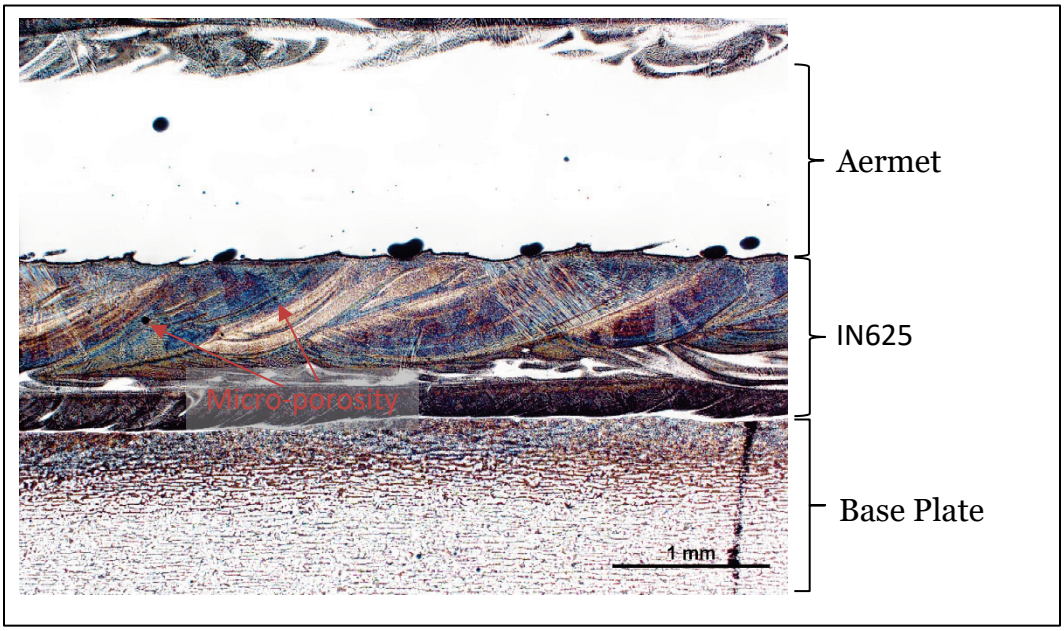
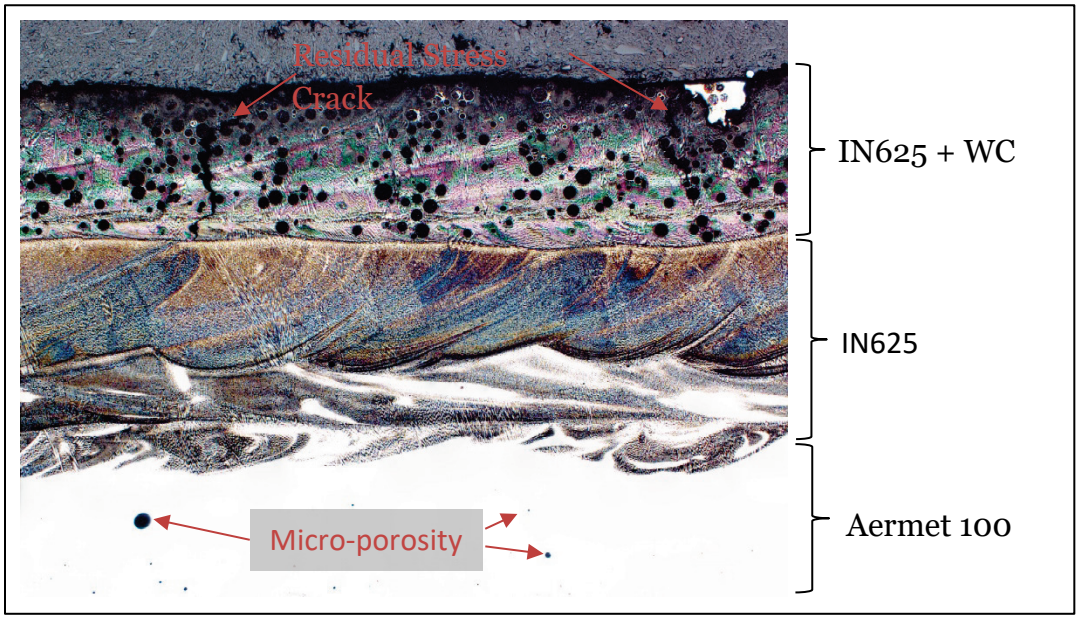


Figure 150. Micrograph of eight-layer build surface.



References

Abaqus ™, Simulia. 1978. Dassault Systemes 6.14-2.

Alvarez, P., J. Ecenarro, I. Setien, M. S. Sebastian, A. Echeverria, and L. Eciolaza. 2016. *Computationally efficient distortion prediction in powder bed fusion additive manufacturing*. *International Journal of Engineering Research and Science* 2(10):39-46.

Bobkov, V. P., L. R. Fokin, E. E. Petrov, V. V. Popov, V. N. Rumiantsev, and A. I. Savvatimsky. 2008. *Thermophysical properties of materials for nuclear engineering: a tutorial and collection of data*. IAEA, Vienna.

Carter, L. N., C. Martin, P. J. Withers, and M. M. Attallah. 2014. The influence of the laser scan strategy on grain structure and cracking behaviour in SLM powder-bed fabricated nickel superalloy. *Journal of Alloys and Compounds* 615:338-347.

DebRoy, T., H. L. Wei, J. S. Zuback, T. Mukherjee, J. W. Elmer, J. O. Milewski, A. M. Beese, A. Wilson-Heid, A. De, and W. Zhang. 2018. Additive manufacturing of metallic components–process, structure and properties. *Progress in Materials Science* 92:112-224.

JMatPro. 2003. CD-ROM, Thermotech Ltd., Version 9.0, Sente Software Ltd., Guildford, U.K.

Keller, N., and P. Ploshikhin. 2014. *New method for fast predictions of residual stress and distortion of AM parts*. *Solid Freeform Fabrication Symposium* 25, Austin, TX.

Kok, Y., X. P Tan, P. Wang, M. L. S. Nai, N. H. Loh, E. Liu, and S. B. Tor. 2018. Anisotropy and heterogeneity of microstructure and mechanical properties in metal additive manufacturing: A critical review. *Materials & Design* 139:565-586.

Lia, Frederick, Joshua Park, Jay Tressler, and Richard Martukanitz. 2017. Partitioning of laser energy during directed energy deposition. *Additive Manufacturing* 18:31-39.

Megahed, M.,H.-W. Mindt, N. N'Dri, H.-Z. Duan, and O. Desmaison. 2016. Metal additive-manufacturing process and residual stress modeling. *Integrating Materials and Manufacturing Innovation* 5(4).

Özel, Tuğrul, Yiğit M. Arısoy, and Luis E. Criales. 2016. Computational simulation of thermal and spattering phenomena and microstructure in selective laser melting of inconel 625. *Physics Procedia* 83:1435-1443.

Paul, C. P., H. Alemohammad, E. Toyserkani, A. Khajepour, and S. Corbin. 2007. Cladding of WC–12 Co on low carbon steel using a pulsed Nd: YAG laser. *Materials Science and Engineering: A* 464(1):170-176.

Sabau, A. S., and W. D. Porter. 2008. Alloy shrinkage factors for the investment casting of 17-4PH stainless steel parts. *Metallurgical and Materials B* 39(2):317-330. DOI: 10.1007/s11663-007-9125-3.

Special Metals. 2013. INCONEL alloy 625. Technical Bulletin by Special Metals Inc. www.specialmetals.com

Special Metals 2017. INCONEL alloy 718. http://www.specialmetals.com/documents/Inconel%20alloy%20718.pdf (accessed 3 February 2017).

Tang, M. 2017. Inclusions, porosity, and fatigue of AlSi10Mg parts produced by selective laser melting. PhD diss. Carnegie Mellon University.

Thermo-Calc Software. 2018. Thermodynamic and phase diagram calculations for multicomponent systems. Thermo-Calc Software, Inc., McMurray, PA.

Thijs, L., F. Verhaeghe, T. Craeghs, J. Van Humbeeck, and J.-P. Kruth. 2010. A study of the microstructural evolution during selective laser melting of Ti–6Al–4V. *Acta Materialia* 58(9):3303-3312.

Xiong, Y., W. H. Hofmeister, Z. Cheng, J. E. Smugeresky, E. J. Lavernia, and J. M. Schoenung. 2009. In situ thermal imaging and three-dimensional finite element modeling of tungsten carbide–cobalt during laser deposition. *Acta Materialia* 57(18):5419-5429.

Weingarten, C., D. Buchbinder, N. Pirch, W. Meiners, K. Wissenbach, and R. Poprawe. 2015. Formation and reduction of hydrogen porosity during selective laser melting of AlSi10Mg. *Journal of Materials Processing Technology* 221:112-120.

REPORT DOCUMENTATION PAGE

Form Approved
OMB No. 0704-0188

Public reporting burden for this collection of information is estimated to average 1 hour per response, including the time for reviewing instructions, searching existing data sources, gathering and maintaining the data needed, and completing and reviewing this collection of information. Send comments regarding this burden estimate or any other aspect of this collection of information, including suggestions for reducing this burden to Department of Defense, Washington Headquarters Services, Directorate for Information Operations and Reports (0704-0188), 1215 Jefferson Davis Highway, Suite 1204, Arlington, VA 22202-4302. Respondents should be aware that notwithstanding any other provision of law, no person shall be subject to any penalty for failing to comply with a collection of information if it does not display a currently valid OMB control number. **PLEASE DO NOT RETURN YOUR FORM TO THE ABOVE ADDRESS.**

1. REPORT DATE *(DD-MM-YYYY)*	**2. REPORT TYPE**	**3. DATES COVERED** *(From - To)*
July 2019	Final report	

4. TITLE AND SUBTITLE

Additive Manufacturing of Metallic Materials with Controlled Microstructures

Multi-Scale Modeling of Direct Metal Laser Sintering and Directed Energy Deposition

5a. CONTRACT NUMBER

5b. GRANT NUMBER

5c. PROGRAM ELEMENT NUMBER

Arjun Tekalur, Jacob Kallivayalil, Jason Carroll, Mike Killian, Benjamin Schultheis, Anil Chaudhary, Zackery B. McClelland, Jeffrey B. Allen, Jameson D. Shannon, and Robert D. Moser

5d. PROJECT NUMBER
L31L42

5e. TASK NUMBER

5f. WORK UNIT NUMBER

7. PERFORMING ORGANIZATION NAME(S) AND ADDRESS(ES)

U.S. Army Engineer Research and Development Center
Geotechnical and Structures Laboratory
Information Technology Laboratory
3909 Halls Ferry Road
Vicksburg, MS 39180-6199

8. PERFORMING ORGANIZATION REPORT NUMBER

ERDC TR-19-9

9. SPONSORING / MONITORING AGENCY NAME(S) AND ADDRESS(ES)

U.S. Army Corps of Engineers
Washington, DC 20314-1000

10. SPONSOR/MONITOR'S ACRONYM(S)

11. SPONSOR/MONITOR'S REPORT NUMBER(S)

12. DISTRIBUTION / AVAILABILITY STATEMENT

Approved for public release; distribution is unlimited.

13. SUPPLEMENTARY NOTES

The report includes work conducted in a collaborative research and development program between Eaton Corporation and the US Army Engineer Research and Development Center focused on novel multi-scale modeling approaches to optimize metal additive manufacturing (AM) processes. The research focused on developing new lower-length scale thermal history predictions with microstructure to property relationships to computationally study a variety of manufacturing parameters and their correlation to defects generation and mechanical properties. Direct metal laser sintering (DMLS – a powder bed AM method) and directed energy deposition (DED – a blown powder AM method) were studied. The results indicated that the developed tools could rapidly predict optimal manufacturing parameters through fast running layer-by-layer thermal models of each respective AM process. Physical test specimens and prototypes were also produced as part of the study to aid in model calibration and validation through mechanical testing and microstructural characterization.

15. SUBJECT TERMS
Additive manufacturing, Modeling, DMLA, DED, Metals, AM, 3-D printing
Multiscale modeling, Microstructure
Laser sintering

16. SECURITY CLASSIFICATION OF:			**17. LIMITATION OF ABSTRACT**	**18. NUMBER OF PAGES**	**19a. NAME OF RESPONSIBLE PERSON**
a. REPORT	**b. ABSTRACT**	**c. THIS PAGE**			**19b. TELEPHONE NUMBER** *(include area code)*
UNCLASSIFIED	UNCLASSIFIED	UNCLASSIFIED		148	